Ultrasound-mediated therapies for metastatic brain tumours

Oliver Vince

St Catherine's College

Supervised by Professor Eleanor Stride

A thesis submitted for the degree of
Doctor of Philosophy in Engineering Science

Statement of originality

I hereby declare that this submission is my own work and, to the best of my knowledge, it contains no materials previously published or written by another person, or substantial proportions of material which have been accepted for the award of any other degree or diploma at the University of Oxford or any other educational institution, except where due acknowledgement is made in the thesis.

Any contribution made to the research by others, with whom I have worked at the University of Oxford or elsewhere, is explicitly acknowledged in the thesis. I also declare that the intellectual content of this thesis is the product of my own work, except to the extent that assistance from others in the project's design and conception or in style, presentation and linguistic expression is acknowledged.

Oliver Vince

October 2019

Acknowledgements

This thesis would not have been possible without support, guidance and advice from many people over the past 3 years.

First and foremost, I am extremely grateful to Professor Eleanor Stride for her support, friendship and encouragement throughout the whole time that we have worked together. Her belief and confidence in my ideas has developed me as both a researcher and a person and enabled me to achieve more in these past 3 years than I ever dreamed would be possible.

During my time in BUBBL, I am incredibly fortunate to have been able to work alongside some excellent scientists; Dr. Sarah Peeters, Dr. Miles Aron, Dr. Michael Gray, Dr. Luca Bau and Dr. Vanessa Johanssen. Many others in the lab, especially Claudia Hill, Alex Richards, Veerle Brans, Dr. Valerio Pereno, Catherine Paverd, Magda Abbas, Dr. Estelle Beguin, and Dr. Joe Blackmore, have been great friends. The other BUBBL supervisors, Prof. Constantin Coussios, Prof. Robin Cleveland and Prof. Robert Carlisle have inspired, challenged and guided me.

I am grateful to the University of Oxford, the Oxford Centre for Drug Delivery Devices, Worcester College and St. Catherine's College for their support. I am also extremely grateful to the Leathersellers' Company and the Institution of Engineering and Technology for their recognition of my work.

Siân; thank you for your unwavering support and confidence in me during all of the ups and downs. You made this all possible. Long may the adventures continue.

Mum, Dad, Harris and Holly; your constant good humour and the knowledge that you are always there for me is what keeps me going. Thank you.

Publications

Antibody targeted microbubbles and unfocused ultrasound enable targeted US-BBBD *in vivo*
S. Peeters,* **O. Vince**,* V. Johanssen, A. Thomas, M. Gray, E. Stride & N. Sibson *In preparation*

Microbubbles containing lysolipid enhance US-BBBD *in vivo*
O. Vince,* S. Peeters,* V. Johanssen, M. Gray, S. Smart, N. Sibson & E. Stride *Advanced Healthcare Materials,* **2021**, 10, 2001343[1]

Entirely off-grid and solar-powered DNA sequencing of microbial communities during an ice cap traverse expedition
G. Gowers, **O. Vince**, J. Charles, I. Klarenberg, T. Ellis & A. Edwards *Genes*, **2019***,* 10(11), 902[2]

Investigating the role of lipid transfer in microbubble mediated drug delivery
M. Aron,* **O. Vince**,* M. Gray, C. Mannaris & E. Stride *Langmuir*, **2019**, 35, 13205-13215[3]

Layered acoustofluidic resonators for the simultaneous optical and acoustic characterisation of cavitation dynamics, microstreaming and biological effects
V. Pereno,* M. Aron,* **O. Vince**, C. Mannaris, A. Seth, M. de Saint Victor, G. Lajoinie, M. Versluis, C. Coussios, D. Carugo & E. Stride *Biomicrofluidics*, **2018**, 12, 034109[4]

**Denotes equal contribution to study*

Conference Presentations

Title	Conference	Month	Year	City
Targeting drug delivery to brain metastases	OxCD3 Drug Delivery Conference	September	2019	Oxford
HIFU to HIUFU: targeting the bubbles, not the ultrasound	Microbubble Symposium	June	2019	Oxford
Optimising the composition of microbubbles to improve the delivery of model drugs *in vitro* and *in vivo*	ISTU Conference	June	2019	Barcelona
Microbubbles to treat microscopic brain tumours	SfB competition, Houses of Parliament	March	2019	London
The role of lipids in sonoporation	Symp. on Ultrasound Contrast Imaging	January	2019	Rotterdam
Nanodroplets for the treatment of brain metastases: a pre-clinical study	ASA Conference	November	2018	Victoria
Nanodroplets for the treatment of brain metastases: a pre-clinical study	Microbubble Symposium	July	2018	Leeds
Nanodroplets for the therapy of brain metastases	Symp. on Ultrasound Contrast Imaging	January	2018	Rotterdam
Mechanisms to target metastatic tumours	Winter School on Therap. Ultrasound	March	2017	Chamonix

Thesis abstract

As oncolytic treatments continue to improve and patient survival times increase, cancer cells have more and more time to metastasise from the primary tumour to other locations in the body. This is particularly dangerous when metastases spread to the brain; the sensitivity of cerebral tissue means that brain metastases often cause severe morbidity or mortality before they are large enough to detect clinically. Current treatments for this condition are palliative and woefully inadequate; their lack of targeting causes such severe side effects that many patients choose to forgo them.

Originally used for clinical imaging, ultrasound is being developed as a low cost, non-invasive and non-ionising therapeutic modality. Microbubbles, originally developed as ultrasound contrast agents, are capable of encapsulating a wide range of therapeutic agents and encouraging uptake of these agents into tissue. The combination of focused ultrasound and circulating microbubbles is capable of locally and transiently permeabilising the blood brain barrier, the main obstacle to drug delivery in the brain.

Chapters 2 and 3 of this thesis show that the specificity of ultrasound-mediated blood-brain barrier disruption (US-BBBD) can be increased by actively targeting microbubbles to disease sites in the brain before ultrasound exposure, removing the need for prior knowledge of the disease site. Chapters 4 and 5 of this thesis show that the efficacy of US-BBBD can be increased by optimising the lipid composition of microbubbles. This increases the delivery to in brain tissue without requiring an increase in ultrasound energy. If successfully translated to clinic, the combination of these techniques has the potential to deliver the first safe, effective and non-invasive therapy for brain metastases.

Graphical Abstract

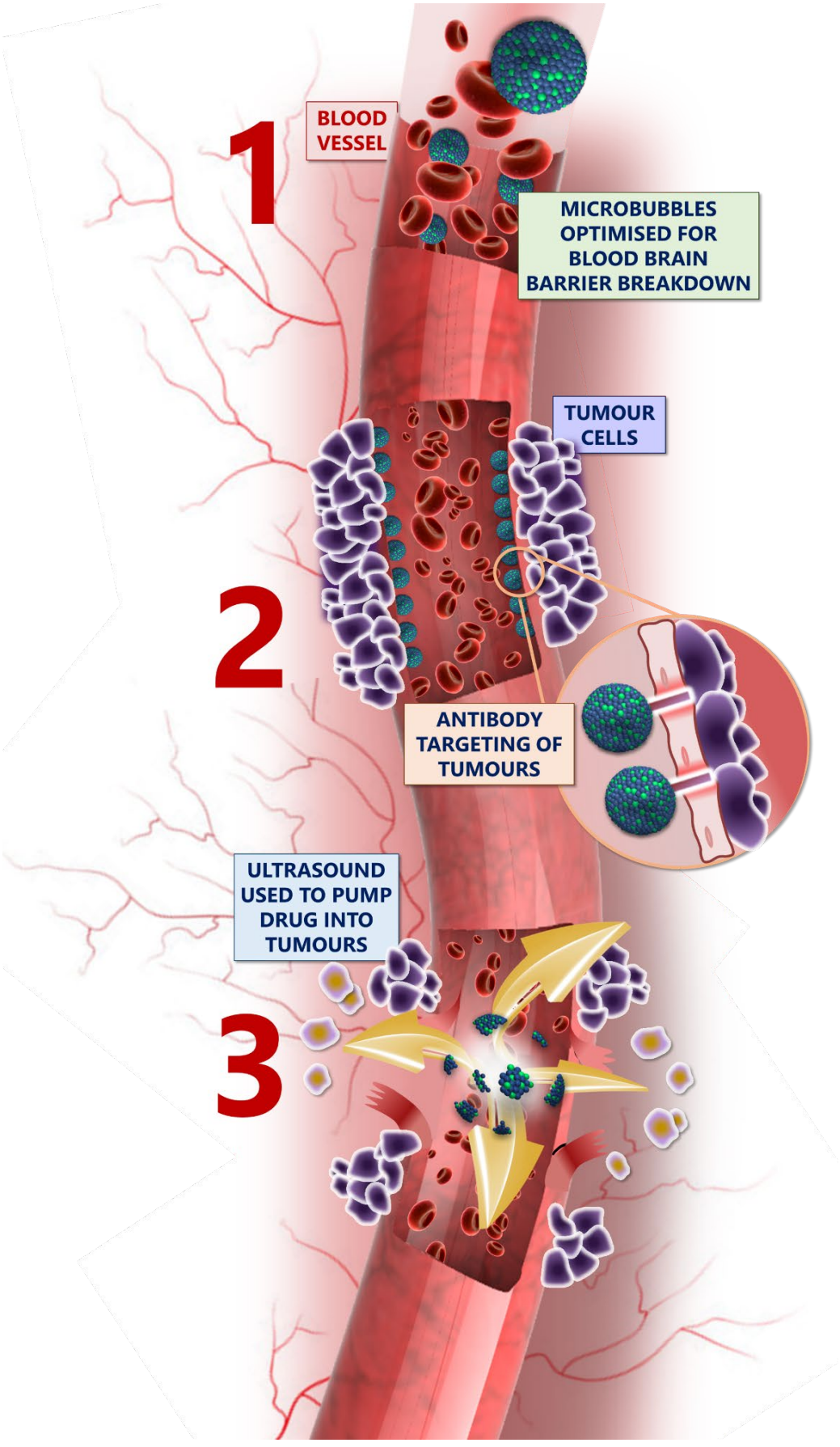

Contents

Abbreviations

Abbreviation	Meaning
ALS	Amyotrophic Lateral Sclerosis
Anti-VCAM-1	The monoclonal antibody to VCAM-1
AV-MBs	Microbubbles conjugated with anti-VCAM-1
BBB	Blood brain barrier
BBBD	Blood brain barrier disruption (without ultrasound)
Biot-MBs	Microbubbles coated in biotin
BTB	Blood Tumour Barrier
Control-MBs	Microbubbles used as controls
CT	Computerised Tomography
DC	Duty Cycle
ECAM	Endothelial Cell Adhesion Molecule
EPR	Enhanced Permeability and Retention (effect)
FUS	Focused Ultrasound
GBM	Glioblastoma Multiforme
Gd-DTPA	Gadolinium-DTPA (ultrasound contrast agent)
GP	Generalised Polariseation
ICAM	Intracellular Cell Adhesion Molecule
IFP	Interstitial Fluid Pressure
IgG	Immunoglobulins
IgG-MBs	Microbubbles conjugated with immunoglobulins
Lyso-MBs	Microbubbles containing lysolipid
MAdCAM	Mucosal Vascular Addressin Cell Adhesion Molecule
MB	Microbubble
MPIO	Microscopic particle of iron oxide

MRI	Magnetic Resonance Imaging
NBD	Nitrobenzoxadiazole
PBS	Phosphate Buffered Saline
PC	Phosphatidylcholine
PCD	Passive Cavitation Detector
PE	Phosphatidylethanolamine
PEG	Poly-ethylene glycol
PET	Positron Emission Tomography
PNP	Peak-negative prtessure
PRF	Pulse Repetition Frequency
RMT	Receptor-mediated transcytosis
SRS	Stereotactic Radio Surgery
Strept-MBs	Microbubbles conjugated with streptavidin
TE	Time to Echo
TR	Repetition Time
UFUS	Unfocused Ultrasound
US	Ultrasound
USPIO	‘Ultra-small’ particle of iron oxide (relative to MPIO)
VCAM-1	Vascular Cell Adhesion Molecule-1
VEGF	Vascular Enothelial Growth Factor
WBRT	Whole-Brain Radiation Therapy

Chapter 1. Introduction

"The stark fact remains that the worldwide burden of cancer remains huge and is escalating, and advanced or metastatic disease is mostly intransigent to treatment. Billions of dollars are riding on the premise that personalized medicine and targeted therapy will come to the rescue."

- ***WHO World Cancer Report 2014***[5]

1. Introduction

1.1. Metastatic brain tumours

As treatments for primary tumours improve and patient survival times continue to increase, there is, unfortunately, an increased risk of cancer cells breaking away from the primary tumour in which they first formed, traveling via the blood or lymph system and forming new tumours elsewhere in the body. Due to their invasive and aggressive characteristics, these metastatic tumours are the leading cause of cancer-related deaths worldwide.[5,6]

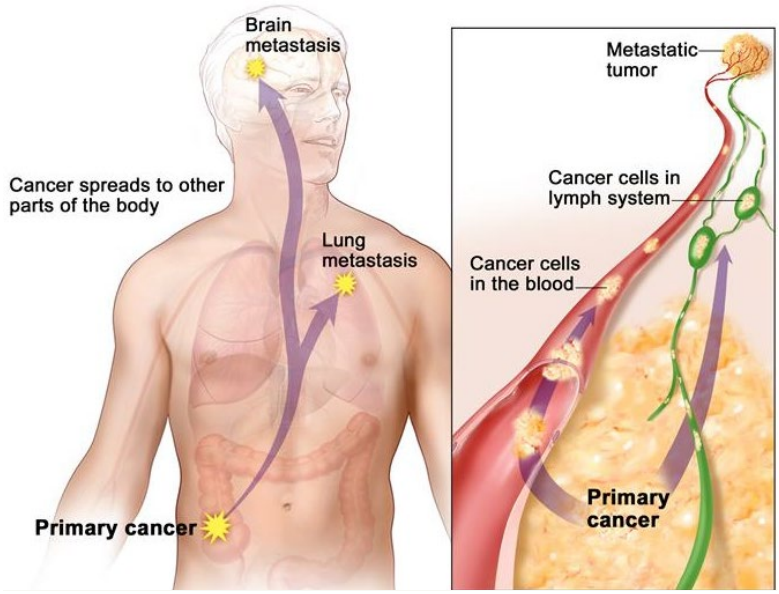

Figure 1.1.1: Cancer metastasis, from the National Cancer Institute.[7]

The first part of this Chapter describes the formation, characteristics and the healthcare burden of brain metastases. The key challenges that currently prevent successful treatment of this disease are then discussed, followed by an outline of how the techniques explored in this thesis could provide solutions to these challenges. This is followed by a thesis summary.

1.1.1. Formation of brain metastases

The spread, or metastasis, of cancer cells away from the primary tumour is a highly selective, non-random process consisting of a series of linked, sequential events.[8] This process has been described as the 'metastatic cascade'[9] and is summarised in Figure 1.1.2.

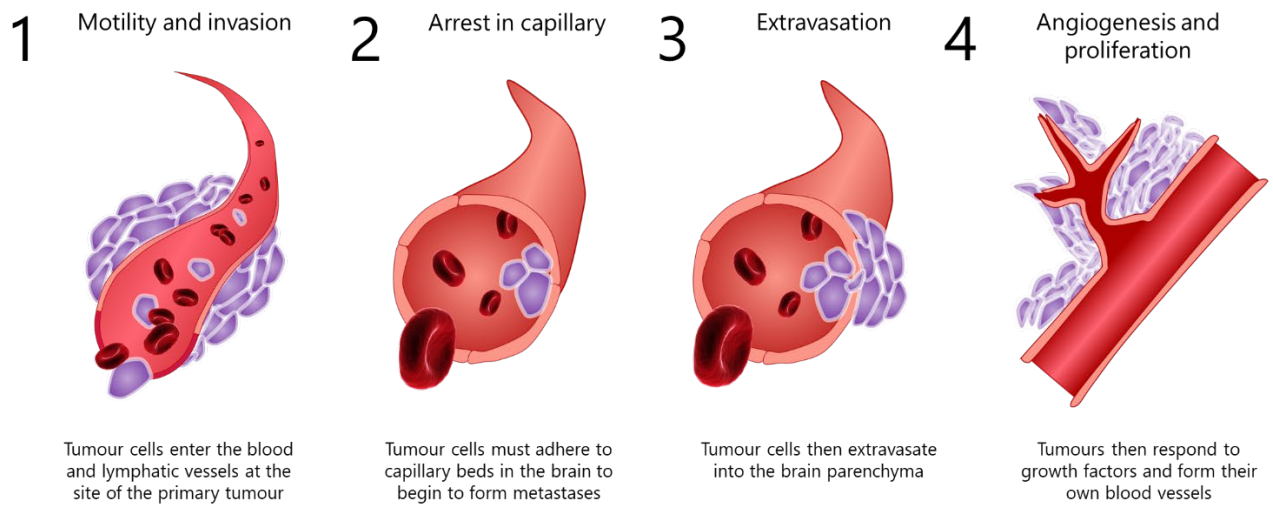

Figure 1.1.2: The metastatic pathway.

A primary tumour consists of a genetically heterogeneous group of cells containing subpopulations of cells with varying degrees of metastatic potential.[8] Primary tumours close to major blood vessels[10,11] with an immature neo-vascular system[12] and a high interstitial pressure[13] are more likely to release haematogenous tumour cells. Once in the circulation, these intravascular tumour cells are subject to non-specific mechanical forces, such as haemodynamic turbulence, which may cause mechanical destruction of the cells, either before or during the extravasation process. The entry into and survival in the blood stream is termed intravasation.[8]

Once they reach the brain vasculature, in order for clinical metastases to form, these tumour cells must arrest in blood vessels, extravasate into the brain parenchyma, induce angiogenesis, and proliferate in response to growth factors.[14–18]

Tumour cells primarily arrest at sites of slow blood flow within the capillary bed at vascular branch points,[19] with size restriction[20,21] and specific adhesive interactions[6] also playing a role. This causes early changes in the brain microenvironment[22] as the tumour cells encounter brain vascular endothelial cells, which seem to promote metastatic tumour cell growth and invasion.[19,23] Cell motility, cell adhesion, and enzymatic remodelling of the extracellular matrix (ECM) are all involved in local brain invasion by the cancer cells.[8] Degradation of the ECM is thought to further aid tumour invasion by clearing a pathway for the invading tumour cells.[24,25] Several genes are known to play a

key role in mediating the migration of cancer cells into the brain tissue,[26] and integrins such as $\alpha_v\beta_3$[27,28] and β_1[23] control tumour cell arrest and adhesion to the vasculature.

Different tumour types are more likely to spread to certain organs; prostate cancer frequently metastasises to bone, whilst melanoma frequently metastasises to the lung, liver and brain.[29,30] The propensity of cancer cells to spread to specific sites has been hypothesised to depend upon two factors: the cancer cell (the 'seed') and the receiving organ environment (the 'soil').[31] This hypothesis is widely regarded as fundamentally correct,[9] and has been expanded to include suggestions that cancer cells (seeds) may bring their own host cells (soil) to the site of metastasis[32] and that in the brain, cancer cells may be able to use the existing vascular basement membrane as 'soil'.[23] Physiologically, this occurs because endothelial cells in the vasculature of different organs express different cell-surface receptors[33] and growth factors that can support or inhibit the growth of metastatic cells.[34]

Once cancer cells have extravasated into brain tissue, the growth and proliferation of metastatic tumours is dependent on an adequate blood supply being established.[35–37] Tumour cells can either grow along pre-existing blood vessels (perivascular growth)[38] or recruit new blood vessels (angiogenesis). If vascular growth fails, tumours cannot grow further than 200µm away from the pre-existing blood vessel as their growth is limited by the maximum distance of diffusion of oxygen in tissue.[39] However, tumours up to 3mm long can grow along pre-existing blood vessels.[40]

For successful metastasis, all steps of the cascade need to be completed.[8] For example, failure to stimulate angiogenesis leads to regression of lung adenocarcinoma cell brain metastases and the inability to locate cerebral vessels for co-option leads to activation of cell death programmes in melanoma brain metastases.[19] As each step of the cascade can be a rate-limiting step, this process is highly inefficient,[9,41] with only 0.1%[5] of haematogenous cancer cells successfully forming metastases. Therefore, therapeutic strategies can target both the cancer cells and the homeostatic factors that promote tumour-cell growth, survival, angiogenesis, invasion, and metastasis.[42]

1.1.2. Characteristics of brain metastases

Even though few cancer cells complete the metastatic cascade, certain aspects of the brain microenvironment act to protect any metastatic tumours that do form. The endothelial cells in the brain (the blood brain barrier (BBB) or blood tumour barrier (BTB), reviewed further in Section 1.5.2) protect metastases from the cytotoxic effects of chemotherapy.[5] Unlike endothelial cells in other parts of the body, the endothelial cells in the brain constitutively express transporters that mediate the efflux of many chemotherapeutic agents and other small-molecule targeted therapies.[5] Astrocytes, glial cells that provide biochemical support to the endothelial cells within the brain microenvironment, might also serve to protect brain metastases from cytotoxicity induced by chemotherapeutic drugs,[43] with protective effects having been demonstrated in human melanoma cell lines,[44] breast cancer cells and lung cancer cells.[45]

Once formed, the new blood vessels in metastatic brain tumours have significantly larger diameters, thicker basement membranes and lower microvascular density than the blood vessels in the surrounding brain parenchyma.[46] As these vessels are structurally and functionally abnormal, they exhibit heterogeneous blood flow and hyperpermeability.[46–49] This creates regions of hypoperfusion where the supply of nutrients and oxygen is reduced and waste removal is impaired. This creates an abnormal metabolic environment, characterised by hypoxia and acidosis.[21] Drug penetration into these tumours is then hindered by the interstitial hypertension and the lack of convective transport.[50,51] It is thus clear that the molecular and cellular changes within metastatic brain tumour vasculature and the microenvironment should be considered when designing strategies to improve the delivery and efficacy of therapeutic agents.[21]

The distribution of brain metastases in the brain correlates with blood flow and tissue volume, with 80% detected in the cerebral hemispheres, 15% in the cerebellum, and 5% in the brainstem[52–54].

1.2. Motivation

Metastases are the leading cause of cancer-related deaths worldwide.[6] Metastases to the brain are particularly dangerous; they are the most prevalent of intracranial malignancies[55] and the median survival for untreated patients is only 5 weeks.[56,57]

The median time from primary diagnosis to clinical presentation with a brain metastasis is 12 months, ranging from 3 to 53 months depending on the type of cancer.[58] For patients who undergo treatment for their metastatic disease, the median duration from presentation with brain metastases to death is 4 months, ranging from 3 to 13 months depending on the cancer cell type.[58] Incidence varies with primary tumour type, ranging between approximately 10% to 30% and 6% to 10% in adult and child cancer patients respectively.[59–61] This incidence is estimated to be between 3 and 10 times higher than the incidence of solid brain tumours.[62] As formal diagnosis is sometimes not obtained if the patient is extremely unwell, the incidence of metastatic brain tumours is found to be even higher at autopsy.[63]

Most brain metastases originate from primary cancers in the lung (40–50%), breast (15–25%) or from melanoma (skin cancer) (5–20%).[64,65] Each year in the United States, an estimated 97,800 to 200,000 new cases of brain metastasis are diagnosed.[59–61,66] This number is increasing as a result of the increased ability of magnetic resonance imaging (MRI) to detect small metastases and improvements in systemic therapy of the primary tumours, leading to longer patient survival.[60,61,67–70] There has also been a global increase in cancer prevalence that has occurred during this time, in particular with cancers such as lung cancer that have a tendancy to metastasize to the brain. The risk of brain relapse for cancer patients today is also increasing,[71–73] partly as a consequence of systemic large-molecule drug therapies that are more effective against extracranial than intracranial cancer deposits.[55,74]

Most patients exhibit multiple tumours at the time of brain metastasis diagnosis.[67] Neuropsychological testing demonstrates cognitive impairment in 65% of patients with brain metastases,[75,76] which might be a result of destruction or displacement of brain tissue by the

expanding tumour, peritumoural edema leading to further disruption of surrounding white matter tracts, increased intracranial pressure, and/or vascular compromise.[67]

The spread of cancer to the brain is a devastating complication that is associated with very poor prognoses. This has been the case for decades, largely because of a lack of effective therapeutics to augment surgery and radiotherapy.[55] In their 2014 World Cancer Report, the World Health Organisation identified the lack of targeted therapies specific for brain metastases as one of the major unmet clinical needs in global cancer care.[5]

1.3. Current clinical therapeutic techniques

Current clinical treatments for brain metastases include surgery, whole-brain radiation therapy (WBRT), stereotactic radiosurgery (SRS), chemotherapy, growth factor inhibitors, or a combination of these therapies.[67] These are summarised in Figure 1.3.1.

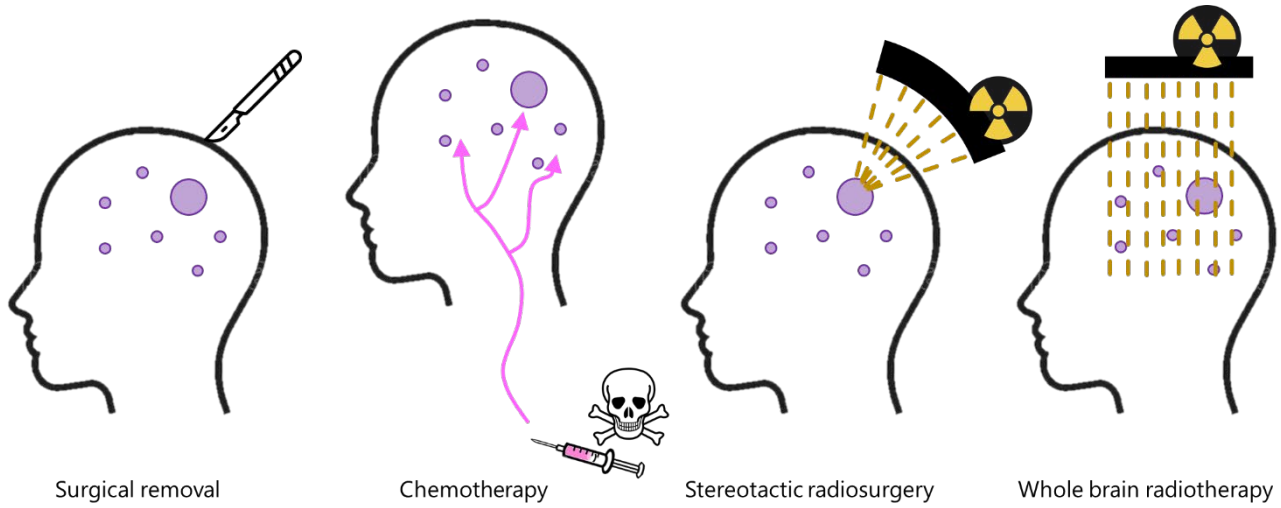

Figure 1.3.1: Schematic representations of the four main treatments currently used in the clinical management of brain metastases

These treatments are, however, palliative and the non-invasive techniques (WBRT, SRS and chemotherapy) have such severe side effects that many patients choose to forgo them.

Surgery is the preferred treatment for accessible, symptomatic lesions in patients with controlled extracranial disease and a good performance status.[77] The addition of radiotherapy to surgery does increase local control.[77–79] Whilst surgery relieves symptoms in 60-90% of patients,[80–82] local tumour recurrence is a persistent problem, occurring in 5-40% of cases.[77] One key advantage of surgery is the ability to study the excised tumour for biomolecular markers which may enable personalisation of subsequent treatments.[55] These markers differ from those of the primary tumour in many cases.[83,84]

Any survival benefit arising from the use of existing therapeutics is primarily due to the stabilisation of extracranial disease, rather than from measurable effects on brain metastases.[55] Aside from the side effects arising from off-target delivery, the efficacy of chemotherapy in the treatment of brain metastasis is severely limited by several factors. Chemotherapeutics have poor blood-brain barrier

(BBB) penetrability and many patients develop multiple resistance mechanisms due to prior rounds of chemotherapy for their primary tumour. It is for this reason that patients with brain metastases have historically been excluded from clinical trials testing new agents.[21,55]

Radiotherapy may be used as the primary treatment for local tumour control, particularly in patients with comorbidities who have multiple, deep, inaccessible lesions.[55] Radiotherapy is more effective on tumours that have metastasised from certain types of primary tumours, and tumours that are small (below 10mm diameter).[85–87] When considering radiotherapy, the total tumour volume is a better predictor of successful disease control than the number of individual lesions (providing it is under 250mm^3).[86,87]

Survival for patients with brain metastases treated with WBRT typically ranges from 4–6 months, but can be as long as 12–24 months for selected patients.[54] Randomized clinical trials have shown that surgery or SRS combined with WBRT improves overall survival when compared with WBRT alone in patients with a single metastasis in the brain. In patients with four or fewer brain metastases, SRS results in equivalent overall survival but worse intracranial disease control compared with SRS plus WBRT.[88,89] The combination of radiotherapy and chemotherapy improves response rate and/or progression-free survival in some studies, but not overall survival.[90,91]

It should be noted that the use of immune checkpoint inhibitors to treat brain metastases is generating increasing interest due to their ability to modulate the immune system to recognise tumour antigens and therefore treat widespread disease.[92] Six clinical trials using immunotherapy to treat brain metastases have concluded so far,[92] with the most promising showing a response in 56% of patients and 25% showing complete elimination.[93] However, upregulating the immune system can present serious risks and unique neurologic toxicities to patients with brain metastases.[94]

1.4. Current clinical imaging techniques

As established in Section 1.3, current therapeutic techniques do not provide a means of satisfactorily treating brain metastases. This fact, combined with a lack of patient screening and a lack of clinical imaging modalities capable of distinguishing micro-metastases (<1mm diameter) means that treatment benefits are only incremental.[95] By the time treatment begins, brain metastases are often already resistant to multiple lines of therapy and are equipped for efficient adaptation to new selection pressures.[55]

Brain imaging is not routinely performed after treatment for primary cancer unless there is a specific indication or new symptoms are presented.[55] The decision has both an economical and clinical basis; misdiagnosis can lead to unnecessary physical harm and serious psychological stress.[55]

Computerised tomography (CT) and MRI are the modalities which have traditionally been used to assess metastatic disease to the central nervous system[96]. An inherently better soft tissue contrast resolution, stronger contrast enhancement, lack of bone artefacts, partial volume effects and direct multi-planar imaging enables MRI to pick up smaller sized as well as a higher number of metastases than a CT scan.[97,98] A technique that has grown rapidly is the combination of Positron Emission Tomography (PET), CT scans and the use of radiolabelled drugs.[99] However, PET is limited by its relatively poor spatial resolution as reconstruction algorithms typically trade off resolution for reduced noise.[100] Even the most advanced algorithms can only resolve objects approximately 3 mm in diameter.[101] Therefore, contrast-enhanced MRI remains the gold standard imaging modality; PET is able to detect only 61-68% of the metastatic lesions found by MRI.[102,103]

Significant research efforts are being directed towards the application of machine learning methods in image analysis,[104,105] and it is becoming possible to correlate more subtle image parameters with the development of brain metastases.[106,107] However, contrast-enhanced MRI relies on passive contrast enhancement arising from blood brain barrier (BBB) breakdown, something that is

physiologically not present in micro-metastases.[108] MRI scanners are also very expensive, making cost a limiting factor.[101]

It is the lack of ability to reliably locate all of the metastatic tumours within a brain, especially those that are small and asymptomatic, that leads to the widespread use of non-targeted treatments which often have incredibly harmful side effects. It is therefore imperative that novel imaging techniques capable of elucidating micro-metastases from healthy brain tissue, such as the antibody targeted MRI contrast agents upon which Part 1 of this thesis is based,[108,109] remain a top research priority.

1.5. Treatment challenges

Whilst there are many problems that need to be overcome before a safe, effective and widespread treatment for metastatic tumours in the brain is realised, this thesis focuses on two key challenges that have fundamentally limited the efficacy of all treatments so far.

1.5.1. Key challenge 1: Targeting therapy

1.5.1.1. Motivation

More effective techniques for delivering therapeutics directly to the site of disease are widely sought after in many healthcare applications, and particularly in oncology. In the treatment of brain metastases, as established in Section 1.3, the systemic therapies that are currently available are inadequate. The first reason for this is a lack of localised drug delivery technologies[110] that enable the majority of the compound to interact with the target tissue.[111] The ability to target the delivery of these therapeutics directly and selectively to the site of brain metastases would lead to a step change both their clinical efficacy and reducing off-target toxicity.

To be effective, a chemotherapeutic must accumulate in sufficient local concentration at the target site. However, achieving this without causing severe off-target damage to healthy tissues in the body has, so far, proved to be an insurmountable obstacle. Thus, chemotherapy doses are limited by the ability of the patient to withstand the side effects, rather than the amount required to eliminate the tumour.[112] This is because the traditional mode of action of chemotherapeutics has been to target fast-dividing cells, which, alongside cancer cells, includes hair cells, bone marrow cells and cells in the gut.[113]

Biological therapeutics, including antibodies and oncolytic viruses, may not exhibit the same degree of systemic toxicity but they do suffer from either rapid clearance from the circulation or neutralisation before they reach their targets.[113,114] This class of therapeutics has shown reasonable success with intra-tumoural delivery, but not for systemic delivery, and thus treatment of metastatic disease has been severely limited.[114] Of the 24 studies investigating one oncolytic virus (the vaccinia

virus) clinically, only the studies delivering the virus via intra-tumoural injection showed improved survival.[113] Therefore, whilst the ability of these therapeutics to infect, propagate and spread throughout poorly diffused tumours may prove critical in the fight against cancer, the fact that they cannot be delivered intact to the site of deep or widespread, microscopic tumours will remain an intrinsic limitation.[115]

As outlined in Section 1.4, the inability of currently available clinical imaging techniques to elucidate micro-metastases in the brain leads to a widespread use of non-targeted therapies. The two targeted therapies in widespread use, surgery and stereotactic radiosurgery (SRS), are incapable of removing micro-metastases, especially once they are widespread throughout the brain. The gold-standard MRI techniques rely on blood-brain barrier (BBB) breakdown by the tumours. Studies of brain metastasis models in mice have indicated that breakdown of the BBB does not occur until tumours are >500μm in diameter.[108] The current size limit of clinical detection of brain metastases is 2–5 mm although they are more typically detected between 5 mm and 1 cm in diameter.[116] This is when the BBB around the tumour becomes permeable to contrast agents.[117]

By the time that metastases are large enough to image, the physical condition of patients is often very poor. On top of this, micrometre-scale tumours (that are currently too small to image) have not yet developed a poorly perfused and hypoxic core, and so are often more susceptible to standard therapeutics. For these two reasons, the ability to treat early stage metastases before BBB breakdown occurs is highly desirable.

Drug delivery in the brain can be targeted invasively, relying primarily on disrupting the BBB integrity by direct intracranial drug delivery through intracerebroventricular, intracerebral or intrathecal administration.[118] However, these approaches are severely limited by poor distribution into the brain parenchyma.[119]

Non-invasive attempts to target therapeutics in the brain, such as lipophilic drug analogues, prodrugs, carrier-mediated drug delivery, receptor/vector-mediated drug delivery and intranasal drug delivery

can be summarised into two categories; passive and active targeting. These approaches are summarised in Figure 1.5.1.

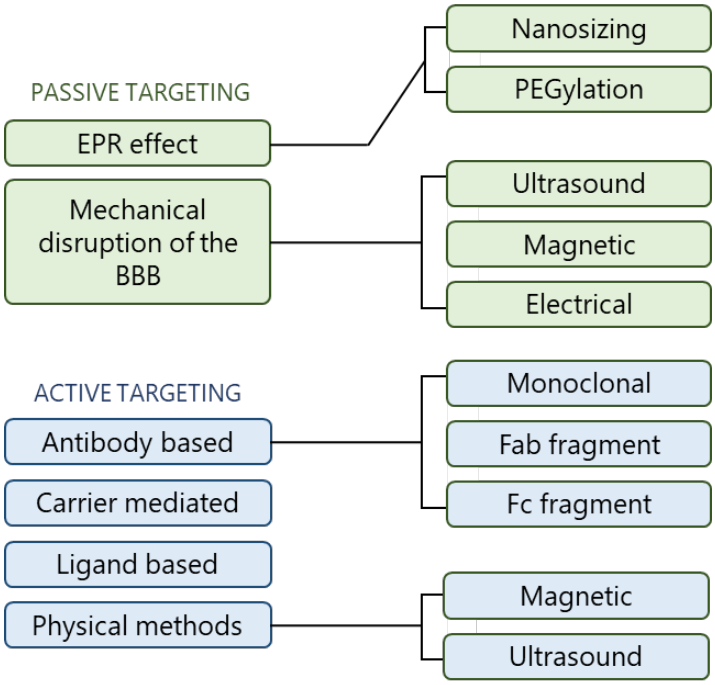

Figure 1.5.1: A summary of the targeting strategies available for targeting therapeutics in the brain.

1.5.1.2. Passive targeting

Passive targeting strategies rely on the preferential accumulation of drug molecules into tumour cells.[120] This preferential accumulation, first described by Maeda and Matsumura in 1986,[121] applies to particles with a nanometre size range and aims to exploit both the leaky vasculature and impaired lymphatic drainage around larger tumours.[122] This is referred to as the enhanced permeability and retention (EPR) effect.

The high levels of cell growth and metabolism in the spatially confined volume in which tumours form causes solid stress and hypoxia.[123] To maintain tumour growth, the establishment of a new blood supply is mandatory for tumours larger than ~1-2 mm in diameter,[124] resulting in the production of pro-angiogenic factors, such as vascular endothelial growth factor (VEGF).[125] VEGF is responsible for endothelial cell survival, sprouting and vascular leakiness,[126] thereby providing the basis for EPR-mediated tumour targeting. Newly formed blood vessels often lack a smooth muscle layer and

pericytes;[127] they have a larger lumen and wider fenestrations. These fenestrations have sizes of up to 4.7 μm, with most being in the range of 1-100 nm.[128]

The ability of nanoparticles to permeate into tumour cells is greatly affected by the solubility of any lipids, surface characteristics, the molecular weight, and the presence of tight junctions.[129,130] Examples of commonly-used nanoparticles include polymeric particles, polymeric micelles, dendrimers, and liposomes.[122] Nanoparticles represent versatile tools to encapsulate various types of drugs by altering their physicochemical parameters and pharmacokinetic profiles.[131] Some of these nanoparticle formulations contain polymers such as polylactic-co-glycolic acid (PLGA) with high cell adhesion properties, designed to increase the contact time between the drug carrier and the target cells.[132]

An important approach for altering the pharmacokinetic behaviour of nanoparticles involves coating them in polyethylene glycol (PEG) to improve the circulation half-life and tissue distribution pattern.[133] PEG mainly protects these particles from being removed by natural particle elimination mechanisms (primarily phagocytosis)[134] and has been shown to significantly increase the clearance time of doxorubicin.[135] PEGylated liposomal doxorubicin has been shown to increase the concentration of drug within intracranial tumours by a factor of 20 when compared to free drug.[136] A particle must be at least 10 nm in diameter to avoid clearance by first-pass renal filtration and the optimal size range of 100-180 nm will ensure longer circulation time, increased accumulation within the tumour mass and lower renal clearance.[137,138] It should, however, be noted that some nanoparticles can produce serious adverse side effects.[139]

However, it has become apparent that the EPR effect is almost non-existant. It accounts for only 3% of nanoparticle uptake into tumours, with the remainder of the uptake accountable to active processes.[140] Any EPR effect that does exist is highly heterogeneous, with significant variation occurring between pre-clinical and clinical studies, between tumours of the same origin, between different stages of tumour development and among tumours and metastases within the same

patient.[141,142] This is because the vascular perfusion in tumours tends to be impaired and blood flow is often sluggish.[143,144] The lack of a fully functioning lymphatic drainage system causes a high interstitial fluid pressure (IFP) to develop. This attenuates nanomedicine accumulation and penetration, especially in the core of tumours.[145] This high pressure also contributes to the compression of blood and lymphatic vessels, further adding to the high IFP, causing blood vessel collapse and inefficient tumour perfusion.[146,147] On top of this, the fenestrations in the blood vessels often have malfunctioning endothelial cells blocking them.[148] A study that compiled the results of more than 100 preclinical studies into larger tumours found that the EPR effect leads to an overall median accumulation in tumours of 0.7% of the injected dose.[149] Considering the heterogeneity of the results, this may be sufficient for some patients, and it is much higher than what standard cytotoxic compounds can typically achieve.[150–152] As an example, one passive targeting study found that paclitaxel-loaded nanocarriers achieved a final concentration of drug in the tumour 3 times greater than free paclitaxel, even though this final concentration amounted to only 0.6% of the total injected dose.[153] Translation of EPR-based passive targeting to clinics has struggled in part due overestimations of this effect; most pre-clinical models are fast-growing xenografted mice models with a dense vasculature that do not recapitulate the majority of solid tumours in humans.[154,155]

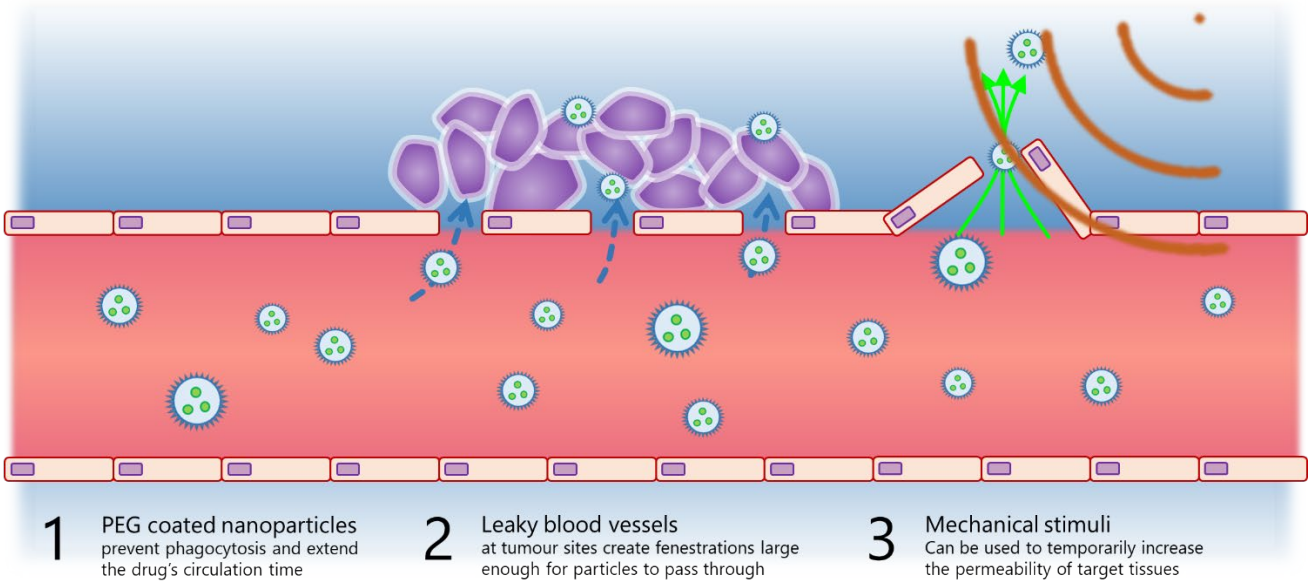

Figure 1.5.2: Some of the key mechanisms for passively targeting therapeutics

Whilst it is clear that there are issues with relying on the EPR effect for tumour targeting, perhaps the most pertinent criticism is that tumours can only be treated once they are large enough to disrupt the vasculature. Whilst this may be sufficient for treating glioblastoma multiforme (GBM), if treatment of brain metastases requires tumours to reach this size, such treatments will almost certainly remain palliative.

Another strategy for encouraging passive targeting in the brain is the use of systems that use physical stimulation (e.g. ultrasound, electricity, magnetism and photonic emission technologies[156]) to mechanically disrupt the BBB in target locations within the brain. To be effective, these techniques currently require accurate knowledge of the location of all tumours. The use of ultrasound to disrupt the BBB will be described in detail later in this Chapter. Some of the key passive targeting mechanisms mentioned in this Section are shown schematically in Figure 1.5.2.

1.5.1.3. Active targeting

Active targeting strategies utilise molecules (ligands, antibodies, antibody fragments and peptides[157]) with a high affinity for receptors and/or antigens that are overexpressed in the tumour vicinity or phagocytose therapeutics to shield them and then exploit specific influx transport systems within the blood-tumour barrier (BTB).[120,158] Active cellular targeting aims to increase the targeting efficiency of nanocarriers and increase their retention at the target site.[159–161] A schematic of the active targeting mechanism employed in Chapters 2 and 3 of this thesis can be found in Figure 1.5.3.

Receptors that have previously been targeted in this way include the $\alpha_v\beta_3$ and $\alpha_v\beta_5$ integrins. These are both overexpressed on the endothelial cells around tumours.[162] A therapeutic targeting of these integrins has been shown to significantly slow metastatic tumour progression.[163] Targeting the $\alpha_4\beta_1$ integrin and its endothelial ligand, vascular cell adhesion molecule-1 (VCAM-1), forms a major focus of this thesis and is reviewed in more depth in Chapter 2. Other targets that have been explored for

targeting brain metastases include mTOR, PI3K, HER2, EGFR, VEGF, VEGFR, BRAF, CLTA-4 and PARP.[164]

Once the specific receptor or antigen has been targeted, receptor-mediated transcytosis can then be employed to transport the conjugate across the BBB.[165] This can increase the delivery of cytotoxic agents to tumours cells whilst simultaneously limiting their exposure to healthy tissues.[164] The low-density lipoprotein receptor-related protein-1 (LRP-1) is one of the receptors capable of mediating transcytosis across the BBB. Targeting LRP-1 has previously been used to increase the transport of an anti-HER2 antibody,[166] paclitaxel[167] and doxorubicin.[168,169]

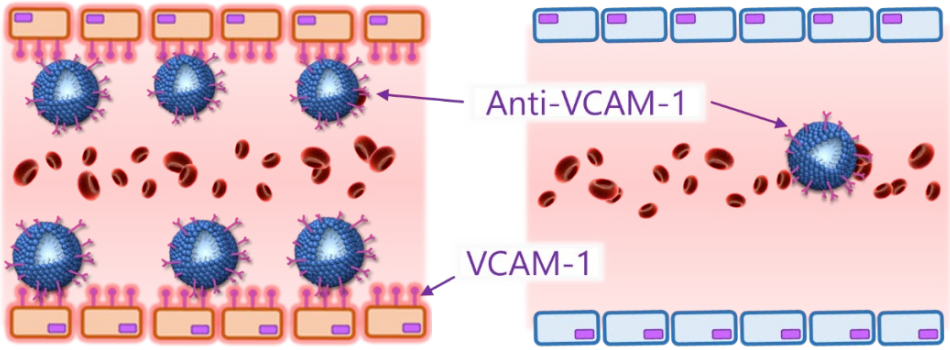

Figure 1.5.3: The active targeting mechanism employed in Chapters 2 and 3 of this thesis. Particles coated in the antibody for VCAM-1 (anti-VCAM-1) selectively bind to cells expressing VCAM-1.

Carrier-mediated transcytosis utilises circulating phagocytic cells such as monocytes or macrophages as 'Trojan horse' vehicles to deliver drug molecules into the brain.[170] Such cells are able to endocytose colloidal materials, including nanoparticles, microparticles and liposomes and then release these materials into their surroundings.[171] The ability of this technique to deliver nanoparticles to within less than the diameter of a tumour cell from brain metastases has been demonstrated.[172] This technique is particularly powerful as macrophages are able to reach lesions behind an intact BBB,[173] meaning that a leaky vasculature is not required. On top of this, macrophages may also be able to hone in on metastases elsewhere in the body.[172]

This leads to a key advantage that active targeting strategies have over passive strategies: whilst the EPR effect can act as an aid, it is not a requirement. Combined with this, the ability of these strategies

to treat a disease that is dissipated around the body opens the door to the treatment of early stage metastatic tumours.[174] These mechanisms could also be extended to treat haematological malignancies (e.g. leukaemia and lymphoma).[174] Active targeting also has the potential to achieve targeting with a cellular level of precision, enabling selective treatment of diseased cells even if they are interspersed amongst healthy cells.

The biggest challenge for active targeting strategies is choosing a suitable target receptor or antigen. Traditionally based on overexpressed disease markers, these targets are often highly relevant for therapeutic monoclonal antibodies but may not be suitable for nanocarriers largely because these nanocarriers then struggle to escape from the blood stream and into the surrounding tissue.[174] This issue is addressed if the nanocarrier is a microbubble capable of permeabilising the BBB and encouraging uptake as in this thesis.

The heterogeneity within and between tumours adds further complexity.[175] Most active, cell-specific nanocarriers target a single cell-surface receptor on tumour cells, thus disregarding tumour heterogeneity and promoting selection toward the survival of resistant clones.[174] Consequently, current treatment usually results in apparent partial or complete responses, immediately followed by disease relapse.[176]

Due to the high cost and complexity of active targeting, GMP manufacture and regulatory approval has proved challenging: 15 passively targeted nanocarriers have been approved for clinical use, whereas no actively targeted nanocarriers have yet advanced past clinical trials.[174] Passive targeting strategies typically require simpler bioconjugate structures which are more easily synthesized with high yield, reduced cost and a high stability profile.[122]

1.5.1.4. Drug release

If drugs are integrated into a carrier system to target them to the site of metastases and/or to shield them during systemic circulation, these drugs can also then be released from these carriers either passively or actively. Passive delivery typically involves coating agents in a polymer that biodegrades

over a pre-determined timescale.[177] Active release requires an external stimulus (e.g. pressure, pH or temperature) to induce delivery and can potentially be controlled much more precisely.[178] For successful therapy there must also be sufficient uptake of the drugs by the target tissue. This can be as a result of the cell's natural metabolic processes but can also be encouraged by external stimuli.[179] A comparison of active and passive drug release can be found in Figure 1.5.4.

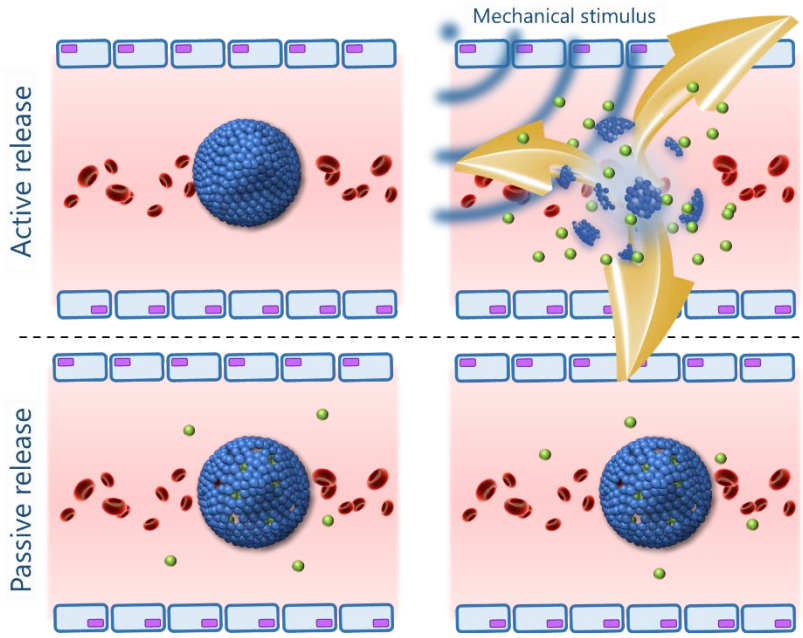

Figure 1.5.4: Active and passive release of drug from carriers into the blood stream. Actively releasing carriers are capable of releasing therapeutics when exposed to an external stimulus; passively releasing carriers release therapeutics over a pre-determined timescale.

1.5.1.5. Transfer across the BBB

Once the drugs have both reached the site of the tumour and have been released from any carrier, their diffusion into the brain can be divided into paracellular diffusion (between the endothelial cells) and transcellular diffusion (through the endothelial cells).[122] To date, clinical BBB-crossing strategies have largely consisted of exploiting either a transcellular lipophilic pathway or transcytosis.[180] However, as is clear from the remainder of this thesis, focused ultrasound is a promising modality for safely, locally and reversibly increasing the permeability of the BBB to large molecule compounds.

1.5.2. Key challenge 2: The blood-brain barrier

The blood-brain barrier (BBB) is a selective barrier between the systemic circulation and the cerebrospinal fluid that regulates brain homeostasis and prevents an uncontrolled flow of substances from the blood into the brain.[181] It is formed by specialized endothelial cells lining the cerebral microvasculature, together with pericytes and astrocytes.[182] As a morphological and physiological barrier, the BBB exists to protect the brain.[183–185]

The junctions between the endothelial cells in the brain are ≈100 times tighter than the junctions elsewhere in the body.[186] These tight junctions between adjacent cells force most molecules to pass through, rather than around, endothelial cells.[21] Only very small or gaseous molecules, such as water,carbon dioxide and glucose can pass through with ease.[187–189] For molecules to passively diffuse through the BBB, they generally must have high lipid solubility, low polar surface area, and low molecular weight.[184] The molecular weight cut-off for transmembrane diffusion varies between 400 and 600 Da depending on the molecule class.[190] P-glycoprotein substrates with a molecular weight above 400 Da have no measurable brain uptake,[191] whereas numerous peptides and proteins have been known to cross the BBB in sufficient quantity to affect CNS function.[190] The largest molecule known to cross the BBB via transmembrane diffusion has a molecular weight of 7800 Da.[192]

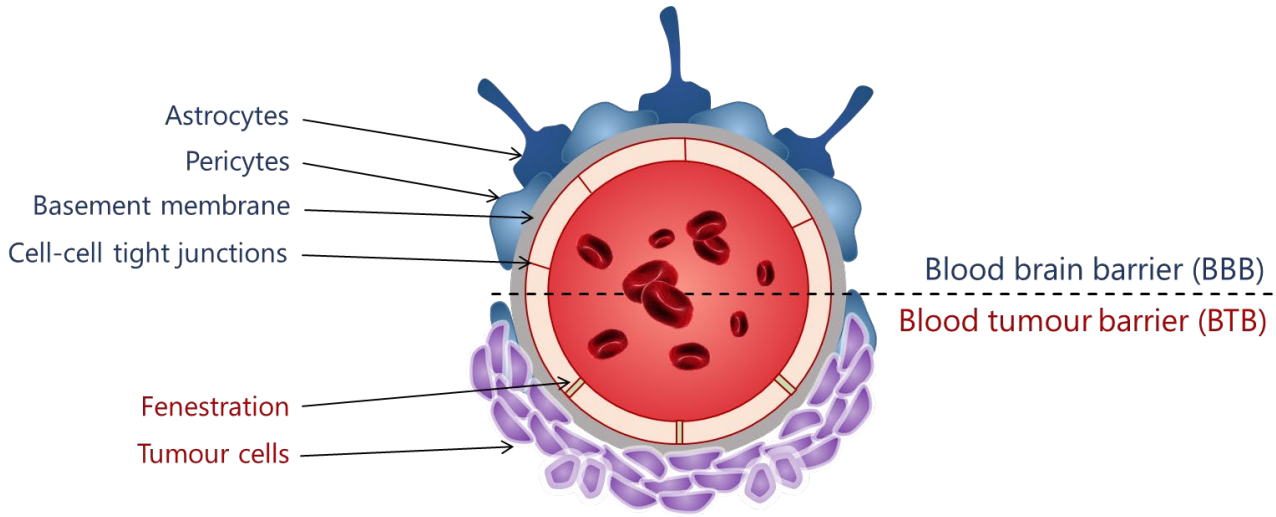

Figure 1.5.5: End-on view of a single blood vessel in the brain highlighting the key components of the blood-brain barrier (BBB) and blood-tumour barrier (BTB).

For these reasons, the BBB is an incredibly important consideration in the treatment of all brain pathologies; the vast majority of large molecule drugs and over 98% of small molecule drugs cannot cross the BBB.[193] The components of the BBB continuously adapt in response to various physiological changes in the brain.[194] These adaptations act to further frustrate drug delivery; at disease sites, the BBB is 'strengthened' via two key mechanisms: the upregulation of multiple drug resistance genes[195,196] and the upregulation of multiple major trans-membrane efflux pumps.[195,197–199] Studies have shown that this directly limits the efficacy of chemotherapeutics in brain tumours.[200,201] When these alterations occur at tumour sites, the BBB's structure is altered to form a blood-tumour barrier (BTB).[187]

Once metastatic tumours grow beyond 1–2 mm in diameter within the brain parenchyma, the BTB becomes structurally and functionally compromised.[202–205] This has led to many investigations into whether the EPR effect can be exploited to enhance passive accumulation of drug in tissue. However, as discussed extensively in Section 1.5.1, this BTB disruption is heterogeneous and more sophisticated techniques for transferring therapeutics across the BTB are highly desirable.

To transport larger substances into the brain, the BBB has vesicular transport mechanisms involving either receptor-mediated transcytosis (RMT) or adsorptive-mediated transcytosis.[184] Hijacking these mechanisms has been attempted to enhance the ability of drugs to reach the parenchyma.[206,207] Cell-penetrating peptides have also been exploited; capable of transporting proteins or peptides into cells in a nonspecific, receptor-independent manner, they have lower off-target effects on the immune systems than antibody-assisted techniques.[172] A PEGylated doxorubicin-peptide conjugate has been shown to accumulate in diffuse cerebral metastases[208] and a combination of 3 peptides has been used to induce mitochondrial damage and cellular apoptosis in metastases.[209] By taking advantage of the rapid angiogenesis in an aggressive tumour, drug moieties conjugated with angiopep-2 have also shown promise.[210] However, as the function of the BBB efflux pumps is preserved, the receptor-mediated mechanisms work both ways (receptor-mediated exocytosis) and the receptors are rarely brain tumour specific, the success of these techniques has so far been limited.

Further pharmacological attempts to enhance drug transport across the BBB, for example, reducing the relative number of polar groups on the drug molecule, have also been attempted.[119] However, these strategies often lead to a loss of activity of the drug.[211]

More broadly, previous attempts to circumvent the BBB include invasive techniques such as stereotactically guided drug insertion through a catheter, intracerebral drug implants and osmotic disruption.[119,211,212] Both high-dose intravenous chemotherapy[213,214] and direct carotid chemotherapy[215–217] have been attempted but are associated with major systemic adverse effects and short-term benefits. Interstitial wafer application in the surgical bed is a further single-use approach that is associated with infections, meningitis and minimal drug distribution.[218,219]

In summary, no current techniques enable safe, localised, effective and reversible opening of the BBB. As the BBB acts to protect cancer cells from the cytotoxic effects of chemotherapy, especially for microscopic tumours, it represents the second major challenge that needs to be overcome before a successful treatment for brain metastases can be achieved.

1.5.3. Summary

In summary, any eventual therapeutic solution for brain metastases will need to fulfil four criteria:

1. **The ability to shield therapeutics during systemic delivery to prevent off-target toxicity and/or pre-target neutralisation by the immune system.**
2. **Site specific targeting to the vascular endothelium surrounding microscopic tumours such that a leaky vasculature is not a required feature of the tumour targets.**
3. **A safe, effective and transient way of transporting the therapeutic agent across the blood-brain barrier (BBB).**
4. **A mechanism for encouraging drug transport deep into the tumour.**

This thesis aims to develop a therapeutic technology capable of addressing all of these challenges simultaneously. This approach is outlined in Section 1.7.

1.6. Ultrasound, microbubbles and US-BBBD

This Section provides an overview of both ultrasound and microbubbles and then details how the combination of these modalities is capable of temporarily increasing the permeability of the blood brain barrier (BBB) in a process known as ultrasound mediated blood brain barrier disruption (US-BBBD). How the research described in this thesis utilises ultrasound, targeted microbubbles and US-BBBD to tackle the challenges outlined in Section 1.5 is then detailed in Section 1.7.

1.6.1. Ultrasound

Ultrasound is defined as sound with a frequency beyond the range of human hearing, i.e. above 20 kHz. Widely used as an imaging modality for over 50 years, ultrasound is associated with numerous beneficial qualities including safety, low cost, portability and 'real-time' imaging. The ability of ultrasound to induce bio-effects has been known for almost 100 years[220] and these effects have gained increasing interest over the past 3 decades. Amongst other uses, therapeutic ultrasound has been used for shock-wave lithotripsy,[221–226] mechanical tissue fractionation,[227] drug activation,[228,229] mild hyperthermia,[230] thermal ablation,[231] breakdown of blood clots,[232] delivery of genes,[233] delivery of chemotherapeutic agents,[234] delivery of oncolytic viruses,[235] increasing membrane permeability to molecules[236–238] and enhancing transport of drugs across the blood-brain barrier.[239]

A large proportion of these bio-effects are induced or enhanced by acoustic cavitation. Cavitation can arise from changes in fluid pressure or temperature, pressure waves or the absorption of radiation[240] and can lead to further therapeutic effects such as the intracellular delivery of molecules,[241] high intensity focused ultrasound (HIFU) surgery[242] and lithotripsy.[243] Whilst a major advantage of ultrasound is the ability to focus in tissue, allowing close control of when and where cavitation occurs, the heterogeneity of endogenous cavitation between tissues means that tissue cavitation is unpredictable and requires relatively high pressure amplitudes.[240] To address this, acoustically active cavitation agents that allow bubbles to be generated more reproducibly and at lower pressure amplitudes are often used to augment both ultrasound imaging and ultrasound mediated therapy.

1.6.2. Microbubbles

Microbubbles (MBs), consisting of a gas core surrounded by a lipid, protein or polymer coating,[244–246] are the most widely studied artificial nuclei to date.[240] The key components of the microbubbles used in this thesis are shown in Figure 1.6.1. The key to the use of MBs as drug delivery vehicles is their activity when exposed to ultrasound; expansion and contraction of the gas core during the rarefaction and compression phases of the pressure wave leads to a wide range of bio-effects.[247] At clinically relevant ultrasound frequencies, the pressures required to produce therapeutically relevant amplitudes of oscillation are typically less than 1 MPa, which is notably lower than the majority of other cavitation agents.[240] MBs are theranostic agents; they can provide simultaneous and co-localized diagnostic imaging and therapeutic delivery.[247]

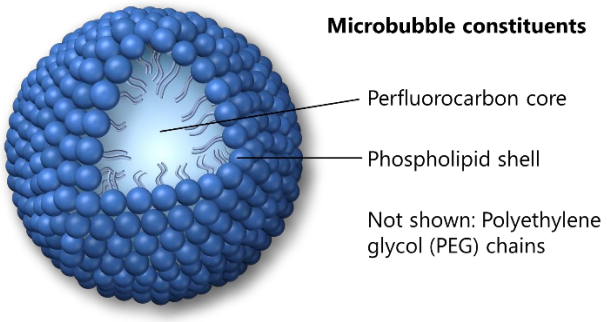

Figure 1.6.1: The key constituents of the microbubbles used in this thesis and in many microbubble formulations used pre-clinically and clinically worldwide

Originally developed as contrast agents for ultrasound imaging, MBs are now used clinically in echocardiography andto measure blood flow using Doppler ultrasonography.[248] MBs are in clinical development for therapeutic applications such as focused ultrasound surgery, sonothrombolysis, ultrasound-mediated blood brain barrier breakdown (US-BBBD) and enhancement of the delivery of a wide range of therapeutics.[249] Clinically approved MB formulations include Optison (albumin shell, perflutren core), Definity (lipid-based shell, perflutren core), Sonovue (lipid shell, sulphur hexafluoride core) and Sonozoid (lipid shell, perfluorobutane core).[250]

To reduce off-target toxicity, increase target dose and increase cellular uptake,[251] drugs can be conjugated to MB shells.[252,253] Hydrophobic drugs can be encapsulated between the gas core and the

MB shell and hydrophilic drugs can be conjugated to the outer surface of the MB.[254] Liposomal drugs can also be conjugated to the outer surface of MBs.[255] As is discussed extensively in Chapters 2 and 3 of this thesis, MBs can also be actively targeted to sites of disease in the body.

MBs have also been loaded with therapeutic gases such as oxygen and nitric oxide.[256] Incorporating iron-oxide nanoparticles into MB shells enables magnetic resonance imaging and magnetic targeting.[257–260] The polyethylene glycol (PEG) coating that is commonly incorporated into MB formulations acts to enhance stability and delay clearance by minimising recognition by the immune system.[55]

One disadvantage of microbubbles is that they typically have a half-life in the body of a few minutes,[261,262] whereas the particles with smaller hydrodynamic diameters exhibit delayed clearance from the body.[263] The relatively large size of MBs (~2 μm diameter) also limits their extravasation from the vasculature, even when inside the leaky vasculature of tumours. Actively targeting microbubbles acts to mitigate both of these issues.[264]

Smaller cavitation agents have been developed. These include nanodroplets, nanoscale particles of liquid perfluorocarbon (PFC) stabilised with a phospholipid outer shell.[265] Nanodroplets exhibit higher stability and higher cavitation thresholds than MBs, and are theoretically able to pass through the endothelial gaps of the defective blood vessels surrounding tumours.[266–269] Solid cavitation nuclei such as sub-micron gas-trapping polymeric cups and gold nanocones have also been developed.[270,271]

Whilst many studies have been published that optimise the ultrasound parameters for different drug delivery applications,[272–276] the studies that have compared MB formulations have mainly compared size distributions,[277,278] with the most in-depth investigations making minimal effort to elucidate the complex interactions between different microbubble formulations and the surrounding tissue.[279] This is despite evidence that constituents of lipid-shelled MBs exchange with the lipids in cell membranes, and that this exchange affects the structural properties of cell membranes.[3,280] Chapters 4 and 5 of this thesis exploits this effect to enhance the delivery of model drugs *in vitro* and *in vivo*.

1.6.3. Ultrasound-mediated blood brain barrier disruption (US-BBBD)

Ultrasound-mediated blood-brain barrier disruption (US-BBBD) is a promising approach for noninvasively, safely and reversibly increasing the permeability of the blood-brain barrier to therapeutics in a localised and targeted manner. As MBs in the brain pass through the ultrasound focus, they undergo volumetric oscillations, displacing the surrounding fluid and transiently opening the BBB. As this technique is not specific to the therapeutic agent delivered, it has the potential to transform the treatment of a wide range of brain diseases and disorders by allowing free passage of molecules up to 2000 kDa into the brain.[281,282] This thesis aims to develop two complementary mechanisms to improve the specificity of US-BBBD by actively targeting the MBs (Chapters 2 and 3) and the efficacy of US-BBBD by optimizing the lipid composition of the MB formulations used (Chapters 4 and 5).

Demonstration of temporary disruption of the blood-brain barrier by ultrasound and microbubbles (US-BBBD) was first published almost immediately after the clinical approval of the ultrasound contrast agent Optison.[283] The combination of microbubbles and ultrasound provided repeatable BBB opening without damage to surrounding tissue, a feat that was not accomplished with focused ultrasound alone.[283,284]

1.6.3.1. Mechanisms of US-BBBD

Microbubble-cell proximity appears critical to the efficacy of US-BBBD, reinforcing the benefit of active targeting strategies.[249,285] Increased drug delivery following US-BBBD appears to result from a combination of cell-cell tight junction widening, increased endocytosis and endothelial cell fenestration.[286] Sonoporation (the formation of pores in cellular membranes following ultrasound exposure) is also hypothesized to play a role. Two distinct sub-populations have been found following exposure to ultrasound and MBs suggesting that cellular responses at low acoustic pressures may be dominated by endocytosis spurred by membrane deformation, and at higher acoustic pressures by pore formation.[287] It is unlikely that thermal mechanisms play a major role in US-BBBD (as studied using

by MRI-based thermometry) and inertial cavitation is not necessary for US-BBBD (as studied by monitoring acoustic emissions).[283,288]

Both ultrasound and microbubble properties can be optimized to adjust the size of molecules that can cross the BBB, offering the potential for size-selective delivery.[272] Passing small molecule chemotherapeutic agents (MW ~500 Da) into the brain has been shown to only require stable cavitation, whereas it has been suggested that inertial cavitation is required to deliver larger molecules including antibodies (MW ~150 kDa) and gene vectors (MW ~4 MDa).[272] The rate at which drugs enter the brain and the disruption time also varies with both ultrasound pressure and blood vessel diameter.[289]

Pore formation occurs when transient holes appear in the cell membrane through which extracellular substances passively diffuse into the cell. An ultra-high speed camera (25 Mfps) has been combined with a confocal microscope and used to obtain direct and simultaneous video footage of both cavitating microbubbles and pore formation in cell membranes as direct evidence of this phenomenon.[290] One study estimated the theoretical maximum pore size at around 100 nm, although this is not a conclusive measurement.[291] It should be noted that sonoporation mechanisms typically occur on timescales of seconds to minutes whereas US-BBBD can last for hours to days, making it unlikely that sonoporation acts alone.[288,289,292]

There is also strong evidence for ultrasound and microbubble induced endocytosis.[287,293,294] It is hypothesised that endocytosis is the main route into cells for large molecules, and that small molecules are more readily transported through membrane pores following sonication.[295,296]

The mechanical phenomena hypothesized to underlie ultrasound and MB mediated cell membrane permeabilisation include fluid shear stresses and acoustic radiation forces pushing the microbubble into the cell with sufficient force to cause membrane rupture.[297–299] Shear stress can be generated by ultrasound alone through acoustic streaming[249] or from a combination of ultrasound and MBs in the form of an oscillatory shear from the pushing and pulling of the microbubble on the fluid. These

oscillatory shear stresses have been predicted to be in the order of ~10^2-10^3.[300–303] A steady shear can also be generated from cavitation microstreaming.[304] A single microbubble (~2 μm diameter) can generate flow streaming patterns with a diameter up to 1 mm and flow speeds up to 1 mm/s.[4] If there is sufficient asymmetry in the acceleration of the fluid on either side of a collapsing bubble, a high-velocity liquid microjet will be developed.[305] Microjetting is also thought to contribute to the increase in permeability of cell membranes during ultrasound mediated drug delivery.[306]

Extracellular mechanical forces that strain the cellular membrane result in conformational changes in the structural proteins of the cytoskeleton. The mechano-sensors of the cell include transmembrane proteins (e.g. integrins), receptor proteins in the plasma membrane (e.g. VEGF receptors) and adhesion molecules.[307] The fluidity of cell membranes also decreases following a step-change in shear stress.[308] Hundreds of genes, including those that code for proliferation, apoptosis, migration and permeability, are also modulated by shear stress.[307] An *in vivo* increase in stress-sensing proteins following US-BBBD has also been found.[309] A spatial gradient in membrane fluidity[310] and an increase in vasodilation of *ex vivo* vessels[307] was found when exposed to a step change in shear stress (analogous to the change arising from ultrasound and MBs) but not when exposed to shear stress with a gentle temporal gradient.

Chemical phenomena are also likely to play a role in US-BBBD; ultrasound increases the production of reactive oxygen species (ROS) resulting in oxidative stress.[311–313] Ultrasound induced increases in the production of ROS have been linked to changes in the cytoskeleton and a transient increase in the permeability of cell-cell tight junctions.[312]

It is also worth noting that US-BBBD causes localized down-regulation in the expression of cellular efflux pumps, one of the significant barriers to conventional chemotherapy and current techniques for transporting therapeutics across the BBB (as reviewed in Section 1.5.2).[314] This expression remains inhibited up to 48 hours after sonication.[315]

1.6.3.2. Uses, efficacy and safety of US-BBBD

Critically, under appropriate exposure conditions, US-BBBD is a transient and reversible process. The time taken for the BBB to close after sonication varies by animal model tested, with times of 3-8 hours[316,317] (rabbit), 6-24 hours[318,319] (rat), 2 days[320,321] (mouse) and 6 days[322] (primate) all being reported. The safety of this technique has been demonstrated in rats,[319] rabbits,[323,324] primates[322,325] and humans.[326] Safety parameters investigated include lack of histological lesions, lack of behavioral consequence, lack of motor consequence and healthy PET scans, MRI scans and EEG signals.

However, it is worth noting that recent studies have found evidence that US-BBBD results in sterile inflammation in the brain. A rapid increase in damage-associated molecular pattern (DAMP) factors and an increased expression of both heat shock proteins and inflammatory markers, including Il-1β, the cytokine used in this thesis.[327,328] This neuroinflammation lasts up to 24 hours and it has been recommended that the neuroinflammatory potential of sonication parameters should be evaluated prior to clinical trials.[329]

US-BBBD has been widely found to cause between a 30 and 500% increase in the uptake of chemotherapeutics in the brain, a factor that has been widely associated with increased survival *in vivo*. Enhanced delivery of drugs including doxorubicin,[319,330–334] paclitaxel,[335] temozolomide,[336,337] and carboplatin[338,339] has been shown. This has led to improved tumour control in animal models being widely reported[331,333,336,340–342] and both progression-free and overall survival of human patients being dramatically increased.[343] US-BBBD has also been used to enhance the delivery of other classes of therapeutics, including antibodies,[286,344] and genes.[345,346]

Oxygen loaded MBs have been used to deliver oxygen to metastatic tumours which, in turn, enhanced their response to radiotherapy.[347] US-BBBD has been used to enhance the delivery of doxorubicin, trastuzumab, immune cells and antibody-drug conjugates to metastatic tumour models.[348–351] However, all of these model tumours had a diameter ranging from 1.5-3 mm when treatment began,

so their location was known and the BBB surrounding them would have been compromised. None of these studies used actively targeted microbubbles.

One of the main obstacles to clinical US-BBBD is focusing ultrasound through the skull; complex correction schemes are required due to attenuation, distortion, and defocusing of the ultrasound beam. Three systems, utilizing very different transducer strategies, have been approved for US-BBBD in a clinical setting so far. These are the Exablate Neuro, manufactured by InSightec, the NaviFUS system, and the SonoCloud system manufactured by CarThera.[352] Consisting of 1024 individual ultrasound transducers (at 220kHz) in a hemispherical array that fits on the head, the Exablate system is designed to be MR guided.[353] Over 2000 patients have been treated with this system in 47 treatment centers globally.[354] The NaviFUS system eliminates the need for stereotaxy and consists of a frameless ultrasound array designed to operate at frequencies as low as 28kHz.[355,356] The SonoCloud is a single element transducer (11.5mm diameter) that is surgically implanted within the skull bone such that it is directed towards the tumour site, thus removing the need for corrective strategies.[357]

1.6.3.3. US-BBBD clinical trials

Two clinical trials using US-BBBD have already taken place.[352] In the first, the SonoCloud system was used to disrupt the BBB of 17 patients with glioblastoma multiforme (GBM) on a monthly basis whilst they were given systemic chemotherapy.[357] US-BBBD was achieved in the majority of all sonications at pressures of 0.8MPa and above, and no treatment-related serious adverse effects were noted.[357] In the second, the Exablate system was used to open the BBB of five patients with moderate Alzheimer's disease.[353] BBB opening was achieved predictably at 50% of the power required to generate cavitation and again, no patient experienced any serious side adverse effects.[353] These results are promising and at the time of writing, ten more clinical trials involving US-BBBD are either active or recruiting (five for GBM, three for Alzheimer's disease, one for ALS and one for Parkinson's disease).[352]

Beyond these, two further clinical trials are also planning to investigate the feasibility of using US-BBBD to treat metastatic tumours in the brain:

- The first of these, trial NCT03714243, currently recruiting 10 patients at the Sunnybrook Research Institute in Toronto, plans to use the ExAblate Model 4000 Type 2 "Neuro-System" to disrupt the blood brain barrier in a temporary and localized fashion in patients with brain metastases from Her-2 positive breast cancer.[358] As this is a safety and feasibility study, no therapeutic agent will be used and patients will be followed up with regular post-procedure MRI scans for 12 weeks. Crucially, the first exclusion criterion of this trial is: "brain metastases not visible on the pre-therapy imaging". This highlights the critical need for a technology capable of treating metastases before they grow large enough to disrupt the BBB. Simultaneously, it demonstrates the appetite of clinical trials centers, regulators and healthcare professionals to both develop US-BBBD technologies and find a treatment for brain metastases.

- The second of these, trial NCT04021420, not yet recruiting 21 patients at the Hôpitaux de Paris, plans to use the Sonocloud device and Nivolumab (an anti PD-1 monoclonal antibody) to treat patients with brain metastases from melanoma.[359] The inability of this technique to treat widespread, microscopic tumours is highlighted by the third trial inclusion criteria: "[Patients must have] at least one measurable brain metastasis between 5 mm and 35 mm in diameter, not previously treated with surgery and/or radiosurgery and located less than 5 cm from the skull."

Whilst US-BBBD represents one of the most promising upcoming therapeutic techniques for a wide range of cerebral pathologies, it is not without its limitations. The need to know the exact target location in the brain prior to treatment represents a particular barrier, particularly to the treatment of metastatic tumours in the brain. Actively targeting microbubbles (removing the need to know the tumour locations) presents one solution to this issue and is addressed in Chapters 2 and 3 of this thesis.

Difficulties in focusing ultrasound deep within the brain without causing significant pre-focal bio-effects represents another challenge. Microbubbles optimized to cause more widespread US-BBBD with the same acoustic energy may provide a solution to this and are developed in Chapters 4 and 5 of this thesis.

1.7. Thesis structure and overview

1.7.1. Challenges and structure

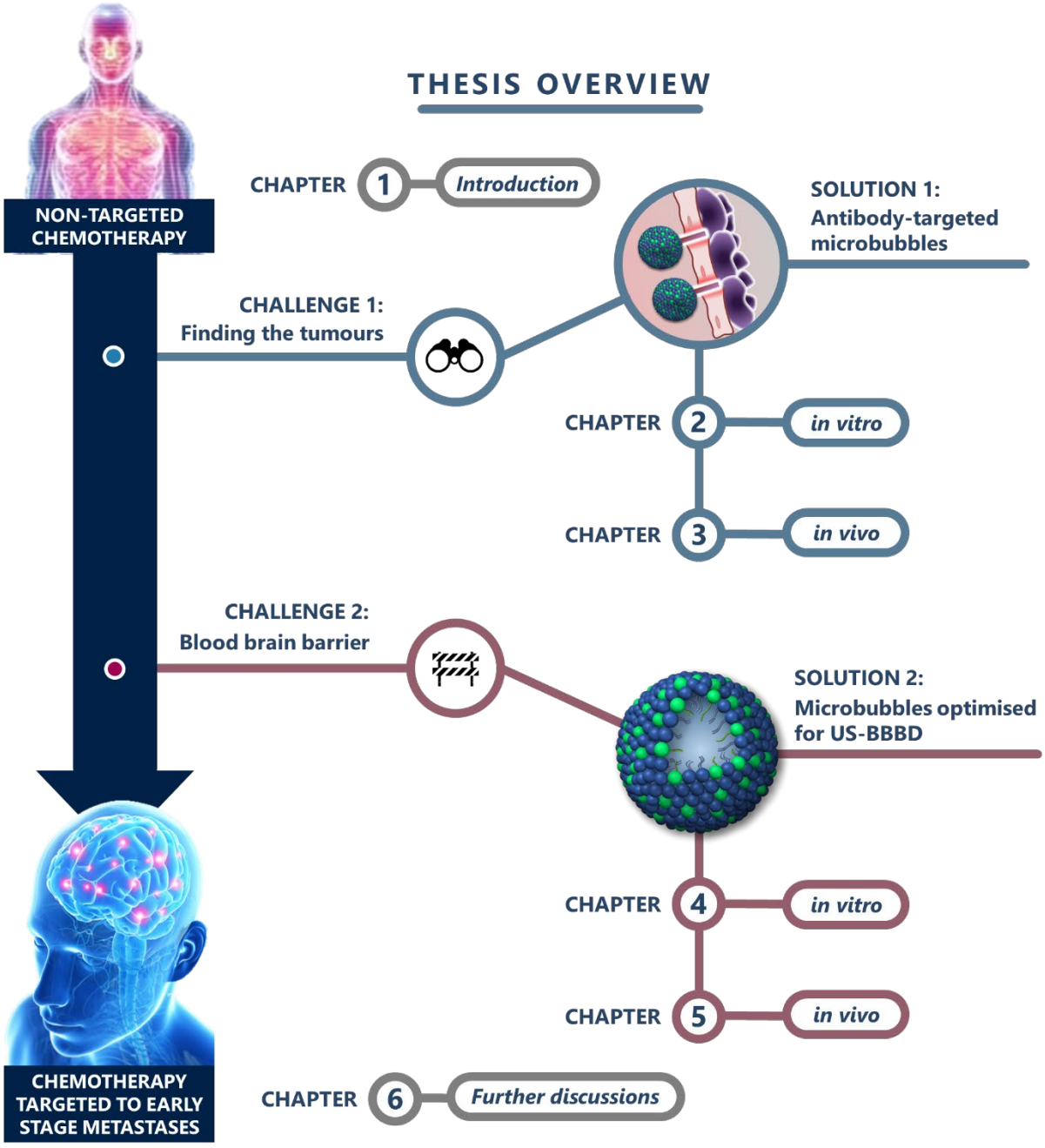

Figure 1.7.1: A visual overview of the aim of this thesis. This thesis aims to progress from the systemic injection of chemotherapy (represented at the top) to the non-invasive and targeted delivery of chemotherapy at the site of microscopic tumours in the brain (represented at the bottom). To do this, solutions to the two principal challenges in the treatment of brain metastases that utilise ultrasound, microbubbles and ultrasound mediated blood brain barrier disruption are developed.

This thesis is formed of two parts, each addressing one of the two challenges identified in Section 1.5. In both parts, mathematical modelling is combined with *in vitro* and *in vivo* experimentation in an attempt to delineate the key obstacles that currently prevent successful treatment of brain metastases. The two challenges and the corresponding solutions developed in this thesis are represented schematically in Figure 1.7.1.

1.7.2. Part 1

Chapters 2 and 3 of this thesis focus on the first of the challenges identified in Section 1.5:

Challenge 1: Targeting therapy selectively to the site of brain metastases

As anti-VCAM-1, the antibody for vascular cell adhesion molecule 1 (VCAM-1) has previously been found to enable sensitive and selective detection of early stage brain metastases, it is hypothesised that MBs conjugated with anti-VCAM-1 (AV-MBs) could use the same mechanism to actively target and then deliver therapy at the site of these tumours. Hence, Part 1 aims to answer two research questions:

1. ***Are antibody-conjugated microbubbles capable of selectively binding to target regions in the brain?***
2. ***Once bound, are antibody-conjugated microbubbles then capable of causing US-BBBD selectively in the target region?***

After *in vitro* demonstrations of the targeting ability of AV-MBs, their ability to deliver a model drug to target regions in the brain *in vivo* is then tested.

1.7.3. Part 2

The second part of this thesis (Chapters 4 and 5) focuses on the second of the challenges identified in Section 1.5:

Challenge 2: Enhancing therapeutic delivery across the blood brain barrier

US-BBBD is a temporary and reversible method of permeabilising the blood brain barrier. Increasing the amount of drug that crosses the BBB in US-BBBD without increasing the acoustic energy required (through manipulation of the physical properties of the MBs) is thus highly desirable for the treatment of a wide range of brain pathologies, including microscopic brain tumours. Part 2 of this thesis investigates whether lipid exchange mechanisms between MBs and cells can be exploited to enhance both cell membrane permeabilisation (*in vitro*) and US-BBBD (*in vivo*). This is represented schematically in in Figure 1.7.1. Two further research questions are addressed:

3. ***How does lipid transfer from microbubbles affect cell membranes?***
4. ***Can microbubble-cell transfer be exploited to enhance therapeutic delivery?***

If these questions can be answered satisfactorily, this will demonstrate a novel optimisation process for MBs intended for use in drug delivery. MBs that are capable of increasing the quantity of drug delivered without increasing the ultrasound energy required could lead to more effective treatment deeper within the brain and other areas of the body where the off-target bio-effects of US would be dangerous.

Part I. Targeting Therapy

“No targeted therapies exist that are specific for brain metastases, and the median survival for untreated patients is 5 weeks.”

- ***WHO World Cancer Report 2014***[5]

Chapter 2. Targeting therapy *in vitro*

2. Targeting therapy *in vitro*

Abstract

In this Chapter, microbubbles conjugated to anti-VCAM-1 (AV-MBs) are developed. Anti-VCAM-1 is an antibody with a selective affinity for early stage metastases that has previously allowed detection of tumours 3 orders of magnitude smaller than those currently visible on MRI. These AV-MBs are then shown to be capable of selectively binding to mouse brain endothelial cells that are overexpressing VCAM-1 in a physiologically relevant flow system.

Graphical Abstract

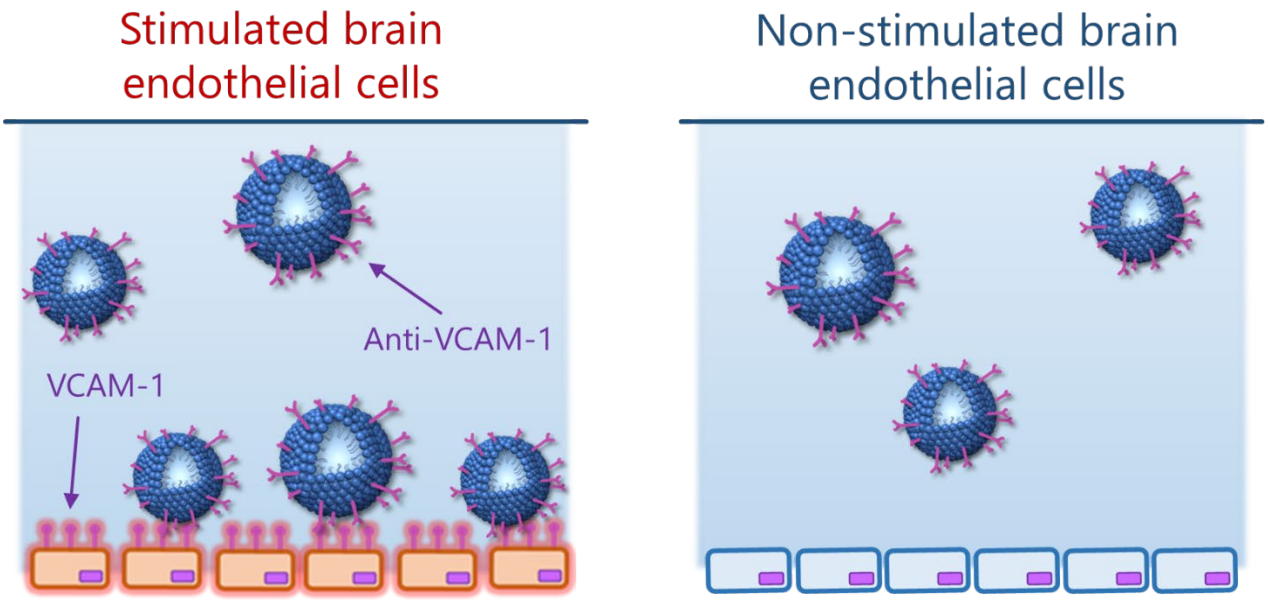

Attributions

The research in Part 1 of this thesis (Chapters 2 and 3) set out to investigate whether the impressive antibody targeting capabilities developed by Professor Nicola Sibson's group (Department of Oncology, University of Oxford) could be adapted to target ultrasound-mediated therapy specifically to brain tumours. Therefore, the understanding of the use of anti-VCAM-1 in the context of tumour targeting was already in place at the beginning of this PhD.

In all of the experiments involving cells in Chapter 2, I worked with Dr. Sarah Peeters from the Department of Oncology. Dr. Peeters carried out all *in vitro* cell culture and cell stimulation.

This work forms the backbone of one of the principal 'Work Packages' in the Oxford Centre for Drug Delivery Devices Research Grant. Professors Eleanor Stride and Nicola Sibson manage the Work Package. Dr. Luca Bau and Luke Richards are also part of the same Work Package, with Dr. Bau researching the formulation of other anti-VCAM conjugated cavitation agents and Luke researching the design of a transducer system designed to expose the whole brain to a uniform ultrasound field.

2.1. Introduction

Section 1.5 identified the two principal challenges that currently limit the treatment of metastatic tumours in the brain: selectively targeting therapy to tumour sites and then delivering this therapy across the blood-brain-barrier (BBB). As outlined in Section 1.7, this thesis is split into two parts each aimed at addressing one of these challenges. Part 1 of this thesis (consisting of Chapters 2 and 3), aims to investigate the feasibility of using an ultrasound and microbubble mediated therapy to tackle the first of these:

Challenge 1: targeting therapy selectively to the site of brain metastases

To do this, the feasibility of combining antibody-targeted MBs with unfocused ultrasound to deliver US-BBBD at target sites is investigated. This technique takes advantage of the ability of antibodies to target cells on a molecular level, whilst simultaneously removing both the need for prior knowledge of the tumour position and the need to focus ultrasound in the brain. The distinctions between this technique and previous US-BBBD studies are shown schematically in Figure 2.1.1.

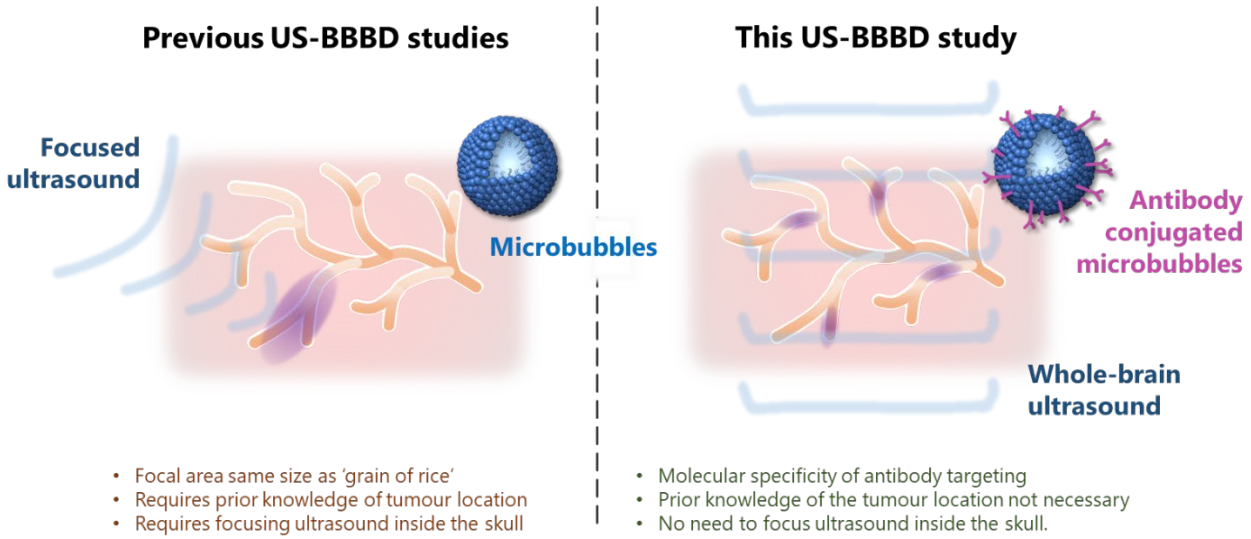

Figure 2.1.1: A schematic representation of the differences between this "whole-brain" US-BBBD study and previous US-BBBD studies.

This is a powerful concept; if successful, this technique has the potential to deliver therapy selectively to microscopic tumours before they have grown large enough to disrupt the blood brain barrier (BBB). More broadly, this concept could improve ultrasound-mediated treatments for other pathologies,

especially those for which candidate receptors for active targeting are known and accurately positioning an ultrasound focus is challenging.

As outlined in Section 1.7, Part 1 of this thesis aims to address two key research questions:

1. ***Are antibody-conjugated MBs capable of selectively binding to target regions in the brain?***
2. ***Once bound, are antibody-conjugated MBs then capable of causing US-BBBD selectively in the target region?***

In this Chapter, an antibody with a high selective affinity for early stage brain metastases is first conjugated to microbubbles. The ability of these antibody-conjugated microbubbles to selectively bind to cells in a physiologically relevant flow system is investigated.

2.1.1. Biomarkers of metastasis

As metastatic tumours form in existing blood vessels in the brain they activate the vascular endothelium (i.e. the cells lining the blood vessels).[23,360] During one of the earliest steps in the metastatic cascade, tumour cells use inducible cell adhesion molecules (CAMs) to promote their adhesion to the endothelium.[361–364] Tumour cells can use CAMs to determine how their tissue distribution around the body.[365] CAMs, which mediate leukocyte rolling, adhesion and transmigration across the BBB are rapidly up-regulated in response to disease or injury.[366] In particular, vascular cell adhesion molecule-1 (VCAM-1) has been shown to play an important role in transporting white blood cells into diseased brains both in animals and humans.[367–370]

There is a close association of early stage tumour colonies with the existing cerebral vasculature in both murine models of brain metastasis and human post mortem brain tissue containing metastatic tumours.[23,40] The activation of the vascular endothelium during metastasis development leads to a local up-regulation of VCAM-1 in the very early stages of metastasis in the brain.[108] This up-regulation has been quantified in two further studies. Both static and dynamic *in vitro* adhesion assays demonstrate that melanoma cells adhere to cytokine pre-treated endothelial cell monolayers through

contact with VCAM-1.[371,372] Some studies have also shown that cancer cells release a cytokine (Il-1α) in concentrations sufficient to upregulate VCAM-1.[373,374]

Anti-VCAM-1 is a monoclonal antibody that binds with human VCAM-1.[375] In animal models of metastasis, the increase in tumour proliferation following cytokine injection can be attenuated by injection of anti-VCAM-1 showing the crucial role VCAM-1 plays in successful metastasis.[376–378]

As microvascular endothelial cells in normal, non-inflamed tissues express minimal levels of VCAM-1,[379] coating MRI contrast agents with anti-VCAM-1 has previously allowed detection of VCAM-1 expression with high sensitivity *in vivo.*[380] By conjugating MRI contrast agents with anti-VCAM-1, it is possible to detect brain tumour volumes two to three orders of magnitude smaller ($0.3–3 \times 10^5$ cells) than those volumes currently detectable clinically ($10^7–10^8$ cells) due to the increase in expression of VCAM-1 around cerebral metastases.[108]

Beyond its selective overexpression at the disease site, VCAM-1 has two key advantages over other receptors or antigens commonly associated with microscopic tumours. Firstly, VCAM-1 is overexpressed on the endothelial cells near to tumours (rather than on the tumour cells themselves) which facilitates active targeting directly from the blood stream. Secondly, whereas many other targets, e.g. vascular endothelial growth factor (VEGF), are overexpressed once metastatic tumours are large enough to undergo angiogenesis, the overexpression of VCAM-1 occurs as soon as metastatic cells begin to adhere to the vascular endothelium in the brain. This is because VCAM-1 and its ligand $\alpha_4\beta_1$ integrin are important mediators of lesion initiation.[381] VCAM-1 is not constitutively expressed on the cerebral vascular endothelium, but is up-regulated with endothelial activation.[382]

Targeting VCAM-1 has been also used to detect acute brain inflammation following multiple sclerosis[380] and atherosclerosis.[383–385] As VCAM-1 participates in other inflammatory conditions including atherogenesis,[386,387] renal inflammation,[384] transplant rejection[388] and other cancers,[389,390] VCAM-1 targeting may allow for therapeutic targeting of a wide range of pathologies.[391,392]

In Part 1 of this thesis, anti-VCAM-1 conjugated microbubbles (AV-MBs) are developed and tested for their ability to selectively bind to target cells and then deliver a measurable therapeutic effect without requiring focused ultrasound.

It is worth noting that other receptor targets for metastatic brain tumours exist and could be tested in future. These include other CAMs, for example ICAM-1, E-selectin and P-selectin.[363,393,394] Targeting three of the genes known to play a key role in the migration of cancer cells into brain tissue enhances brain metastasis free survival.[26] The integrin $\alpha_v\beta_3$, responsible for upregulating VEGF, could be inhibited to discourage angiogenesis and the formation of a hypoxic tumour core.[27] Inhibition of the HER2 gene would decrease the incidence of brain metastases.[395] The BRAF gene and corresponding BRAF protein that encourage cancer cells to grow and divide is present in around 50% of patients with metastatic melanoma, leading to efficacy of small molecule targeted therapies.[396] The potential of vascular endothelial growth factor (VEGF), an angiogenic growth factor, as a suitable target for brain metastases has been widely explored.[18,38,126,360,397] VEGF inhibition has decreased vascular permeability at tumour sites,[397] decreased tumour proliferation[18,398] and increased apoptosis.[398]

2.1.2. Targeted microbubbles

As established in Section 1.5.1, targeted drug delivery has many notable advantages over systemic delivery, including higher localised drug concentrations, greater therapeutic efficacy and lower off-target side effects. Active targeting methods such as antibody binding[399] benefit from excellent specificity, and could potentially be used to target pathologies without prior knowledge of their location.[400]

Actively targeting microbubbles presents numerous advantages over other drug targeting strategies, particularly for the treatment of brain metastases. This technique has the potential to meet all four of the requirements for a brain metastases treatment, first identified in Section 1.5.3:

1. **The ability to shield therapeutics during systemic delivery to prevent off-target toxicity and/or pre-target neutralisation by the immune system.**

   As described in Section 1.6.2, microbubbles have the ability to shield therapeutics during systemic delivery, preventing both off-target toxicity and pre-target neutralisation by the immune system.

2. **Site specific targeting to the vascular endothelium surrounding microscopic tumours such that a leaky vasculature is not a required feature of the tumour targets.**

   Actively targeted microbubbles, particularly those targeted to a receptor as selective as VCAM-1, have the potential to achieve specific targeting to the blood vessel endothelial cells surrounding early stage metastases such that a leaky vasculature is not a required feature of the tumour targets.

3. **A safe, effective and transient way of transporting the therapeutic agent across the BBB.**

   As described in Section 1.6.3, ultrasound and microbubble mediated blood brain barrier disruption (US-BBBD) presents one of the most promising technologies for safely, effectively and reversibly transporting therapeutic agents across the BBB. The efficacy of US-BBBD further enhanced in Part 2 of this thesis.

4. **A mechanism for encouraging drug transport deep into the tumour.**

   Section 1.6.3 also found that US-BBBD enhances the uptake of a wide range of therapeutics into tumours and has a significant impact on both tumour progression and survival.

Targeting of microbubbles to VCAM-1 has been successfully demonstrated in previous studies. Pathologies imaged *in vivo* using diagnostic ultrasound and MBs conjugated with anti-VCAM-1 (AV-MBs) include atherosclerosis,[383,400–402] carotid plaques,[403] Crohn's disease[404] and tumours.[405] In these studies, an increase in contrast enhancement through vascular accumulation was the only objective. AV-MBs have also been used to enhance the delivery of microRNA and DNA to abdominal aortic

aneurysms and smooth muscle cells respectively.[406,407] These studies combine to demonstrate that AV-MBs are capable of accumulating *in vivo* in a wide range of vessel types and sizes. Whether this accumulation in the brain sufficient and selective enough to cause localised US-BBBD at the site of disease remains to be seen.

MBs have also been widely targeted to other receptors. VEGF-conjugated MBs have been used to image tumour angiogenesis,[408–412] stroke[413] and prostate tumours.[414] P-selectin-conjugated MBs have been used to target renal tissue injury,[415] myocardial ischaemia,[400] activated platelets,[416] thrombosis[417] and inflammatory bowel disease.[418] ECAM-conjugated MBs have been used to image inflammation,[419] MAdCAM-1-conjugated MBs to target Crohn's disease[420] and ICAM-1-conjugated MBs have been used to image endothelial inflammation surrounding atherosclerosis.[399,421]

Whilst the vast majority of these MBs were manufactured using a biotin-streptavidin-biotin bridging strategy, some studies have used pre-made avidin coated bubbles.[422,423] Manufacturing protocols with a single incubation step are desirable as they increase the likelihood of targeted microbubbles that can be personalised to different patient/tumour types in a clinical setting. Other studies have successfully conjugated targeting ligands to MBs using a maleimide-thiol link.[424–426] This is advantageous as streptavidin is immunogenic, potentially impeding application in humans.[424]

To address some of the disadvantages of antibody targeting, including low targeting efficiency[427] and strong dependence on flow conditions,[428] magnetic microbubbles have also been developed. Whilst the use of these was not explored in this thesis, it is worth noting that magnetic MBs conjugated with antiVCAM-1 have also been developed.[429] Use of a magnet significantly increased the binding of these AV-MBs to atherosclerotic plaques *in vivo*[429] highlighting a line of research that could, in future, be pursued to further improve the results from Chapters 2 and 3 of this thesis.

A different, but related strategy for increasing the specificity and efficacy of US-BBBD has been to combine antibody-targeted, drug loaded liposomes and non-targeted MBs. One study used doxorubicin-loaded liposomes targeted to interleukin-4 and SonoVue to enhance drug uptake into

glioblastoma.[430] This technique resulted in a higher concentration of drug in the tumour than in the surrounding, healthy tissue.[430]

Further strong supporting evidence for the feasibility of utilising AV-MBs and unfocused ultrasound to cause US-BBBD selectively at the site of brain metastases comes in the form of three studies published by a multi-centre Taiwanese team.[431–433] Using a combination of MBs targeted to either folate or VEGF and focused ultrasound, delivery of both small molecule drugs and genetic material to solid brain tumours (glioblastoma multiforme) *in vivo.* Crucially, therapeutic accumulation in the tumour tissue was found to be much greater and distinctly different than that in neighbouring, healthy tissue, both of which were inside the ultrasound focus (see Figure 2.1.2).

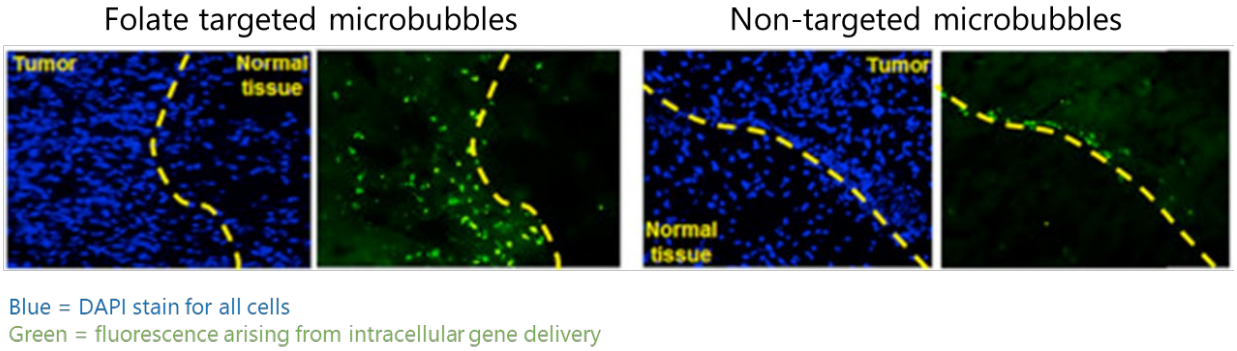

Figure 2.1.2: Figure adapted from Fan et al. 2016[432] showing distinct spatial differences in cellular uptake of a therapeutic between tumour cells and healthy tissue for targeted microbubbles but not for non-targeted microbubbles

In summary, the aim of Chapters 2 and 3 of this thesis is test whether AV-MBs, in combination with unfocused whole-brain ultrasound are capable of selectively opening the BBB selectively at the site of increased VCAM-1 expression.

If possible, this technique has wider applications; by removing the need for prior knowledge of the disease site, the specificity of molecular targeting can be taken advantage of. As established throughout this introduction, VCAM-1 and other disease targets are, in principle, widely interchangeable. On top of this, removing the need to focus ultrasound inside the skull may remove many of the complexities currently associated with achieving US-BBBD in the clinic.

2.2. Microbubble manufacture

2.2.1. Formulation overview

The anti-VCAM conjugated microbubbles (AV-MBs) used Chapters 2 and 3 of this thesis were prepared using a biotin-streptavidin-biotin bridging methodology.

AV-MB manufacture began with the preparation of biotinylated microbubbles (biot-MBs). These biot-MBs were centrifugally washed three times, then incubated with streptavidin to form strept-MBs. These were then washed three more times, before incubation with biotinylated anti-VCAM. These AV-MBs were then washed once more to remove excess antibody from the suspension, and then sized and counted before use in experiments. For all *in vitro* experimentation (this Chapter), NBD-DSPE (Avanti Polar Lipids Inc., US) was also added to the initial biot-MBs to enable fluorescence imaging of the microbubbles.

A schematic overview of the microbubble formulations used in Chapters 2 and 3 can be found in Figure 2.2.1.

2.2.2. Preparation of biotinylated microbubbles (biot-MBs)

DBPC, DSPE-PEG2000 and DSPE-PEG2000-Biotin (Avanti Polar Lipids Inc., US) were mixed in a glass vial in the quantities given in Table 1. If the AV-MBs were to be used for fluorescence microscopy *in vitro* (all experiments in this Chapter), DSPE-NBD was also added at this point. The mixture was heated on a hotplate at 58ºC for 12h, to allow for the chloroform (in which the lipids are supplied) to evaporate to form a lipid film. This lipid film was suspended in 5 mL of filtered phosphate buffered saline (PBS) solution (ThermoFisher Scientific, UK) for 1h on a hotplate at 85ºC under constant magnetic stirring. Lipids were then dispersed for 90s using a sonicator (XL 2000, probe diameter 3 mm, 20 W, 22.5 kHz, Misonix, US) with the tip completely immersed in the lipid-PBS solution (power setting 4). The glass vial was then placed in an 85˚C water bath for 60s to keep the solution above the melting point of the lipids. The solution was then sonicated for a further 30s at power setting 4 to ensure homogeneous dispersion. Biot-MBs were then formed by

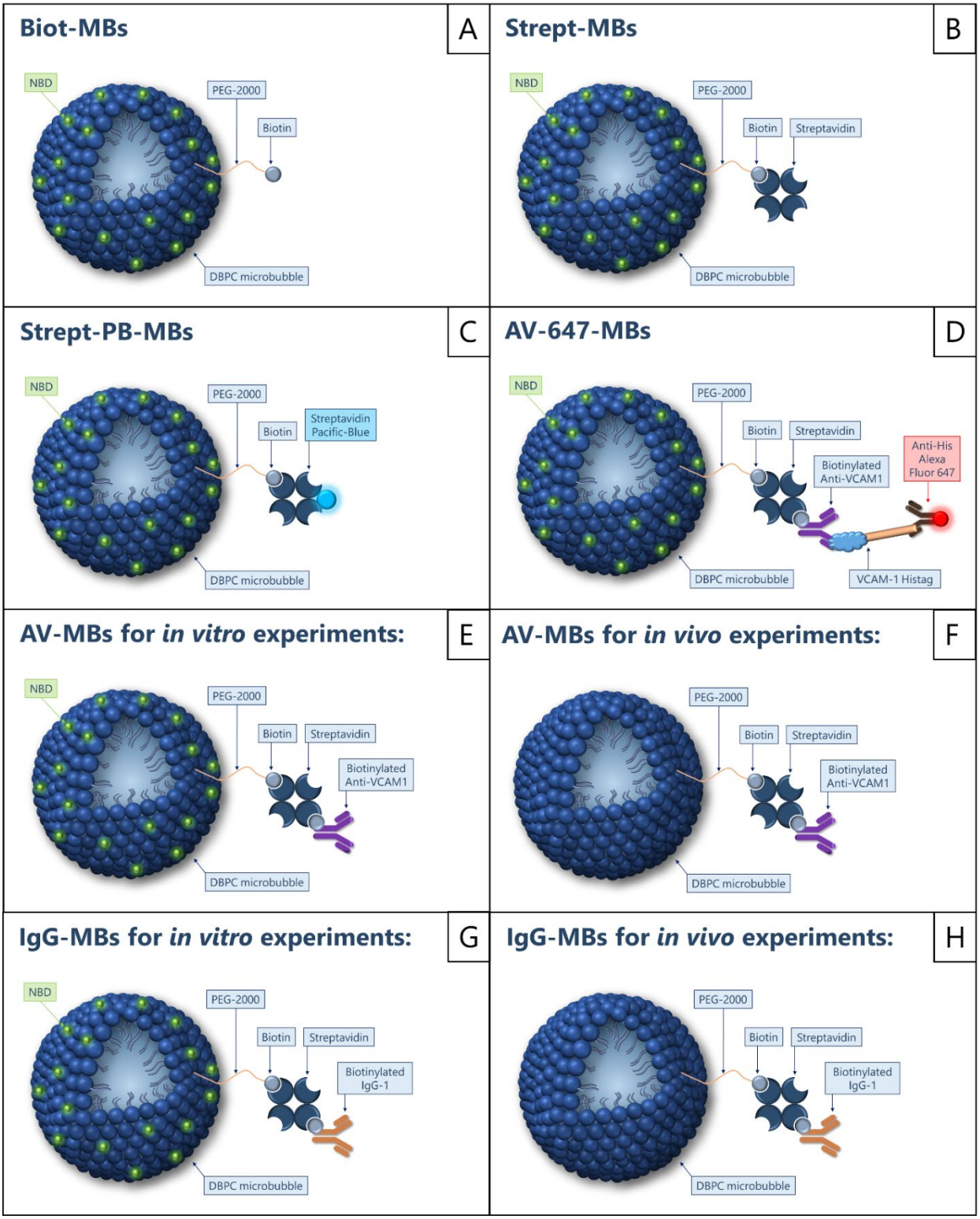

Figure 2.2.1: A schematic of the microbubble formulations used in Chapters 2 and 3: (A) Microbubbles conjugated with biotin (Section 2.2.2), (B) Microbubbles conjugated with streptavidin (Section 2.2.4), (C) Microbubbles conjugated with streptavidin Pacific-Blue (Sections 2.3.1 and 2.4.1), (D) Multi-step conjugation strategy used to verify binding of anti-VCAM-1 to AV-MBs (Sections 2.3.2 and 2.4.3), (E and F) Microbubbles conjugated with anti-VCAM-1 that were used for in vitro and in vivo experimentation respectively (Chapters 2 and 3), (G and H), Microbubbles conjugated with IgG-1 that were used for in vitro and in vivo experimentation respectively (Chapters 2 and 3).

placing the sonicator tip at the air-water interface under constant sulphur hexafluoride (SF_6) flow (The BOC Group plc, UK) and sonicating for 30s (power setting 14). Immediately after production, the vial containing the biot-MB suspension was capped and placed in ice for at least 20 minutes. A schematic of the biotinylated microbubble formulation can be found in Figure 2.2.1A.

Component	Mass (mg)	Molar ratio
DBPC	14.6	90
DSPE-PEG2000-Biotin	2.7	5
DSPE-PEG2000	2.53	5
DSPE-NBD *(only added for in vitro experiments)*	0.17	1
TOTAL	**20**	

Table 1: The molar ratios of the constituent components of biot-MBs

2.2.3. Microbubble washing

To ensure efficient and uniform binding of the streptavidin to the biot-MBs, it was important to first remove the free DSPE-PEG2000-Biotin from solution. This was done via centrifugal washing and is shown schematically in Figure 2.2.2.

1. Biot-MBs were added to a 10ml syringe (BD life sciences, US). This syringe was then capped and placed inside a 50ml centrifuge tube.
2. The biot-MBs were then centrifuged at 350g for 5 minutes at 4˚C.
3. The syringe plunger was then gradually lowered to remove the subnatant, leaving only the biot-MB cake in the syringe.
4. The biot-MBs were then re-suspended by drawing 2ml PBS into the syringe.
5. Steps 2 to 4 were repeated for each washing step. To incubate microbubbles with the next solution (e.g. streptavidin or antibody), the 2ml PBS in Step 4 is replaced with the desired solution.

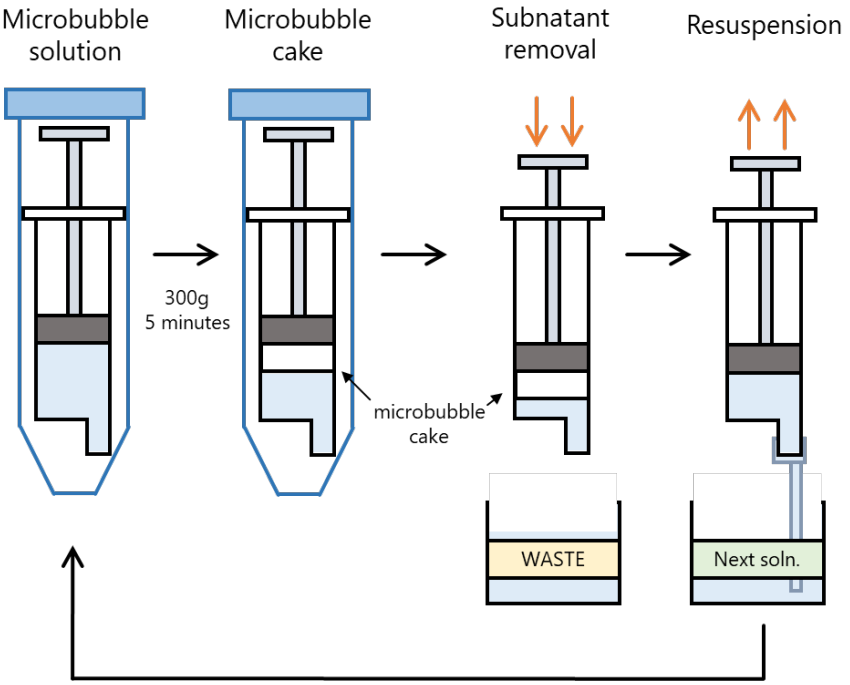

Figure 2.2.2: Centrifugal microbubble 'washing'

2.2.4. Preparation of streptavidin coated microbubbles (strept-MBs)

To generate microbubbles coated with streptavidin, biot-MBs were washed three times to remove excess biotinylated lipid in solution. After the third centrifugal wash, the cake of biot-MBs was re-suspended in a solution at 4˚C made from 2ml PBS and 0.2mg streptavidin (ThermoFisher Scientific, UK). This mixture was mixed gently for 15 minutes using a roller shaker (Cole-Palmer, UK). A schematic of the streptavidin coated microbubble formulation can be found in Figure 2.2.1B.

2.2.5. Preparation of anti-VCAM-1 coated microbubbles (AV-MBs)

To generate microbubbles coated with anti-VCAM-1, strept-MBs were washed three times to remove excess streptavidin in solution (not bound to the microbubble surface). After the third centrifugal wash, the cake of strept-MBs was re-suspended in a solution at 4˚C made from 1.2ml PBS and 0.8ml Rat Anti-Mouse CD106-BIOT at 0.5mg/ml in PBS/NaN_3, (Southern Biotech, US). This mixture was mixed gently for 30 minutes using a roller shaker (Cole-Palmer, UK). These microbubbles were then washed a final time to remove excess antibody. A schematic of the anti-VCAM-1 conjugated microbubble formulation can be found in Figure 2.2.1 E and F.

2.2.6. Preparation of IgG-1 coated microbubbles (IgG-MBs)

IgG coated microbubbles (IgG-MBs) were prepared using the same method as AV-MBs, except the antibody used was Rat IgG1-BIOT at 0.5mg/ml in PBS (0116-08, Southern Biotech, US). A schematic of the IgG-1 conjugated microbubble formulation can be found in Figure 2.2.1 G and H. These IgG-MBs will serve as control microbubbles throughout the Part 1 of this thesis (Chapters 2 and 3 of this thesis) as a control for non-specific antibody binding.

2.2.7. Microbubble size and concentration matching

For quantification of microbubble size and concentration, 10 μL of the microbubble suspension was transferred onto a Neubauer improved cell counting chamber (Hausser Scientific Company, US) under a 24 mm × 24 mm glass coverslip (VWR International, US). At least 10 images of microbubbles were acquired at 40x magnification using a Leica DM500 microscope (Leica Microsystems GmbH, Germany) coupled with a CCD camera (MicroPublisher 3.3 RTV, QImaging, Canada). Microbubble sizing and counting was performed using a purpose-written code in MATLAB® (The MathWorks Inc., US).[434]

2.2.8. Theoretical antibody loading on microbubbles

The average concentration of biot-MBs immediately after production was 1.67 x 10^9 microbubbles per ml, so that the total number of biot-MBs in 5ml of microbubbles was approximately 8.36 x 10^9 microbubbles. Normalising this figure against the average microbubble size distribution immediately post-sonication (before any microbubble washing) allows an estimation of the total surface area of biot-MBs as 1.43 x 10^{11}μm^2, or 0.143m^2.

Applying the assumption that all of the biotinylated lipid (DSPE-PEG2000-Biotin, 0.895μM total) in the lipid film prior to sonication was both completely incorporated into the microbubbles and evenly distributed around the microbubble shells gives an approximate maximum density of biotin molecules on the microbubble surface of 3.77 x 10^6 biotin molecules per μm^2. This density is related to the molar ratio of lipids in the microbubble shell. Thus, the highest possible density of biotin molecules

that could be expected on the surface of a stable bubble (9:2 ratio of shell lipid to PEG-biotinylated lipid) would be 15.1 x 10^6 biotin molecules per μm^2.

Conjugated species	Approximate microbubble surface density (x10^6 molecules per μm^2)
Biotin	3.77
Streptavidin	0.0211
Anti-VCAM-1	0.0154

Table 2: Approximate maximum microbubble surface densities of biotin, streptavidin and anti-VCAM-1.

As the vast majority of the microbubbles that are lost during washing are lost during the first two washes (evident from the clear subnatent from the third microbubble wash onwards), it can be assumed that both the streptavidin and antibody encounter microbubbles with a concentration and size distribution very similar to that of the final AV-MBs. The microbubbles lost during washing are the smaller bubbles meaning that the distribution's peak moves from 0.688µm to 1.376µm after the washing steps. Analogous calculations give the approximate microbubble surface densities of streptavidin and anti-VCAM-1 as 2.11 x 10^4 and 1.54 x 10^4 molecules per μm^2 respectively.

For comparison, the anti-VCAM-1 conjugated micro-particles of iron oxide (AV-MPIOs) that achieved the sensitive detection of brain metastases upon which this work is based had a maximum potential anti-VCAM-1 surface density of 5.11 x 10^4 molecules per μm^2.[108,380] Liposomes conjugated to anti-VCAM-1 with a surface density of 2.4 x 10^3 molecules per μm^2 also showed effective and selective accumulation in tumours up to 24 hours later.[435] This indicates that the time scales over which anti-VCAM-1 conjugated microbubbles remain bound to tumours *in vivo* are likely to be limited by the stability of the microbubbles in the circulation rather than the antibody-antigen interaction.

2.2.9. Theoretical VCAM-1 concentration in tumours

Whilst the co-localisation of VCAM-1 overexpression and metastatic brain tumours has been well established immunohistochemically in both animals and *ex vivo* human tissue,[108] this overexpression has proved difficult to quantify due to the extreme heterogeneity of tumours. The most relevant quantification[365] found that VCAM-1 expression increased from 28 to 98 nanograms of VCAM-1 per gram of brain tissue after 28 days (whole brain comparisons between healthy brains and brains of mice with a heavy non-cranial tumour burden). This measurement was obtained from a pulmonary metastasis model where only 25% of the animals had yet developed histological evidence of cerebral metastases. On top of this, the cell line used in this study (B16-BL6), despite having aggressive extra-cranial metastatic characteristics,[436] is unable to form metastases in the parenchyma and as such, all cerebral metastases are confined to the leptomeninges and ventricles.[437] This figure is also an average of the whole brain, and so the actual ratio of VCAM-1 expression between metastatic sites from other cell lines and healthy brain tissue is likely to be much greater.

A reasoned estimation of the true ratio is as follows. Exact volumetric tumour burdens of brain metastases are rarely quantified due to the tumour heterogeneity and the practical difficulties associated with making such measurements, particularly with widespread tumours. However, as only 25% of the mice had yet developed visible cerebral metastases, it is reasonable to assume that the average cerebral tumour burden was not more than 1%. A brain weight of 400mg[438] gives a maximum tumour weight of 4mg. Given that the molecular weight of VCAM is ~100kDa,[439] 28 ng VCAM-1/g brain gives an estimated 1.69×10^{11} VCAM-1 molecules in a healthy brain (4.4×10^{8} VCAM-1 molecules/mm^3 assuming total brain volume of 380 mm^3 [440]). Assuming that the increase of 70 ng VCAM-1/g brain arising from the presence of tumours (an extra 4.23×10^{11} VCAM-1 molecules) is all in close proximity of the tumours, the estimated tumour concentration of VCAM-1 molecules is then 1.11×10^{11} VCAM-1 molecules/mm^3.

This simple analysis therefore suggests that the volumetric concentration of VCAM-1 molecules inside tumours may be over two orders of magnitude greater than that in healthy brain tissue. This figure may be even higher in certain parts of tumours/certain stages of metastasis development due to the heterogeneity of the processes involved. The experimental sensitivity of anti-VCAM-1 conjugated MRI contrast agents (MPIOs) to brain metastases provides intuitive support for this result.[108]

Whilst it is possible to distinguish a single MPIO using MRI,[108,441] the lowest local concentration of microbubbles required to cause detectable US-BBBD is not known. The few studies that have investigated the effect of microbubble concentration on US-BBBD have used a range of doses, all higher than the extremely low equivalent doses likely to arise from antibody conjugation.[442,443] As established in Section 2.1.2, previous studies with VEGF targeted microbubbles indicate that US-BBBD can be enhanced by exploiting antibody targeting; what remains to be seen is whether antibody targeting alone enables a sufficient number of bubbles to bind to open the blood brain barrier.

This Chapter now proceeds to test the microbubble formulations developed in this Section to investigate the feasibility of antibody conjugation and the ability of microbubbles to bind to cells in physiologically relevant flow conditions. Chapter 3 then covers further *in vivo* investigation.

2.3. Experimental Methods

2.3.1. Verification of streptavidin conjugation to MBs

Streptavidin Pacific-Blue (ThermoFisher Scientific, UK) was used to verify that the streptavidin conjugation strategy (detailed in Section 2.2.4) resulted in uniform and consistent coating of streptavidin on the strept-MBs. Strept-MBs were manufactured using the protocol in Section 2.2.4, with the streptavidin being replaced with 0.2mg streptavidin Pacific-Blue to form strept-PB-MBs. These strept-PB-MBs were then centrifugally washed once (as detailed in Section 2.2.3) to remove excess Pacific-Blue from solution. A schematic of the streptavidin Pacific-Blue conjugated microbubble formulation can be found in Figure 2.2.1C.

10µl of these strept-PB-MBs were then placed between a glass microscope slide (ThermoFisher Scientific, UK) and a glass coverslip (VWR International, US). They were then imaged in the fluorescence channels of NBD (green, excitation/emission maxima ~463/536 nm), Pacific Blue (blue, excitation/emission at 410/455 nm) and brightfield on a Nikon Eclipse Ti microscope (Nikon, USA). NBD and Pacific-Blue fluorescence images were then compared to enable visual verification of streptavidin-Pacific Blue binding on each MB.

As a control in this experiment, the binding of streptavidin Pacific-Blue to non-biotinylated microbubbles was also tested using the same method. The results can be found in Section 2.4.1.

2.3.2. Verification of anti-VCAM-1 conjugation to MBs

To verify the uniform conjugation of anti-VCAM-1 to AV-MBs, AV-MBs were incubated with a solution of fluorescent VCAM-1 protein at 4˚C for 60 minutes to form AV-647-MBs. This solution was prepared by incubating 10ng of polyhistidine-tagged Mouse VCAM-1 protein (50163-M08H, Sino Biological, Beijing, China) with 10ng of Alexa Fluor 647 anti-His Tag Antibody (ThermoFisher, US) in 2ml PBS at 4˚C for 30 minutes. These AV-647-MBs were then centrifugally washed once (as detailed in Section 2.2.3) to remove excess Alexa Fluor-647 from solution. A schematic of the AV-647-MB formulation can be found in Figure 2.2.1D.

10ul of these AV-647-MBs were then placed between two glass coverslips (VWR International, US) and imaged in the fluorescence channels of NBD (green, excitation/emission maxima ~463/536 nm) and Alexa Fluor 647 (red, excitation/emission at 650/665 nm) on a Zeiss LSM 780 confocal microscope (Carl Zeiss AG, Germany). NBD and Alexa Fluor 647 fluorescence images were then compared to enable visual verification of anti-VCAM binding on each MB.

As a control in this experiment, the binding of Alexa Fluor 647 to IgG-MBs was also tested using the same method. The results can be found in Section 2.4.3.

2.3.3. Cell preparation

B.end3 cells (mouse brain endothelial cells, Sigma Aldrich, US) were cultured in DMEM Ham-F12 medium with 10% FBS and 2mM L-glutamine for use in both the static flotation tests of AV-MBs (Section 2.3.4) and the flow testing of AV-MBs (Section 2.3.5). Cells were seeded on day 0 in 35mm µ-Dishes or µ-Slides (Ibidi, Germany) for the static flotation and flow testing respectively. After 24 hours, the culture medium was removed and replaced with fresh medium, either with or without lipopolysaccharide (LPS, 10µg/ml). Exposure to LPS increases the expression of VCAM-1.[444] Binding experiments were conducted at least 20 hours post LPS stimulation.

2.3.4. Static flotation testing

Antibody conjugated MB binding to LPS stimulated endothelial cells was tested using static flotation. A 2ml solution of either AV-MBs or IgG-MBs (at $5x10^7$ per ml) in PBS was added to a 35mm µ-Dish (Ibidi, Germany) containing cells. The dish was then inverted and placed on a shaker (Cole Palmer, UK) for 5 minutes. This allowed the MBs to float into contact with the cells and ensured gentle mixing. After the incubation, the cells were washed twice gently with PBS, then incubated for 5 minutes with 1µl of CellMask Deep Red plasma membrane stain in 1ml PBS. After a further 2 gentle washes with PBS, dual fluorescence microscopy (Eclipse Ti, Nikon, US) was used to visualise any MBs (using the NBD stain in the MB shell) still on the cell membrane (using the CellMask stain).

ImageJ[445] software was then used to threshold each image and count the number of pixels that were cells and MBs rather than background. MB-cell binding efficiency for each condition was then calculated by dividing the number of green (MB) pixels by the number of red (cell) pixels. These results are presented in Section 2.4.4.

2.3.5. Flow testing

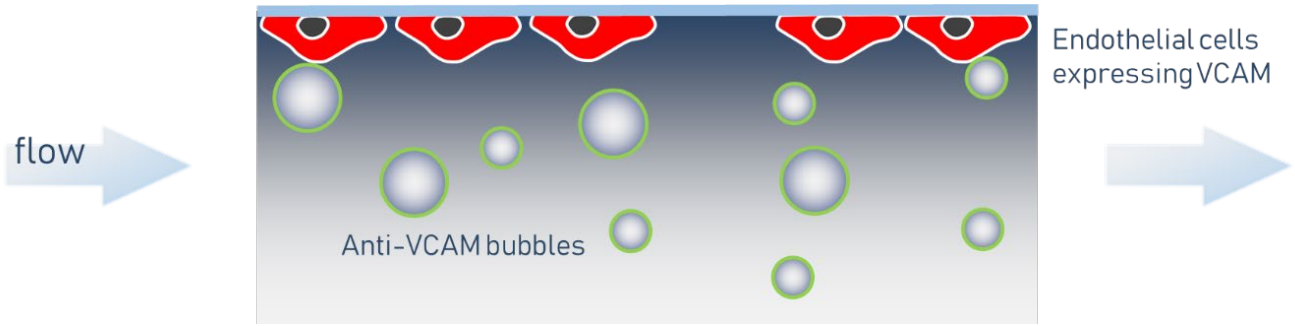

Figure 2.3.1: Schematic diagram showing the arrangement of cells and microbubbles in the µ-Slides.

The ability of antibody conjugated MBs to bind to LPS stimulated cells and stay bound under flow was tested using µ-Slides containing B.end3 endothelial cells (introduced in Section 2.3.3). A 3ml solution of either AV-MBs or IgG-MBs (at $1.25x10^8$ per ml) was loaded into a syringe (BD Life Science, US). This syringe was then connected via Teflon tubing to a µ-Slide channel and placed in a syringe pump. The flow rate of the syringe pump was calculated such that the wall shear stress experienced by the cells was 10 dynes/cm^2 (1 Pa). This was chosen as a representative mean wall shear stress for the capillaries and small venules (varying between 5 and 20 dynes/cm^2 [446,447]) as this is where brain metastases are most likely to occur. It is worth noting that wall shear stresses in diseased, arterial vessels with stenosis can reach 1500 dynes/cm^2.[448] The cells were then gently washed twice with PBS using the protocol recommended by the µ-Slide manufacturer to remove any MBs still in suspension, before the addition of CellMask Deep Red plasma membrane stain at a 1000 times dilution in PBS. After allowing 5 minutes for the CellMask incubation, the cells were washed gently twice more. As with the static flotation testing, dual fluorescence microscopy (Eclipse Ti, Nikon, US) was then used to visualise any MBs (using the NBD stain in the MB shell) still on the cell membrane (using the CellMask stain).

These images were then processed in the same way using ImageJ[445] software. These results are presented in Section 2.4.5.

2.4. Results

2.4.1. Microbubble size

Figure 2.4.1 shows the normalised average size distributions of AV-MBs and IgG-MBs used experimentally. There is a slightly higher proportion of IgG-MBs in the 2.6 to 5.7µm range when compared to the AV-MBs and this may have had a small influence on MB targeting as larger MBs experience greater viscous drag forces in fluid flow. However, there is no significant difference between the mean and modal sizes of these MB distributions and so the size distributions are not expected to materially impact the targeting results shown elsewhere in this Chapter.

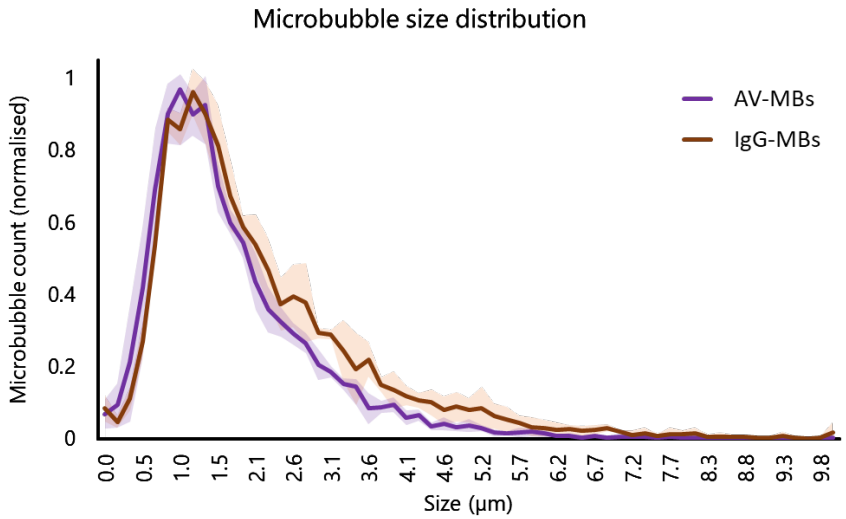

Figure 2.4.1: Size distribution (microbubble diameter) of AV-MBs and IgG-MBs. Averaged over all formulations used experimentally and normalised. The shaded areas show the standard deviation of the populations.

MBs were manufactured on the day of each experiment and stored at 4˚C until immediately prior to use. MB concentrations were matched to remove the impact of any inconsistencies arising from the MB manufacturing process.

2.4.2. Verification of streptavidin conjugation

MBs conjugated with streptavidin Pacific-Blue (strept-PB-MBs) were prepared as detailed in Section 2.3.1 and Figure 2.2.1C. A uniform coating of Pacific-Blue was observed on all strept-PB-MBs, in contrast to non-biotinylated MBs that had been incubated with streptavidin Pacific-Blue and washed equally (Figure 2.4.2).

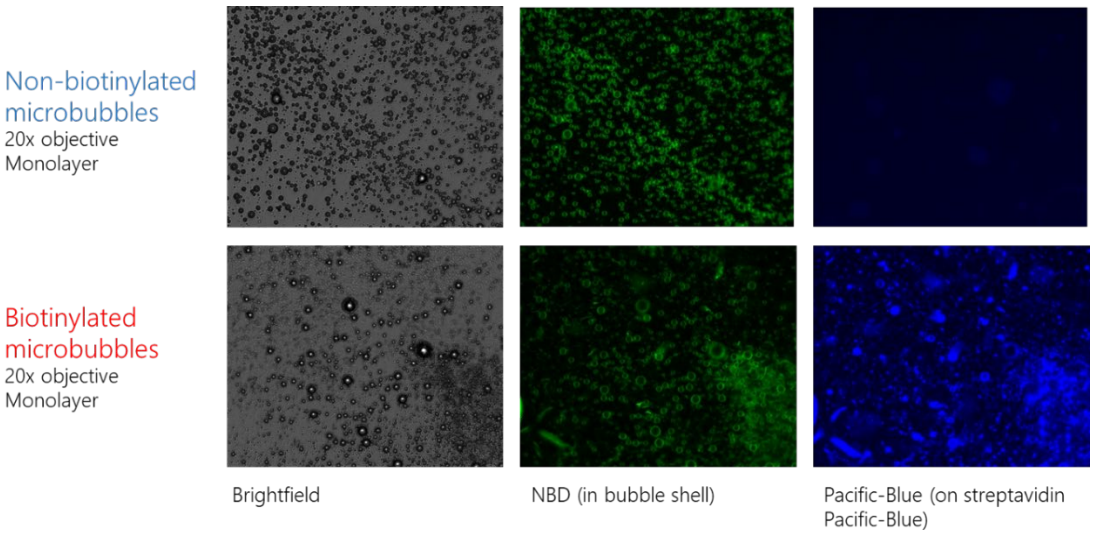

Figure 2.4.2: Representative brightfield and fluorescence microscopy images of biotinylated and non-biotinylated MBs that were incubated with streptavidin Pacific-Blue (strept-PB) and then washed. Green shows the NBD in the microbubble shells. Blue shows the strept-PB that was only observed (after washing) on the biot-MBs. Images taken at plane of maximum fluorescence intensity on a Nikon Eclipse Ti microscope.

2.4.3. Verification of anti-VCAM-1 conjugation

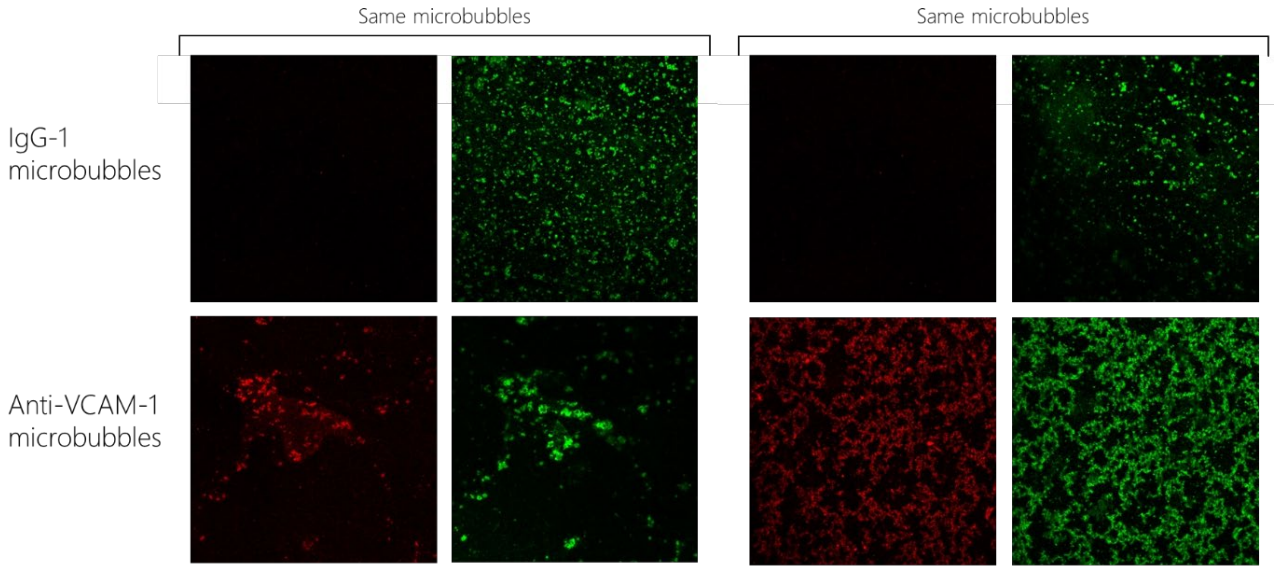

Figure 2.4.3: Representative fluorescence microscopy images of AV-MBs and IgG-MBs that were incubated with a solution of fluorescent VCAM-1 protein as detailed in Section 2.3.2 and Figure 2.2.1D. Each pair of images shows the same microbubbles, imaged in the red and green fluorescent channels respectively. Red shows the Alexa Fluor 647 on the VCAM-1 protein and is only visible (after washing) on the AV-MBs. Green shows the NBD in the microbubble shell. Images taken at plane of maximum fluorescence intensity on a Nikon Eclipse Ti microscope.

AV-MBs and IgG-MBs were incubated separately with a solution of fluorescent VCAM protein as detailed in Section 2.3.2 and Figure 2.2.1D. A uniform coating of Alexa Fluor 647 was observed on all AV-MBs, in contrast to IgG-MBs where no Alexa Fluor 647 fluorescence was observed (Figure 2.4.3).

2.4.4. Static flotation testing

One of the *in vitro* techniques used to quantify MB-cell binding was static flotation (as detailed in Section 2.3.4). Figure 2.4.4 shows representative dual-fluorescence microscopy images of the three conditions tested. It is immediately clear that whilst some IgG-MBs bound non-specifically to the membranes of LPS stimulated cells (Figure 2.4.4B), the binding of AV-MBs was much higher (Figure 2.4.4A). Some AV-MBs also bound to non-stimulated cells (Figure 2.4.4C), but this was to be expected due to the fact that non-stimulated cells are not fully quiescent.

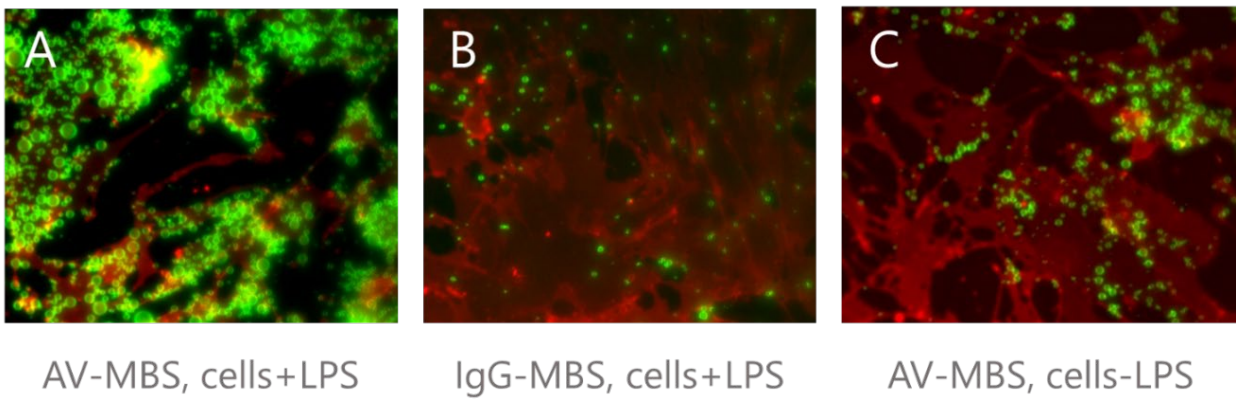

Figure 2.4.4: Representative images showing MB-cell binding in each of the three conditions tested. AV-MBs exhibited a much higher binding to LPS stimulated cells (A) than IgG-MBs (B). There was also some visible binding of AV-MBs to non-stimulated cells (C).

Figure 2.4.5 compiles the results from multiple cell samples and Figure 2.4.6 shows that, although there is a slight difference between the confluence of the cell samples at the time of testing, there is no correlation between the MB-cell binding and the cell confluence.

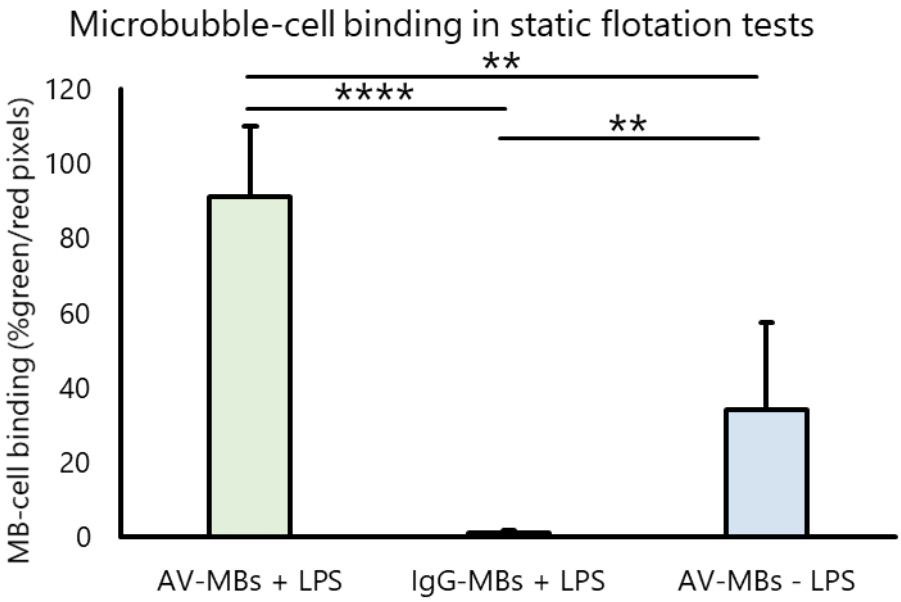

Figure 2.4.5: Graph showing MB-cell binding efficiency in static flotation tests. Binding percentage calculated by the proportion of each dual fluorescence microscopy frame occupied by microbubbles divided by the proportion of the frame occupied by cells. N = 5 per group.

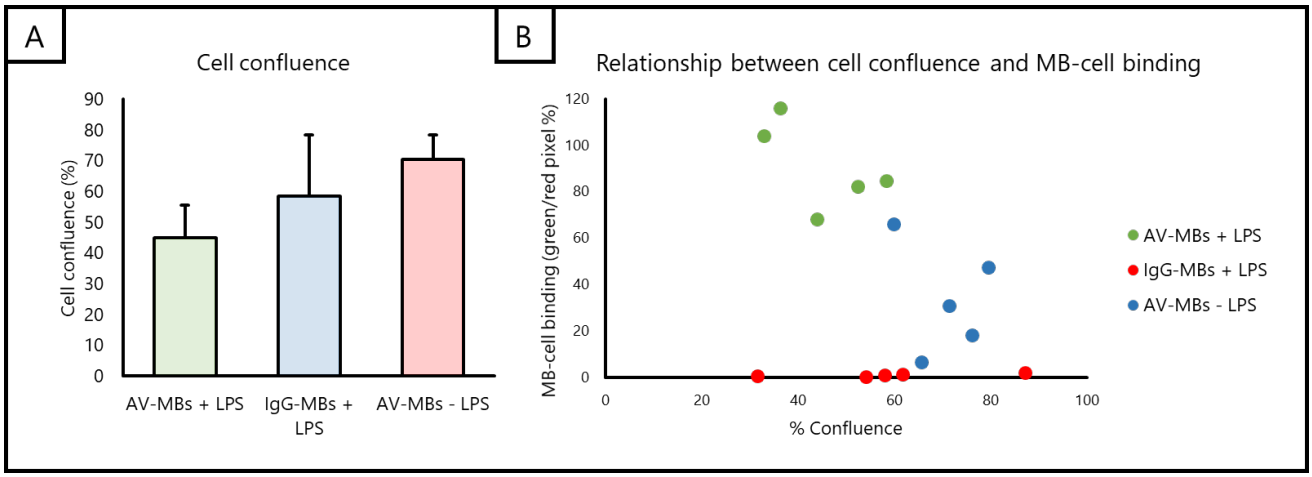

Figure 2.4.6: (A) The average confluence of the cells used in the testing of each condition (B) A plot showing the confluence and MB-cell binding of each sample tested. No obvious correlation is apparent.

2.4.5. Flow testing

The second *in vitro* test of the ability of AV-MBs to bind to LPS stimulated cells was conducted in µ-Slides as described in Section 2.3.5. This test was more physiologically relevant than the static flotation testing as the MBs had to remain bound to the cell endothelium when exposed to a wall shear stress of 10 Dynes/cm^2 (1 Pa). As the results from this test agreed well with those from other very similar tests with AV-MBs, other wall shear stresses were not tested.

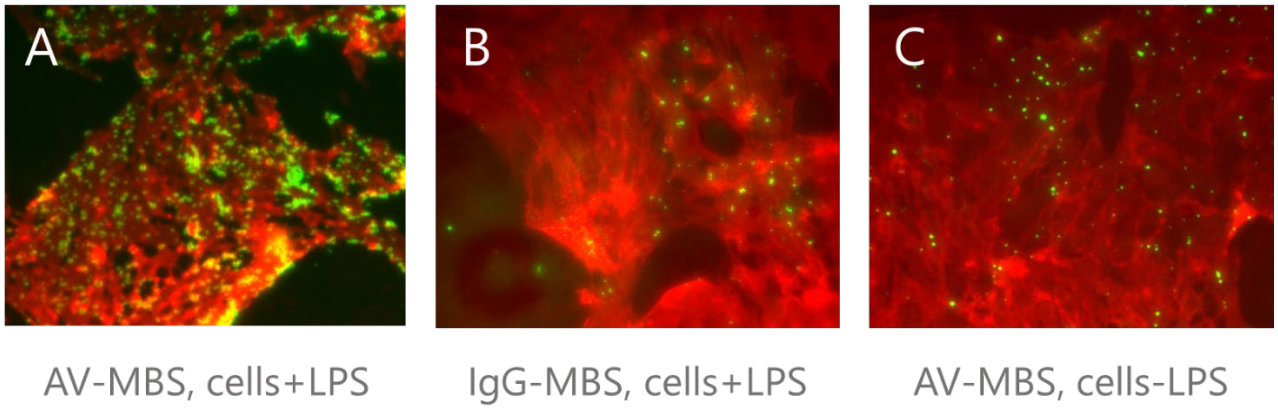

Figure 2.4.7: Representative dual fluorescence microscopy images showing the AV-MBs and IgG-MBs bound to B.end3 endothelial cells exposure under flow as described in Section 2.3.5.

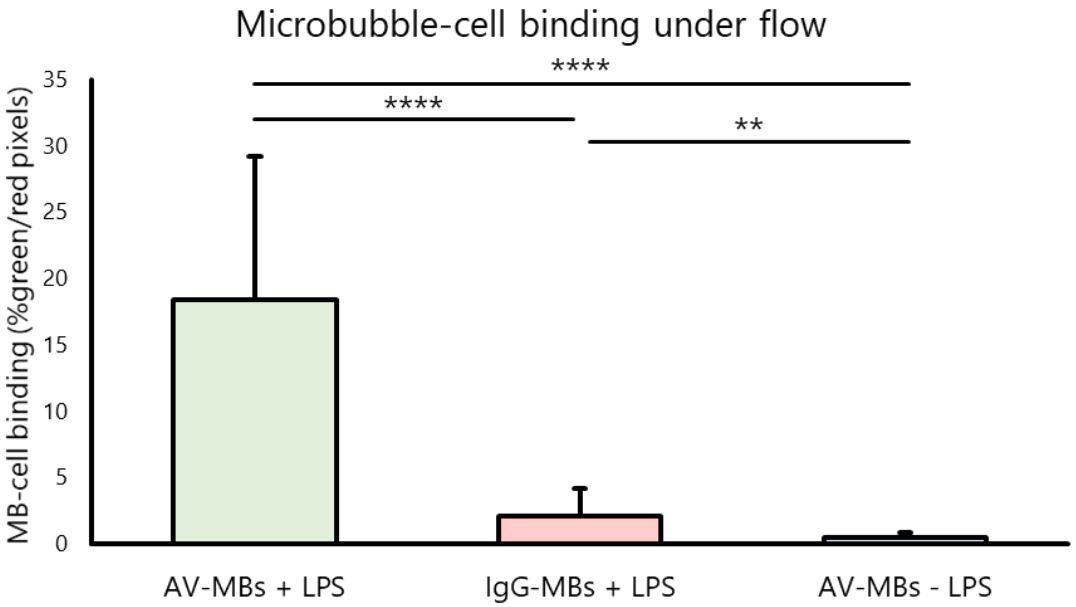

Figure 2.4.8: The binding of AV-MBs and IgG-MBs to B.end3 endothelial cells. Binding percentage calculated by the proportion of each dual fluorescence microscopy frame occupied by microbubbles divided by the proportion of the frame occupied by cells.

Figure 2.4.7 shows representative dual-fluorescence microscopy images of MBs (green, from the NBD in the MB shell) and cells (from the CellMask Deep Red plasma membrane stain). Again, visibly more AV-MBs (Figure 2.4.7A) bind to stimulated cells than IgG-MBs (Figure 2.4.7B), and this is again larger than the number of AV-MBs that bind to unstimulated cells (Figure 2.4.7C). These results are corroborated by the full results shown in Figure 2.4.8. In contrast to the results in Section 2.4.4, there is very minimal binding of AV-MBs to unstimulated cells when under flow. Figure 2.4.9A shows that there were no significant differences in the mean cell confluence for each of the tested

groups. However, Figure 2.4.9B shows that, by chance, the lowest cell confluence in both of the control groups was lower than the lowest cell confluence in the experimental group. Whilst there is potentially a slight relationship between cell confluence and MB-cell binding, it is clear from these plots that the MB-cell binding in the experimental group is much larger than that in either of the control groups.

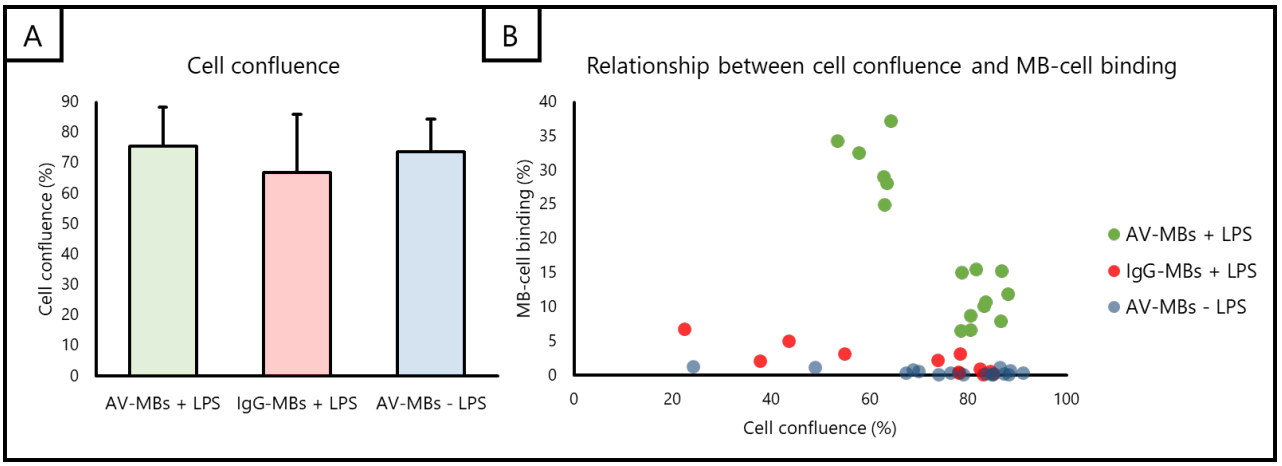

Figure 2.4.9: (A) The average confluence of the cells used in the testing of each condition (B) A plot showing the confluence and MB-cell binding under flow of each sample tested. No obvious correlation is apparent.

2.5. Discussion of *in vitro* results

The results presented in this Chapter demonstrate that both streptavidin and anti-VCAM-1 can be conjugated to the surface of microbubbles using a relatively simple manufacturing protocol. Whilst fluorescence microscopy is not a quantitative measure of streptavidin or antibody loading, the distinctly visible differences seen in Figure 2.4.2 and Figure 2.4.3 provide sufficient evidence of conjugation.

Evidence that AV-MBs selectively bind to LPS-stimulated mouse brain endothelial cells in both a static system and under physiologically relevant fluid flow is also shown (Figure 2.4.4 and Figure 2.4.7). Minimal binding was observed between either the AV-MBs with unstimulated cells or IgG-MBs (with equivalent surface concentrations of unbound streptavidin and/or biotin) and inflamed cells. This confirms first that binding was due to the antibody, and second, since the anti-VCAM-1 antibody has a selective affinity for the VCAM-1 protein, that the AV-MBs were binding selectively to the VCAM-1 on the endothelial cells.

There are several important differences between the flow system used to test these microbubbles and physiological conditions. These include the presence of blood, pulsatility in the flow, varying vessel diameters, vessel compliance and vessel junctions. Whilst some *in vitro* models have been developed that could address some of these concerns, it has been shown that the binding results of AV-MBs in flow systems with similar limitations translate well to *in vivo* experimentation.[400] Therefore, the next Chapter focuses on *in vivo* testing to provide data that is more clinically relevant than further *in vitro* data.

In Chapter 3, AV-MBs are injected *in vivo* and then exposed to unfocused ultrasound to investigate whether this combination is capable of selectively increasing US-BBBD in the target region. Measuring US-BBBD is important; many teams have used antibodies to target agents to brain metastases, and many teams have used ultrasound to transport therapeutics across the BBB. To the author's knowledge, this is the first time that these techniques have been combined.

If targeted US-BBBD is achievable without focusing the ultrasound transducer, the door is then opened to future investigations that compare the therapeutic efficacy and off target side effects of this technique with those that arise from systemic delivery.

The extent to which the research questions of Chapters 2 and 3 are answered is discussed in full in Section 3.4.

2.6. Conclusion

The *in vitro* results in this Chapter indicate that microbubbles conjugated with anti-VCAM-1 (AV-MBs) are capable of binding to the endothelium of cells stimulated with lipopolysaccharide (LPS). This binding enables bubbles to be retained under physiologically relevant flow rates and in significantly larger numbers than either IgG-MBs with stimulated cells or AV-MBs undergo to non-stimulated cells. These findings indicate that the anti-VCAM-1 on the AV-MBs selectively binds to the elevated VCAM-1 expression on stimulated cells and separately, that they should be capable of inducing wide reaching bio-effects. Hence, further *in vivo* investigation is warranted into the ability of AV-MBs to bind to areas with increased VCAM-1 expression in the brain and then deliver a therapeutic effect. This investigation is the subject of the next Chapter.

Chapter 3. Targeting therapy *in vivo*

3. Targeting therapy *in vivo*

Abstract

Whilst ultrasound and microbubble mediated blood-brain barrier disruption (US-BBBD) presents one of the most promising techniques for safely and transiently increasing the uptake of therapeutics into the parenchyma, all clinical and pre-clinical studies so far have used focused ultrasound. This presents numerous practical challenges; most crucially, prior knowledge of the disease site is required. The research in this Chapter asks whether the combination of antibody targeted microbubbles and unfocused ultrasound could be used to deliver therapeutics selectively. Such a technique has the potential to achieve a molecular level of specificity for pathologies whose exact location is unknown, for example cerebral metastases.

An injection of a cytokine (Interleukin-1β, Il-1β) into the left striatum was used to cause a localised upregulation of VCAM-1. The AV-MBs (developed in Chapter 2) were then injected via the tail vein and given time to clear from the systemic circulation. An ultrasound transducer aligned co-axially with the centre of the brain was then used to expose the whole brain to ultrasound. Ultrasound-mediated blood brain barrier breakdown was then measured using both MRI (gadolinium uptake) and histology (serum IgG extravasation).

AV-MBs caused a significant increase in US-BBBD between the inflamed area and the non-inflamed area. This did not occur with microbubbles conjugated with a non-specific Rat-IgG, indicating that this specificity arose from VCAM-1 binding in the brain. This also did not occur in animals that underwent analogous intra-striatal injections of PBS.

This demonstrates the potential of an exciting new approach for targeting drug delivery in the brain and warrants further testing in an *in vivo* model of brain metastases.

Graphical Abstract

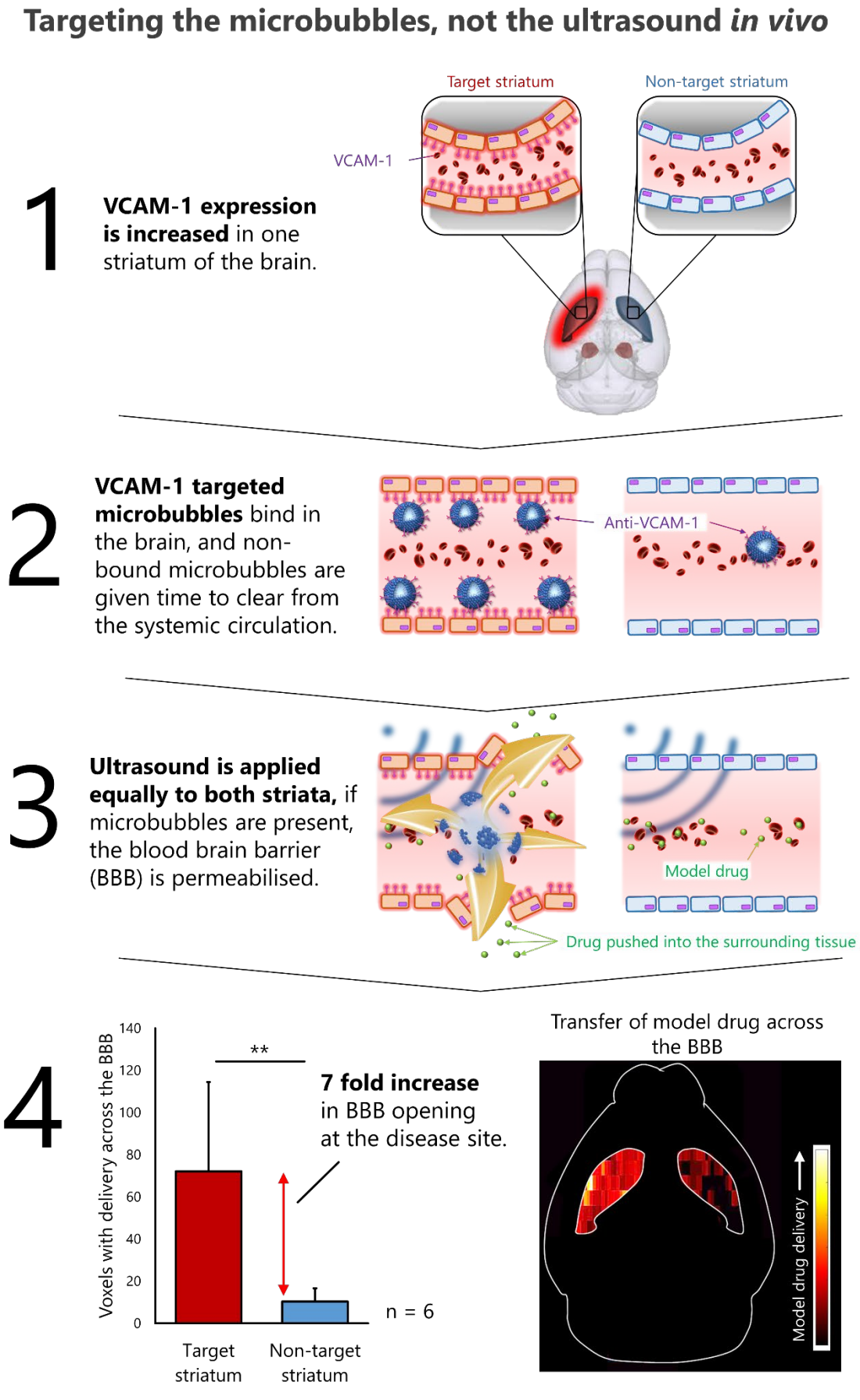

Attributions

In all of the experiments in Chapter 3, I am incredibly fortunate to have been able to work with Dr. Sarah Peeters from the Department of Oncology. Dr. Peeters was responsible for all MRI imaging, histology and animal care. Dr. Vanessa Johanssen provided occasional assistance with animal handling on busy experiment days. Dr. Michael Gray and Sean Smart designed the system used to expose mice to ultrasound which was then manufactured by James Fisk and David Salisbury of the IBME workshop.

3.1. Introduction

3.1.1. Chapter aim

The aim of the work described in Chapter 3 was to test the ability of the AV-MBs (developed in Chapter 2) to bind selectively to target regions in the brain, and then, in combination with whole-brain ultrasound, cause ultrasound-mediated blood brain barrier breakdown (US-BBBD) selectively in the target regions.

3.1.2. Model used: an intra-striatal injection of cytokine

To create a target region in the brain that imitates the VCAM-1 upregulation surrounding metastatic tumours, an injection of cytokine into one striatum of the brain was used. When this cytokine, interleukin-1beta (Il-1β) is injected, the endothelium is activated selectively in the cerebral hemisphere that received the injection, particularly in the striatum and around the injection site. The ensuing inflammation leads to a local upregulation of VCAM-1 (in the injected hemisphere) and has been used previously as a proxy for both multiple sclerosis[380] and brain metastases.[109] A schematic for the injection is shown in Figure 3.1.1.

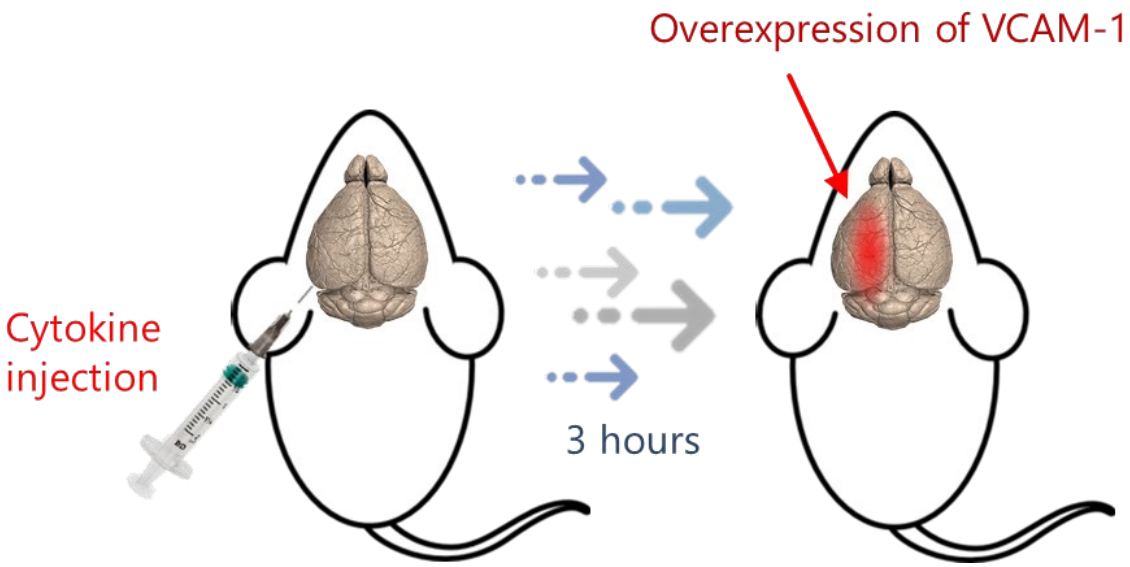

Figure 3.1.1: A schematic of the intra-striatal injection of cytokine and subsequent inflammation (and upregulation of VCAM-1) in the left cerebral hemisphere particularly close to the site of injection.

This model is a highly relevant precursor to an *in vivo* brain metastasis model, particularly with regards to the aim of Part 1 of this thesis. By upregulating VCAM-1 expression selectively in one half of the brain, the ability of antibody targeted MBs and whole-brain ultrasound to cause US-BBBD in a selective area of the brain can be measured by comparing the US-BBBD in each half of the brain.

3.1.3. Advantages of the cytokine injection model

This model was chosen for scientific, experimental and ethical reasons. Firstly, the upregulation of VCAM-1 and other effects on the cerebral microenvironment from an intra-striatal injection of Il-1β have been well characterised,[109,380,394,449] and shown to provide a relevant model for predicting the selective targeting efficacy of anti-VCAM-1 conjugated contrast agents to metastatic tumours.[108,450]

Secondly, early stage metastatic tumours consist of only a few thousand cells and are therefore too small to image on MRI and challenging to accurately locate using histology. An intra-striatal injection of Il-1β causes an upregulation of VCAM-1 at a pre-defined target site,[109,380,394,449] making it straight-forward to compare US-BBBD between the target site and the remainder of the brain.

Finally, animals that undergo an intra-striatal injection of Il-1β are exposed to ultrasound and microbubbles after 3 hours, and are alive for a maximum of 5 hours after cytokine injection. This is in contrast to the timescale of days or weeks over which animals implanted with tumour cells have to be kept alive in order for metastatic tumours to develop. Therefore, it is ethically more appropriate to use a cytokine injection for initial testing.

3.1.4. Weaknesses of the cytokine injection model

This model is, however, not a perfect replica of the conditions around metastatic tumours.

The increase in VCAM-1 expression arising from an intra-striatal IL-1β injection is far smaller than the estimated difference between the expression of VCAM-1 in early stage metastases and healthy brain tissue.[451] Section 2.2.10 of this thesis estimated that the expression of VCAM-1 surrounding brain metastases is 2 to 3 orders of magnitude greater than that in healthy brain tissue., see).

By contrast, preliminary experimental work conducted by Dr. Sarah Peeters found that the VCAM-1 expression in the injected hemisphere was, on average, only 2.3 times greater than the VCAM-1 expression in the non-injected hemisphere. Similar analysis by Dr. Vanessa Johanssen found that, in the region of the brain close to the injection site, the number of blood vessels with histologically visible VCAM-1 expression in the cytokine injected hemisphere was only double that in the non-injected hemisphere. These increases were also associated with a high inter-animal variability.

The number of microbubbles capable of binding to the VCAM-1 upregulation after a cytokine injection may also be low; a comparison between micrometre-scale (MPIO) and nanometre-scale (USPIO) MRI contrast agents (both conjugated with anti-VCAM-1) found that while MPIOs could sensitively detect the cytokine injection site, USPIOs could not as not enough of them accumulated in the inflammed region.[109]

Beyond the upregulation of VCAM-1, the cytokine injection may also have other physiological effects on the brain vasculature, most notably influencing the BBB and the cerebral blood flow. These are effects that may or may not be present around early stage metastases and may impact the results in this Chapter, something that is discussed in detail in Section 3.4.

3.1.5. Experimental procedure

An overview of the *in vivo* experimental protocol used in Chapter 3 can be found in Figure 3.1.2. A full experimental timeline and description can be found in Section 3.2.1. Briefly, once VCAM-1 has been upregulated at the injection site, microbubbles are injected and allowed to clear from the systemic circulation. Then, ultrasound is applied to the whole brain. If there is a sufficient difference between the number of microbubbles bound to the target site and the rest of the brain, a corresponding difference in US-BBBD would be expected.

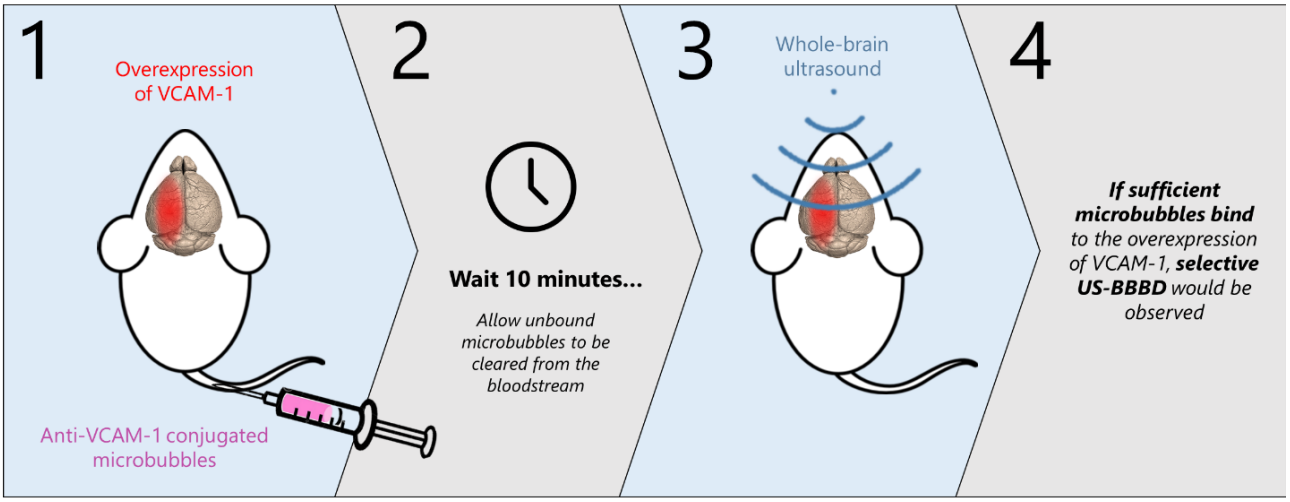

Figure 3.1.2: The experimental protocol using mice with a local upregulation of VCAM-1 in the brain (in the cerebral hemisphere that received the intra-striatal injection of cytokine). Microbubbles (conjugated with either anti-VCAM-1 or Rat-IgG-1) are injected and then allowed to clear from the systemic circulation. After ten minutes of clearance, the whole brain was exposed to ultrasound using a transducer co-axially aligned with the centre of the brain. If there is a sufficient difference in the concentration of microbubbles bound to the injected hemisphere and the non-injected hemisphere, a corresponding difference in US-BBBD would be expected.

3.1.6. Experimental groups

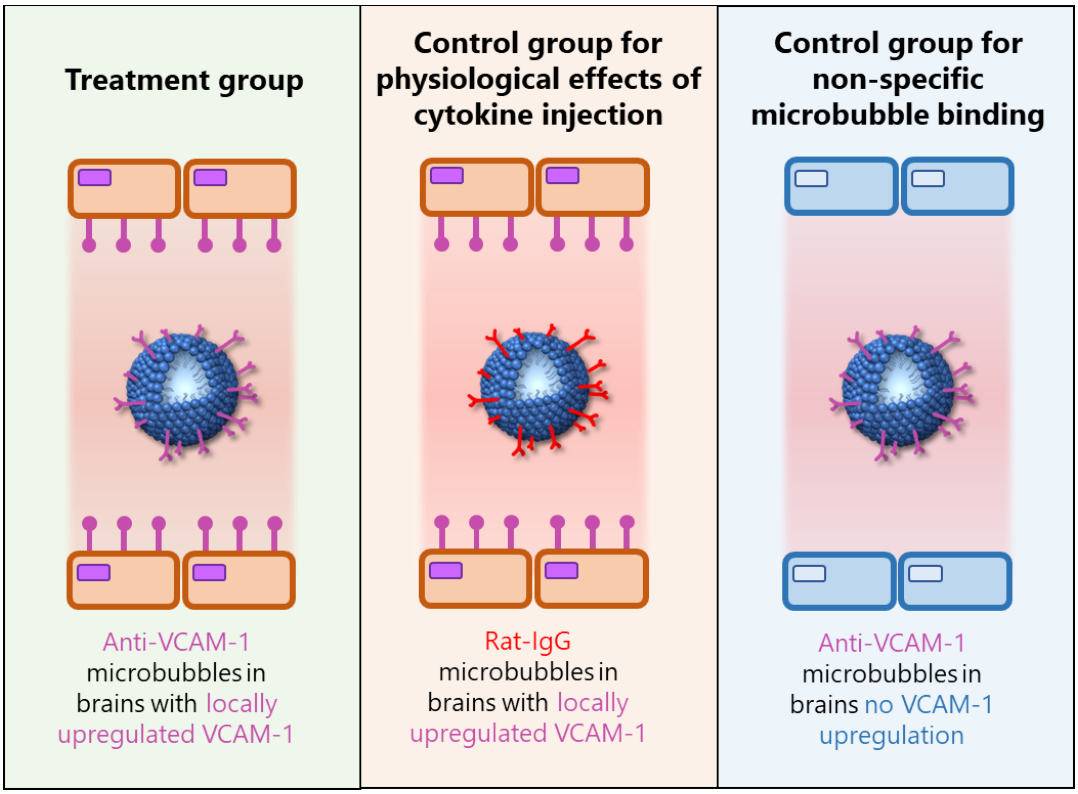

Figure 3.1.3: The experimental groups used in this Chapter. In the treatment group, AV-MBs were injected into mice that had received an intrastriatal injection of IL-1β to upregulate VCAM-1 in the left cerebral hemisphere of the brain. In the second group, IgG-MBs were injected into mice that had

also undergone this injection of IL-1β. This was designed to control for physiological effects of the cytokine injection. In the third group, AV-MBs were injected into mice that had received an analgous intrastriatal injection of PBS. This was designed to control for any effects of the injection itself on BBB disruption. These groups are detailed in full in Sections 3.1.6.1, 3.1.6.2 and 3.1.6.3.

Three experimental groups were used in this Chapter. These are outlined in Figure 3.1.3 and detailed one by one in Sections 3.1.6.1, 3.1.6.2 and 3.1.6.3. The results from all three groups can be found in Section 3.3 and the implications of these results for this Chapter's research questions is discussed in Section 3.4.

3.1.6.1. Treatment group

In the treatment group, the AV-MBs developed in Chapter 2 were injected into mice that had undergone a cytokine injection (and therefore had an upregulation of VCAM-1 at the target site). If the combination of AV-MBs and whole-brain ultrasound is capable of selectively causing US-BBBD at the target site, a difference in US-BBBD between the injection site and the non-injected hemisphere would be expected from this group.

3.1.6.2. Control for physiological effects of the cytokine

In the second group, designed to test for any physiological effects that the cytokine may have had on the brain, the IgG-MBs developed in Chapter 2 were also injected into mice that had undergone a cytokine injection. If the cytokine injection acted to enhance BBB breakdown in mechanisms other than via the upregulation of VCAM-1, this group would also show a difference in US-BBBD between the injection site and the non-injected hemisphere.

However, as IgG-1 antibodies play an important role in the body's immune response, and there is a high cross-reactivity between mouse and rat[452,453] (IgG-MBs are conjugated with Rat IgG-1), some non-specific binding of IgG-MBs in the brain may occur. Moreover, as one of the principle roles of IgG-1 antibodies is to defend the body from harmful foreign substances and toxins, an increase in non-specific binding at the site of the cytokine injection could also reasonably be expected.

Therefore, the results for this control need to be analysed with care.

3.1.6.3. Control for non-specific binding of AV-MBs

The third group, designed to test for US-BBBD arising from either AV-MBs bound to endogenous VCAM-1 expression or remaining in the systemic circulation, underwent analogous intra-striatal injections of phosphate buffered saline (PBS) and injections of AV-MBs.

3.1.7. Measurement techniques

Blood brain barrier disruption was measured using two different methods; gadolinium uptake into the parenchyma was measured on MRI and serum IgG extravasation was measured histologically. Acoustic emissions from brain were collected using a single element passive cavitation detector (PCD). Details of the exact methods used and the results from each of these measurement techniques can be found in Section 3.2 and Section 3.3 respectively. These techniques are also summarised in Figure 3.1.4.

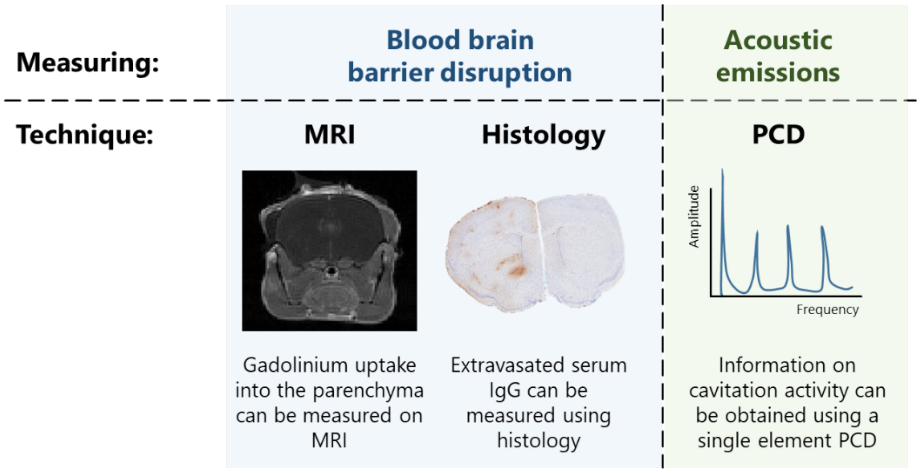

Figure 3.1.4: The measurement techniques used in this Chapter

3.2. Experimental Methods

3.2.1. Experimental timeline

Gadolinium uptake into the parenchyma and serum IgG extravasation were used to compare the US-BBBD caused by both Lyso-MBs and Control-MBs. Female BALB/C mice (8-11 weeks old, Charles River, UK) were anaesthetized using isoflurane (1.5-2.0%) in 30% O_2: 70% N_2O), then had the top of their head shaved before an intra-striatal injection of cytokine (Section 3.2.2) was carried out to induce unilateral vascular activation (inflammation only in the injected cerebral hemisphere).[109,380] Three hours later, mice were then placed in an MRI cradle with purpose built compatibility with the ultrasound set-up used and were injected with 1 x 10^8 microbubbles (either AV-MBs or IgG-MBs, Section 2.2.1). A first MRI scan was conducted (Section 3.2.4) followed by positioning of the mouse on the ultrasound setup using the same cradle to maintain the animal's position between MRI scans. 10 minutes after microbubble injection and 30 seconds after 30µl of gadolinium was injected, mice were exposed to ultrasound for 2 minutes (500 kHz, 820 kPa, 1 Hz PRF, 1% DC, Section 3.2.3). The 10 minute delay was included to allow clearance of the MBs from systemic circulation, leaving behind only those bound to the endothelium. This time was determined experimentally by observing US-BBBD on naïve animals; if naïve mice were exposed to ultrasound 10 minutes after microbubble injection no increase in US-BBBD was observed relative to the US-BBBD that occurs in the absence of microbubbles. The ultrasound frequency was chosen as it is most practical for transmission through the skull in clinical translation and the pressure and PRF were chosen based on the US-BBBD efficacies observed in Chapter 5.

A second MRI scan was then performed. Comparison of the pre- ultrasound and post-ultrasound MRI scans allowed quantification of gadolinium uptake in the parenchyma (Section 3.2.4). Mice were then sacrificed using an overdose of pentobarbitol administered via intraperitoneal injection, followed by transcardial perfusion and fixation to preserve the blood vessels for histological analysis (Section 3.2.5). A summary of the full experimental timeline can be found in Figure 3.2.1

Comparison of the pre and post ultrasound MRI scans allowed quantification of gadolinium uptake in the parenchyma. All animal procedures were performed in accordance with the guidelines of the University of Oxford and approved by the UK Home Office. A summary of this timeline can be found in Figure 5.2.1.

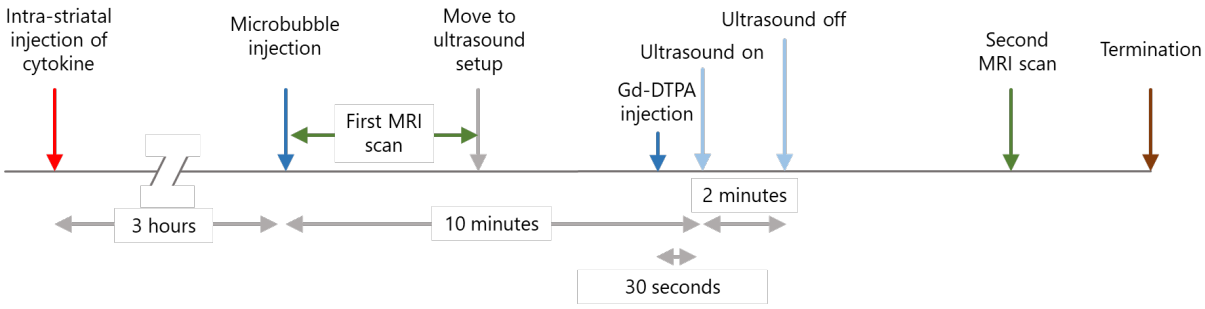

Figure 3.2.1: Timeline of in vivo experiments in this Chapter.

3.2.2. Intra-striatal injection

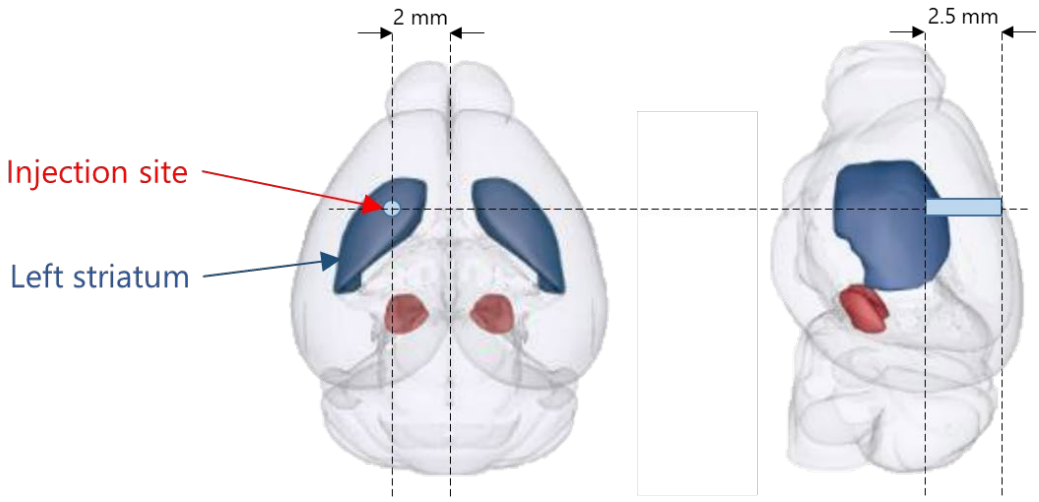

Figure 3.2.2: Diagram showing the cytokine injection site relative to the brain and the left striatum.

All animal procedures were performed in accordance with the guidelines of the University of Oxford and approved by the UK Home Office. Female BALB/C mice (8-11 weeks old, Charles River, UK) were anaesthetized using isoflurane (1.5-2.0% in 30% O_2: 70% N_2O), hair on the scalp was removed and the animal was placed in a stereotaxic frame. The skin on the scalp was then opened by a sterile incision followed by the drilling of a burr hole in the skull (co-ordinates from bregma: anterior +0.5mm; left 2.0mm; depth 2.5mm, Figure 3.2.2). Mouse recombinant interleukin-1β (1 ng, IL-1β,

Peprotech EC, UK) in 1 µl sterile PBS was injected using a glass microcannula to induce unilateral vascular activation. After suturing the scalp, the mice were recovered from anaesthesia. After 3 hours, the mice were imaged using MRI and then treated with microbubbles and ultrasound as detailed in Section 3.2.1.

3.2.3. Ultrasound exposure

Ultrasound exposure was carried out using a purpose built setup that allowed reproducible exposure of mice in an MRI cradle (Figure 3.2.3). The ability to maintain the position of the mouse skull relative to the MRI cradle via a stereotaxic frame allowed comparison of the pre and post ultrasound MRI scans, thus allowing visualisation of image hyperintensity caused by gadolinium uptake into the parenchyma and thus visualisation of US-BBBD. It also maintained anaesthesia throughout ultrasound exposure via cheek bars and a nosecone.

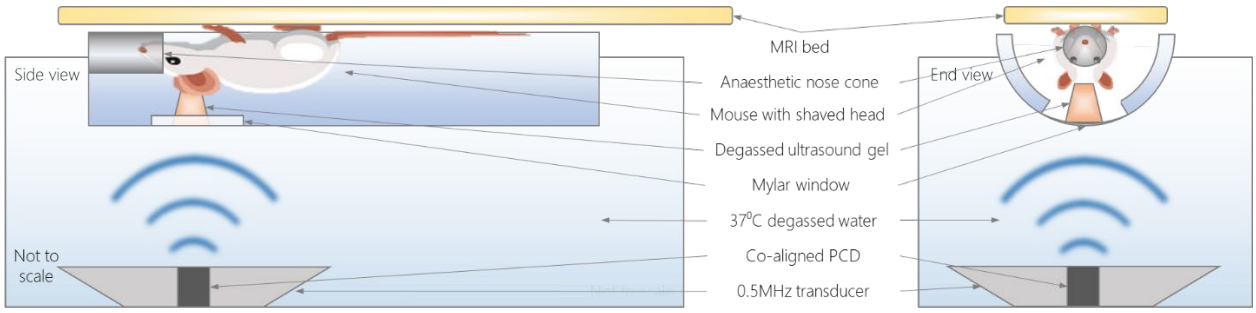

Figure 3.2.3: A schematic diagram of the key components in the set-up used to expose mice to ultrasound.

The setup consisted of a H107 transducer (Sonic Concepts, US), mounted directly below a holder for the MRI cradle. The ultrasound transducer was driven through a matching transformer by a 0.5 MHz sinusoidal signal from a function generator amplified 55 dB by a radiofrequency amplifier (E&I 1040L, Rochester, NY). The distance between the transducer and the mouse's brain was calibrated such that the brain lay directly in the ultrasound focus. The mouse was inverted to allow ultrasound to pass through the top, rather than the bottom, of the skull. The mouse's head was shaved and coupled to the water tank using degassed ultrasound gel and a mylar window. The water in the tank was degassed prior to experimentation and held at 37˚C using an aquarium thermometer. Importantly, the

MRI cradle was simple to align in the ultrasound setup ensuring that the focal volume of the ultrasound transducer was aligned coaxially down the centre of the brain. This ensured that there were no discrepancies between the pressures experienced by each half of the brain. The MRI cradle was also simple to transfer to the MRI machine, allowing straightforward pre and post ultrasound imaging.

Ten minutes after microbubble injection (to allow clearance of non-bound microbubbles from the brain), and 30 seconds after gadolinium injection (to ensure the presence of circulating gadolinium if the BBB was permeabilised), the mice were exposed to 120 seconds of 0.5MHz ultrasound at 820kPa peak negative pressure. A 1 Hz pulse repetition frequency and a 1% duty cycle was used.

3.2.4. MRI analysis of gadolinium extravasation into the parenchyma

All MRI procedures were performed using a horizontal wide-bore superconductive 7.0 T MRI system (Agilent Techonologies Inc., US) with a 26mm inner diameter transmit/receive birdcage RF coil (Rapid Biomedical, Germany). All mice were imaged pre- and post- gadolinium injection/ultrasound exposure using a Spin Echo Multi Slice (SEMS) sequence. The parameters were Repetition Time (TR) = 500ms, Time to Echo (TE) = 8ms, number of averages = 4, field of view = 22.5x22.5x22.5 mm^3, acquisition matrix size = 128x128x32, with a scan time of 4 minutes and 24 seconds.

To analyse differences in BBB breakdown, grey intensity on the pre- versus post-treatment scan were measured and compared between hemispheres. Both pre and post- scans were masked and the post-treatment scan was split in a left and right hemisphere using Matlab®. Average grey intensity per slice was calculated from the pre-treatment MRI and these averages were corrected for gadolinium injection (calculated on naïve animals). On the post-treatment MRI scan, voxels having values more than 3 standard deviations above the corrected mean of the pre-treatment scan (thus indicating enhanced gadolinium uptake into the parenchyma) were considered to be hyper-intense voxels. A purpose written Matlab® script was then used to compare the number of hyper-intense voxels between the left and the right hemisphere for each animal. The number of hyper-intense voxels in the

front, mid and rear thirds of the brain was also calculated to allow more detailed comparisons of the spatial distribution of US-BBBD. These results can be found in Section 3.3.1.

3.2.5. Histological analysis of serum IgG extravasation

After perfusion and fixation of the mice, brains were isolated and kept in PLP-light for 4 hours, after which they were placed in a 40% sucrose solution until they sank. Brains were frozen in isopentane and stored at -20°C. Each brain was sectioned into slices 20 μm thick, collecting the region of the brain that contains the striatum in a series of 10. This meant that when used for staining, every 10^{th} slice was stained with the same protocol, and these slices were 200 μm apart from each other.

Slides were then air dried and rehydrated in PBS, placed in 1% H_2O_2 in methanol for 20 minutes, and washed in PBS and PBS-tween. After blocking in 10% Tris-NaCl-blocking buffer (TNB), slides were washed in PBS, and then exposed for 45 minutes to a secondary antibody (biotinylated anti-mouse IgG) at a dilution of 1:100 in PBS. After, they were washed, incubated with an Avidin-Biotin Complex solution (Vector Labs, UK) and washed again. Slides were then exposed to DAB-peroxidase substrate solution in 0.1M phosphate buffer, counterstained using cresyl violet (to show neurons), dehydrated in an increasing concentration of alcohol followed by Xylene, and mounted in DPX.

Images of the histology slides were analysed using Aperio ImageScope® (Leica Biosystems, Germany). After manually marking the areas of the histology slices corresponding to the left and right cerebral hemispheres, pixels with a value of 0-175 in the red channel (corresponding to the areas with dark DAB staining) were considered to be locations of serum IgG extravasation. These pixels are referred to as IgG positive elsewhere in this Chapter. The total number of IgG positive pixels for each cerebral hemisphere of each animal was then calculated. These results can be found in Section 3.3.2.

3.2.6. Acoustic emissions monitoring

Acoustic emissions monitoring during *in vivo* experiments was achieved using a single element passive cavitation detector (PCD) with a 3.5MHz centre frequency (Olympus, US) co-aligned with

the H107 ultrasound transducer. This allowed subsequent analysis of any acoustic emissions from the brain.

A HS3 digital oscilloscope (TiePie, The Netherlands) and the PCD were triggered with a function generator. The PCD signal was first passed through a 500 kHz notch filter (hardware) to remove the fundamental. Each recorded voltage trace from the PCD was then truncated in the time domain to remove the portion of the signal prior to the first reflection. A Hanning window was applied to the voltage trace to reduce edge effects. Matlab® (Mathworks, US) was used to compute the fast Fourier transform (FFT) and the power spectral density (PSD) for each voltage trace. The harmonic and ultraharmonic signal powers were determined by integrating the power spectral density with respect to frequency over 30 kHz bands at each harmonic and ultraharmonic from 1 to 8 MHz. The broadband power was determined by integrating the power spectral density with respect to frequency over the remaining frequencies between 1 and 8 MHz. The total energy of acoustic emissions for each sample was calculated by integrating the powers (harmonic, ultraharmonic and broadband) with respect to time. These results can be found in Section 3.3.3.

3.3. Results

3.3.1. MRI results

This Section details the US-BBBD in each of the three experimental groups, calculated from the MRI hyper-intensities arising from gadolinium uptake into the parenchyma as detailed in Section 3.2.4.

Figure 3.3.1 shows heat maps of the transverse and sagittal distributions of US-BBBD for each experimental group; the brighter the pixel, the higher the aggregate US-BBBD in that location. The colour of each pixel corresponds to the number of hyper-intense pixels either vertically (for the transverse plots) or horizontally (for the sagittal plots), aggregated all 6 animals in each group.

Figure 3.3.2 plots the average US-BBBD for each experimental group, split by cerebral hemisphere and brain region. The three sections of the brain (the anterior, mid and posterior thirds) correspond to those indicated by the dashed white lines in Figure 3.3.1.

As the aim of this chapter is to investigate the ability of antibody conjugated microbubbles and whole-brain ultrasound to cause US-BBBD selectively in the target region, the key comparisons to be made are between the left (target) and right (non-targeted) hemispheres, particularly close to the site of the injection (the striatum).

In the treatment group (cytokine + AV-MBs), there is a visible difference between the left and right hemispheres in Figure 3.3.1, particularly close to the injection site. This difference is not apparent in either of the control groups. This is reinforced in Figure 3.3.2 as the only statistically significant differences between hemispheres are for the whole brain and for the injection site (mid brain) in the treatment group. As all MRI enhancements are calculated relative to the endogenous uptake of gadolinium in the brain in the absence of microbubbles and ultrasound, Figure 3.3.1 and Figure 3.3.2 indicate that the IgG-MBs underwent some non-specific binding to both hemispheres of the brain and that in the PBS control, some AV-MBs were either still circulating 10 minutes after microbubble injection or bound to endogenous VCAM-1 sufficiently to cause detectable US-BBBD, particularly in the posterior of the brain.

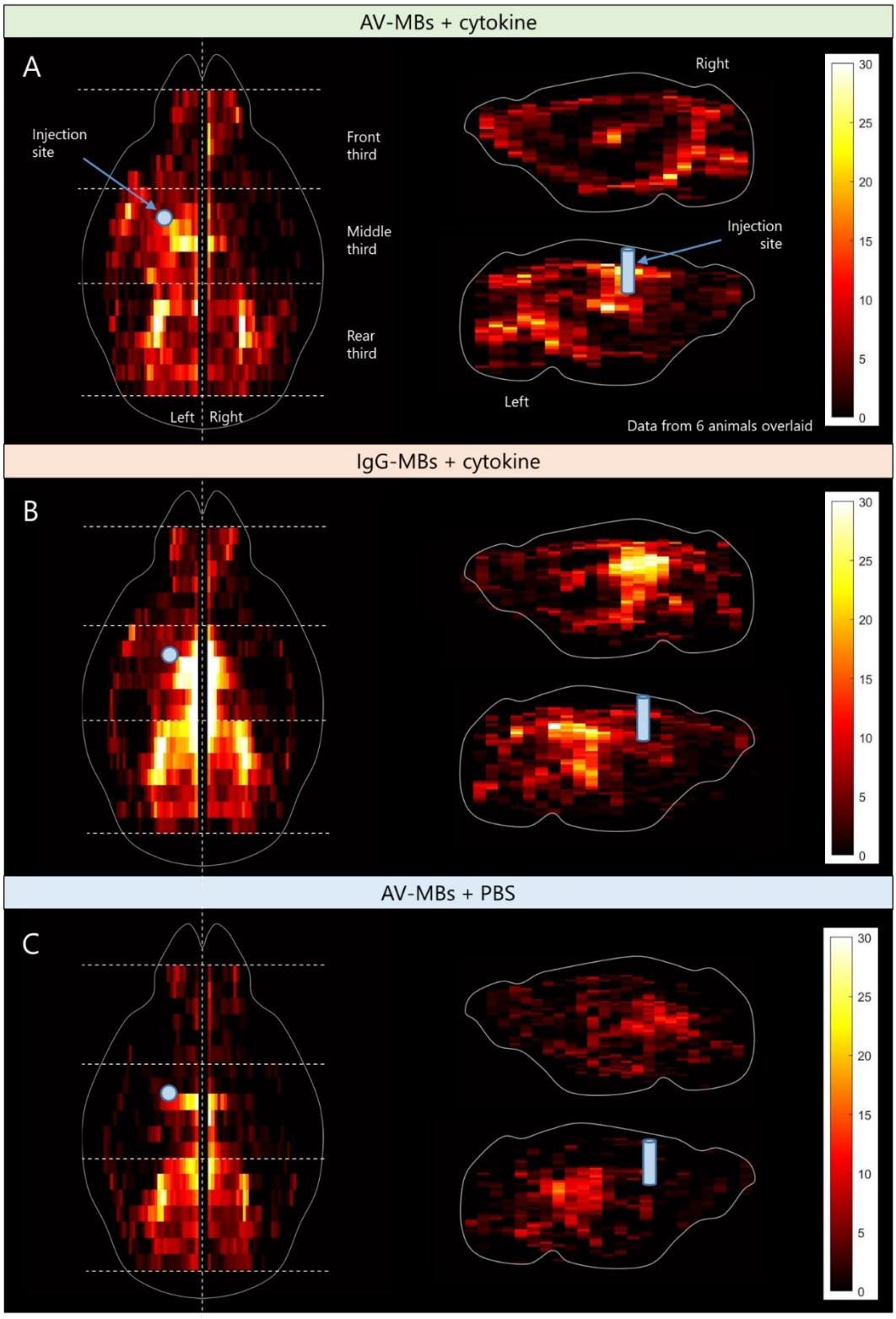

Figure 3.3.1: Transverse and sagittal heat maps of the distribution of US-BBBD in the brains for each experimental group. The colour scale corresponds to the number of hyper-intense voxels in each location for each projection. The MRI data for all 6 animals in each group has been overlaid. The approximate location of the injection site is shown. The dashed lines show how the brain was divided up for plots in Figure 3.6.2. With regards to the aim of this Chapter, inspection of the difference in US-BBBD between left (target) and right (non-targeted) hemispheres is warranted at the mid brain (injection site). A difference is only visually apparent for the treatment group (cytokine + AV-MBs). All colour bars have the same scale for ease of comparison between experimental groups.

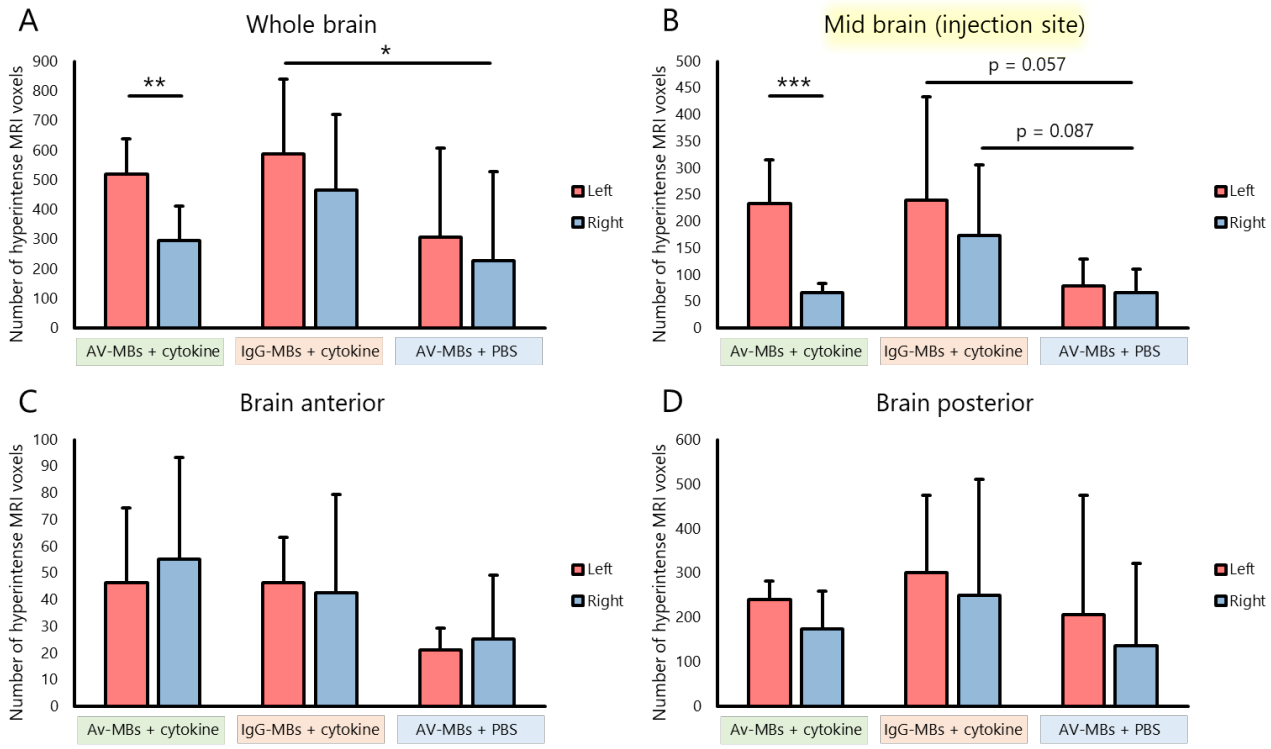

Figure 3.3.2: Average US-BBBD for each of the three experimental groups (6 animals in each group) as measured by gadolinium uptake into the parenchyma. All plots are split between left (target) and right (non-target) cerebral hemispheres to allow comparisons of the locations of US-BBBD. Hyper-intense voxels are those in the post-ultrasound MRI scan that have a brightness higher than 3 standard deviations above the average intensity of the brain in the pre-ultrasound MRI scan. (A) The US-BBBD for the whole brain; only the treatment group (cytokine + AV-MBs) has a significant difference between the hemispheres ($p<0.01$). (B) The US-BBBD for the mid brain (the site of the cytokine or PBS injection). The treated group has a significant ($p<0.001$) difference in US-BBBD between hemispheres. The elevation of the IgG-MBs control above the PBS control suggests non-specific binding of the IgG-MBs in both hemisphere of the brain. (C and D) The US-BBBD results in the anterior and posterior of the brain where none of the experimental groups had a significant difference between hemispheres.

Figure 3.3.3 acts to reinforce the results from Figure 3.3.2B. The percentage change between left and right cerebral hemispheres at the injection site is significantly greater for the treatment group than for either of the controls. There is also a significant difference in the absolute US-BBBD between the two groups with AV-MBs, demonstrating an increase in gadolinium delivery that correlates spatially with the upregulation of VCAM-1. The lack of significant difference in either percentage or absolute increase in US-BBBD between the two control groups indicates that the cytokine injection had no greater effect on the BBB than the PBS injection and therefore the increase in delivery in the treatment

group are attributable to the increase in VCAM-1 in the target hemisphere, not secondary physiological effects of the cytokine. These results will be discussed further in Section 3.4.

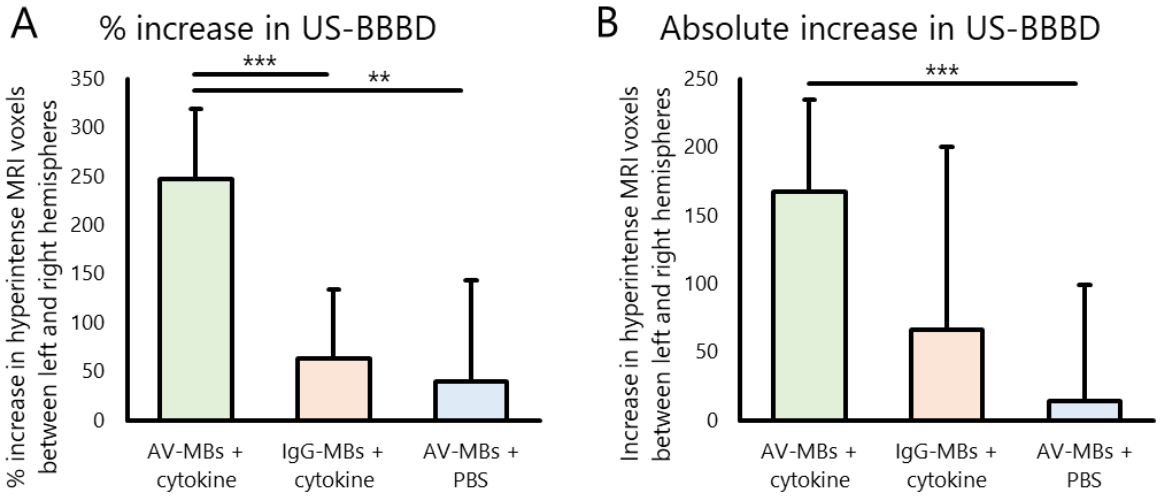

Figure 3.3.3: The average percentage and absolute increase in US-BBBD as measured by MRI between the left (target) and right (non-target) cerebral hemispheres for the mid brain (injection site). The significant differences shown in (A) indicate that the increase in US-BBBD in the treatment group in Figure 3.3.2B did not arise from effects of the cytokine apart from the upregulation of VCAM-1.

3.3.2. Histology results

This section details the results of the US-BBBD measurements obtained by staining histology slices for extravasated serum immunoglobulins (IgG) as detailed in Section 3.2.5. These slices cover the striatum and thus are analogous to the mid brain results in Figure 3.3.2B. This technique is complementary to the MRI measurements of US-BBBD in Section 3.3.1.

Figure 3.3.4 shows the number of pixels that have IgG positive staining (defined in Section 3.2.5). IgG positive staining indicates that the permeability of the BBB to immunoglobulins (IgG) and other endogenous proteins has increased.

In agreement with Figure 3.3.2A and B, the treatment group (cytokine + AV-MBs) was the only group that had significantly more US-BBBD in the left (target) hemisphere than the right (non-target) hemisphere. This reinforces the findings in Section 3.3.1 and helps to answer this Chapter's research questions.

In the first control (cytokine + IgG-MBs), both hemispheres had significantly greater US-BBBD than the non-injected hemisphere of the PBS group. This indicates non-specific binding of IgG-MBs in both hemispheres arising from cross-reactivity between the mouse endothelium and Rat-IgG-1. In contrast to the MRI results, the difference between left and right hemispheres in the first control is close to being significant ($p = 0.059$). Whilst this elevation is likely to have arisen from increased IgG binding to inflammatory markers around the cytokine injection site, the physiological effects of the cytokine on the BBB should not be immediately discounted. This will be discussed further in Section 3.4.

Similar to the results in Section 3.3.1, the US-BBBD measured in the second control (PBS + AV-MBs) shows that either residual AV-MBs were present in the systemic circulation at the time of ultrasound exposure or sufficient AV-MBs had bound to endogenous VCAM-1 to cause detectable US-BBBD.

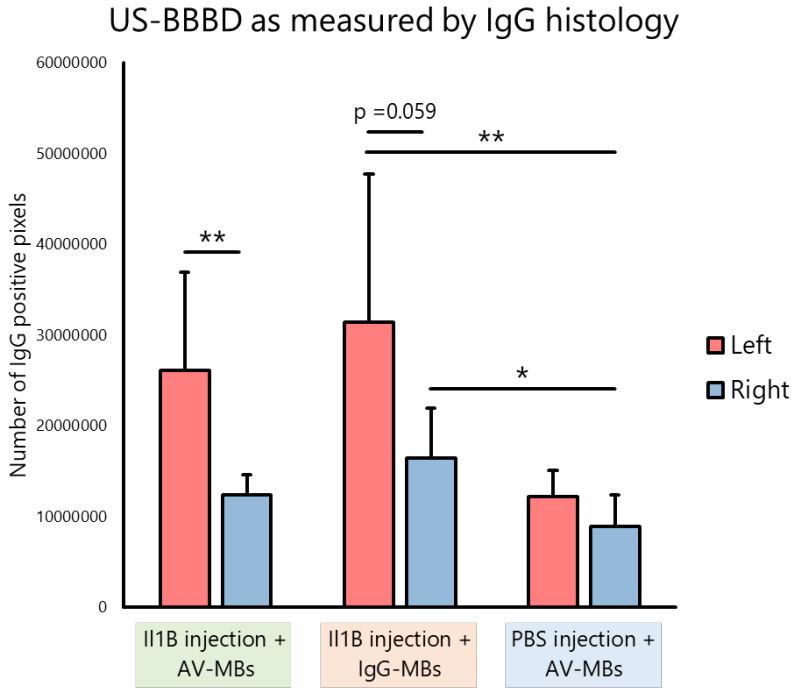

Figure 3.3.4: US-BBBD for each of the three experimental groups as measured by immunostaining for extravasated serum IgG. A significant increase ($p<0.05$, two tailed t-test) in US-BBBD between left (target) and right (non-target) hemispheres was observed in the treatment group. A significant difference was almost ($p=0.059$, two tailed t-test) also observed in the first control group (cytokine + IgG-MBs), but not in the PBS injection + AV-MBs group. The US-BBBD in both IgG-MB injected hemispheres was significantly elevated above that in the non-injected hemisphere of the PBS group.

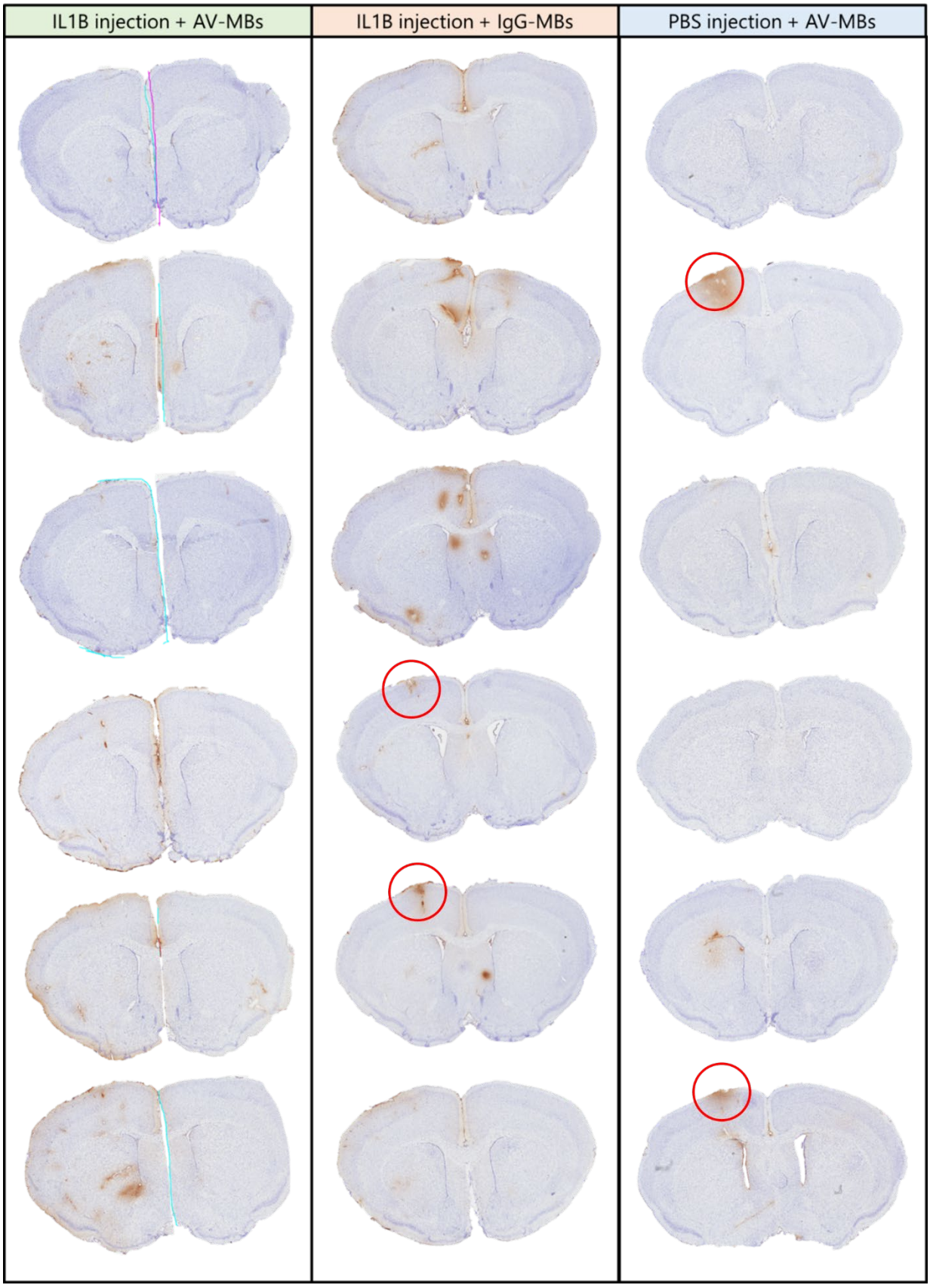
IL1B injection + AV-MBs
IL1B injection + IgG-MBs
PBS injection + AV-MBs

Figure 3.3.5: A representative immunostained histology slice for each animal in the three groups, showing extravasated serum IgG in the red-brown colour of the DAB-peroxidase stain used. The extravasation of serum IgG is used as a measure US-BBBD. Cresyl violet staining of all cells in the brain can also be seen. The distribution of US-BBBD clearly differs between experimental groups, and also between animals within one experimental group. A clear left-right difference is visible in both the treatment group. The IgG-MBs control seems to have caused localised US-BBBD around major blood vessels and brain structures, whereas the treatment group seems to have had a lower level but more widespread effect. Some suspected damage from the injection itself can be seen in both of the control groups (red circles).

Figure 3.3.5 shows a representative stained histology slice from each of the animals tested. This gives an overview of the inter-animal variation and differences between US-BBBD patterns between experimental groups. Comparing the first two columns illustrates how the cytokine + IgG-MBs group seemed to cause damage in isolated spots around key brain structures and major blood vessels, whereas the treatment group tended to cause lower level but wider spread BBB disruption. It is clear that at least some of the BBB disruption in the PBS injected group arose from the injection itself, something that is less visible in the first two groups. This damage from the injection is one of the inherent weaknesses of the intra-striatal injection model. These results will be discussed further in Section 3.4.

3.3.3. Acoustic emissions

Figure 3.3.6 shows the average power-time and total energy plots of the harmonic, ultraharmonic and broadband components of the acoustic emissions measured by the single element passive cavitation detector (PCD) during the experiments in this Chapter. Section 3.2.6 details how these signals are obtained.

It is clear from large shaded areas (each shaded area represents ± 1 standard deviation) that there is large inter-animal variability primarily due to the large effect that small variations in animal structure or positioning have on the reflected acoustic signal. Cavities elsewhere in the PCD focus (e.g. jawbone) can also have a large impact on the PCD signal. This is especially pertinent for the *in vivo* acoustic emissions in this Chapter, as the experimental protocol did not allow the baseline acoustic response of each animal to be established prior to microbubble injection (unlike in Chapter 5). This

makes extracting the signal (acoustic signal from microbubble cavitation) from the noise (acoustic signal from reflections from elsewhere in the mouse/set-up).The elevations in the PCD signals at the beginning of the time traces qualitatively correspond to the acoustic emissions arising from the mouse brains themselves and other inconsistencies in the experimental setup (as observed in Section 5.3.3).

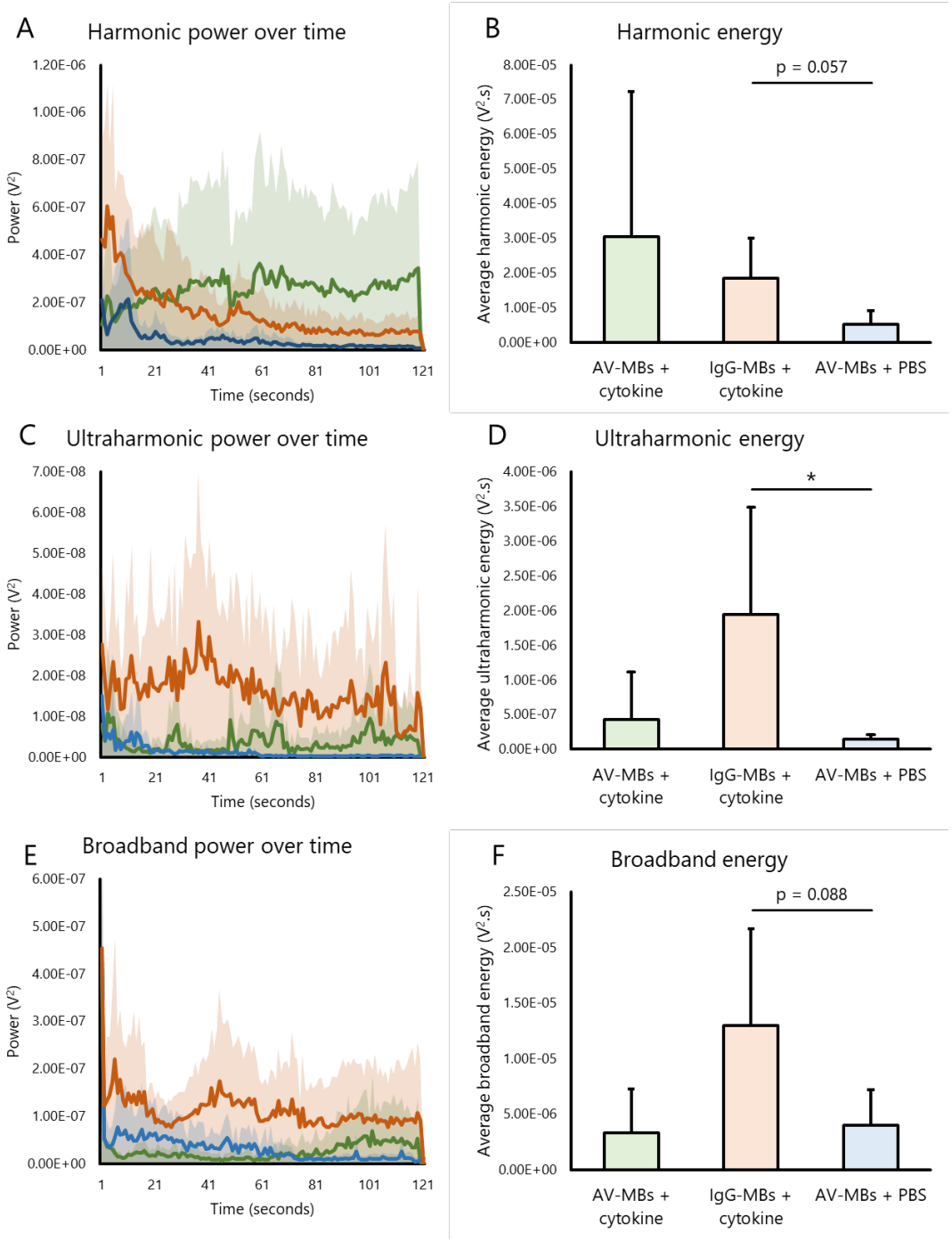

Figure 3.3.6: The average acoustic signals received by the passive cavitation detector (PCD) during ultrasound exposure for each experimental group. A, C and E show the harmonic, ultraharmonic and powers against time. Shaded area represents ± 1 standard deviation. B, D and F show the harmonic, ultraharmonic and broadband energies associated with each experimental group (calculated as the

integral of the power-time plot for each experimental group). Both groups injected with cytokine appear to exhibit sustained cavitation throughout ultrasound exposure, although, due to the large inter-animal variability, there is only one significant difference in total energies between experimental groups ($p<0.05$, two tailed t-test, in D).

However, the use of a notch filter to remove the fundamental, a PCD with a high centre frequency relative to the fundamental and filtering in the time domain allows a clear difference between the experimental groups to be seen. Whilst there is only one significant difference in acoustic energy between groups (Figure 3.3.6D), both of the cytokine injected groups exhibit sustained emissions, especially when compared to the rapid decrease in emissions observed for the PBS injected group.

These plots are consistent with the hypothesis that both the treatment group and the IgG-MBs + cytokine group exhibited cavitation activity whilst bound within the brain. In contrast, the acoustic response of the AV-MBs + PBS appears to diminish during ultrasound exposure, implying either a low concentration of AV-MBs bound to endogenous VCAM-1 within the brain or low concentrations of microbubbles in systemic circulation being cleared. These results will be discussed further in Section 3.4.

3.4. Discussion

3.4.1. Discussion overview

Chapters 2 and 3 of this thesis aim to investigate whether or not a combination of unfocused ultrasound and antibody targeted microbubbles could be used to address the first of the key challenges for the treatment of brain metastases that was identified in Section 1.5:

Challenge 1: targeting therapy selectively to the site of brain metastases

To do this, two research questions are addressed:

1. ***Are antibody-conjugated MBs capable of selectively binding to target regions in the brain?***
2. ***Once bound, are antibody-conjugated MBs then capable of causing US-BBBD selectively in the target region?***

In the treatment group in this Chapter, anti-VCAM-1 conjugated microbubbles (AV-MBs) were injected into mice that had undergone an intra-striatal injection of cytokine into the left cerebral hemisphere. This cytokine injection induces inflammation, and hence an upregulation of VCAM-1, in the injected hemisphere, particularly close to the injection site. Hence, the treatment group was designed to test the ability of AV-MBs to bind selectively to overexpression of VCAM-1 and, once bound, cause a measurable increase in US-BBBD at the injection site. Thus, the spatial distribution of US-BBBD was analysed to address both of this Chapter's research questions simultaneously.

In the first control group, designed to test for any physiological effects of the cytokine injection on BBB breakdown, the treatment group was replicated aside from the use of microbubbles conjugated to Rat-IgG-1 (IgG-MBs) instead of AV-MBs. In the second control group, designed to test for both non-specific binding and binding to endogenous VCAM-1 of AV-MBs, the cytokine injection was replaced with an analogous injection of PBS.

3.4.2. Discussion on the results of the treatment group

Both techniques used to measure US-BBBD (Sections 3.3.1 and 3.3.2) found that in the treatment group, AV-MBs caused a significant increase in US-BBBD in the target hemisphere when compared to the non-target hemisphere. The US-BBBD in the target hemisphere is also significantly greater than that measured in either of the hemispheres in the PBS + AV-MBs group. These differences are amplified when only the area around the injection site (the mid brain) is considered (Figure 3.3.2B).

The sustained acoustic emissions (implying sustained cavitation activity of microbubbles in the brain) in the treatment group (Figure 3.3.6), compared to the PBS control, correlates with the elevation in US-BBBD observed. Moreover, the average difference in US-BBBD between left and right hemispheres (roughly double) is very similar to the estimated increase in VCAM-1 expression between the two hemispheres (Section 3.1.4).

As the VCAM-1 elevation in metastatic tumours is expected to be 2 to 3 orders of magnitude higher (Section 2.2.9), it is reasonable to expect that the selective targeting of AV-MBs would be even higher in metastatic tumours than it was in these experiments.

The ultrasound focus was coaxially aligned with the centre of the mouse brain, and these aggregate left-right differences cannot therefore be attributed to differences in ultrasound pressures. However, it is important to establish whether or not the left-right differences in the treatment group could have been enhanced by other physiological effects that the cytokine injection may have had on the brain (beyond the upregulation of VCAM-1). For this, it is important to consider the results of the IgG-MBs control group (which also received a cytokine injection, Section 3.4.3) and analyse any effects of the cytokine (Sections 3.4.4 and 3.4.5).

Taking into account the pressure distribution of the transducer focus, the assumption that the ultrasound focus is co-axially aligned with the centre of the brain and the assumption that the ultrasound focus has not been distorted in anyway by the skull, the volume weighted mean pressure received by both the left and right halves of the brain is approximately 575 kPa PNP.

3.4.3. Discussion on the results of the IgG-MBs control group

There was no significant difference in US-BBBD between the hemispheres injected with IgG-MBs in either the MRI or histology measurements (Figure 3.3.2 and Figure 3.3.4). Figure 3.3.3 indicates that any differences that did arise were no greater than those arising from the injection itself in the PBS group. However, in the histology measurements, this difference in US-BBBD is almost significant ($0.1>p>0.05$, two tailed t-test). Therefore, it is important to analyse where this difference may have arisen from.

The first, and most probable cause, is related to cross-reactivity of the Rat-IgG-1 bound to the IgG-MBs. Two other potential causes related to the presence of cytokine are analysed in Sections 3.4.4 and 3.4.5.

As established in Section 3.1.6.2, IgG-1 is an immune antibody primarily responsible for the removal of toxins. Section 3.1.6.2 also established that there is a high cross-reactivity between rat and mouse. Combining these two facts leads to the conclusion that IgG-MBs bound non-specifically in the brain, and that this binding increased in the presence of the cytokine. This is corroborated by the fact that the US-BBBD in the right (non-injected) hemisphere of the IgG-MB control group is higher than that in the right hemisphere of the PBS control group (statistically significant when measured using histology ($p < 0.05$, Figure 3.3.4) and nearly significant in all MRI measurements ($0.1>p>0.05$, Figure 3.3.2). The most probable cause of this difference is non-specific binding of the Rat-IgG-1 to the brain.

3.4.4. Effect of cytokine on the BBB

It is possible that the inflammation arising from the cytokine injection weakens the BBB sufficiently to enhance US-BBBD and is therefore a possible contributing factor to the high US-BBBD in the injected hemisphere in both the treatment group and the IgG-MBs control. Indeed, many studies[454–458] have linked cerebral inflammation caused by other sources (e.g. traumatic brain injury) to a

weakened or permeable BBB. *In vitro* studies[459–462] have also shown an increase in the permeability of brain derived cellular monolayers in response to exposure to Il1-β.

Set against this, however, two studies[394,449] that used an intrastriatal injection of Il1-β (with an near-identical experimental method) demonstrated that the injection alone does not increase the permeability of the BBB to gadolinium complexes (the BBB permeability indicator used in the MRI section of this Chapter) or have an observable effect on the brain structure over the time scales used this Chapter.

A pertinent point is that primary brain tumours,[463–465] metastatic brain tumours,[466–468] and many other brain diseases[469–471] cause severe local neuro-inflammation similar to the inflammation induced by the cytokine injection used in this chapter. Indeed, at least one study[463] has found that the modulation of Il-1β (the cytokine used in this Chapter) is nearly 6 times higher in glioblastoma patients. Thus, if the cytokine injection did act to enhance US-BBBD in the cytokine injected hemispheres in this Chapter, it can reasonably be expected that this enhancement is somewhat representative of the physiological conditions at the disease site.

3.4.5. Effect of cytokine on cerebral blood flow

It is also possible that the inflammation arising from the cytokine injection increased blood flow to the injected hemisphere, something that has been shown to occur on experimentally relevant timescales using MRI perfusion imaging.[449] It is possible that a mismatch in blood flow between hemispheres may have increased the proportion of microbubbles flowing through the inflamed hemisphere when compared to the control hemisphere.

However, this increase in cerebral blood flow this would have decreased the transit times of these microbubbles through the brain. Therefore, to obtain an increase in acoustic emissions in the brain (Figure 3.3.6), these microbubbles would still have to be bound to the endothelium, thus this Chapter's research questions have still been addressed.

3.4.6. Differences in the spatial distribution of US-BBBD

Further evidence against the cytokine having a non-negligible impact on the BBB breakdown observed in this Chapter can be found by comparing the the spatial distributions of BBBD in the two cytokine injected groups. As discussed in Section 3.3.1, the spatial distributions have clear differences. This even more apparent in the histology slices in Figure 3.3.5 where it is visibly apparent that IgG-MBs tended to cause US-BBBD and visible damage in spots around key brain structures and in major blood vessels, whereas AV-MBs caused lower level, wide spread US-BBBD around the whole injection site. Differences in microbubble binding is the only probable explanation for these differences.

3.4.7. Summary of discussion

In summary, the data presented in this Chapter provides convincing evidence that AV-MBs, in combination with whole-brain ultrasound, were able to bind sufficiently to an increase in VCAM-1 expression to selectively enhance US-BBBD in the target region, thus addressing both of this Chapter's research questions. As the MRI detection of US-BBBD relied on the uptake of a small molecule compound (gadolinium) into the parenchyma, this is a good initial proxy for the selective transfer of a detectable quantity of a small molecule drug across the BBB.

From the above discussion, it is also apparent that the expected increase in VCAM-1 expression around early stage metastatic tumours (relative to the VCAM-1 expression arising from the cytokine injection used here) would be expected to further enhance the selective US-BBBD efficacy of AV-MBs in a clinical treatment for brain metastases.

Whilst it can be concluded, from the analysis conducted here, that the cytokine had a negligible effect on the observed enhancement in US-BBBD around the target region, the effect of the cytokine can never be entirely eliminated when using the experimental model in this Chapter. Thus, further testing of this technique in an *in vivo* model of metastatic tumours is warranted. This is discussed further in Chapter 6.

3.5. Conclusions

Chapter 3 follows on from the microbubble development and *in vitro* testing in Chapter 2 to test the ability of anti-VCAM-1 conjugated microbubbles (AV-MBs) to bind selectively to an area of the brain with increased VCAM-1 expression. Significant differences in ultrasound-mediated blood brain barrier breakdown (US-BBBD) between the target and non-target regions of the brain were observed in the treatment group indicating the potential of antibody-conjugated microbubbles, in combination with whole brain ultrasound, to bind to target regions and selectively enhance the transfer of small molecule compounds across the BBB.

Whilst further testing is required to establish whether this result translates to metastatic brain tumours, these findings represent the development of a novel drug delivery concept that promises to the ability to safely, reversibly and predictably open the blood brain barrier with a molecular level of disease-targeting specificity.

Part II. Enhancing Therapy

“The blood-brain barrier excludes ~100% of large-molecule neurotherapeutics and more than 98% of all small-molecule drugs from the brain”

- ***W.M. Pardridge, 2005***[472]

Chapter 4. Enhancing therapy *in vitro*

4. Enhancing therapy *in vitro*

Abstract

The permeabilisation of cell membranes following exposure to microbubbles and ultrasound (sonoporation) has considerable potential for therapeutic delivery. Recent studies have demonstrated that material transfers between phospholipid-coated microbubbles and cell membranes, especially during ultrasound exposure. This Chapter investigates the impact of this transfer on cell membrane properties and cell sonoporation

The molecular packing of cancer cell membranes was found to be significantly affected by the transfer of different phospholipids from microbubble shells to the cell membrane. This was then exploited to develop microbubbles containing lysolipids (Lyso-MBs) which promoted a ~5-fold increase in the cellular uptake of a model drug compared to control microbubbles.

Graphical abstract

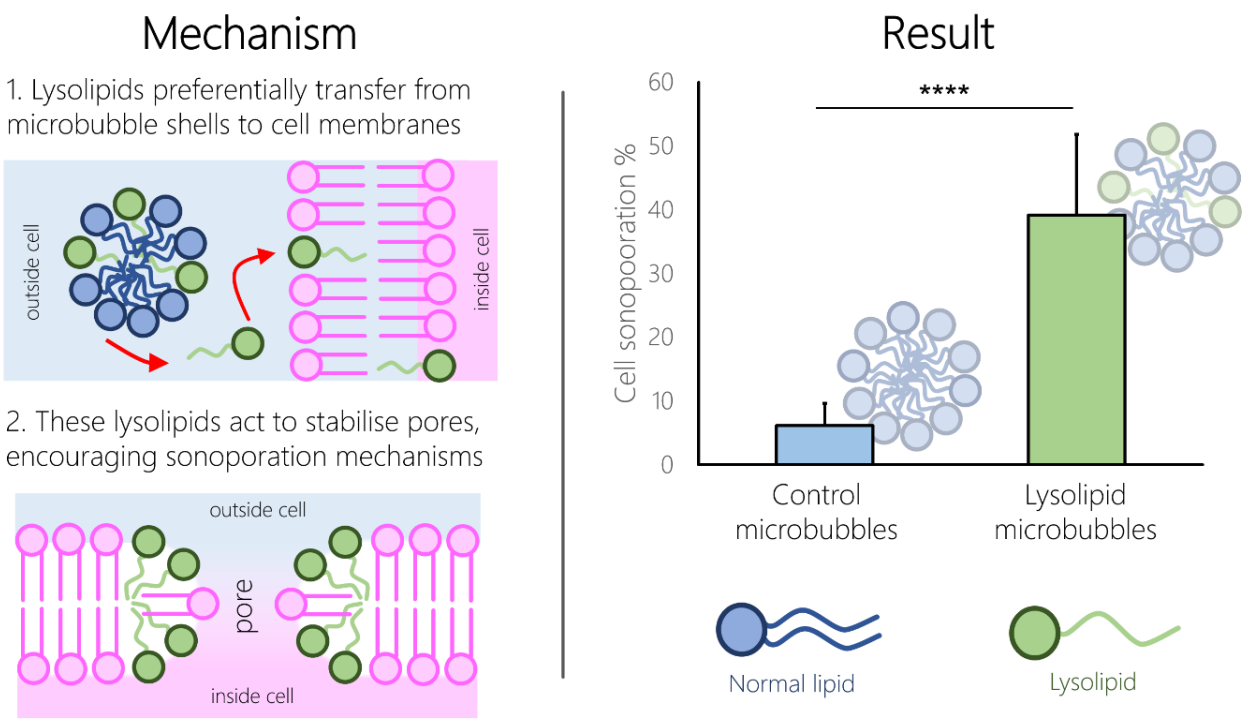

Attributions & Publication

The sonoporation and lipid order studies described in this Chapter were performed in collaboration with Dr. Miles Aron as, owing to the timescales involved, performing the experiments required two people. This research has been published in Langmuir under the title “Investigating the Role of Lipid Transfer in Microbubble-Mediated Drug Delivery”.[3]

The measurements of lysolipid transfer from microbubble shells to cell membranes (in Section 7.4) were performed in collaboration with Veerle Brans, another PhD student in BUBBL.

4.1. Introduction

Section 1.5 identified the two key challenges that currently limit the treatment of metastatic tumours in the brain; selectively targeting therapy to tumour sites and then delivering this therapy across the blood-brain-barrier (BBB). As outlined in Section 1.7, this thesis is split into four research Chapters, each aimed at addressing one of these challenges either *in vitro* or *in vivo*.

Whilst the uptake of gadolinium (a model drug) into brain tissue was demonstrated in Chapter 3, the ability of antibody targeted microbubbles to cause US-BBBD is likely to be limited by the number of microbubbles bound to each cell. There are also difficulties associated with the creation an ultrasound field of sufficient intensity to cause US-BBBD at locations deep within the brain. This is due to pre-focal skin and tissue heating, and pre-focal microbubble cavitation.

If microbubbles could be optimised to deliver therapy across cellular membranes and cellular barriers, in particular the BBB, this could either reduce the ultrasound pressures required for US-BBBD or increase the volume of tissue that experiences US-BBBD.

Part 2 (Chapters 4 and 5) of this thesis details the steps taken towards enhancing the ability of ultrasound and microbubbles to address the second challenge associated with the treatment of brain metastases:

Challenge 2: Enhancing therapeutic delivery across the blood brain barrier

To do this, two research questions are addressed:

1. ***How does lipid transfer from microbubbles affect cell membranes?***
2. ***Can microbubble-cell transfer be exploited to enhance therapeutic delivery?***

Firstly, the potential effect of different lipids on cellular membranes is discussed theoretically. The ability of microbubbles containing different combinations of these lipids to disorder cell membranes and to promote cell sonoporation is then measured *in vitro*, along with the propensity of similar lipids to transfer from microbubble shells to cell membranes. The ability of the most promising microbubble

formulation to increase US-BBBD *in vivo* relative to that caused by a control microbubble formulation is then measured in Chapter 5.

To the author's knowledge, this is the first time that microbubbles have been engineered in this way. It is conceivable that microbubbles which to act sensitize cells for therapeutic delivery could achieve ultrasound mediated drug delivery with lower ultrasound energies in the clinic, reducing the likelihood of ultrasound related off-target effects and/or damage. It also increases the likelihood of a low concentration of microbubbles causing a therapeutic effect. This is particularly useful if the microbubbles are antibody-targeted as in Chapters 2 and 3 of this thesis.

4.1.1. Phospholipids

The term 'lipids' refers to any substances of a biological origin that are soluble in nonpolar solvents, consisting of glycerides (fats and oils), phospholipids and steroids.[473] Lipids play an important role in the physiology and pathophysiology of living systems.[474,475] Unless specified otherwise, the term lipids in this Chapter is used to refer to phospholipids.

Amphiphilic phospholipids, formed of a polar (hydrophilic) phosphate "head", and two hydrophobic fatty acid "tails" are a major component in cell membranes. Certain phospholipids arise naturally, including derivatives such as egg-PC and soy-PC, although many are synthetically manufactured.

Phosphatidylcholines (PCs) are phospholipids that have a choline head group and, along with phosphatidylethanolamines (PEs), are among the most abundant lipids in biological membranes.[476] PCs and lyso-PCs (PCs that have been partially hydrolysed such that one fatty acid tail is removed) are the phospholipids analysed extensively in this Chapter.

For brevity, lipids in this Chapter are referred to by the length of their carbon chains and head group. For example, 1,2-dibehenoyl-sn-glycero-3-phosphocholine (DBPC) is referred to as 22PC in reference to the 22 carbon atoms in each fatty acid tail and the phosphocholine head group. One lysolipid is used predominantly in this Chapter and has a fatty acid tail with 16 carbon atoms in its

tail. Therefore, this lysolipid is referred to as lyso-PC unless otherwise specified. Figure 4.1.1 shows an overview of the different lipids used in this Chapter.

Abbreviation	Full name	Structure
10PC	1,2-didecanoyl-sn-glycero-3-phosphocholine (DDPC)	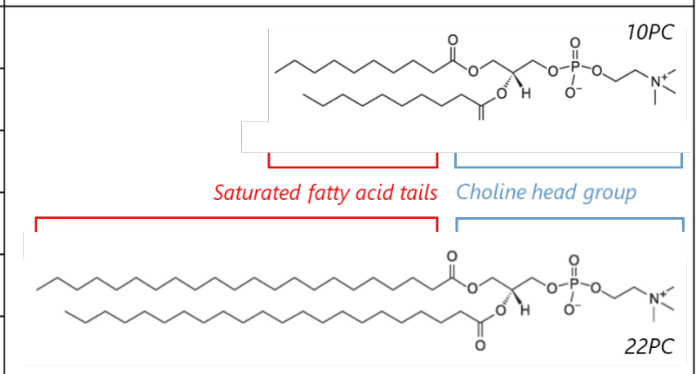
12PC	1,2-dilauroyl-sn-glycero-3-phosphocholine (DLPC)	
14PC	1,2-dimyristoyl-sn-glycero-3-phosphocholine (DMPC)	
16PC	1,2-dipalmitoyl-sn-glycero-3-phosphocholine (DPPC)	
18PC	1,2-distearoyl-sn-glycero-3-phosphocholine (DSPC)	
22PC	1,2-dibehenoyl-sn-glycero-3-phosphocholine (DBPC)	
Lyso-PC	1-palmitoyl-2-hydroxy-sn-glycero-3-phosphocholine	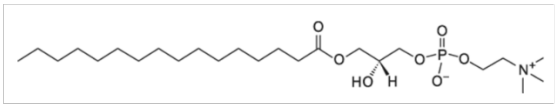

Figure 4.1.1: An overview of the lipids used in this Chapter

4.1.2. Phospholipids in microbubbles

As discussed in Section 1.6.2 and elsewhere in this thesis, microbubbles are acoustically responsive cavitation agents consisting of a gas-core, stabilised by a lipid, protein or polymer coating[244–246] As three of the four microbubble formulations approved for clinical use are lipid-shelled, this is perhaps the most relevant type of microbubble to optimise. The amphipathic properties of lipids provide excellent stabilization of the gas core hydrophobic liquids and can be loaded with therapeutic compounds including DNA, chemotherapeutics, antibodies, and liposomes to increase local drug concentration at a target site while reducing off-target side-effects. To increase the *in vivo* lifetime of microbubbles, steric stabilisers such as poly(ethylene)glycol (PEG) chains are often incorporated into their outer surface.[477]

4.1.3. Phospholipids in cell membranes

Mammalian cell membranes consist of a lipid bilayer composed primarily of phospholipids and cholesterol.[478] Other proteins that have important cellular functions, such as receptors, transporters, and enzymes are also embedded in the lipid bilayer. Cells actively modulate the composition of the

cytoplasmic (inner) and outer leaflets of their membranes with phosphatidylethanolamines (PEs) being predominantly confined to the cytoplasmic side of the lipid bilayer.[479] On the other hand, phosphatidylcholines (PCs) and sphingolipids are enriched in the outer layer of the lipid bilayer.[480–482] Considerable metabolic energy is expended in both synthesizing the wide variety of fatty acids that comprise the cell membrane and in ensuring that each membrane and each phospholipid class maintain a characteristic composition.[483] Unlike longer chain PCs, short to medium chain length (e.g. 10 to 14) PCs are found only in scarce quantity in biological membranes. These shorter chain PCs are known to transfer more readily to cell membranes than their longer chain length counterparts.[484]

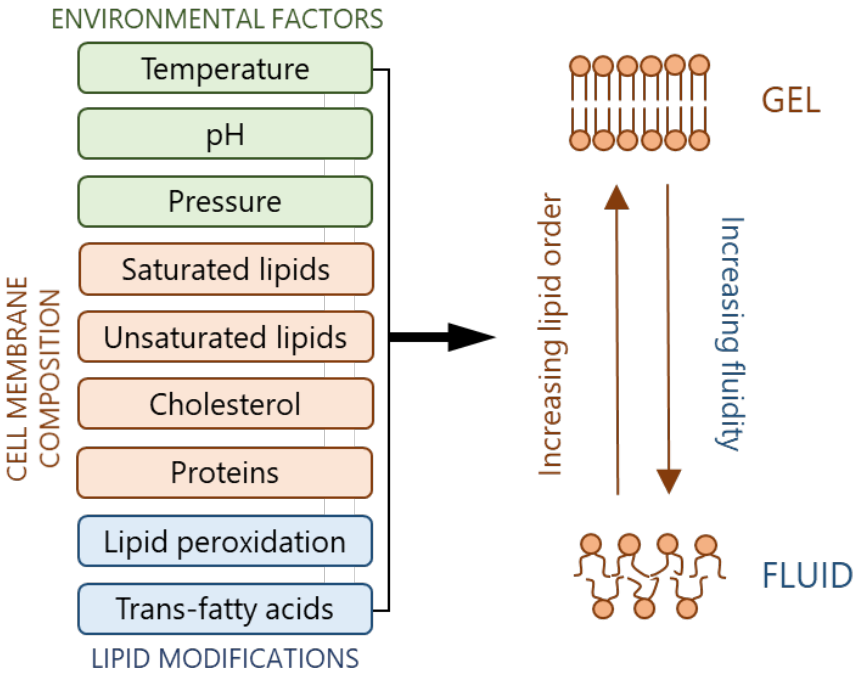

Figure 4.1.2: Summary of the some of the main factors that influence cell membrane fluidity and therefore the permeability of the lipid bilayer to small molecule compounds.

The cell membrane can be characterised in terms of its "lipid order", a term arising from the parameter used in NMR studies of hydrocarbon chains of the lipids in the bilayer.[485–487] The lipid order is inversely related to the membrane permeability to water, ions, and small molecules.[488–490]

Lipid exchange between cells and the surrounding environment is commonplace. Cells can take up large quantities of phospholipids from uni-lamellar vesicles without their viability being affected.[491] About 20-30% of this uptake remains within the cell membrane, with the rest transferring into the

nuclear membrane, mitochondria, and Golgi apparatus.[478] At 37˚C, the predominant lipid-transfer mechanism that occurs is fusion of the lipid vesicle with the cell membrane[492] whereas at lower temperatures, phospholipid exchange occurs between the outer leaflet of nearby lipid vesicles and cell membranes.[493] Phospholipids that incorporate into cell membranes in this way include PEs and PCs.[494–497]

The composition of lipids in a cell membrane, particularly the ratio of saturated to unsaturated lipids, has a large effect on the structural integrity and permeability of that cell membrane.[495,498–501] Whereas saturated lipids fit neatly together in the cell membrane, the 'kink' in the hydrocarbon chains of unsaturated lipids (arising from the carbon-carbon double bond) disorders the bilayer and increases the permeability of that bilayer.[488,489] The membrane permeability is also affected by a range of other factors,[502] summarised in Figure 4.1.2.

It follows that lipid transfer between the cell membrane and the cell's microenvironment could be exploited to modulate the lipid composition of target cells and thus modulate the permeability of the cell membrane to small molecules.

4.1.4. Phospholipid transfer between microbubbles and cell membranes

When phospholipid-shelled microbubbles cavitate, they shed lipids into the surrounding fluid.[503] This results in a deposition of microbubble lipids into surrounding lipid bilayers during ultrasound excitation.[504] One study[280] has shown that this lipid transfer influences the lipid order of cell membranes. Critically, this effect was found to be highly dependent on the MB formulation (i.e. lipid chain length, PEG emulsifier, and molar ratio of lipid to emulsifier). Direct visualisation of transfer of a fluorescently-tagged lipid between microbubble shells and cell membranes can be found in Section 7.4 of this thesis. Cavitation-assisted deposition of lipids in the rat kidney has been demonstrated *in vivo*, suggesting that lipid deposition plays a broader role in many *in vivo* drug delivery studies.[505]

It is important to recognise that, in addition to causing localised lipid deposition, microbubble cavitation also influences cell membranes and lipid behaviour in other ways. These include pore-formation in cell membranes[291,506] increased rates of endocytosis,[287,293,295] penetration of cell membranes[287,294] and cell membrane distension.[507,508] The mechanical and chemical effects associated with cavitation also modify lipid thermal behaviour.[509,510] Shear stresses with high temporal and spatial gradients associated with microbubble microstreaming and the reactive oxygen species generated by collapsing microbubbles also affect lipid order.[307,510–512] Other cavitation-mediated bio-effects that would be expected to influence lipid order include degradation of the actin cytoskeleton, opening of ion channels and rapid hyperpolarisation of the cell membrane.[280,295,311,513–517]

Whilst it is clear that there are many cavitation-mediated effects on cell membranes, it is not known whether the microbubble-mediated modulation of the lipid composition of these lipid bilayers can be can be exploited to enhance cellular drug delivery and ultrasound-mediated blood brain barrier breakdown (US-BBBD).

4.1.5. Effect of lipid shape on cell membrane stability

As mentioned in Section 4.1.3, the shape of phospholipids in cell membranes can impact the permeability of lipid bilayers to small molecules. Phospholipids can be grouped into three groups depending on their shape: cylindrical, conical and inverted conical, (Figure 4.1.3). As these lipids exert curvature stresses on cell membranes, it was hypothesised in Part 2 of this thesis that certain lipids, once transferred from the microbubble shell to the cell membrane, would act to destabilise those membranes, allowing enhanced transfer of small molecules into the cell. Moreover, any lipids which acted to stabilise pores formed in the cell membrane by microbubble cavitation would further enhance therapeutic uptake.

By balancing the energy required to perturb a lipid bilayer with the energy released by the reduction in bilayer surface area, the following equation can be derived[3] for the minimum energy required to form a single cylindrical pore in a continuous, uniform lipid membrane as:

$$\Delta E_c = \frac{\pi^3}{16} B \left(\frac{l}{a_{h,eq}}\right)^2$$

Where ΔE_c is the energy required, B is the head group repulsion strength, l is the length of the hydrocarbon chains and a_h is the average area of the bilayer that the head of a single lipid molecule occupies including a proportional share of any free space between adjacent lipid molecules. B primarily arises from electrostatic contributions, can be further defined under various assumptions as desired.[518] Interestingly, as the derivation of this equation is based on energies per unit length of pore circumference, the pore radius does not feature in the critical energy equation above. This is because the energies are associated with the creation of a 2D micelle-like region at the boundary of the pore and the bilayer.

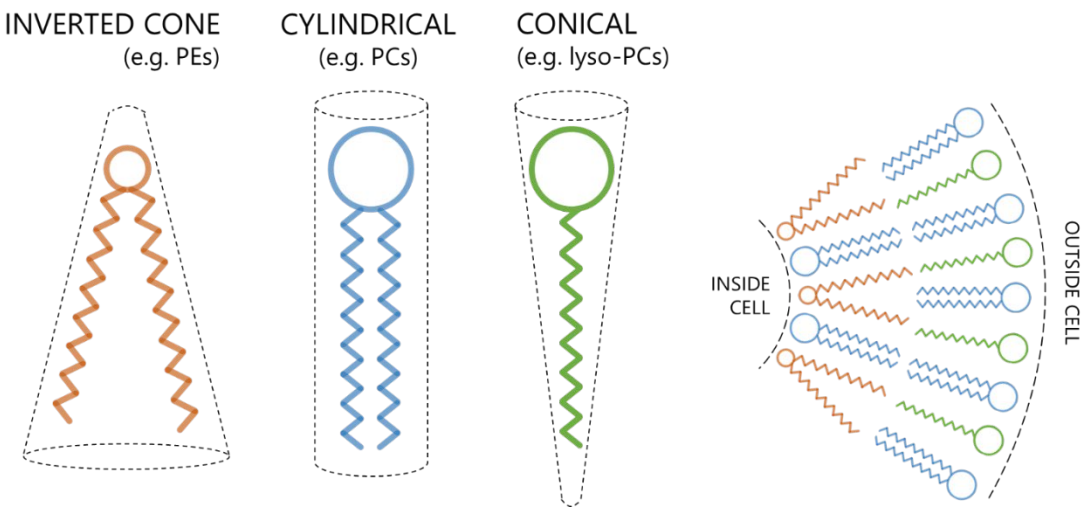

Figure 4.1.3: Phospholipids can be grouped into three categories depending on their shape. Some, for example phosphatidylethanolamines (PEs), have an inverted conical shape, some, for example phosphatidylcholines (PCs), have a cylindrical shape and some, for example lyso-phosphatidylcholines (lyso-PCs), have a conical shape. A simplified schematic of how these lipids might co-exist to create curved lipid bilayers is also shown. Intuitively, it follows that lipid bilayers containing a high concentration of lipids with a geometrical pre-disposition to exert curvature strains on the bilayer would require less energy to porate or permeabilise.

From this equation, it can be seen that the energy required for pore formation is directly related to the characteristics of the lipid molecules. Specifically, the $\frac{l}{a_h}$ term relates to the geometric shape of the lipid molecules surrounding the site of pore formation. Typically, for disordered lipid bilayers, there is greater space between lipid molecules (a_h increases), resulting in a decrease in the energy required for pore formation. The opposite is true for ordered lipids.

Aslipids transfer from microbubble shells to cell membranes, they are able to modulate the lipid composition of those cell membranes. If microbubble shells contain lipids that have a geometrical pre-disposition to destabilise lipid bilayers, once these lipids transfer to the cell membrane (from the microbubble shells), these cells may be less stable and thus more susceptible to cavitation-mediated delivery of small molecules.

As the lipid chain length is reduced, the solubility of PCs in aqueous solution increases, resulting in higher lipid transfer rates to membranes.[3] In addition to the altered transfer kinetics, shorter PCs introduce a chain-length mismatch in cell membranes, promoting increased hydration and decreased lipid order. The equation above suggests that transfer of shorter PCs into the cell membrane (lowering the average cell membrane lipid chain length (l) whilst maintaining the same head group area (a_h)) would reduce the energy required for pore formation. Therefore, as detailed in Section 4.4.6, PCs with a range of hydrocarbon chain lengths are tested in this Chapter.

Alternatively, it can be seen from the above equation that as a lipid becomes more conical, the $\frac{l}{a_h}$ term decreases. This is under the assumption that the volume of lipid molecules with the same lipid chain length remains constant (if both volume and l remain the same, a_h must increase), an assumption under which the energy equation above is derived. Even if this assumption is not entirely accurate and lipid volumes do not remain constant, it is likely that a_h does increase as conical lipids are well known to exert curvature stresses on lipid bilayers.

Crucially, the value of head group repulsion strength (B) is almost entirely related to the properties of the lipid head group. As the experiments in this Chapter work entirely with PCs, the B is considered to remain constant throughout.

Thus, as the $\frac{l}{a_h}$ term decreases, the energy required for pore formation is lowered. Consequently, conical lipids act to stabilize pores. It was therefore hypothesized that lipids more conical in shape such as lyso-PCs would be better suited to promoting pore formation and pore stability in cell membranes. This concept has been employed previously in the design of thermosensitive liposomes that use lyso-PCs to stabilize liposomal pores upon exposure to mild hyperthermia, enabling triggered release.[519] Lyso-PCs, PCs with one hydrocarbon chain removed by hydrolysis, are more soluble in aqueous solution than PCs of equivalent chain length giving them higher lipid transfer rates. The reduction of the hydrophobic region of lyso-PCs compared to PCs gives them negligible transverse diffusion or membrane "flip-flop" rates, meaning that they are confined to the extracellular membrane leaflet, imparting significant curvature stresses in the cell membrane. Lyso-PC is also known to have effects on cell membrane lipids in red blood cells.[520,521]

As detailed in Section 4.4.6, the ability of lyso-PCs (once they have been incorporated into microbubbles) to enhance cellular delivery is tested in this Chapter.

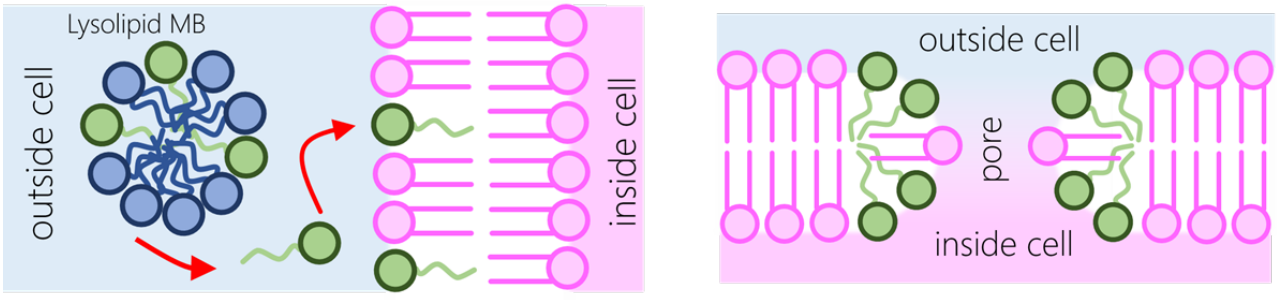

Figure 4.1.4: A schematic of the lipid transfer from microbubble shells to cell membranes and the pore stabilising effect of lysolipids that was hypothesised to enhance the delivery of model drugs in Chapters 4 and 5 of this thesis. Green lipids are lysolipids (lyso-PCs) and blue lipids are non-hydrolised lipids (PCs).

4.1.6. Experimental overview

Previous work[280] has shown that lipids transfer from microbubble shells to cell membranes, especially in the presence of ultrasound. This Chapter investigates the effect that this transfer has on cell membranes, and then investigates whether this mechanism can be exploited to enhance the cellular delivery of model drugs (sonoporation). This work provides the motivation for the *in vivo* experiments described in Chapter 5.

To do this, two sets of experiments were carried out. Firstly, the effect of various lipids on cell membrane lipid order was established to allow the identification of two candidate lipids that may, by altering the physiochemical environment of the cell membrane, enhance cell sonoporation (Section 4.5). These two candidate lipids, 12PC and 16-lyso-PC, were then either mixed with or incorporated into microbubbles to determine their effect on sonoporation relative to that achieved by Control-MBs alone. Both 12PC and 16-lysoPC significantly altered the cell membrane fluidity, although only 16-lyso-PC had a significant effect on sonoporation efficacy (Section 4.6). The results are discussed in Section 4.7.

4.1.7. A note on terminology

To keep this Chapter concise, the term *sonoporation* is used to describe all transfer of model drug from the exterior to the interior of cells. *Poration* is used for the same process in the absence of ultrasound. However, from the analyses performed in this Chapter, it is impossible to elucidate the exact mechanism via which model drug has entered the cell, as it is likely a combination of membrane permeabilisation, the formation of pores, endocytosis and other membrane transfer mechanisms.

In a similar way, US-BBBD is used as an umbrella term for all Gadolinium and serum IgG extravasation in the brain in Chapter 5. In the absence of ultrasound, this process is referred to as blood brain barrier disruption (BBBD).

4.2. Microbubble design

4.2.1. Lipid overview

In the cell lipid order experiments in Section 4.5, cells are exposed to various lipids in PBS. These lipids are phosphatidylcholines (PCs) with hydrocarbon chain lengths ranging from 10 to 22 carbon atoms (10PC to 22PC). A medium chain length conical lipid, with 16 carbon atoms in its hydrocarbon chain (16-lyso-PC) is also used. These lipids are shown schematically in Figure 4.2.1.

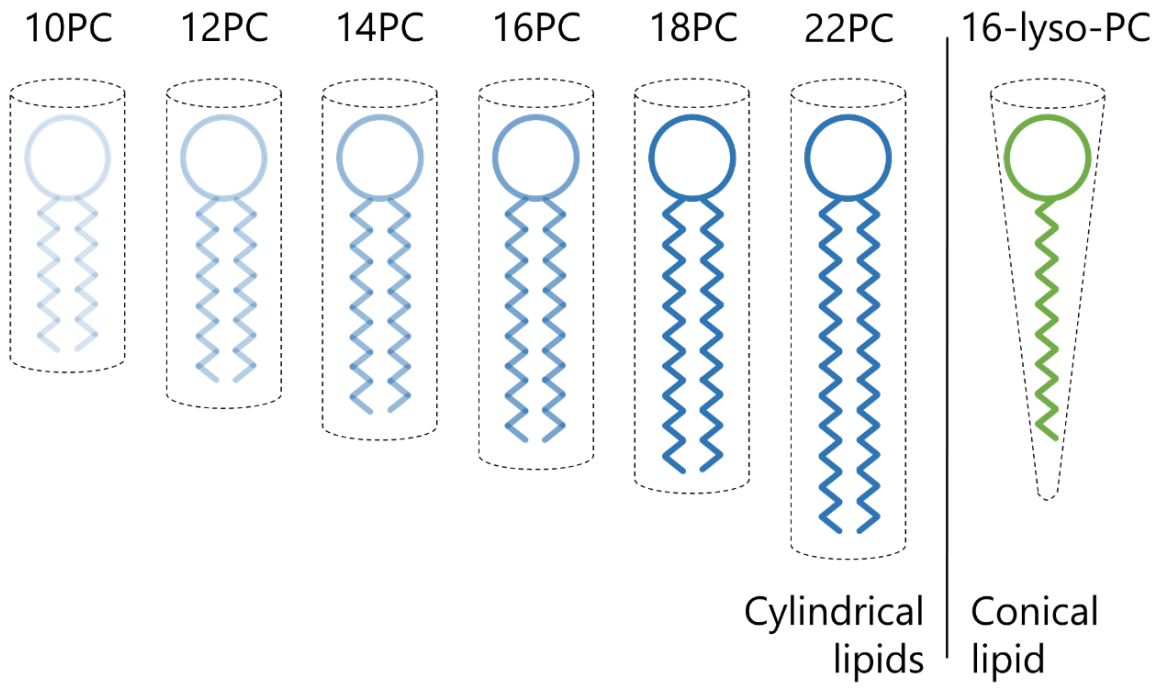

Figure 4.2.1: A schematic representation of the lipids used in this Chapter. The effect of these lipids on the fluidity of A-549 cell membranes is measured in Section 4.5. Two of these lipids (12PC and 16-lyso-PC) are assessed for their ability to potentiate sonoporation in Section 4.6.

These lipids were chosen to allow a systematic analysis of both lipid size and shape on cell membrane properties, particularly regarding those lipids that have a realistic potential of being incorporated into microbubbles in a clinical setting. Of the four commercially available microbubble agents worldwide, three are based on phospholipids combined with lipid emulsifiers (SonoVue(R) (Bracco, Italy), Definity(R) (Bristol Myers Squibb, US) and Sonazoid(R) (GE Healthcare, US)). It should be noted at

this point that the effects of other coating materials upon cellular membranes, and hence therapeutic delivery, are also worthy of investigation.

Table 3 shows a quantitative estimation for the critical energy required for pore formation in a uniform lipid bilayer of each of the lipids used in this Chapter. B, the head group repulsion strength, is assumed to be equal for all lipids as they are all PCs and so will have the same electrostatic repulsion.[522] The average area of the bilayer that the head group of a single lipid molecule occupies, a_h, and the lipid chain length, l, has been measured for 12PC, 14PC, 16PC and 18PC.[523] Linear extrapolation has been used to estimate the values of a_h and l for 10PC and 22PC. The lipid chain length of 16-lyso-PC is assumed to be equal to that of 16PC, whilst the a_h of 16-lyso-PC is estimated based on the conical shape assumption (rather than cylindrical shape assumption of 16PC) and the assumption that lipids with the same chain length occupy the same volume in the lipid bilayer.

These approximate calculations reveal that, for a uniform lipid bilayer, the energy requirements for pore formation in 16-lyso-PC are an order of magnitude lower than that of 18PC and 22PC, the two most common shell lipids for microbubbles. These energy requirements are also 6 times lower than the shortest cylindrical lipid tested in this Chapter, 10PC.

It is important to acknowledge that these are approximate calculations and that these pore energies will differ greatly in a real cell membrane where there is a wide range of lipid and protein molecules.

Lipid	**B ($J.nm^2$)**	**a_h (nm^2)**	**l (nm)**	**ΔE_c ($J \times 10^{-21}$)**
10PC	2.14×10^{-20} [522]	5.86	1.49	0.85
12PC	2.14×10^{-20} [522]	6.08 [523]	1.63 [523]	0.95
14PC	2.14×10^{-20} [522]	5.99 [523]	1.84 [523]	1.24
16PC	2.14×10^{-20} [522]	6.4 [523]	1.95 [523]	1.22
18PC	2.14×10^{-20} [522]	6.3 [523]	2.12 [523]	1.44
22PC	2.14×10^{-20} [522]	6.67	2.43	1.75
16-lyso-PC	2.14×10^{-20} [522]	19.2	1.95	0.14

Table 3: An estimation of the minimum energy required to form a single, cylindrical pore in a continuous, uniform lipid bilayer of each of the lipids used in this Chapter.

18PC is the principle lipid component of SonoVue and 16PC is the principle lipid component of Definity. As the effect on cellular membranes is expected to increase with decreasing hydrocarbon chain length (due to the reduction in similarity between the added PC and endogenous lipids), 10PC, 12PC and 14PC were also tested. 22PC, the longest lipid tested was chosen to study the effect of increasing lipid chain length above that commonly used in MB formulations. As 22PC had no measurable effect on the fluidity of the lipids on cell membranes, it represented an ideal lipid to use in the Control-MBs.

4.2.2. Microbubble overview

In this Chapter, five different microbubble formulations are considered. These are Control-MBs, consisting of 22PC and polyethylene glycol (40) stearate (PEG40S) in a 9:1 molar ratio, two formulations of microbubbles incorporating 16-lyso-PC (Lyso-MBs) and two incorporating 16PC (PC-MBs). These formulations, their constituents and their molar ratios are summarised in Figure 4.2.2. This information is also tabulated in Table 3.

Microbubble formulation	Constituents	Molar Ratio
Control-MBs	22PC, PEG40S	9:1
Lyso-MBs	22PC, PEG40S, 16lyso-PC	9:1:1
Lyso-MBs	22PC, PEG40S, 16lyso-PC	9:1:4
Lyso-MBs	22PC, PEG40S, 18:1 NBDlyso-PC	9:1:0.1
PC-MBs	22PC, PEG40S, 16PC	9:1:1
PC-MBs	22PC, PEG40S, 16PC	9:1:4

Table 4: The microbubble formulations, their constituents and their molar ratios.

PC-MBs were employed as a control for the inclusion of a second lipid in the MB shell. 22PC is used for the shell of Control-MBs due to it having the least effect on cell membrane fluidity (as seen in Section 4.5). Of all of the lipids analysed in this Chapter, 22PC is expected to have the lowest lipid transfer rate due to it having the longest hydrocarbon chain length.[484]

A microbubble formulation that incorporated a fluorescent lysolipid (NBD-lyso-MBs) is also shown in Figure 4.2.2. NBD-lyso-MBs were employed to visualise the transfer of a lysolipid from microbubble shells to cell membranes (Appendix, Section 7.4).

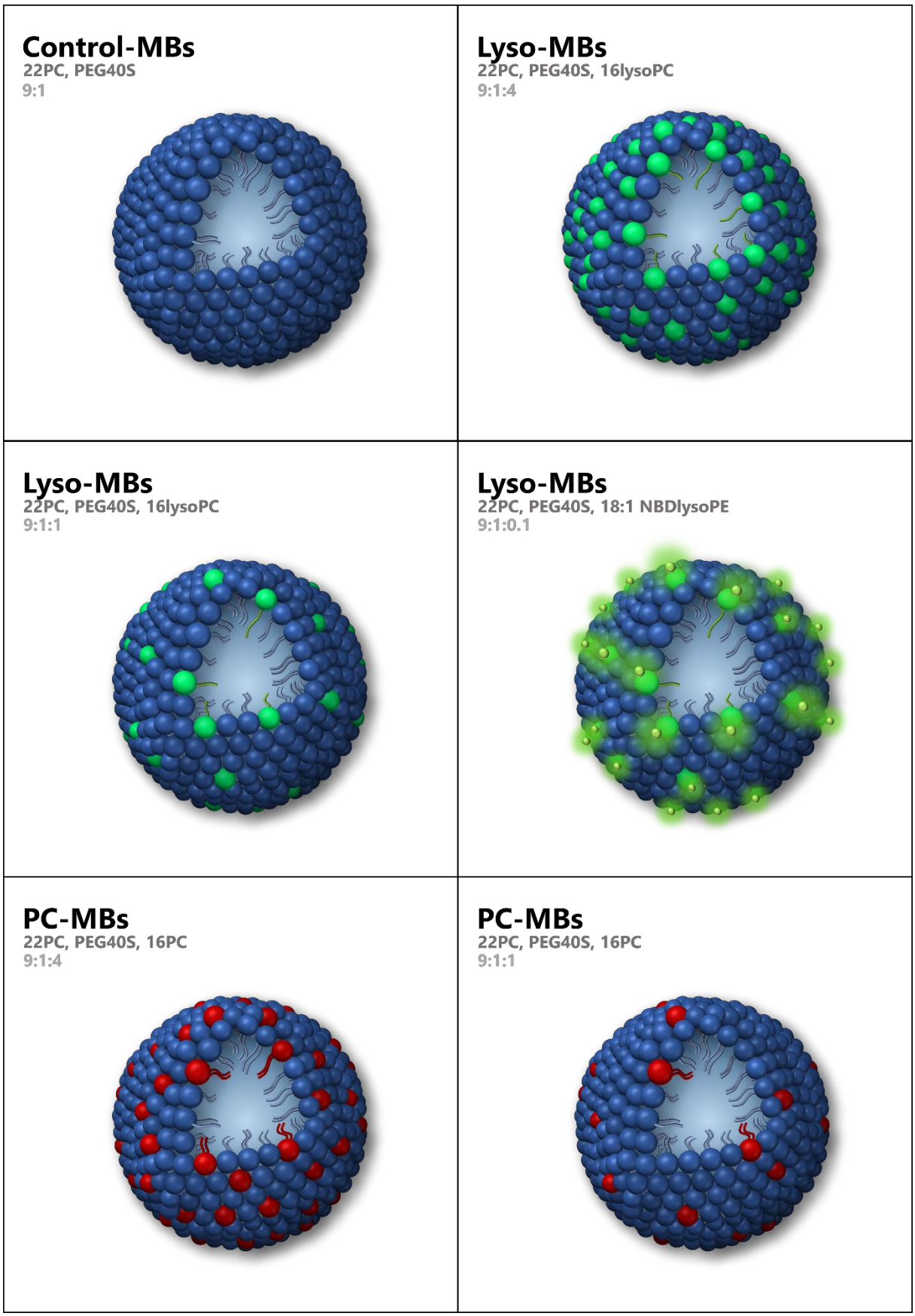

Figure 4.2.2: A schematic representation of the microbubbles used in this Chapter, their constituents and their molar ratios

4.3. Experimental Methods

4.3.1. Lipid preparation

The chloroform in which all of the lipids are supplied (Avanti Polar Lipids Inc., US), was first removed by leaving the lipids on a hotplate at 60˚C overnight to make a lipid film. Filtered phosphate buffered saline (PBS) solution (ThermoFisher Scientific, UK) was then added to the lipid film, which was then heated to 85˚C and magnetically stirred for 30 minutes. The solution was then fully dispersed using a low power sonication and it is assumed that, due to the hydrophobic tails and hydrophilic heads of the PCs, they self-assembled into liposomes.

4.3.2. MB preparation

The MBs in this Chapter were manufactured using a very similar protocol to that used to produce the biot-MBs in Chapter 2. Briefly, the relevant lipid (Avanti Polar Lipids Inc., US) and emulsifier (Sigma Aldrich, US) constituents in chloroform were added to a glass vial in the molar ratios detailed in Figure 4.2.2 such that the total weight of 22PC and PEG40S was 20mg. This mixture was then heated on a hotplate at 58ºC for 12h, to allow the chloroform to evaporate to form a lipid film.

This lipid film was suspended in 5 mL PBS for 1h on a hotplate at 85ºC under constant magnetic stirring. Lipids were then dispersed for 90s using a sonicator (XL 2000, probe diameter 3 mm, 20 W, 22.5 kHz, US) with the tip completely immersed in the lipid-PBS solution (power setting 4). The glass vial was then placed in an 85˚C water bath for 60s to keep the solution above the melting point of the lipids. The solution was then sonicated for a further 30s at power setting 4 to ensure homogeneous dispersion.

MBs were then formed by placing the sonicator tip at the air-water interface under constant sulphur hexafluoride (SF_6, The BOC Group plc, UK) flow (flowrate estimated to be 7×10^{-4} litres/second) and sonicating for 30s (power setting 14). Immediately after production, the vial containing the MB suspension was capped and placed in ice for at least 20 minutes.

4.3.3. Measuring MB size and concentration

The size and concentration measurements of MBs were obtained using the same protocol as detailed in Section 2.2.7. Dilution for concentration matching was always performed immediately prior to experimentation to limit the effects of dilution on MB size distribution, concentration, and stability.

4.3.4. Cell culture

Immortalized human alveolar adenocarcinomic cells (A-549s), were grown in Dulbecco's Modified Eagle Medium (DMEM) with 10% fetal bovine serum (FBS) and 1% penicillin/streptomycin (P/S). Cells were grown in a temperature and CO_2 controlled incubator at 37°C and 5% CO_2. Cells were removed from T-75 culture flasks at ~80% confluence by ~2 min exposure to 0.25% trypsin/EDTA. Cells were then suspended in 10 ml culture medium (DMEM with 10% FBS) to deactivate the trypsin and centrifuged for 5 min at 200g to form a pellet. Cells were then re-suspended in 10 ml culture medium. Cell concentration and viability was measured using trypan blue and a Countess® Automated Cell Counter (Invitrogen).

Cells were plated at ~40% seeding density in 8-well Ibidi μ-Slides for cell GP experiments, in 6.5mm Corning Transwell plates for lipid transfer experiments, and 35 mm Ibidi μ-Dishes for sonoporation experiments and were used in experiments ~16 hours after plating. Sub-confluent cells were used to improve the reliability of image segmentation and to reduce uncertainty of the effect of cell-cell contacts on cell membrane properties at confluence. All cell culture materials were purchased from ThermoFisher Scientific, unless stated otherwise.

4.3.5. Measuring cell membrane lipid order

To measure the effect of the addition of different lipids on the lipid order of the lipids in A-549 cell membranes, the generalised polarisation (GP) of the cells' lipids were quantified using C-Laurdan.[524] C-Laurdan is an environmentally-sensitive probe that has different fluorescent emissions depending on the lipid order of any surrounding lipids. This reveals how densely packed those lipids are.[525]

C-Laurdan fluorescence emission spectra were measured for each pixel at 63X magnification by spectral imaging on a confocal microscope equipped with a 32-channel GaAsP detector array (Zeiss LSM 780, Carl Zeiss AG, Germany), following a method previously reported.[526] C-Laurdan was excited at a wavelength of 405 nm and emissions with wavelengths between 415nm and 691nm were measured. GP was calculated as follows:

$$GP = \frac{I_{440} - I_{490}}{I_{440} + I_{490}}$$

In this equation, I_{440} and I_{490} correspond to the fluorescence intensity at 440 nm and 490 nm emission wavelengths respectively. 440 nm corresponds to a blue emission in the wavelength spectrum and is associated with a less fluid cell membrane, resulting in GP = +1 when only this wavelength is emitted. This indicates higher lipid order and means that lipids are in the gel-phase. Conversely, 490 nm corresponds to a red emission and is associated with greater hydration and polarity, resulting in GP = −1. This indicates lower lipid order and the prevalence of a liquid-crystalline phase.

For experiments, A-549 cells were cultured in an 8 well μ-Slide (Ibidi, Germany) as detailed in Section 4.3.4. After washing once with PBS, the relevant PC (outlined in Section 4.2.1) was added to the cells. Between 90 seconds and 10 minutes later (depending on the experiment), the lipid solution was removed, cells were washed again with PBS, and labelled with 400 nM C-Laurdan in PBS for 60 seconds before imaging.

Temperature control (37˚C) was achieved using the incubation chamber of the confocal microscope and verified using a thermocouple. PBS was also preheated in a water bath. Samples were measured with a thermocouple after imaging was completed to confirm temperature control to within ±1°C. A custom image processing routine[527] for batch processing spectral images was then used to obtain a GP value for both the cells and cell membranes.

4.3.6. Measuring cell viability in lipid order experiments

To assess cell viability after GP measurements (for 10PC, Section 7.1 and 16-lyso PC, Section 4.5.3), cells were washed with PBS, and then labelled with 15 μM propidium iodide (PI) to identify cells with compromised cell membranes. Calcein-AM at 5 μM was also used to identify living cells. Cell permeabilisation and viability were then assessed qualitatively by confocal microscopy. Whilst not a direct measure of cell viability, cells with only PI staining were never observed to recover over the timescales tested.

4.3.7. Cell sonoporation

Cells for sonoporation experiments were cultured in 35mm Ibidi μ-Dishes as detailed in Section 4.3.4. For the sonoporation experiments with 12PC, 1ml of 5mM 12PC was added to the μ-Dish for either 5 or 10 minutes prior to ultrasound exposure. Analogous incubations prior to ultrasound exposure were also used in experimental groups designed to investigate the impact of lipids on cell membrane integrity (when not part of the microbubble formulation). Immediately prior to ultrasound exposure, the μ-Dish was fitted with a 'Sonolid', a thin PDMS lid designed for ultrasound exposure.[528] A 10 ml solution of microbubbles (5.5 x 10^7 microbubbles/ml final concentration) and propidium iodide (40 μL at 10 mg/ml) prepared at 37°C was then added to the cells via needle injection through the Sonolid inlet, ensuring that there were no entrapped air bubbles. The MBs were either Control-MBs, Lyso-MBs or PC-MBs depending on the particular experiment and were warmed to this temperature just prior to experimentation due to their reduced stability at 37°C. The 'Sonolid' inlet and outlet were then plugged and the μ-Dish was inverted to increase microbubble-cell proximity.

Ultrasound exposure for the sonoporation experiments was conducted in a water tank system (~1 L) consisting of a 1MHz ultrasound transducer (Imasonic 8233 A101, 40 mm diameter, 120 mm radius of curvature), a purpose-built sample holder, acoustic absorber, and passive cavitation detector (PCD, 7.5 MHz centre frequency, V320 Panametrics, Olympus). The acoustic absorber was placed opposite the transducer to attenuate reflections. The sample holder was designed to hold cell culture dishes (μ-

Dishes, Ibidi) with plastic substrates much thinner (~100 μm) than the acoustic wavelength in water enclosed with a custom polydimethylsiloxane (PDMS) lid (~1.2 mm thick). The ultrasound transducer was driven by a 1 MHz sinusoidal signal from a function generator amplified 55 dB by a radiofrequency amplifier (E&I 1040L, Rochester, NY). Figure 4.3.1 shows both a schematic diagram and a photograph of this ultrasound setup, along with a plot of the normalised spatial distribution of the ultrasound pressure amplitude (Figure 4.3.1B).

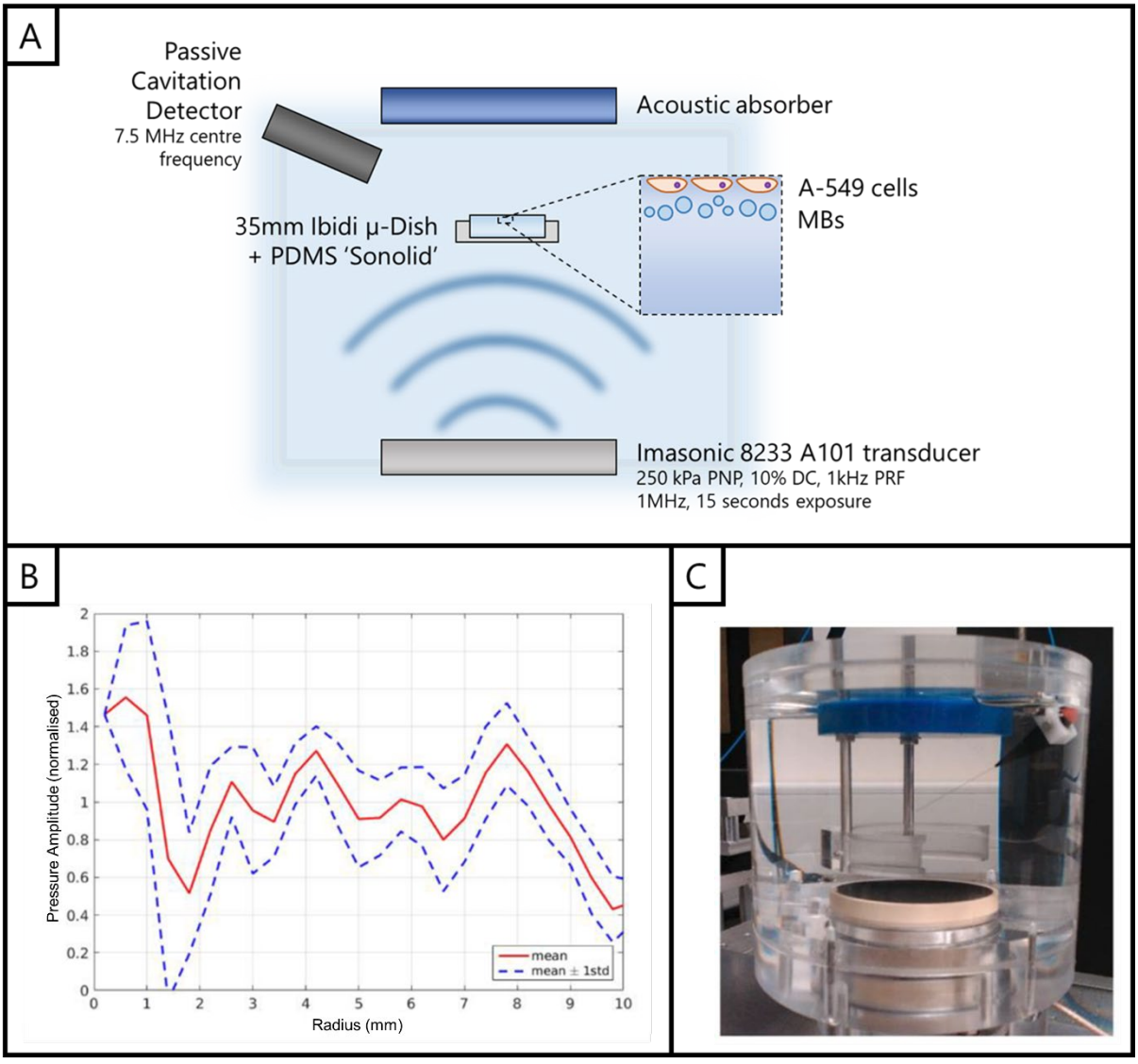

Figure 4.3.1: The ultrasound system used for cell sonoporation experiments. (A) A schematic diagram of the setup. Cells were placed in the pre-focal region of a 1MHz transducer such that the MBs could float into contact with the cells. An acoustic absorber reduces reflections and the PCD allows acoustic emissions monitoring. (B) The circumferentially averaged radial pattern of the ultrasound

pressure field in the ultrasound setup measured ~32 mm above the transducer. (C) Photograph of the ultrasound setup.

The μ-Dish was placed into the ultrasound system such that it was in the pre-focal region of the ultrasound source in order to expose a broad (~19mm diameter) area of the culture dish to a spatially average peak negative pressure of 0.25 MPa (hydrophone measurement uncertainty +/- 10%). The water in the setup filled with filtered, distilled, deionised, and degassed water at 37°C and exposed to 15 seconds of ultrasound at 1 MHz, 0.25 MPa PNP with a 10% duty cycle and 1 kHz PRF, during which acoustic emissions were monitored using the PCD (Section 4.3.8). These ultrasound settings were found to reliably produce both sonoporation in around 10% of the cells and negligible cell death by the time the cells were imaged in each control sample.

Upon removal from the water tank, the Sonolid was removed from the μ-Dish, the cells were washed twice with PBS and incubated at 37°C with Calcein-AM (5 μM) for five minutes prior to imaging. Further details on how cell sonoporation was evaluated can be found in Section 4.3.9.

All sonoporation was conducted at 37°C. This was achieved by preheating degassed water in a water bath and then pouring it into the ultrasound system immediately prior to each sonication. A thermocouple was used to verify the temperature of a no-cell sample under equivalent preparation each day of experiments to confirm temperature control to within ±1°C.

4.3.8. Acoustic emissions monitoring during *in vitro* ultrasound exposure

Acoustic emissions monitoring during both sonoporation and lipid transfer experiments using a PCD allowed for characterization of inter-sample variability and differences in cavitation dynamics between MB formulations. A digital oscilloscope (Handyscope HS3) and the PCD were triggered with a function generator. The PCD signal for sonoporation experiments was passed through a 2.0 MHz high-pass filter, amplified by a factor of 5 (Stanford Research Systems), and sent through a 50Ω coupler to maximise power transmission of the signal. For the lipid transfer experiments in Section 7.4, a 500 kHz notch filter was used. For each recorded voltage trace from the PCD, the voltage sample was then truncated in the time domain to include only the portion with cavitation noise and a

Hanning window was applied to the voltage trace to reduce edge effects. The fast Fourier transform (FFT) was computed for each voltage trace along with the power spectral density (PSD). The harmonic and ultraharmonic powers were determined by integrating the power spectral density with respect to frequency over 30 kHz bands at each harmonic and ultraharmonic from 3 to 8 MHz. The broadband power was determined by integrating the power spectral density with respect to frequency over the remaining frequencies from 3 to 8 MHz. The total energy of acoustic emissions for each sample was calculated by integrating the powers (harmonic, ultraharmonic and broadband) with respect to time.

4.3.9. Assessment of cell membrane sonoporation

Upon removal from the ultrasound system, the cells were washed with PBS and incubated with Calcein-AM for five minutes before imaging as mentioned in Section 4.3.7. Propidium iodide (PI), and Calcein-AM staining were evaluated using dual wavelength fluorescence microscopy (Nikon Eclipse Ti, Melville NY, USA) with multipoint scanning to account for inhomogeneity of the ultrasound field and other area effects that may originate from cavitation events.

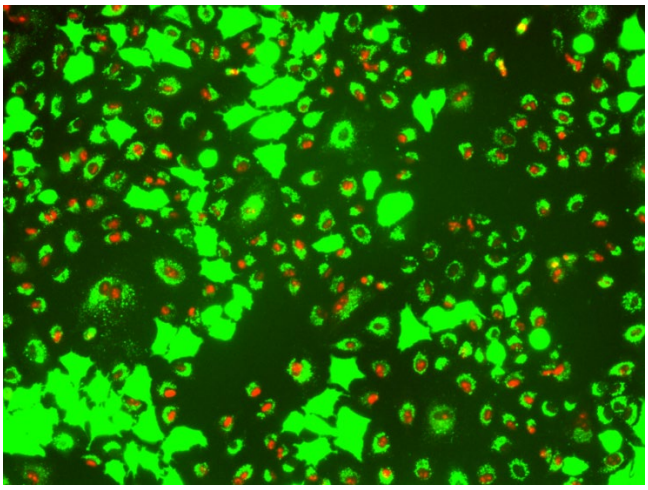

Figure 4.3.2: An enhanced dual fluorescence microscopy image showing cells stained with just Calcein-AM (green, alive and not sonoporated), just PI (red, dead) and both Calcein-AM and PI (sonoporated)

PI is normally cell impermeant and thus is widely used as a model drug as its uptake indicates membrane permeabilisation.[529] Calcein-AM is cell permeant and converts to green fluorescent

calcein upon uptake by viable cells thus providing a useful indicator of toxicity.[530] The microscopy images from both the green (Calcein-AM) and red (PI) channels were first merged using ImageJ software to create RGB Tiff image. The brightness and contrast were also adjusted to allow easier visual analysis of the cells. An example of an enhanced two-channel microscopy image showing a high percentage of sonoporated cells is shown in Figure 4.3.2. To count the number of sonoporated cells in each sample, a purpose written MATLAB® script used Otsu's method[531] and size filtering to extract red stained nuclei.

The percentage of sonoporated cells was is calculated by:

$$sonoporation\,\% = \frac{number\ of\ red\ (PI\ stained)\ nuclei}{total\ number\ of\ cells}$$

Where:

$$total\ number\ of\ cells = \frac{area\ of\ dish\ covered\ in\ cells}{average\ area\ of\ a\ cell}$$

4.4. Microbubble properties

Figure 4.4.1 shows the normalised average size distribution of Control-MBs and Lyso-MBs and representative images of both formulations. Control-MBs are formed of 22PC and PEG40S in a 9:1 molar ratio, Lyso-MBs are formed of 22PC, PEG40S and 16-lysoPC in a 9:1:4 molar ratio. Microbubbles were formed by the sonication method described in Section 4.3.1.

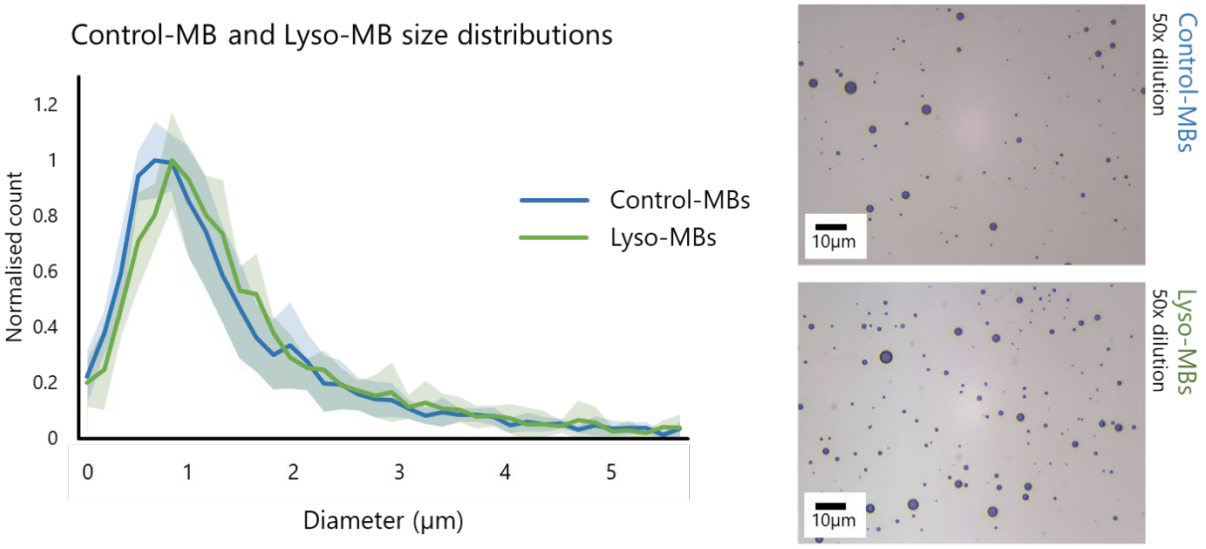

Figure 4.4.1: Normalised average size distributions and representative microscope images of Control-MBs and Lyso-MBs. Images captured at 40x and microbubbles diluted by a factor of 50 prior to imaging.

Control-MBs and Lyso-MBs are used in both the cell sonoporation experiments in this Chapter and *in vivo* US-BBBD experiments in Chapter 5. For sonoporation experiments, microbubbles were diluted to 5.5×10^7 MBs/ml. For the *in vivo* experiments in Chapter 5, 1×10^8 microbubbles were injected.

4.5. Cell membrane lipid order results

In this Section, generalised polarisation (GP, Section 4.3.5) is employed as a quantitative measure of whole cell and cell membrane lipid order. As cell lipid order increases, the fluidity of those membranes decreases and vice versa.

The aim of this Section is to quantify the effects that the addition of different PC lipids has on membrane lipid order, and to identify lipids that may enhance ultrasound mediated drug delivery via lipid exchange from the microbubble shell to the cell membrane.

4.5.1. Effect of different chain length lipids on cell membrane lipid order

This Section summarizes the effect that a 90 second exposure to PCs with different chain lengths (5 mM, ranging from 10PC to 22PC) had on both the cell membrane GP and the whole cell GP. GP was measured using the methodology detailed in Section 4.3.1.

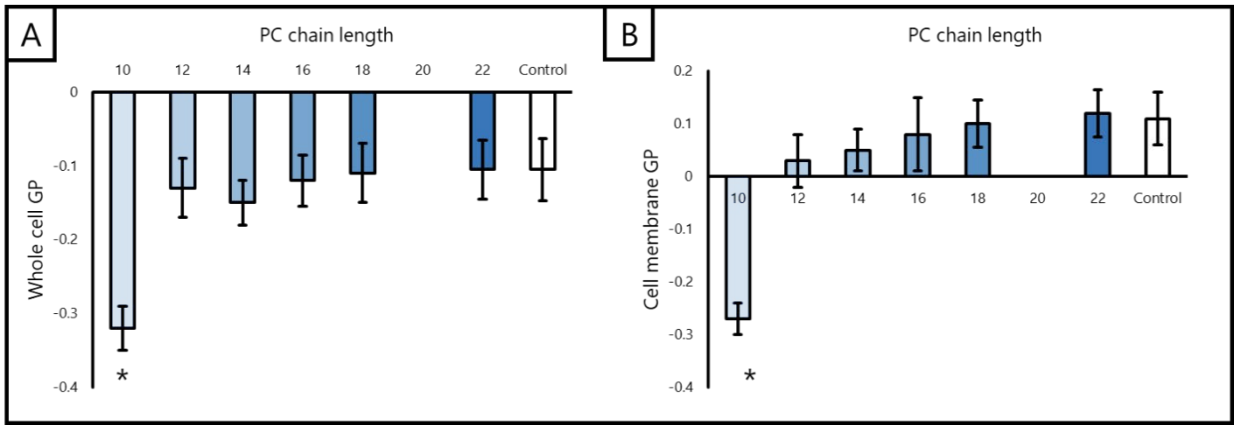

Figure 4.5.1: The effect of saturated phosphatidylcholine (PC) lipids of varying hydrocarbon chain length on A-549 cell lipid order. Cells were exposed to 5mM PC at 37°C for ~90 seconds prior to spectral imaging with C-Laurdan (n = 5 each) as detailed in Section 4.3.1. (A) GP of whole cells and (B) GP of segmented cell membranes.

Figure 4.5.1 shows the effect on both whole cell and cell membrane lipid order of the different PCs. Only 10PC was found to induce a significant effect ($p < 0.05$, two-tailed t-test), reducing the membrane GP by nearly the entire physiological range[524] ($\Delta GP = -0.38$). The effects of 10PC, 12PC and 14PC are evaluated in more detail in Sections 7.1, 4.5.2 and 7.2 respectively.

Figure 4.5.2 shows a representative spectral image of a C-Laurdan stained cell for each PC tested (90 seconds exposure at 5mM). Visual inspection reveals a clear difference between the control and 10PC cells, especially between the two cell membranes. In agreement with the results in Figure 4.5.1, this effect reduces as the lipid chain length increases.

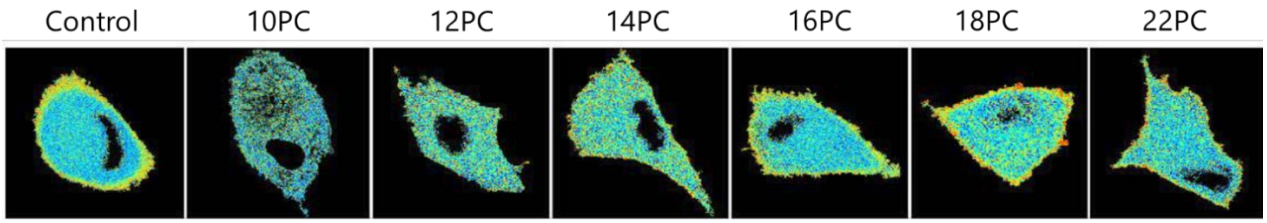

Figure 4.5.2: A representative spectral image of a C-Laurdan stained cell after 90 seconds exposure to each PC at 5mM. Cells exposed to the shorter chain length lipids (10-14PC) have a visually different membrane to control cells, in agreement with the GP measurements presented in Figure 4.5.1.

4.5.2. Further effects of 12PC on cell membrane fluidity

Unlike longer chain PCs, short to medium chain length (e.g. 10 to 14) PCs are found only in scarce quantity in biological membranes. These shorter chain PCs are known to transfer more readily to cell membranes than their longer chain length counterparts.[484]

Having found that 10PC rapidly increased the fluidity of A-549 cell membranes (Section 7.5), it was hypothesised that 12PC might be capable of altering cell lipid order with less severe consequences and ideally without inducing widespread cell death. This hypothesis was based on the increased similarity between 12PC (compared to 10PC) and endogenous lipids and the results in Figure 4.5.1. Thus, these lipids may also be suitable for modulating the fluidity of cell membranes in such a way that modulates the susceptibility of those cells to ultrasound and microbubble mediated therapeutic delivery, whilst remaining non-toxic in the absence of ultrasound.

Figure 4.5.3 shows the results of 12PC exposure for different lengths of time on whole cell GP. 12PC at 5 mM exhibited a time-dependent lipid disordering effect on A-549 cell membranes and intracellular lipids, having a significant effect ($p < 0.05$) on whole cell and cell membrane GP at 150 seconds and greater. This effect increased with exposure time until the longest time tested (10

minutes). Exposure to 5 mM 12PC for 10 min lowered cell membrane GP by -0.12 compared to control samples on average (Figure 4.5.3B).

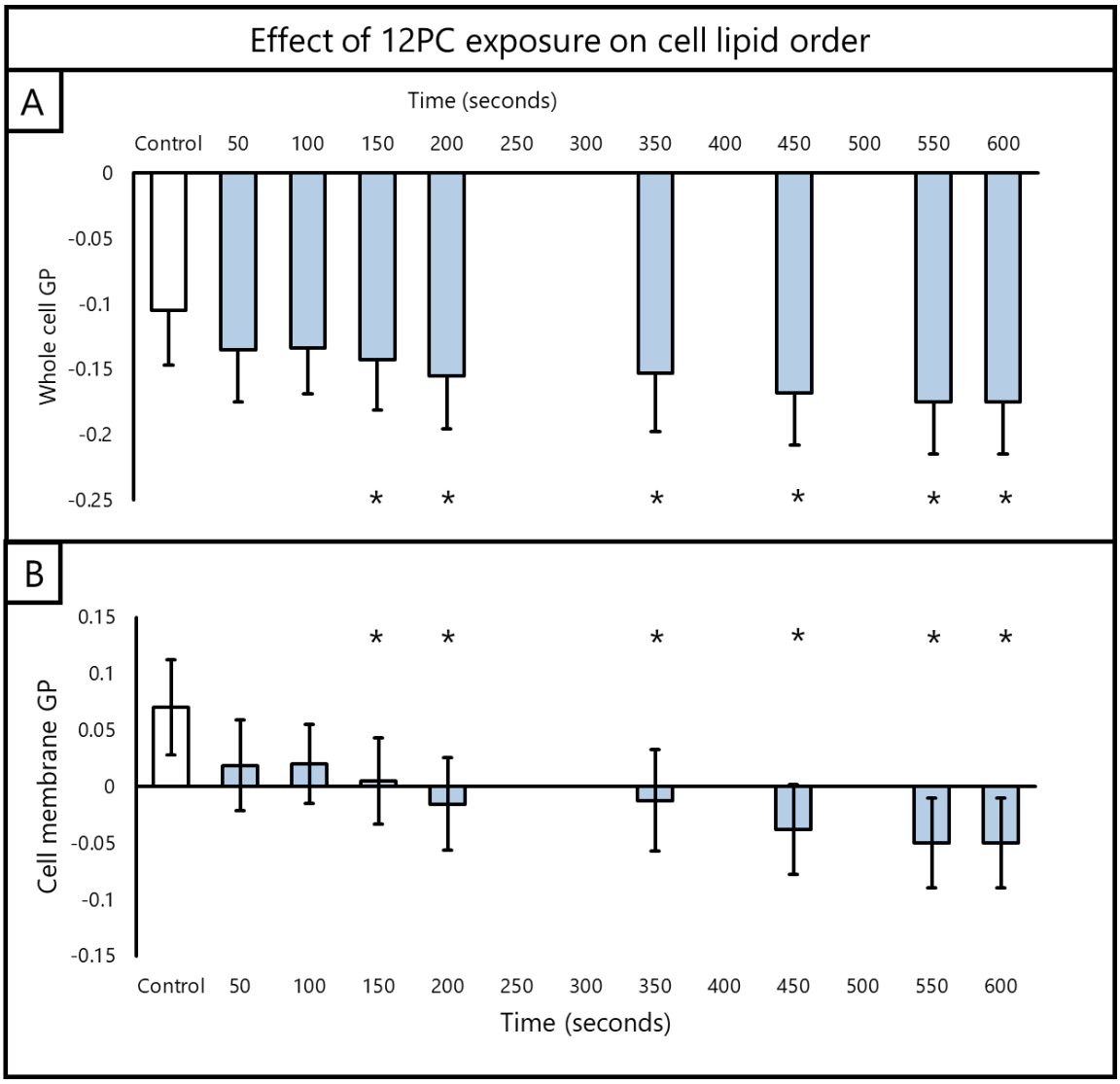

Figure 4.5.3: Effect of 12PC on A-549 lipid order. A-549 cells were exposed to 5 mM 12PC at 37°C for 10 minutes and measured concurrently using C Laurdan and spectral imaging. A significant ($p<0.05$) decrease in whole cell and cell membrane lipid order can be observed from 150 s exposure onwards.

4.5.3. Effect of lysolipid on cell membrane fluidity

The lysolipid tested in this Chapter, 16-lyso-PC, was found to cause a significant decrease in the GP of A-549 cell membranes. 16-lyso-PC at 80µM was found to have a significant disordering effect on cell membranes after a 90 second exposure (Figure 4.5.4A). Cells were also counter-stained with PI and Calcein-AM to assess cell membrane permeability (Figure 4.5.4B). Cells found to be

permeabilised (PI staining in the nucleus) exhibited, on average, more disordered cell membranes. The concentration of 16-lyso-PC required to permeabilise cells and significantly reduce GP in all cells was over an order of magnitude lower than that of 10PC.

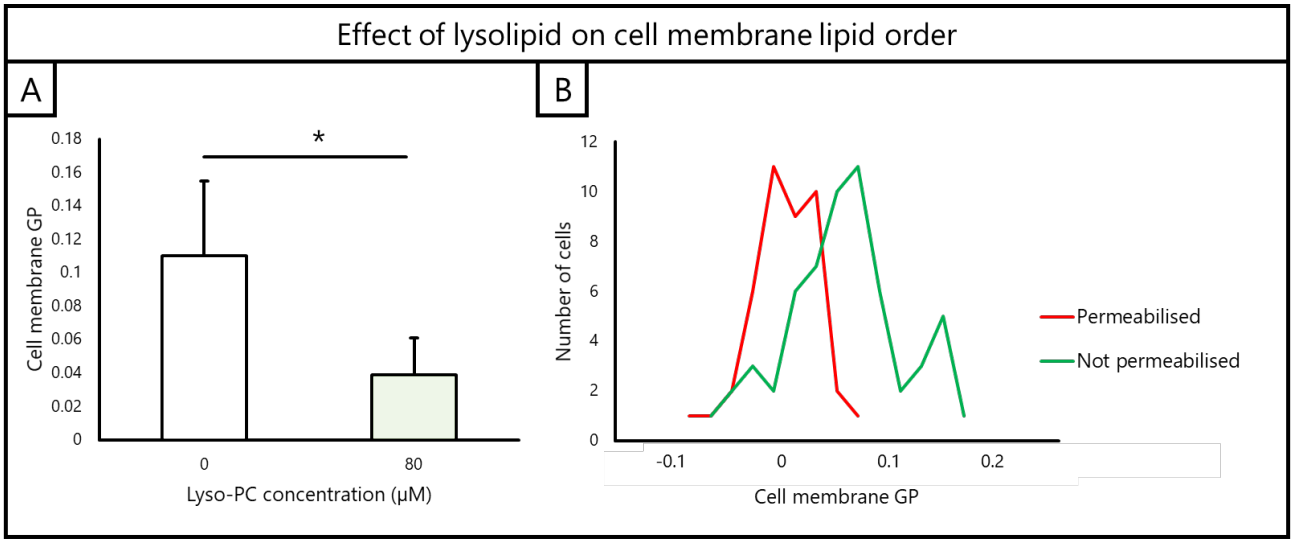

Figure 4.5.4: (A) Effect of 16-Lyso-PC at 80 μM and 37°C on A-549 cell lipid order. Cells were exposed for ~90 seconds. (B) Histograms for cell membrane GP from samples counter-stained with propidium iodide for marking permeabilisation after exposure to 16-lyso-PC and spectral imaging with C-Laurdan. Cells permeabilized by 16-lyso-PC exposure had lower GP on average ($GP_{permeabilized}$ = 0.002 ± 0.034 and $GP_{not\text{-}permeabilized}$ = 0.058 ± 0.055).

Therefore, along with 12PC, 16-lyso-PC was taken forward as a candidate lipid for incorporation into MBs with the aim of enhancing cell sonoporation via lipid-exchange mechanisms.

4.6. Cell sonoporation results

4.6.1. Cell sonoporation with 12PC

Of the different chain length phosphatidylcholine lipids (PCs) investigated in Section 4.5, results from the 12PC were the most promising for non-toxically modulating cell membrane fluidity to enhance sonoporation. 12PC significantly disordered both cell membrane lipids and intracellular lipids (Figure 4.5.3) without the rapid cytotoxic effects of 10PC. In this Section, cells were pre-treated with 12PC for either 5 or 10 minutes prior to exposure and microbubbles. Pre-treatment was used instead of co-injection with microbubbles to avoid the added complexity of 12PC potentially altering the acoustic behaviour of the microbubbles.

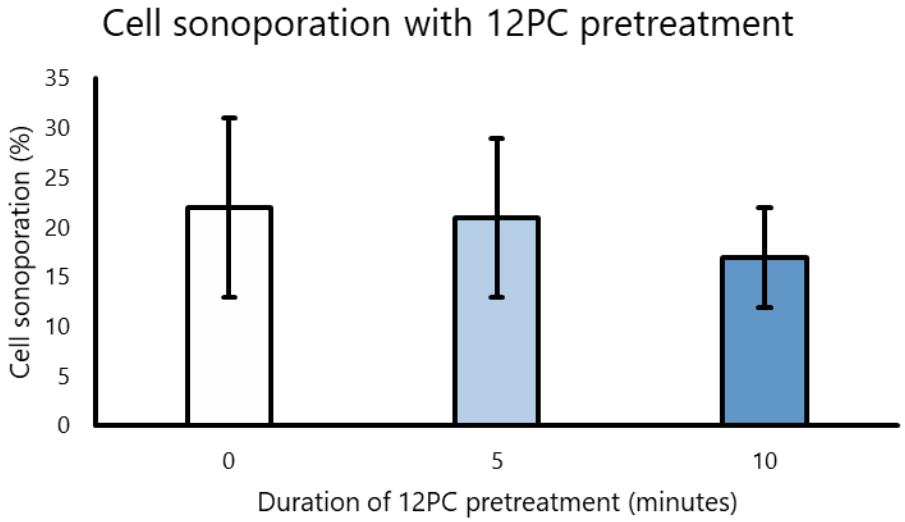

Figure 4.6.1: Effect of 12PC pre-treatment on sonoporation efficiency. Mean and standard deviation of cell sonoporation percentage as a function of 12PC pre-treatment time (n = 6 for each condition).

Despite the significant effect on cell lipid order (Figure 4.5.3), it was found that pre-treatment with 12PC had no significant effect on sonoporation (Figure 4.6.1, $p > 0.05$, $n = 6$ for each condition).

Microbubble sizes were not statistically different and microbubble concentrations were matched to 5.5×10^7 microbubbles/ml across all experiments. Cell morphologies across the conditions tested were qualitatively indistinguishable (Figure 4.6.2). No relationship between the slight variations in cell density the percentage of cells sonoporated was found. No statistically significant differences

were observed for average harmonic energies in the acoustic emissions between samples that did and did not receive 12PC (Figure 4.6.3).

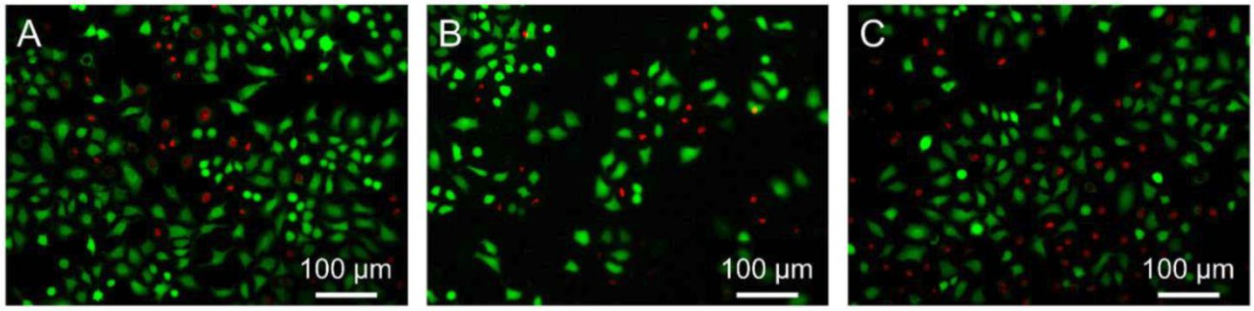

Figure 4.6.2: Representative microscopy images of cells following sonoporation with and without pretreatment with 5 mM 12PC. Cells were exposed to ultrasound and microbubbles in the presence of propidium iodide, a permeability tracer (red). Cells were then labelled with calcein-AM to mark non-permeabilised cells (green). Cells in (A) were not exposed to 12PC. Cells in (B) and (C) were pre-treated with 12PC for 5 minutes and 10 minutes respectively prior to sonoporation with ultrasound and microbubbles. No overall differences in cell morphology were visibly evident across the three conditions.

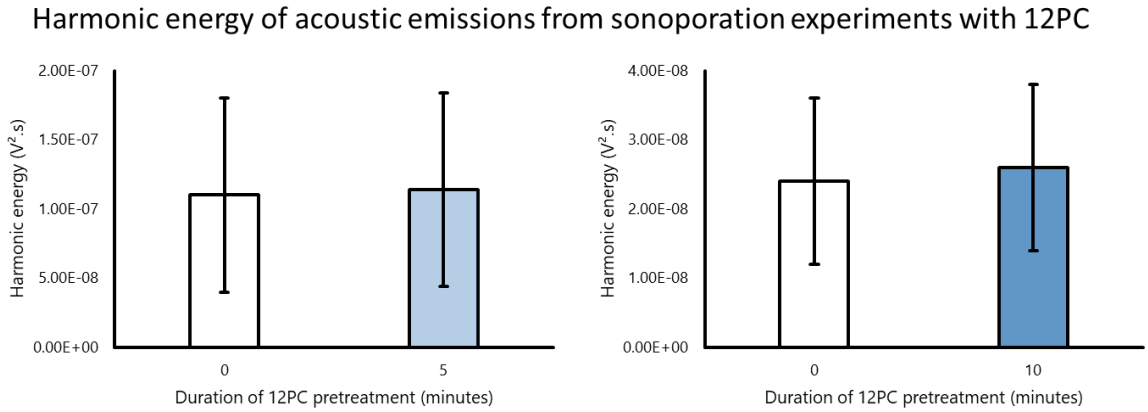

Figure 4.6.3: Average harmonic energy in the acoustic emissions from Control-MBs during cell sonoporation experiments at 37°C with and without pre-exposure of the cells to 12PC at 5 mM for 5 minutes (left) and 10 minutes (right). The data in these two plots were collected using different filters and so comparison of absolute energies between these plots is to be avoided.

4.6.2. Cell sonoporation with lysolipid

This Section tests the ability of 16-lyso-PC, to enhance cell sonoporation by incorporating it into MBs (Lyso-MBs, Section 4.2.2).

Lyso-MBs with a final 16-lyso-PC concentration of 80µM were found to significantly increase sonoporation efficiency ($p < 0.0001$), achieving cell permeabilisation of 38.1 ± 13.2% of cells (n =

7), compared to 7.2 ± 3.9 % of cells permeabilised following equivalent exposure to Control-MBs (22:0 PC-PEG40S MBs) and ultrasound (n = 7) (Figure 4.6.4).

Interestingly, neither 25 µM or 80 µM Lyso-MBs without ultrasound significantly increased the percentage of cells permeabilised when compared to Control-MBs without ultrasound (Figure 4.6.5). This, along with the effect of 80µM 16-lyso-PC (Figure 4.6.5), suggests that lyso-PC was successfully incorporated into the MB shell rather than exclusively forming 16-lyso-PC micelles.

Separately, it was found that adding 16PC lipids to MBs (to form PC-MBs as a control for inclusion of the second lipid in the MB formulation), did not have a significant impact on sonoporation compared to Control-MBs, (Figure 4.6.4). This provides evidence for attributing the enhancement of sonoporation to the presence a lysolipid in the Lyso-MB formulation and not just the presence of a second, shorter chain lipid.

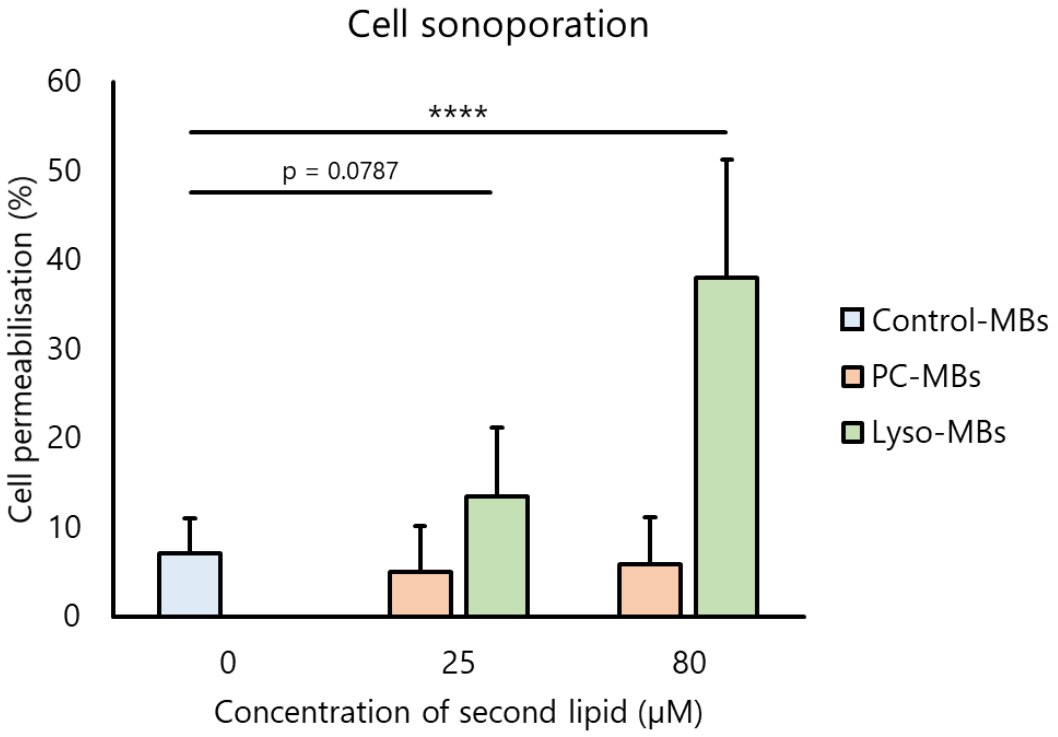

Figure 4.6.4: Effect of PC-MBs and Lyso-MBs (with two different concentrations of the second lipid) on sonoporation efficiency relative to the sonoporation caused by Control-MBs. Cell permeabilisation is measured using the method outlined in Section 4.3.9.

To further investigate the effect of the Lyso-MBs on cell membrane permeabilization, cells were exposed to either Lyso-MBs, destroyed Lyso-MBs, or Control-MBs spiked with Lyso-PC immediately prior to exposure for ~90 s at 37°C (Figure 4.6.5).

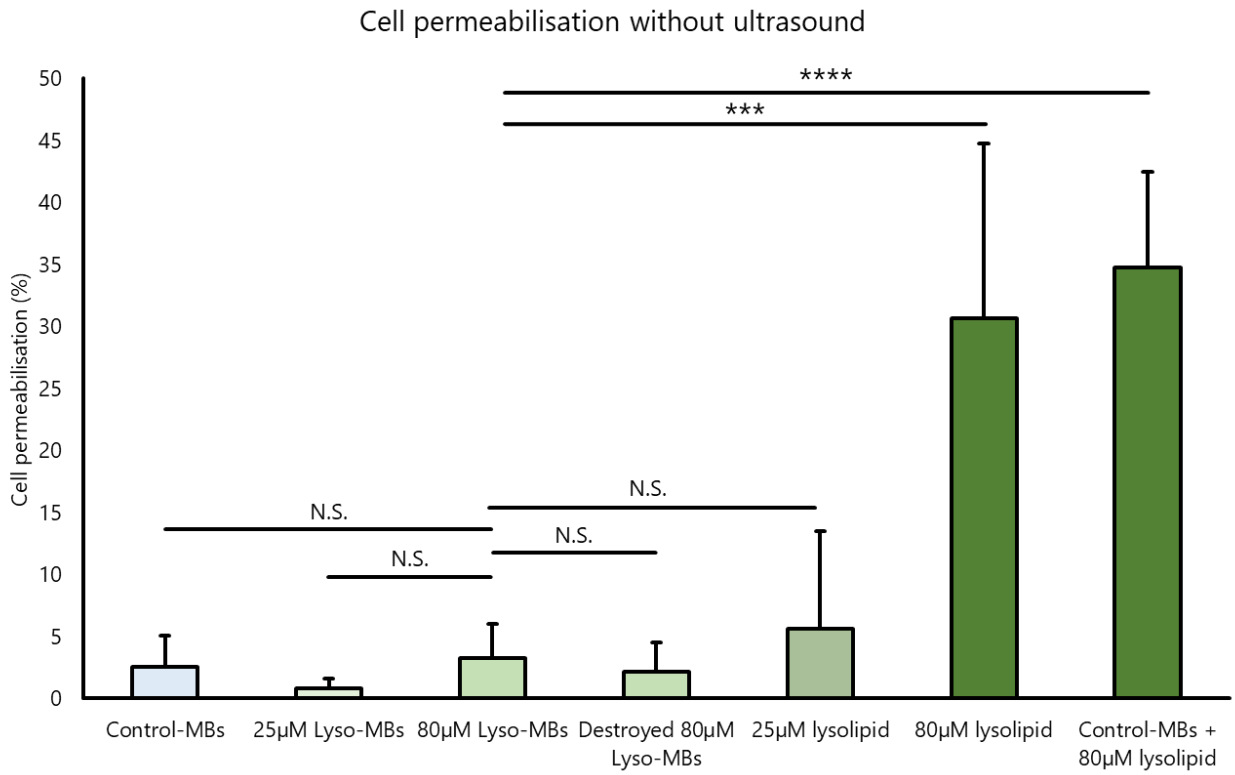

Figure 4.6.5: Cell membrane permeabilisation without ultrasound. In the absence of ultrasound, the permeabilisation caused by Control-MBs, free lysolipid at 25µm and Lyso-MBs destroyed by repeated heating to 85°C and sonication caused was not significantly different to the permeabilisation caused by the Lyso-MBs. Exposure to both free lysolipid at 80µm and Control-MBs spiked with lysolipid at 80µm significantly permeabilised cells ($p < 0.001$) relative to Lyso-MBs providing strong evidence for the successful incorporation of the majority of the 16-lyso-PC into the MB shell. 16-lyso-PC concentration was 5 µM, incubation time was ~90 s, and cells were kept at 37°C for all conditions.

There was no difference in cell permeabilisation between cells exposed to Lyso-MBs and destroyed Lyso-MB. This provides further evidence that Lyso-PC was successfully incorporated into Lyso-MB shells rather than forming Lyso-PC micelles exclusively. In addition, the Lyso-MBs do not appear to be any more toxic to cells than Control-MBs for the exposure conditions tested.

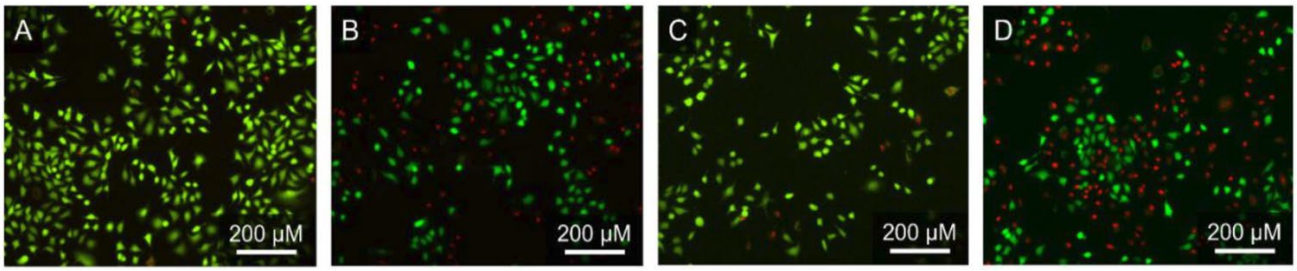

Figure 10: Representative fluorescence microscopy images of cells exposed to ultrasound and MBs. The cells in (A) were exposed to 25µM PC-MBs. The cells in (B) were exposed to 25µM Lyso-MBs. The cells in (C) were exposed to 80µM PC-MBs. The cells in (D) were exposed to 80µM Lyso-MBs. Propidium iodide (PI, red) indicates permeabilisation. Those cells that are not stained with PI and exhibit calcein fluorescence (green) from calcein-AM staining, were not permeabilised. No differences were visually apparent in the permeabilisation or morphology of the cells across all conditions.

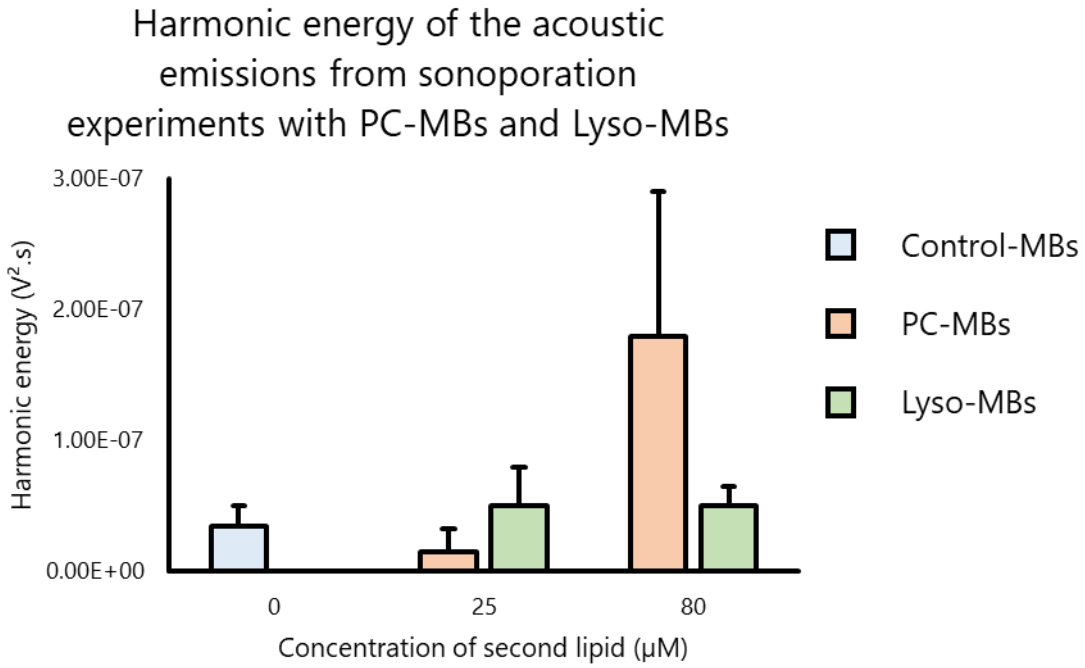

Figure 4.6.6: Average harmonic energies of the acoustic emissions from sonoporation experiments with Lyso-MBs and PC-MBs. Whilst PC-MBs containing 80µM 16PC produced greater acoustic emissions, the p values were greater than 0.01 compared to the other conditions. Specifically, p = 0.031, p = 0.017, p = 0.044, and p = 0.064 for comparison with Control-MBs, PC-MBs at 25µM, Lyso-MBs at 25µM and 80µM respectively.

The acoustic emissions from Control-MBs, Lyso-MBs (25 and 80µM), and PC-MBs (25 and 80µM) were measured in sonoporation experiments by passive cavitation detection (PCD) using the methods outlined in Section 4.3.8. The energy in the harmonic acoustic emissions was indistinguishable for Control-MBs and Lyso-MBs at both concentrations of lysolipid used. The energy in harmonic

acoustic emissions from PC-MBs was, however, more varied. Notably, two 80μM PC-MB samples produced significantly more harmonic emissions than the other formulations tested. Nonetheless, it is clear from these results that the significant increase in sonoporation efficiency between Lyso-MBs containing 80μM 16-lyso-PC and the other conditions tested cannot be attributed to microbubble size distributions, concentration, or acoustic emissions.

4.7. Discussion of *in vitro* results

The aim of this Chapter was to identify lipid candidates that, through lipid exchange mechanisms, were capable of modulating the permeability of cell membranes such that ultrasound and microbubble mediated delivery of model drugs to those cells could be enhanced.

Initially, in Section 4.5, different saturated phosphatidylcholine (PC) lipids (the primary component in phospholipid-shelled microbubbles) were screened for their effect on cell membrane fluidity. These lipids were cylindrical lipids with different hydrocarbon chain lengths and a conical lysolipid, 16-lyso-PC. They were then investigated for their ability to enhance sonoporation (Section 4.6). The solubility of PCs in aqueous solution increases as the chain length is reduced, resulting in higher lipid transfer rates. Additionally, the transfer of shorter PCs to cell membranes introduces a chain length mismatch. As expected, it was found that cells exposed to PCs exhibited cell membrane disordering that was inversely proportional to the PC hydrocarbon chain length. The shortest PC investigated, 10PC, rapidly altered the lipid order of cancer cell plasma membranes and intracellular lipids. This effect on cell membrane permeabilisation and cell cytotoxicity is found to be concentration-dependent in Section 7.1. 12PC, which was found to significantly disorder cell membrane lipids without permeabilising cells on its own, was further investigated for its impact on sonoporation. However, exposure to 12PC prior to sonoporation did not increase the proportion of cells permeabilised. Due to the discrete constraints of lipid properties, the results of this research suggest that enhancing non-toxic sonoporation by a lipid-transfer mechanism from microbubbles is unlikely to be possible using saturated PCs under the exposure conditions investigated here.

A further investigation into the role of PC shape in ultrasound-mediated drug delivery was conducted. It was hypothesized that lipids more conical in shape, in this case saturated lysophosphatidylcholine (lyso-PC), would be better suited to promoting pore formation and pore stability in cell membranes for reasons discussed earlier in this Chapter.

It was found that lyso-PCs had strong lipid disordering and permeabilising effects on cell membranes. It was found that exposing cells to Lyso-MBs (containing lyso-PC) and ultrasound resulted in a ~5-fold increase in the percentage of cells permeabilised compared to either Control-MBs or PC-MBs (microbubbles containing the same quantity of a non-hydrolysed PC with an equal chain length (16PC)). This enhancement could not be attributed to microbubble size distributions, concentrations, microbubble stability or acoustic emissions. Thus, it can be concluded that sonoporation can indeed be enhanced by designing microbubbles to exploit lipid transfer mechanisms.

Compelling evidence for the successful incorporation of lyso-PC into MB shells is presented in this Chapter. Microbubbles spiked with lyso-PC caused widespread cell permeabilisation but when cells were exposed to Lyso-MBs containing an equivalent concentration of lyso-PC, no significant change in permeabilisation was observed. If the majority of the lyso-PC in solution was not incorporated into Lyso-MB shells, significant permeabilisation would be expected without ultrasound exposure. Furthermore, following ultrasound exposure, Lyso-MBs permeabilised more cells than Control-MBs or PC-MBs. It thus appears that ultrasound exposure triggered the release of lyso-PC from Lyso-MBs resulting in additional cell membrane permeabilisation. The results in Section 7.4 show direct incorporation of a fluorescent lysolipid into MB shells, which then transferred to cell membranes under ultrasound exposure.

From the acoustic emissions, which were sustained throughout ultrasound exposure, and by visual inspection of samples after ultrasound exposure, it was clear that not all of the Lyso-MBs were destroyed in the sonoporation experiments. Interestingly, exposure of cells to Lyso-MB previously destroyed by heating and sonication did not result in the permeabilisation expected from exposure to lyso-PC micelles. Taken together, this suggests that lyso-MB fragments resulting from MB destruction may not transfer efficiently to cell membranes, owing to the presence of 22PC and/or PEG40S. It is thus hypothesised that lyso-PC, which is much more soluble in aqueous solution than 22PC, is preferentially shed from Lyso-MBs during sonication. Once released, the lyso-PC from Lyso-MBs appears to promote cell permeabilisation by either directly permeabilising cells, or by

reducing the energy barrier to pore formation such that cavitation-mediated permeabilisation is more readily achieved.

The high lipid transfer rate of lyso-PC and the presence of specific enzymes for its clearance *in vivo* are both beneficial and problematic for the clinical translation of lyso-MBs. These factors may lead to the rapid onset of biological effects upon ultrasound triggered release followed by the enzymatic degradation of lyso-PC. However, there is also a risk of blood toxicity if lyso-PC is not retained in MB shells *in vivo*, and transfers to blood cells or the endothelium prior to ultrasound exposure. While this must be evaluated experimentally, lyso-PC desorption from lyso-PC-containing thermosensitive liposomes has already been used in clinical trials.[532] No blood toxicity has been reported.

It is likely that the lyso-PC in Lyso-MBs could be replaced by a number of structurally similar synthetic lysolipids which may provide additional therapeutic benefit. For example, Edelfosine, similar to Lyso-PC but with better metabolic stability *in vivo* has been shown to inhibit tumour cell proliferation.[533] Edelfosine was also the first cancer drug to specifically target the cell membrane, with a mechanism involving the disruption of lipid rafts which ultimately induces apoptosis.[534] Mitelfosine, which is lyso-PC without the glycerol residue, has also been investigated to this end but its clinical translation, like that of Edelfosine, was hindered due to systemic toxicity.[533] Perifosine has since been developed in which the head group on the Mitelfosine lipid is substituted to improve the stability and half-life of the drug. Perifosine has had clinical success when orally administered in combination with other cancer therapies and exhibits selective cancer kill *in vitro*.[533] The clinical potential of these other lipids could be enhanced when incorporated into an ultrasound-mediated triggered-release delivery system.

In summary, lyso-MBs have been found to cause a ~5 fold increase in cell sonoporation when compared to microbubbles containing no lysolipid. This exciting result shows the potential improvements in therapeutic efficacy that are possible from engineering the chemical properties of

the microbubble formulation. Further investigations into whether these exciting cellular delivery results translate to an *in vivo* setting are also warranted. For this, please see Chapter 5.

4.8. Conclusions

The aim of the research in this Chapter was to investigate whether the transfer of material from lipid-coated microbubbles into cell membranes would affect their sensitivity to sonoporation. The effects of different phosphatidylcholines (PCs) were investigated, specifically those with varying hydrocarbon chain lengths and a conical lyso-PC.

Changes in A-549 cancer cell membrane lipid order following exposure to ultrasound were quantified by changes in generalized potential (GP) using spectral imaging. Permeabilisation was measured by the proportion of cells showing the uptake of a model drug (propidium iodide) before and after ultrasound exposure. Exposing cells to shorter-chain PCs lowered the membrane lipid order compared to control samples, with 10PC exhibiting rapid toxicity. 12PC significantly reduced both cell membrane and whole-cell GP after 10 minutes.

The lyso-PC tested significantly reduced cell GP and permeabilised cell membranes in the absence of ultrasound. Microbubbles containing this lyso-PC were therefore prepared and found to produce a ~5-fold increase in the proportion of cells permeabilised to a model drug compared to control microbubbles. Importantly, the lyso-PC was found to be incorporated within the microbubble shell and only produced a permeabilising effect upon exposure to ultrasound. The transfer of a lysolipid from microbubble shells to cells was observed to occur only under ultrasound exposure. These findings indicate that potential improvements in therapeutic efficacy may be achieved by optimizing the lipid composition of microbubbles to facilitate delivery.

Chapter 5. Enhancing therapy *in vivo*

5. Enhancing therapy *in vivo*

Abstract

The research in Chapter 4 found that the molecular packing of cancer cell membranes can be affected by the transfer of phospholipids from microbubble shells to the lipid bilayer and that this transfer can be exploited to enhance drug delivery *in vitro*. Microbubbles containing lysolipids (Lyso-MBs) promoted a ~5-fold increase in cellular uptake of a model drug compared to Control-MBs containing no lysolipid.

This Chapter tests the ability of these Lyso-MBs to enhance ultrasound mediated blood brain barrier breakdown (US-BBBD) *in vivo*. Lyso-MBs were shown to double the volume of brain in which US-BBBD was detected compared Control-MBs. This enhancement could not be attributed to differences in microbubble size, concentration or acoustic emissions.

These findings indicate that optimising the composition of microbubble shells has the potential to improve the therapeutic efficacy of ultrasound mediated treatments, particularly in the brain. This is particularly relevant for techniques where a low local concentration of microbubbles might be expected, such as when antibody conjugated microbubbles are used to target brain metastases as in Chapters 2 and 3 of this thesis.

Graphical abstract

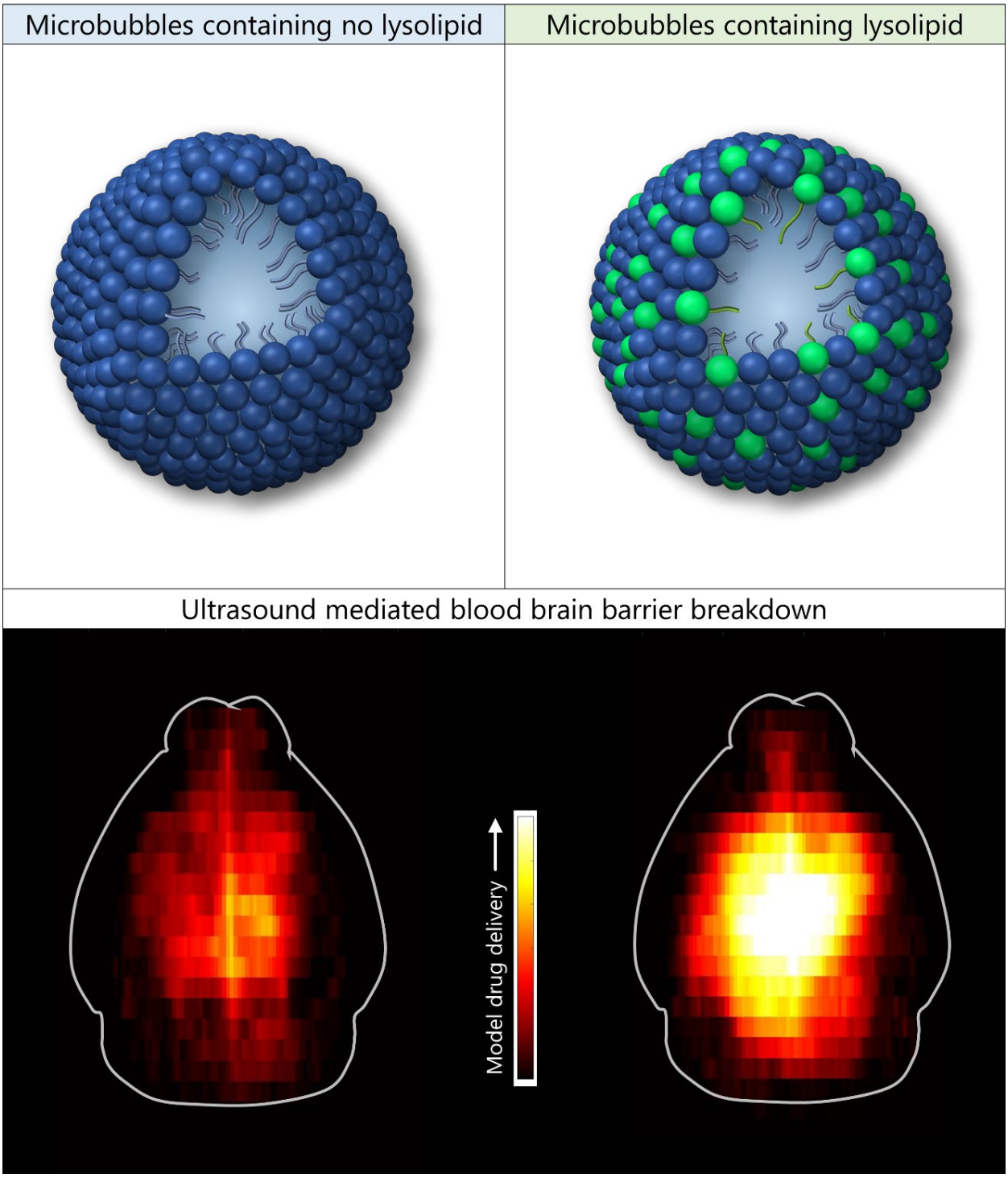

Attributions

I worked with Dr. Sarah Peeters on all of the experiments in this Chapter. Sarah took responsibility for all aspects of animal care, MRI imaging and histology. I was responsible for all aspects of experimental design, ultrasound exposure, animal positioning, acoustic monitoring and microbubble manufacture. Dr. Vanessa Johanssen provided occasional assistance with animal handling on busy experiment days. Dr. Michael Gray and Sean Smart designed the system used to expose mice to ultrasound which was then manufactured by James Fisk and David Salisbury of the IBME workshop.

The work in this Chapter currently under review for publication in Biomaterials under the title currently being prepared for publication under the title “Microbubbles containing lysolipid enhance US-BBBD *in vivo*.”

5.1. Introduction

In Chapter 4, microbubbles containing lysolipid (Lyso-MBs) were shown to cause a 5 fold increase in cell membrane sonoporation when compared to microbubbles without lysolipid (Control-MBs). It has also been shown that lysolipids significantly affect the fluidity of cell membranes (Chapter 4), transfer between microbubble shells and cell membranes under ultrasound exposure (Section 7.4) and cause a transient reduction in trans-endothelial electrical resistance (TEER) in an *in vitro* model of the BBB.[535] Therefore, this Chapter assesses whether Lyso-MBs are also capable of increasing US-BBBD when compared to Control-MBs.

As discussed extensively elsewhere in this Thesis, the BBB is one of the major barriers to therapeutic delivery, and as such, microbubbles that are capable of increasing US-BBBD without requiring an increase in ultrasound energy requirements may permit safe ultrasound mediated treatments deeper within the brain. More generally, if this enhancement is due to lipid exchange mechanisms, these findings would warrant further research into the effect of other microbubble constituents on therapeutic delivery.

5.2. Experimental Methods

5.2.1. Method overview

Gadolinium uptake into the parenchyma and serum IgG extravasation were used to compare the US-BBBD caused by both Lyso-MBs and Control-MBs. Female BALB/C mice (8-11 weeks old, Charles River, UK) were anaesthetized using isoflurane (1.5-2.0%) in 30% O_2: 70% N_2O), then had the top of their head shaved and were then placed in an MRI cradle with purpose built compatibility with the ultrasound set-up used. Animals were then transferred to the ultrasound setup before 3 minutes of ultrasound exposure (Section 5.2.2) to allow for the (highly variable) endogenous acoustic response to be accounted for (Section 5.2.3). 30 seconds before the injection of 1 x 10^8 microbubbles (either Lyso-MBs or Control-MBs), 30µl of gadolinium was injected into the tail vein. Ultrasound exposure continued for a further 2 minutes whilst the microbubbles were circulating. The cradle was then placed back in the MRI and a second MRI acquisition was performed using the same settings as for the first scan. Mice were then sacrificed using an overdose of pentobarbitol administered via intraperitoneal injection, followed by transcardial perfusion and fixation to preserve the cerebral blood vessels for histological analysis (Section 5.2.5). Comparison of the pre and post ultrasound MRI scans allowed quantification of gadolinium uptake in the parenchyma. All animal procedures were performed in accordance with the guidelines of the University of Oxford and approved by the UK Home Office. A summary of this timeline can be found in Figure 5.2.1.

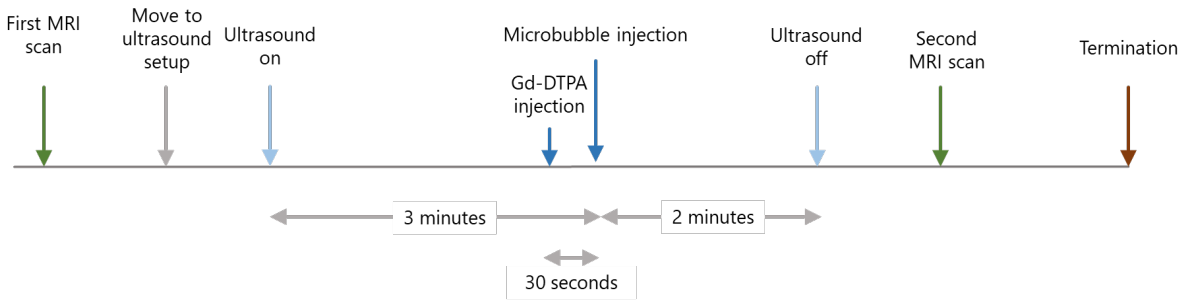

Figure 5.2.1: Experimental timeline of the experiments comparing US-BBBD potential of Lyso-MBs and Control-MBs.

5.2.2. Ultrasound exposure

Ultrasound exposure was carried out using a purpose built setup that allowed reproducible exposure of mice in an MRI cradle (Figure 5.2.2). This setup was also used in Chapter 3 and is summarised in Section 3.2.3. The ability to maintain the position of the mouse skull relative to the MRI cradle via a stereotaxic frame allowed comparison of the pre and post ultrasound MRI scans, thus allowing visualisation of image hyperintensity caused by gadolinium uptake into the parenchyma and thus visualisation of US-BBBD. It also maintained anaesthesia throughout ultrasound exposure.

Mice were exposed to 120 seconds of 0.5 MHz ultrasound with varying peak negative pressures (summarised in Table 3). A 1 Hz pulse repetition frequency and a 1% duty cycle was used.

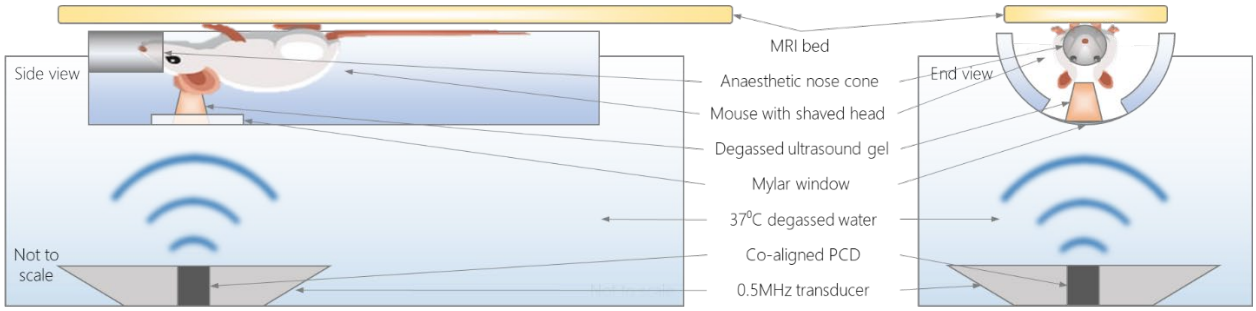

Figure 5.2.2: A schematic diagram of the key components in the set-up used to expose mice to ultrasound.

5.2.3. Acoustic emissions monitoring

As in Chapter 3, acoustic emissions monitoring during *in vivo* experiments was achieved using a single element passive cavitation detector (PCD) with a 3.5 MHz centre frequency (Olympus, US) co-aligned with the ultrasound transducer. This allowed analysis of any acoustic emissions from microbubbles in the brain. The powers and total acoustic energies of the harmonic, ultraharmonic and broadband components of the emissions were calculated as in Section 3.2.6. In contrast to the experiments in Chapter 3, subtraction of the background PCD noise (recorded immediately prior to microbubble injection) was conducted to remove inter-animal variations in acoustic response (Figure 5.2.3).

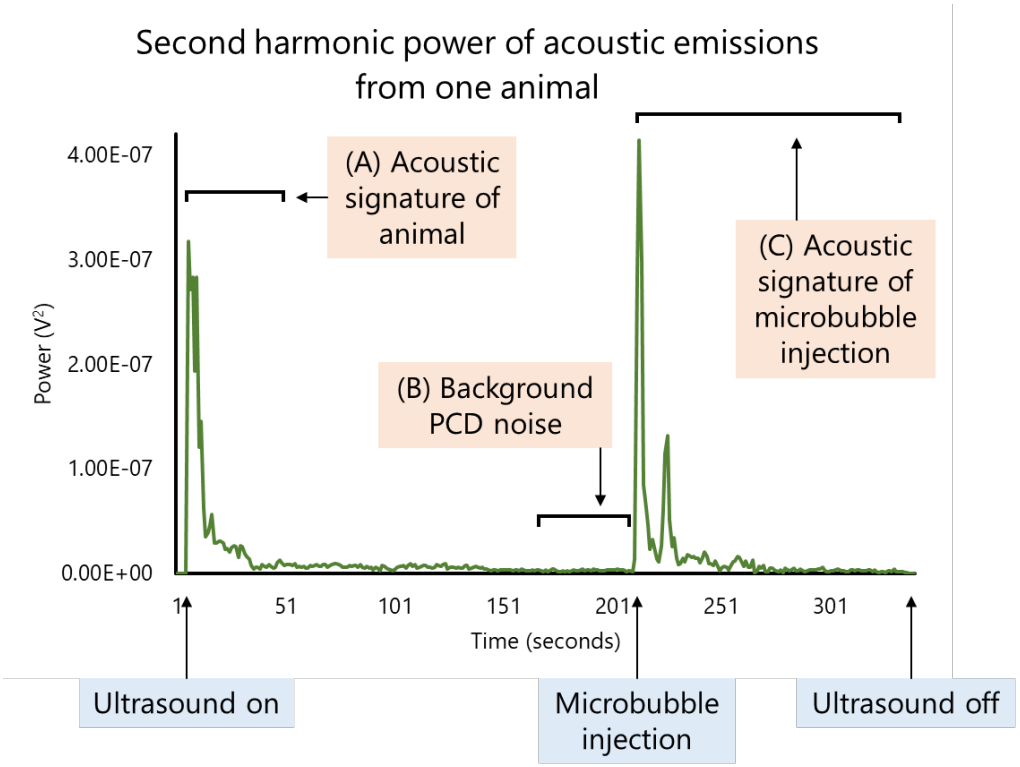

Figure 5.2.3: Diagram showing key elements of representative PCD trace from the in vivo experiments in this Chapter. To reduce the influence of acoustic emissions arising from elsewhere in the animal, the background PCD noise (B) was subtracted from the acoustic signature from the microbubble injection (C). The acoustic signature of the animal (A) often had a greater power amplitude than the subsequent microbubble injection.

5.2.4. MRI analysis of gadolinium uptake into the parenchyma

All MRI procedures were performed as in Section 3.2.4. However, it was not necessary to quantify left/right differences in this Chapter.

5.2.5. Histological analysis of extravasated serum IgG

All histological analysis was performed as in Section 3.2.5.

5.2.6. Animal overview

Table 3 outlines each of the experimental groups for which US-BBBD was tested in this Chapter and the number of animals in each group. The no ultrasound, ultrasound only and the lyso-PC groups were used to investigate any measurable effect on the BBB of the different MB formulations, the ultrasound alone and free lysolipid respectively.

Condition	Number of animals
No ultrasound	4 with Control-MBs, 4 with Lyso-MBs
160kPa PNP	5 with Control-MBs, 5 with Lyso-MBs
240kPa PNP	5 with Control-MBs, 5 with Lyso-MBs
320kPa PNP	8 with Control-MBs, 8 with Lyso-MBs
480kPa PNP	8 with Control-MBs, 8 with Lyso-MBs
US only (640kPa PNP)	4
Lyso-PC only (10x amount injected in MBs)	4

Table 5: A summary of the number of animals in each group

5.3. Results

5.3.1. MRI results

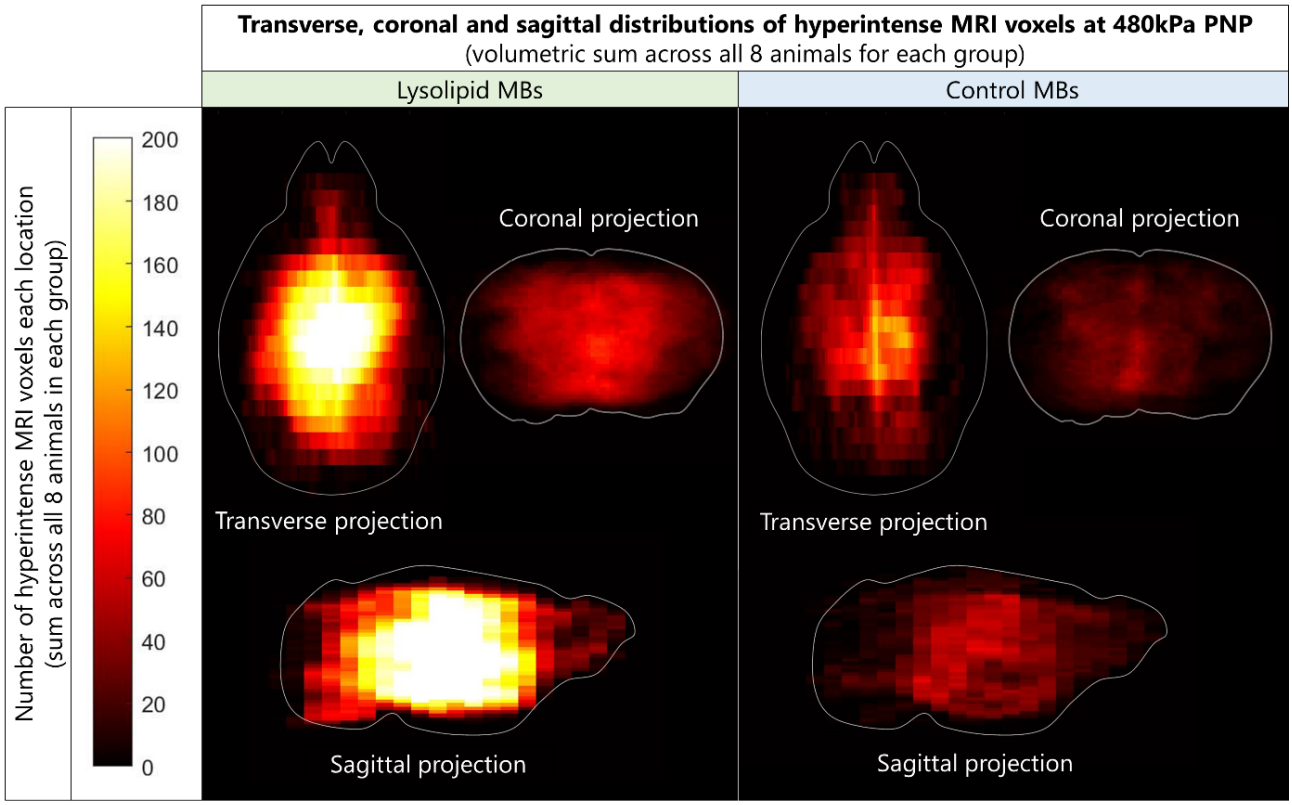

Figure 5.3.1: Heat maps of the ultrasound-mediated blood brain barrier breakdown in all 8 animals for both Lyso-MBs and Control-MBs at the highest pressure tested (480kPa PNP). Plots show sagittal, transverse and coronal projections of the volumetric sum of hyper-intense voxels (as measured by MRI), summed across all 8 animals in each group. The colour scales are equal for each plot to aid visual comparison between the two groups (brighter represents more US-BBBD). An illustrative line is shown around each projection indicating the edge of the brain.

Figure 5.3.1 shows sagittal, transverse and coronal heatmaps of the average distribution of US-BBBD for Lyso-MBs and Control-MBs at the highest pressure tested (480kPa PNP) as measured by MRI. Visual inspection reveals a clear difference in gadolinium uptake between the two microbubble formulations.

Figure 5.3.2 shows the US-BBBD in each of the experimental groups outlined in Table 3, calculated from the MRI hyper-intensities as detailed in Section 5.2.4. The total number of MRI voxels with an intensity greater than 3 standard deviations above background (hyper-intensity) is shown. In agreement with the heat maps in Figure 5.3.1, these results show that Lyso-MBs caused significantly

more US-BBBD than Control-MBs at 480kPa (p = 0.0026). There were no significant differences between microbubble types at any other pressures.

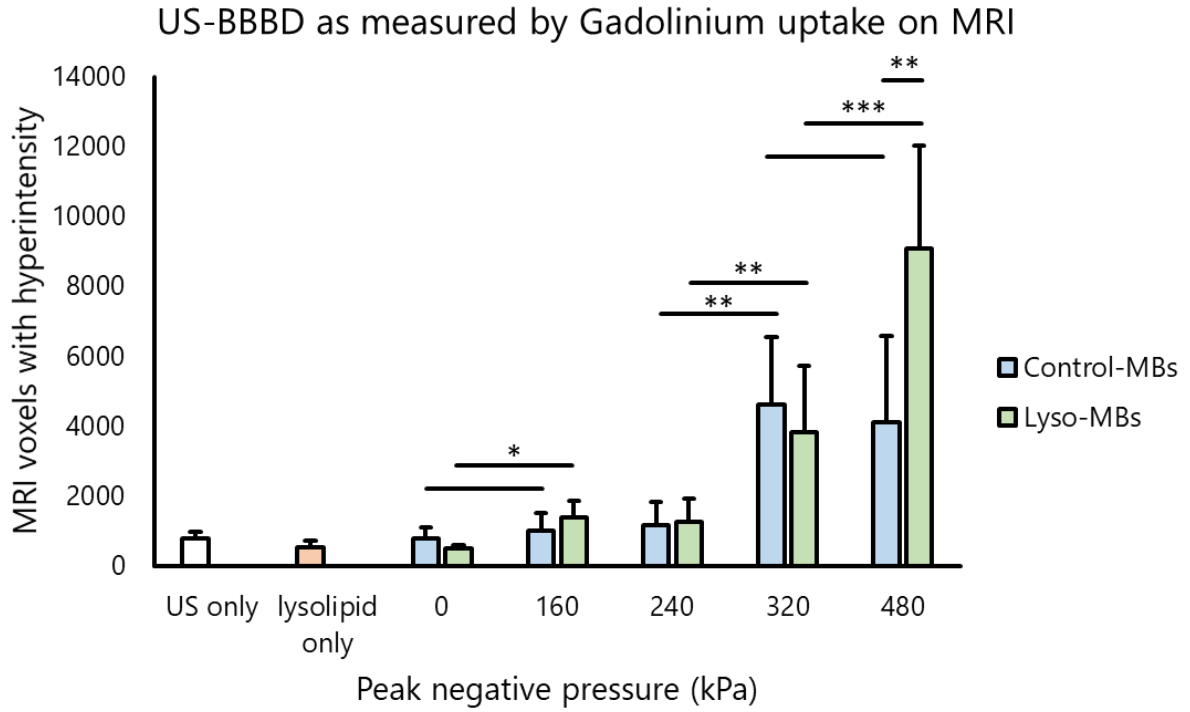

Figure 5.3.2: US-BBBD for each of the conditions tested (detailed in Table 3) as measured by gadolinium uptake into the parenchyma. Hyperintense voxels are those that have a brightness higher than 3 standard deviations above background when comparing the pre-US and post-US MRI scans. At the highest pressure tested, Lyso-MBs significantly increase US-BBBD when compared to Control-MBs ($p<0.05$, two tailed t-test). At all other pressures tested, there was no significant difference between Control-MBs and Lyso-MBs.

When comparing the results at 320kPa and 480kPa, the only significant difference in US-BBBD is with Lyso-MBs (p = 0.0008), with Control-MBs having a p value of 0.67. Both microbubble formulations significantly increase US-BBBD between 240kPa and 320kPa whereas neither microbubble formulation had a significant effect between 160kPa and 320kPa. Only Lyso-MBs have a significant effect on US-BBBD between the no ultrasound and 160kPa groups. There are no significant differences in BBBD between the ultrasound only, lysolipid only, and microbubble only groups. These results indicate that Lyso-MBs are more effective than Control-MBs at the highest pressure tested and should be analysed in tandem with the histological measurements of US-BBBD, shown in Section 5.3.2.

Whilst not a direct measure of toxicity, the MRI measurements of BBBD show that Lyso-MBs on their own do not enhance Gd uptake across the BBB.

5.3.2. Histology results

This Section details the US-BBBD results obtained via immunostaining histology slices for extravasated serum IgG as detailed in Section 5.2.5 for each of the experimental groups identified in Table 3. This technique is complementary to the MRI/gadolinium enhancement results in Section 5.3.1.

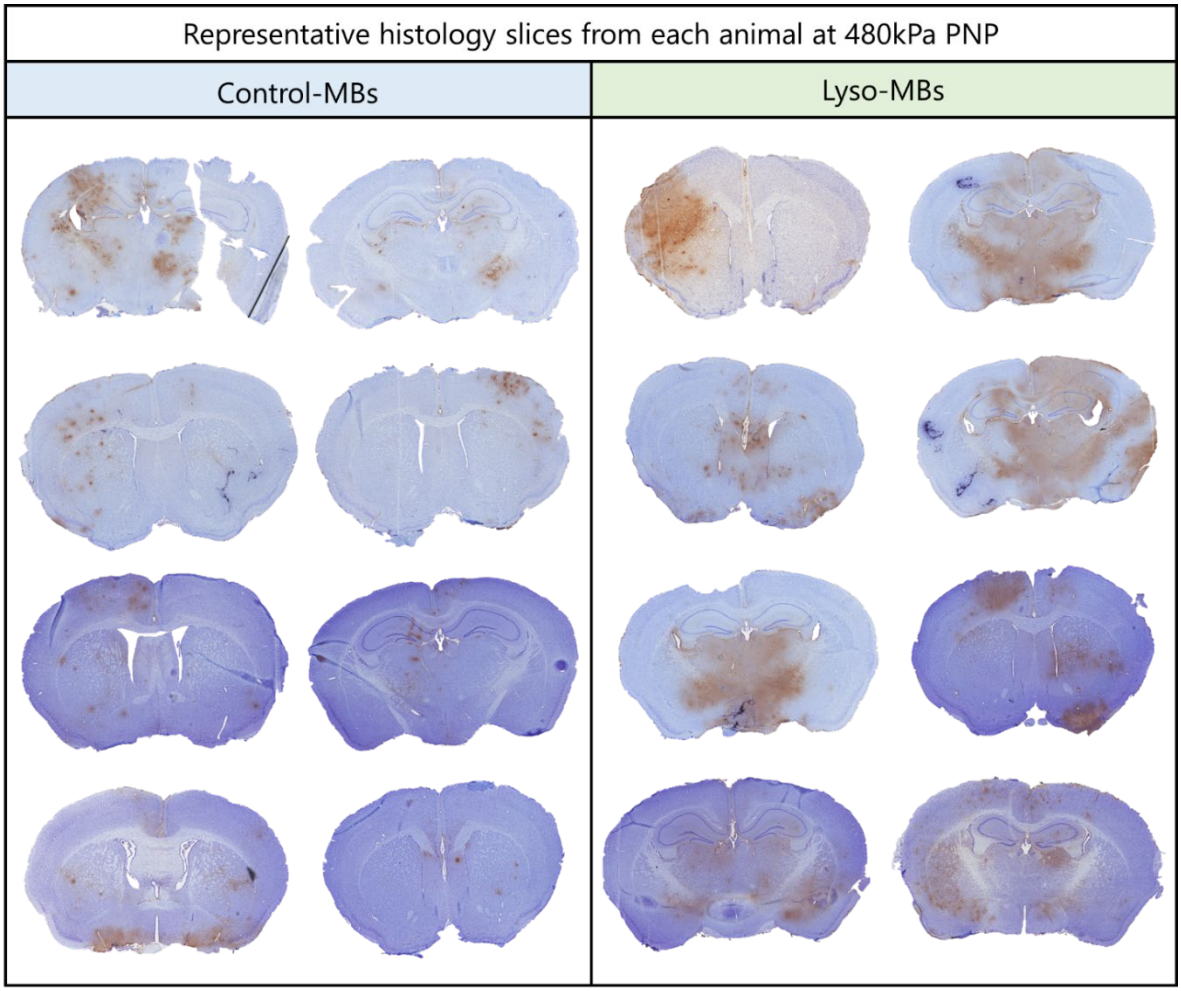

Figure 5.3.3: A representative histology slice from each animal in the 480kPa group. Extravasated serum IgG is visible in brown (DAB-peroxidase substrate solution). Differences in blue cresyl violet staining arise from differences in the local concentration of dye and do not affect measurements of US-BBBD.

Figure 5.3.4 shows a representative histology slice from each of the animals in the 480kPa groups. The blue colouring is cresyl violet (a cellular stain) and the brown colouring is a DAB-peroxidase substrate solution and acts as a stain for extravasated serum IgG (full protocol explained in Section

5.2.5). While it is visibly clear that, on average, the animals injected with Lyso-MBs have more widespread US-BBBD, the coronal distribution of US-BBBD is highly irregular in both groups. It is likely that these differences result from slight differences in positioning of the animals within the cradle and perhaps small differences in skull shape leading to the establishment of different intracranial standing wave patterns.

Visual inspection reveals that the US-BBBD caused by Control-MBs appears more punctate than that caused by Lyso-MBs, suggesting that it has arisen primarily around major blood vessels in the ultrasound focus.

Figure 5.3.3 shows the mean number of strong positive voxels in the whole brain for each experimental group. Strong positive voxels are those with dark DAB-peroxidase staining (with an intensity value between 0 and 175 in the red channel). This is defined further in Section 3.2.5.

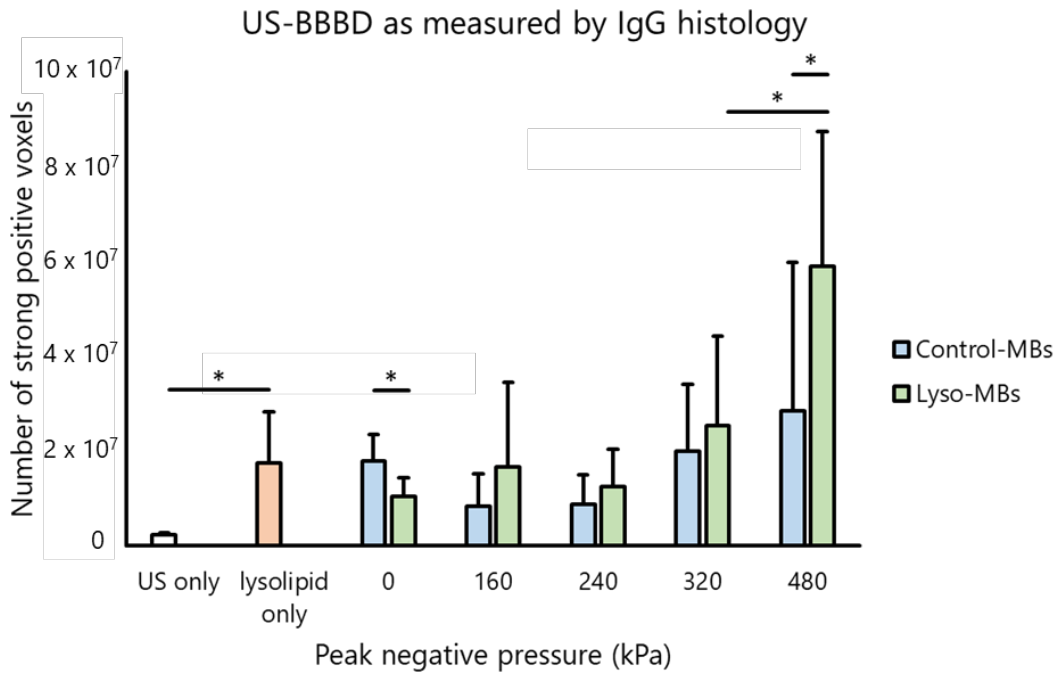

Figure 5.3.4: US-BBBD for each of the conditions in Table 3 as measured by immunostaining for extravasated serum IgG. In agreement with the MRI results, a significant increase ($p<0.05$, two tailed t-test) in US-BBBD was observed between the Lyso-MBs and Control-MBs at 480kPa. Although not significant, Lyso-MBs also cause more US-BBBD than Control-MBs at all other pressures tested. The ultrasound only group represents a control for the extravasated serum IgG that is present around major blood vessels and certain brain structures after ultrasound exposure.

Figure 5.3.3 shows that Lyso-MBs caused a greater amount of US-BBBD than Control-MBs at every pressure tested, but that this result was only significant ($p<0.05$, two tailed t-test) at the highest pressure, in agreement with Figure 5.3.2. In the microbubbles only groups, Control-MBs caused significantly more BBBD than Lyso-MBs. This result, combined with that for the ultrasound only group, suggests that both microbubble formulations have an effect on the BBB on their own, but this effect is lower with Lyso-MBs. In contrast to the results in Figure 5.3.2, free lysolipid (10 times the amount of lysolipid present in an MB injection) has a significant effect on the BBB when compared to the ultrasound only group.

5.3.3. Acoustic emissions

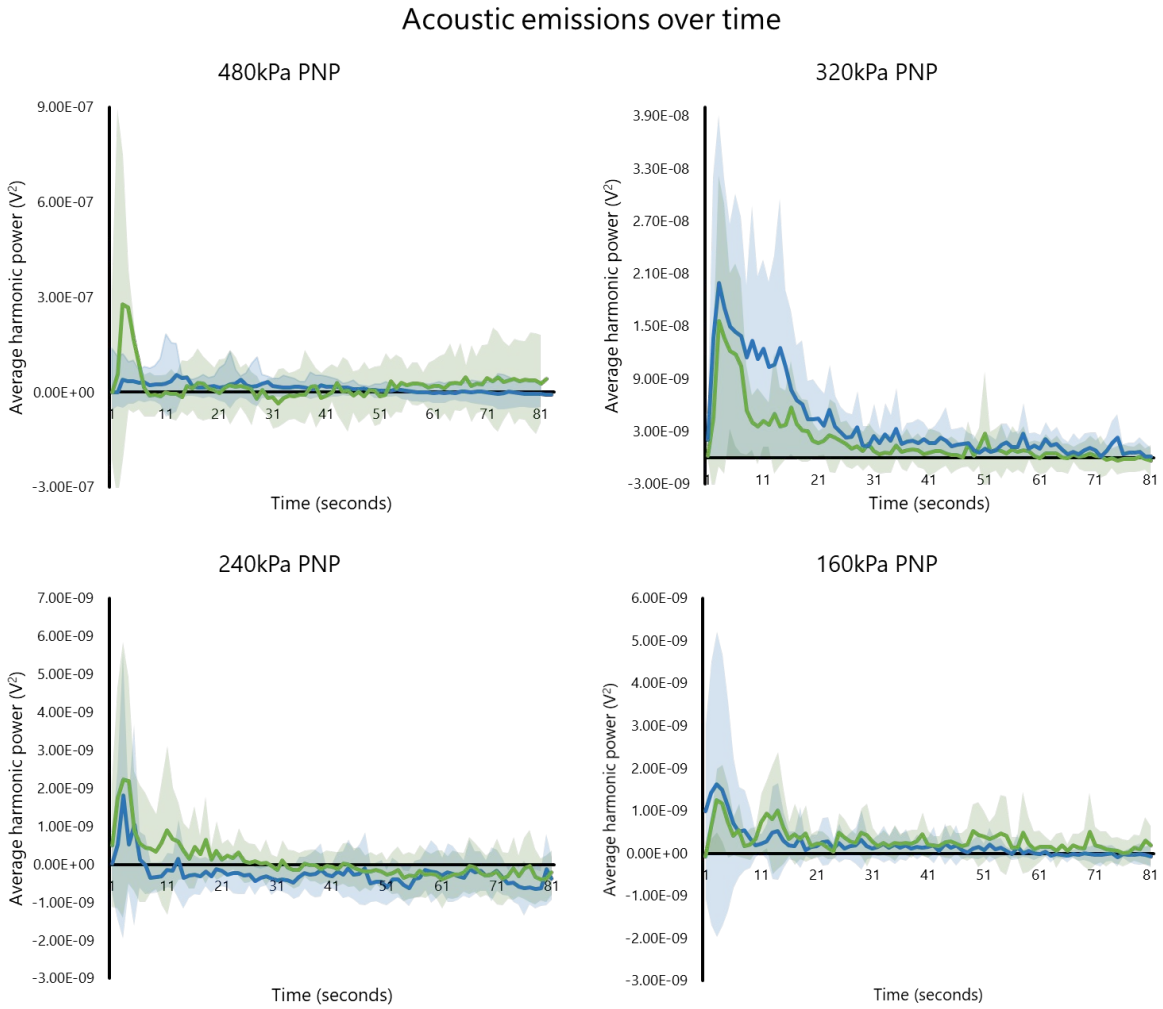

Figure 5.3.5: The average harmonic power of the acoustic emissions, split by microbubble type (green – Lyso-MBs and blue – Control-MBs) at each pressure over the duration of ultrasound exposure. Error bars indicate ± 1 standard deviation.

Figure 5.3.5 shows the average power of the harmonic acoustic emissions over the duration of ultrasound exposure for all animals, split by microbubble type and ultrasound pressure. These results, in combination with those in Figure 5.3.6, Figure 5.3.7 and Figure 5.3.8 show that there were no significant differences in acoustic emissions between the microbubble types. This is particularly important at 480kPa PNP which observed a significant difference in US-BBBD.

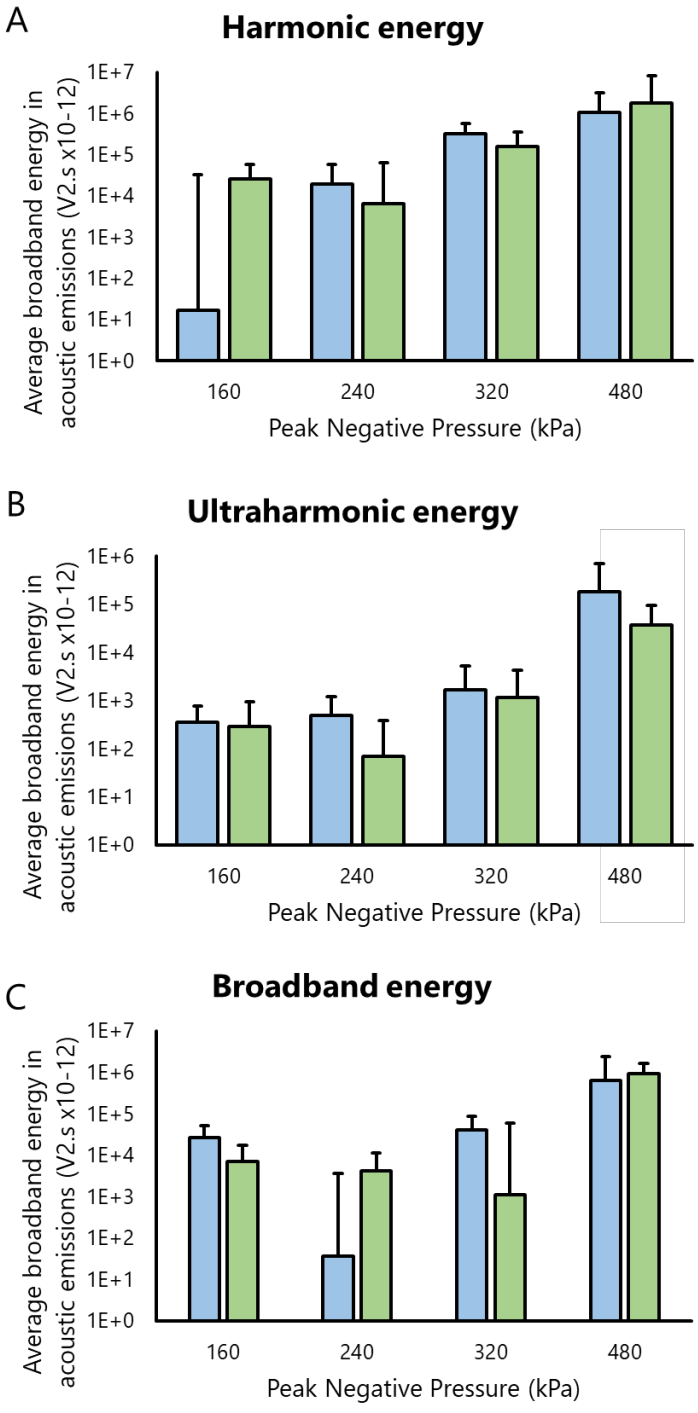

Figure 5.3.6: An overview of the average acoustic emissions from the animals at all pressures. (A) Average harmonic energy of acoustic emissions, (B) average ultraharmonic energy of acoustic emissions, (C) average broadband energy of acoustic emissions. Blue bars represent Control-MBs, green bars represent Lyso-MBs.

Figure 5.3.6 shows the average harmonic, ultraharmonic and broadband emissions of the animals in each group, split by microbubble type (blue bars represent Control-MBs, green bars represent Lyso-MBs). At the highest pressure tested, the harmonic and broadband emissions of Lyso-MBs are slightly higher those of the Control-MBs. However, the ultraharmonic emissions of the Lyso-MBs are lower.

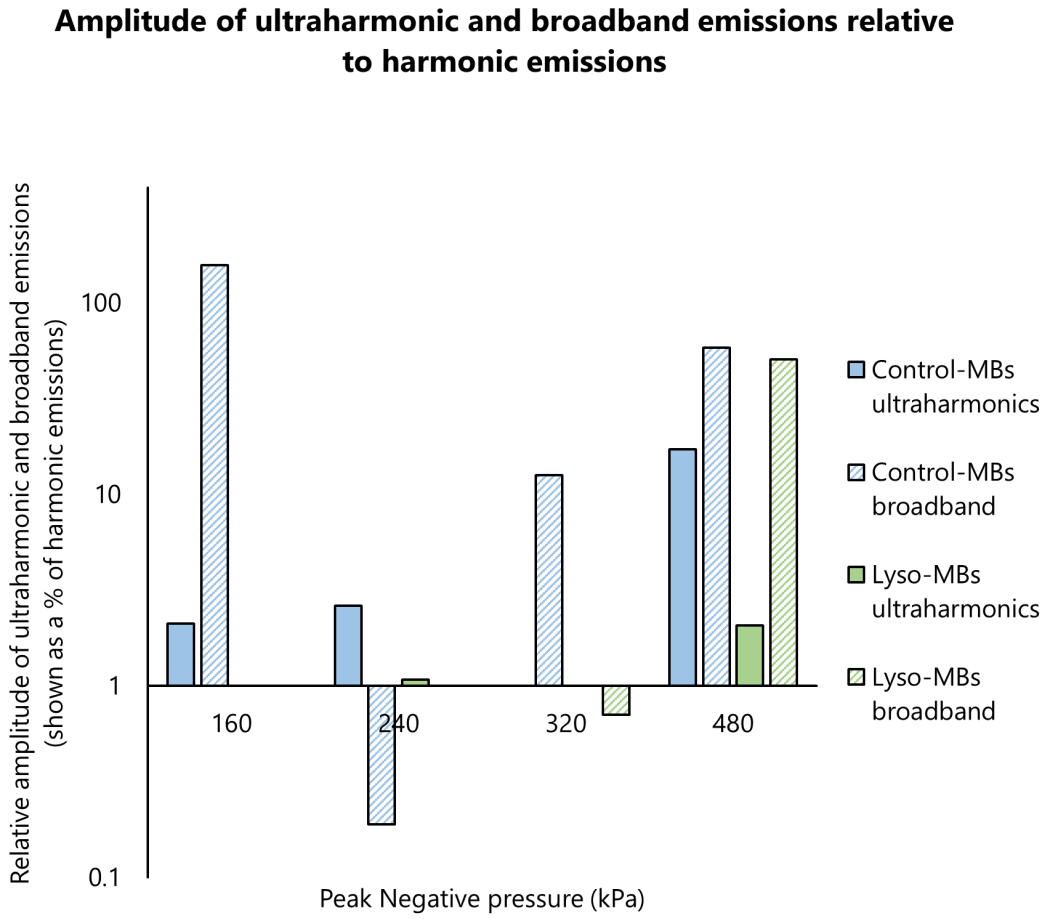

Figure 5.3.7: The relative amplitude of emissions as a percentage of the harmonic energy. Note the log_{10} scale on the y-axis.

The relative amplitude of harmonic, ultraharmonic and broadband components is important when monitoring acoustic emissions from cavitation activity. Figure 5.3.7 shows the average amplitude of the ultraharmonic and broadband components for each microbubble type normalised by the harmonic component for that microbubble type. This allows quantification of any elevation in either

ultraharmonic emissions or broadband emissions that is disproportionate to the increase in ultrasound pressure. From this plot it can be seen that at the three lowest pressures, the relative elevation in either ultraharmonic emissions or broadband emissions is greater for Control-MBs than for Lyso-MBs. At the highest pressure where a significant difference in US-BBBD was observed, relative broadband emissions are roughly equal and ultraharmonic emissions are higher for Control-MBs than for Lyso-MBs. Figure 5.3.7 also shows that the only ultrasound pressure where the relative amplitude of the ultraharmonic and the broadband emissions was comparable to the harmonic emissions was the highest pressure. This correlates with the significant difference in US-BBBD between microbubble types.

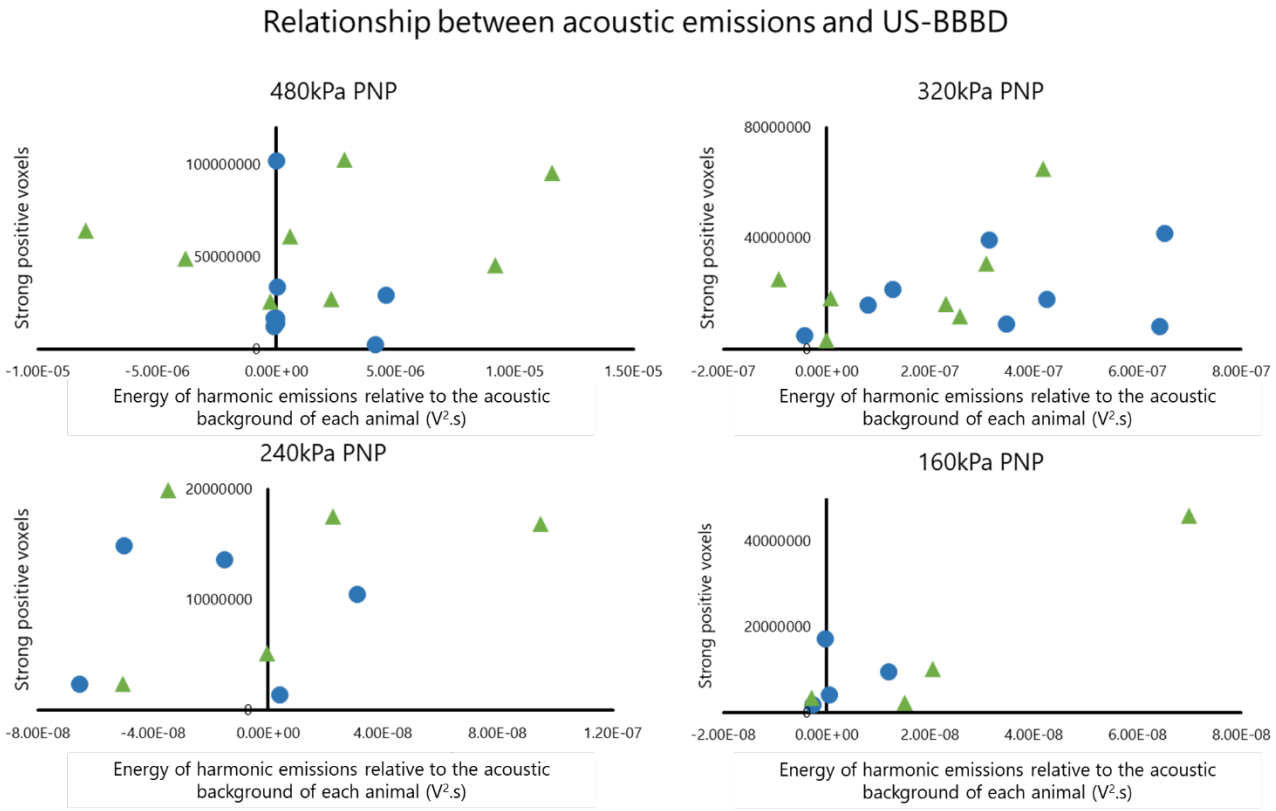

Figure 5.3.8: Scatter graphs showing the relationship between the energy of harmonic emissions (relative to the acoustic background of that animal, as defined in Section 5.2.3) and US-BBBD as measured by IgG histology for each pressure. Circles represent Control-MBs whereas triangles represent Lyso-MBs.

Figure 5.3.8 shows the correlation between the harmonic component of the acoustic emissions and the US-BBBD (as measured by histology) for each animal. The lack of clear correlations provides further evidence that the difference in US-BBBD cannot be attributed to increased cavitation activity. However, it should be noted that, despite the elevations in harmonic and ultraharmonic emissions after microbubble injection, it is possible that microbubble cavitation was not actually detected.

5.4. Discussion

Part 2 (Chapters 4 and 5) of this thesis set out to address to the second major challenge facing the successful treatment of brain metastases:

Challenge 2: Enhancing therapeutic delivery across the blood brain barrier

The aim of the work in this Chapter was to discover whether the enhanced cellular delivery observed with Lyso-MBs *in vitro* in Chapter 4 could be translated to an *in vivo* model and enhance US-BBBD beyond the current capabilities of the phospholipid-shelled microbubbles used clinically. To do this, animals were injected with either Control-MBs (containing no lysolipid) or Lyso-MBs. Ultrasound was applied to the whole brain during which time acoustic emissions were monitored using a single element PCD. US-BBBD was then measured by gadolinium uptake into the parenchyma (via MRI) and by the extravasation of serum IgG (via histological immunostaining).

Lyso-MBs were found to significantly increase US-BBBD above that caused by Control-MBs at 480kPa PNP, something that is not attributable to differences in microbubble size, microbubble concentration or microbubble cavitation activity (as measured by acoustic emissions).

Whilst all animals were positioned and aligned relative to the ultrasound transducer using the same method, there are clearly large differences in the position of US-BBBD within the brains (Figure 5.3.4). It is likely that this occurs due to slight differences in both the physiological make-up of the mice (e.g. skull thickness and brain perfusion) and slight differences in the position of the mice in the cheek bars of the MRI cradle. Mouse positioning in these experiments was conducted by a scientist with a wealth of experience with the positioning system used and so these differences represent the practical difficulties associated with these experiments and demonstrate the need for many repeats to establish confidence in the results.

The research goal of this Chapter was to test the hypothesis that the composition of microbubbles has an effect on US-BBBD. Therefore, the systemic toxicity of the Lyso-MBs was not measured directly in this experiment. Whilst, according to histology, free lysolipid caused some damage to the BBB,

Lyso-MBs had significantly less effect than Control-MBs. In agreement with the results in Chapter 4, the incorporation of lysolipid into MBs seems to remove its harmful effects. The endpoint of this experiment however did not permit measurement of the reversibility of the US-BBBD caused by these MB formulations and should be investigated before further clinical developments.

Whilst no therapeutic effect was shown in this Chapter, the enhanced delivery of gadolinium serves as a proxy for the enhanced delivery of small molecule therapeutics. Now that optimising the composition of microbubbles has been shown to enhance transport across the BBB, future teams can explore whether or not this enhancement translates linearly to similar small molecules and, if it does, whether it leads to an enhanced therapeutic effect of those small molecules in the brain.

A final point of discussion is that the significant increase in US-BBBD was only observed at the highest pressure. However, this correlates with the pressure at which both ultraharmonic and broadband emissions were of comparable magnitude to the harmonic emissions, thus indicating that this was the first pressure for which cavitation activity was detected. As the pressure inside the mouse skull is likely to be at least 18% lower than that measured in free space,[536] higher pressures may see a further enhanced effect. It is also worth noting that in the histology results (Figure 5.3.3) indicate that US-BBBD was higher (although not significantly) for Lyso-MBs than Control-MBs at all other pressures, apart from those without ultrasound, where Lyso-MBs caused significantly less damage to the brain.

These results build on those in Chapter 4 to show that the lipid-transfer from microbubbles to cell membranes can be exploited to enhance the ultrasound-mediated delivery of model drugs across the blood brain barrier *in vivo*. This therefore represents a novel approach for optimising microbubbles that may improve clinical treatments in the future. This is especially true for treatments for which low local concentrations of microbubbles are expected at the disease site, such as those relying on actively targeted microbubbles to treat pathologies such as metastatic brain tumours.

5.5. Conclusions

The physical properties (size, size distribution, stability and acoustic response) of cavitation agents and ultrasound exposure parameters have previously been optimised to increase drug delivery. The results in Chapter 4 and Section 7.4 show that lipids transfer from microbubble shells to cell membranes and that this transfer affects the membrane lipid order. Moreover, this transfer can be exploited to enhance ultrasound-mediated cellular uptake of a model drug.

This research in this Chapter has shown that microbubbles containing lysolipid (Lyso-MBs) significantly increase the ultrasound-mediated delivery of a model drug across the blood brain barrier *in vivo*. These results cannot be attributed to microbubble size, microbubble concentration or cavitation behaviour. Moreover, no toxic effects arising from the presence of lysolipid in the Lyso-microbubbles were observed.

These findings show that the composition of microbubbles can be adapted to enhance ultrasound-mediated blood brain barrier disruption, and therefore opens up an exciting new optimisation strategy for the delivery of drugs in the brain.

6. Thesis overview

6.1. Thesis summary

This thesis set out to exploit ultrasound and microbubbles to tackle two of the key challenges that currently impede the successful treatment of brain metastases. These challenges are:

Challenge 1: Targeting therapy selectively to brain metastases

Challenge 2: Enhancing therapeutic delivery across the blood brain barrier

As outlined in Section 1.7, the following research questions were addressed:

1. ***Are antibody-conjugated microbubbles capable of selectively binding to target regions in the brain?***
2. ***Once bound, are antibody-conjugated microbubbles then capable of causing US-BBBD selectively in the target region?***
3. ***How does lipid transfer from microbubbles affect cell membranes?***
4. ***Can microbubble-cell lipid transfer be exploited to enhance therapeutic delivery?***

Questions 1 and 2 are tackled in the first part of this thesis (Chapters 2 and 3) which focuses on targeting therapy specifically to the site of brain metastases. Questions 3 and 4 are tackled in the second part of this thesis (Chapters 4 and 5) which focuses on enhancing the delivery of therapeutics across the blood brain barrier, something that is critical for treating early stage metastatic tumours in the brain.

The contributions of this thesis can be summarised as follows:

- Demonstrating that microbubbles conjugated to anti-VCAM-1, an antibody with a high, selective affinity to early stage brain metastases, selectively bind to mouse brain endothelial cells that are overexpressing VCAM-1 under physiologically relevant flow conditions. This binding is much greater than that achieved by microbubbles conjugated to a control antibody.

- Demonstrating that anti-VCAM-1 conjugated microbubbles can bind selectively in a region of the brain where VCAM-1 expression is upregulated. This binding, combined with whole-brain ultrasound, was sufficient to enhance US-BBBD selectively in the target zone. To the author's knowledge, this is the first time that the combination of targeted microbubbles and unfocused ultrasound has been shown to be capable of causing selective US-BBBD. This technique potentially has far reaching consequences as it removes the requirement for prior knowledge of the disease site. This is particularly important for early stage metastases.
- Demonstrating that the lipids from phospholipid-shelled microbubbles transfer to cell membranes under ultrasound exposure and this transfer influences the fluidity of the lipid bilayer. Based on this optimisation, microbubbles containing lysolipid were developed and shown to be capable of enhancing the delivery of model drugs to cells *in vitro*. Direct transfer of a fluorescent lysolipid from microbubble shells to cell membranes is also shown.
- Demonstrating that microbubbles containing lysolipid were able to double the volume of the brain in which US-BBBD was caused without increasing the ultrasound energy and without causing any observable systemic toxicity or brain damage. Optimisation of microbubbles for drug delivery purposes has the potential to increase the efficacy of treatments that are either deep within the brain or treatments where the local concentration of microbubbles is low, for example when the microbubbles have been antibody targeted to brain metastases.

The research in this thesis identifies, investigates and demonstrates the potential of two powerful, novel concepts for the field of ultrasound-mediated therapeutic delivery. The concept developed in Chapters 2 and 3 removes the need for knowledge of the disease site prior to treatment. The concept developed in Chapters 4 and 5 enhances delivery in the brain without requiring an increase in ultrasound energy. Whilst it is clear that a significant quantity of work is required to translate these concepts to clinic, the findings in this thesis, when presented together, provide compelling evidence that ultrasound and microbubbles have the potential to provide the first curative treatment for

metastatic tumours in the brain. This presents the first realistic treatment option for the vast and growing cohort of patients worldwide who suffer from this debilitating and terminal disease.

It is important to recognise that whilst this research focuses on developing a treatment for brain metastases, the principles of non-invasive and targeted therapy examined in this thesis could, potentially, be extended to the treatment of many other pathologies, both in the brain and elsewhere.

Targeted drug delivery systems could facilitate the use of many types of pharmaceutical compound that are currently ineffective if administered intravenously or orally. These include poorly soluble drugs and large molecules such as proteins and DNA.[537] Furthermore, significantly increasing the localised dose of existing drugs could reduce the need to develop new medicines, currently estimated to cost between $500 million and $2.6 billion per drug.[538–541] Mitigation of patent expiry provides an additional commercial motivation for the clinical development of novel drug delivery systems. In addition, new delivery methods for existing products are in considerable demand due to the commercial value of such systems and to mitigate patent expiration.[542]

As the incidence of metastatic cancers and the need for novel drug delivery systems continues to rise, this research is both pertinent and timely. This thesis represents a small step on the collective quest to achieve the curative treatment that the world is waiting for.

The key findings of this thesis are shown schematically in Figure 6.1.1.

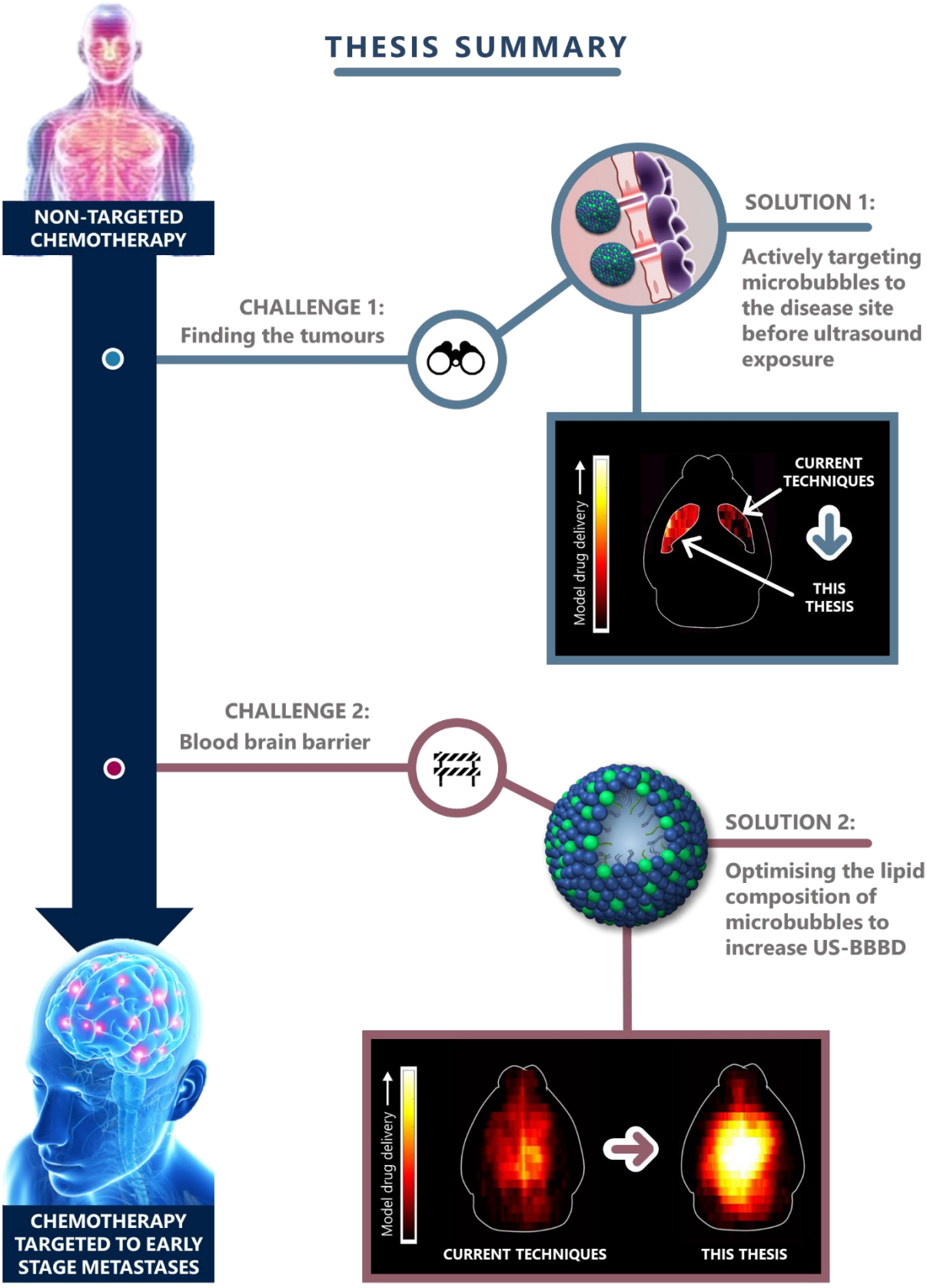

Figure 6.1.1: The key aims and achievements of this thesis

6.2. Future work

6.2.1. Chapter 2: further work (anti-VCAM-1 microbubbles *in vitro*)

Building on the work in Chapter 2, there are many additional *in vitro* studies that could be undertaken on antibody conjugated microbubbles that warrant investigation by future teams.

Firstly, the microbubble formulations used could be further optimised. Whilst it is clear that anti-VCAM-1 has been conjugated to these microbubbles, quantification of the exact antibody loading, the free surface biotin and streptavidin, the inter-sample antibody loading variability and the stability in blood are all required. Further quantification of the binding dynamics, targeting efficiency, flow resistance (including in the presence of flow pulsatility or blood) is also necessary.

The *in vitro* experimental groups used show that the anti-VCAM-1 antibody is the moiety responsible for attachment to inflamed cells and that this is capable of selectively distinguishing between inflamed and non-inflamed cells. Experiments utilising capillaries conjugated with VCAM-1 protein or pre-treating inflamed cells with anti-VCAM-1 antibody would act to further confirm the VCAM-1 specificity of AV-MBs.

Biotin-streptavidin-biotin conjugation is a simple and widely used strategy for actively targeting microbubbles pre-clinically. However, further research into other conjugation strategies with less immunogenic properties is important for eventual clinical translation.

Further enhancement of the targeting or retention capabilities, for example incorporating iron oxide nanoparticles into the MB shell for magnetic targeting or adding a second antibody for dual targeting, is also warranted.

6.2.2. Chapter 3: further work (anti-VCAM-1 microbubbles *in vivo*)

Future teams could elucidate the exact mechanisms at work in the intra-striatal injection model by further testing with MBs conjugated with antibodies that would be less susceptible to cross-species reactivity (such as anti-goat or anti-horse IgG) and MBs without antibodies. A systemic injection of

anti-VCAM-1 prior to MB injection could be used to establish the specificity of AV-MB binding *in vivo.* More reliable fluorescence-based methods of measuring the upregulation of VCAM-1 following cytokine injection could be used to more accurately quantify the VCAM-1 expression in the brain of each individual animal. This would remove the influence of endogenous VCAM-1 expression and remove the influence of other brain structures in the histological analysis. More detailed spatial analysis of the co-localisation of VCAM-1 expression and US-BBBD could also be carried out.

It should be emphasised that the underlying motivation behind the work in Part 1 of this thesis is to develop a targeted therapy for metastatic brain tumours, not neuro-inflammation. Therefore, in the author's opinion, this Chapter presents sufficient evidence for the ability of antibody-conjugated MBs to cause targeted US-BBBD. The experimental resources of future teams would be much better allocated to investigating the ability of AV-MBs to selectively cause US-BBBD around the sites of microscopic tumours in an *in vivo* model. Suitable models include an intra-cardiac injection of MDA231BR cells (metastatic human breast carcinoma) that preferentially metastasize to the brain and begin to form microscopic brain metastases within 5 days.[108] It makes practical sense to begin with a model that has been shown to work well, before moving on to other models/pathologies where the target antibody is less clearly overexpressed relative to background.

6.2.3. Chapter 4: further work (lysolipid microbubbles *in vitro*)

The dependency of both microbubble-cell lipid transfer and enhanced cellular delivery on the ultrasound parameters used warrant further investigation, especially as the *in vivo* results in Chapter 5 indicate a pressure dependence. Similarly, the response of other cell lines to these effects is important; these results may reveal locations in the body and/or pathologies that are more susceptible to treatment. The effects of lysolipids on the other mechanisms suspected to play a role in cellular delivery and/or US-BBBD should also be investigated further. These include endocytosis and cell-cell tight junction opening.

Whilst a handful of lipids were investigated in this Chapter, there are many more that would be reasonably expected to influence cellular uptake of therapeutics. These include structurally similar synthetic lipids (discussed in Section 4.10) and lipids with different shapes (for example PEs). Other microbubble components, e.g. emulsifiers, also have a significant effect on cell membrane properties and are worthy of further investigation. In the same line of reasoning, it may be possible to design microbubbles containing 3 or more different lipids that act synergistically to enhance therapy further. It is important to recognise that the microbubble components that have been used interchangeably for many years may have a significant effect on the outcome of ultrasound-mediated therapeutic studies.

6.2.4. Chapter 5: further work (lysolipid microbubbles *in vivo*)

Whilst a clear increase in US-BBBD was shown at the highest pressure tested in Chapter 5, there are many further avenues of research which should be pursued to aid the progress of these techniques towards clinical trial.

Further testing of the two microbubble formulations should be carried out with different ultrasound settings, most notably higher pressures. As the research in this Chapter indicates that a significant effect was only observed once cavitation activity was detected, it is hypothesised that the more cavitation that microbubbles undergo, the more US-BBBD will occur. The use of passive acoustic mapping in larger animals would provide further information on the onset of cavitation.

No cellular damage or lesion formation was observed in any of the brains. However, further analysis of the systemic toxicity, clearance routes and longer term effects of microbubbles containing lysolipid is required. On top of this, the reversibility of the US-BBBD caused by each type of microbubble is an important consideration. It is likely that lyso-MBs could improve delivery to other tissues and across other membranes in the body, especially those that are deep within the body where delivering high ultrasound energies presents practical and safety challenges. Potential high-value targets include delivery to the pancreas and crossing the tight cellular membranes in the kidney.

Once the effect of a range of other microbubble constituents on *in vitro* cellular delivery and other processes likely to affect US-BBBD have been analysed as proposed previously, testing them *in vivo* is warranted. It is likely that the results of many ultrasound mediated delivery experiments could be enhanced through engineering of the composition of the microbubble shell.

6.3. Further discussions

6.3.1. FUS to UFUS?

Whilst Part 1 (Chapters 2 and 3) of this thesis supports the proposal that antibody conjugated microbubbles and unfocused ultrasound (UFUS) can be combined to cause US-BBBD selectively at the site of disease, it is important to emphasise the wider clinical applications that this technique could have. Not needing to focus the ultrasound means that beam distortion, especially within complex bone structures such as the skull, would become less of an issue. As microbubbles can produce therapeutically relevant effects at much lower ultrasound pressures than the majority of other cavitation agents, they are the most likely to see clinical translation for this application initially.

Figure 6.3.1 shows some of the other pathologies that may be susceptible to direct treatment using AV-MBs. Also shown are some pathologies for which likely disease biomarkers are known but a safe, selective and reversible method for opening the blood brain barrier at sites expressing those biomarkers does not currently exist. Part 1 of this thesis is proposing UFUS and actively targeted microbubbles as a potential viable solution.

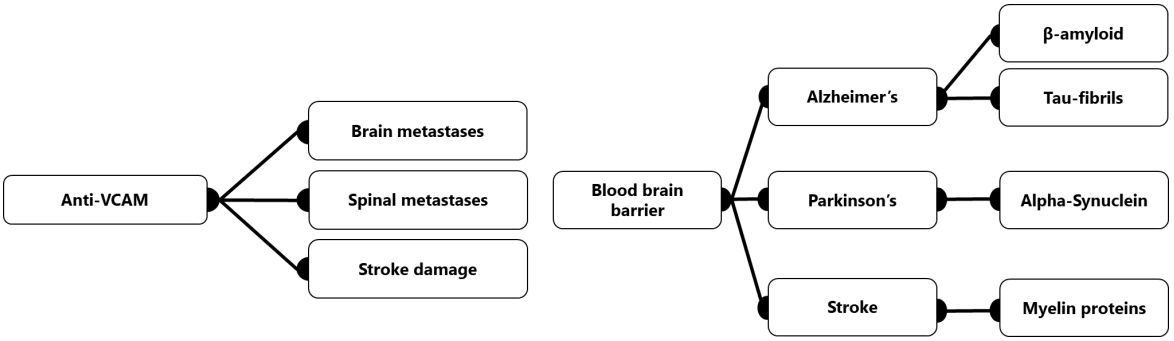

Figure 6.3.1: Some of the other pathologies that could be targeted using anti-VCAM-1 conjugated microbubbles (left) and some of the other pathologies that could benefit from the ability to actively target US-BBBD with a molecular level of specificity in the brain (right).

6.3.2. Long-term feasibility of the solutions in this thesis

It was established in Section 2.1.2 that antibody-microbubbles meet the four essential requirements (identified in Section 1.5.3) for a therapy for brain metastases. There are several additional desirable characteristics that such a therapy should possess. These are:

i. Low cost.

ii. Formulation using FDA approved materials to accelerate regulatory approval.

iii. Manufacturing protocols that are simple, robust, repeatable and possible on a large scale.

iv. Practical suitability for use in real-world clinical settings.

v. Utility as a platform technology to allow personalised therapy, e.g. straightforward procedure for adapting tumour targeting molecules for individual patients/tumour characteristics.

The suitability of the techniques developed in this thesis with regards to these additional characteristics is now discussed:

i. Microbubbles are low in cost compared to many therapeutics.[543,544] Conjugation with an expensive drug is the only factor likely to significantly increase this cost. The clinically available ultrasound systems vary significantly in cost. The Exablate system costs between $750,000 and $1.5 million and requires an MRI system for operation.[545] The cost of the SonoCloud system is not publicly available but as it is a single transducer and doesn't require MRI, the majority of the cost is likely to be associated with the surgery.

ii. Three microbubble formulations (Optison, Definity, Sonozoid and Sonovue) have achieved regulatory approval and are in widespread clinical use.[3] The main components of Sonovue are very similar to those in the microbubbles formulations tested in this thesis. As initial clinical studies focus on enhancing the delivery of pre-approved therapeutics, approval of this technique is not expected to face insurmountable regulatory challenges.

iii. Microbubble manufacturing protocols do not present significantly greater manufacturing challenges than the vast majority of systemic therapeutics.

iv. In the clinic, Sonovue® is manufactured in less than 30 seconds via manual agitation. Therefore, it is hoped that more advanced, actively targeted microbubble formulations would also not present significant practical challenges during clinical use.

v. As is mentioned elsewhere in this thesis, there are many other receptors that could be targeted for a wide range of intracranial diseases and many different ligand-microbubble conjugation

strategies are available that has the potential to allow this technique to become a platform technology for personalised therapy that can be adapted for individual patients/tumour characteristics.

6.3.3. Implications of these results for potential therapies

As the principle aims of this study were not related to therapeutic outcomes, no direct link can be drawn between the results here and eventual therapeutic benefits for patients with brain metastases. However, there are several aspects that are clinically relevant and should act as the pre-cursor and feasibility test for future therapeutic tests involving antibody targeted microbubbles and unfocused ultrasound to enable drug delivery in the brain with a molecular level of specificity.

The small molecule compound (gadolinium-DTPA, a 590kDa, ionic MRI contrast agent) used in Chapters 3 and 5 of this thesis is a widely used proxy for small molecule drugs. It has been shown to be co-localised with the delivery of larger molecule compounds across the BBB[546] and some estimations state that gadolinium may underestimate the true extent of BBB breakdown.[185] Therefore, it can be assumed that if gadolinium can be selectively delivered across the BBB in the target region, delivery of small molecule chemotherapeutics such as doxorubicin or paclitaxel should be a straightforward extension.

The acoustic emissions recorded from the brains of the mice in this study found a significant increase in cavitation activity arising from microbubbles bound within the brain. As an increase in microbubble cavitation energy has been directly linked to more effective therapy in the brain, it can be hypothesised that this cavitation would have a therapeutic effect on any nearby tumours.[547–550]

US-BBBD is now widely regarded as a low risk technique for reversibly increasing the permeability of the BBB (see Section 1.6.3). Although the longevity of BBB opening was not investigated in this study, no brain tissue damage or intracerebral lesion formation was observed during histology of any of the animals. This indicates that, if necessary, the acoustic energy delivered and/or microbubble concentration could be further increased to enhance therapeutic efficacy

6.3.4. Further challenges

Whilst the main two challenges associated with treating metastases have begun to be addressed in this thesis, there are a host of other challenges to consider.

- Once tumours get large enough to develop blood vessels of their own, they develop abnormal perfusion dynamics, a high interstitial pressure and a hypoxic core. Whilst the aim of this thesis is to treat tumours before these problems develop, the practical constraints of clinical diagnosis mean that this is unlikely to happen all of the time. All of these factors would limit the efficacy of the techniques in this thesis. However, they also limit the delivery of every other systemically administered therapy.
- At the time of diagnosis, metastases in the same patient normally span a wide range of characteristics, most notably in size. Whilst microscopic tumours may be susceptible to the techniques developed in this thesis, it is likely that larger metastases, due to the reasons outlined above, would not. Therefore, it is likely that any clinical translation of these ultrasound-mediated techniques would be combined with either surgery or stereotactic radiotherapy to treat larger tumours.
- The condition of patients with brain metastases presents another challenge. Most of these patients will have undergone many previous rounds of surgery, chemotherapy and radiotherapy for lesions elsewhere in the body. Therefore, whilst enhanced and more selective delivery of chemotherapeutics will help, patients may have already developed resistance to many of the small-molecule therapeutics that are most suitable for initial use with the techniques in this thesis. The physical condition of patients is also likely to be very poor, limiting their willingness or eligibility to trial novel clinical techniques.
- All of the techniques in Part 1 of this thesis require the use of unfocused ultrasound transducers capable of exposing large areas of the brain to a semi-uniform field without setting up dangerous standing waves or under-exposing large swathes of the target region. The design, construction

and clinical approval of a system capable of adapting to different patients with relative ease is non-trivial.

- Whilst many components of this thesis are in either late-stage pre-clinical or early stage clinical trials, combining them all together as suggested throughout this thesis would require a host of new regulatory approval. The willingness of industry, regulators and academia to pursue this may be limited in the short to medium term future.
- Most metastatic lesions in the brain are not detected until they are widespread, and currently none are detected until they are large enough to disrupt the blood brain barrier on their own (1 - 2mm diameter). By this stage, metastases have adapted to their microenvironment and undergone clonal selection which greatly increases their resistance to all forms of treatment. Whilst various methods for improving early stage detection are in late-stage pre-clinical trials, including the anti-VCAM-1 conjugated MRI contrast agents upon which Part 1 of this thesis is based, none are yet available clinically.

6.3.5. Combining lysolipids and VCAM?

As Part 1 of this thesis focuses on targeting therapy by exploiting the local overexpression of VCAM-1 at the site of brain metastases, and Part 2 of this thesis focuses on incorporating lysolipids into microbubble shells to enhance the delivery of small molecules across the blood brain barrier, it is perhaps interesting to note that there is a wealth of information from over two decades ago on how the presence of lysolipids upregulates the expression of VCAM-1.[551–557] Although nothing appears to have been published since then, it follows that combining both Parts of this thesis could lead to a synergistic feedback loop where microbubbles containing lysolipid and anti-VCAM-1 reach tumour sites, then further upregulate VCAM-1, causing more microbubbles to bind and so on. In the author's opinion, this is an avenue of research worthy of investigation.

7. Appendix

7.1. Further effects of 10PC on cell membrane fluidity

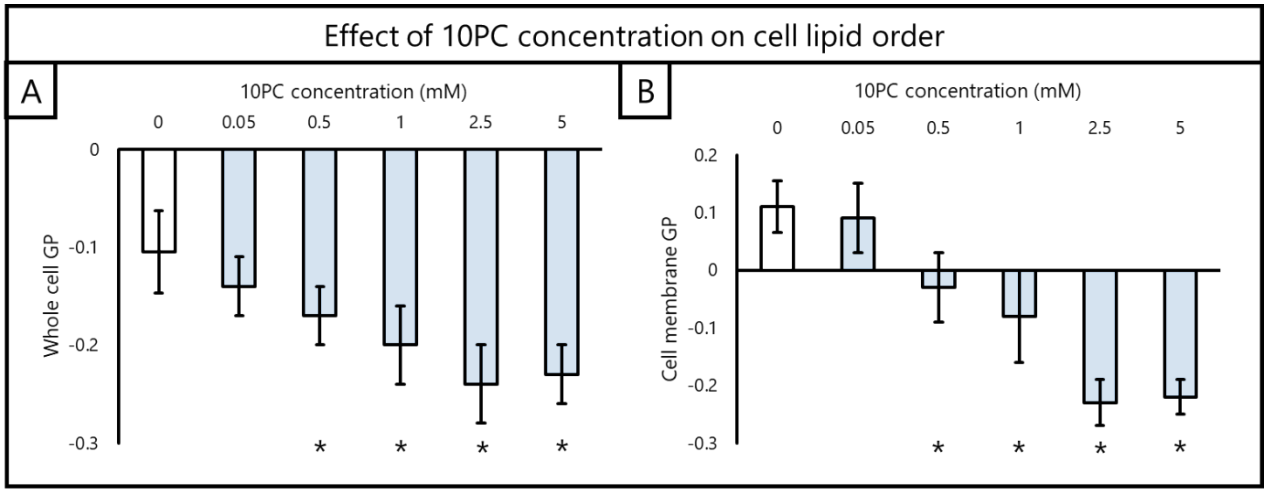

Figure 7.1.1: Effect of 10PC concentration on A-549 cell lipid order. Cells were exposed to 10PC at a range of concentrations at 37°C for 90 s prior to spectral imaging with C-Laurdan. Results are split into the GP of the whole cell (A) and the segmented cell membranes (B). For both, all concentrations above 0.5mM significantly reduced GP when compared to the control.

In Section 4.5.1, it was shown that 10PC significantly reduces the lipid order of cells, an effect that was not observed for the other hydrocarbon chain lengths. Figure 7.1.1 shows that this effect is concentration dependant. At all concentrations tested above 0.5mM, 10PC is capable of significantly reducing both cell membrane and whole cell GP in 90 seconds. This effect appears to saturate above 2.5 mM.

The permeability of cells exposed to 10PC was evaluated using a propidium iodide (PI) and calcein-AM assay performed by confocal fluorescence microscopy (Figure 7.1.2). The permeabilisation of cell membranes correlates with the lipid disordering induced by 10PC (Figure 7.1.1), and exhibits the same concentration dependence and threshold levels for effect onset and saturation.

Figure 7.1.3 shows cells were labelled with both C-Laurdan for spectral imaging of lipid order and PI and Calcein-AM for measuring permeabilisation after 90 seconds of 0.5mM 10PC exposure. These results show that only the cells that have their membranes fluidised (lipids disordered) are permeabilised. This makes it clear that in the concentrations at which 10PC has an effect on cell lipid

order, it also completely permeabilises the cell membrane. 10PC is also cytotoxic (measured by MTS assay[3]) at these exposure conditions.

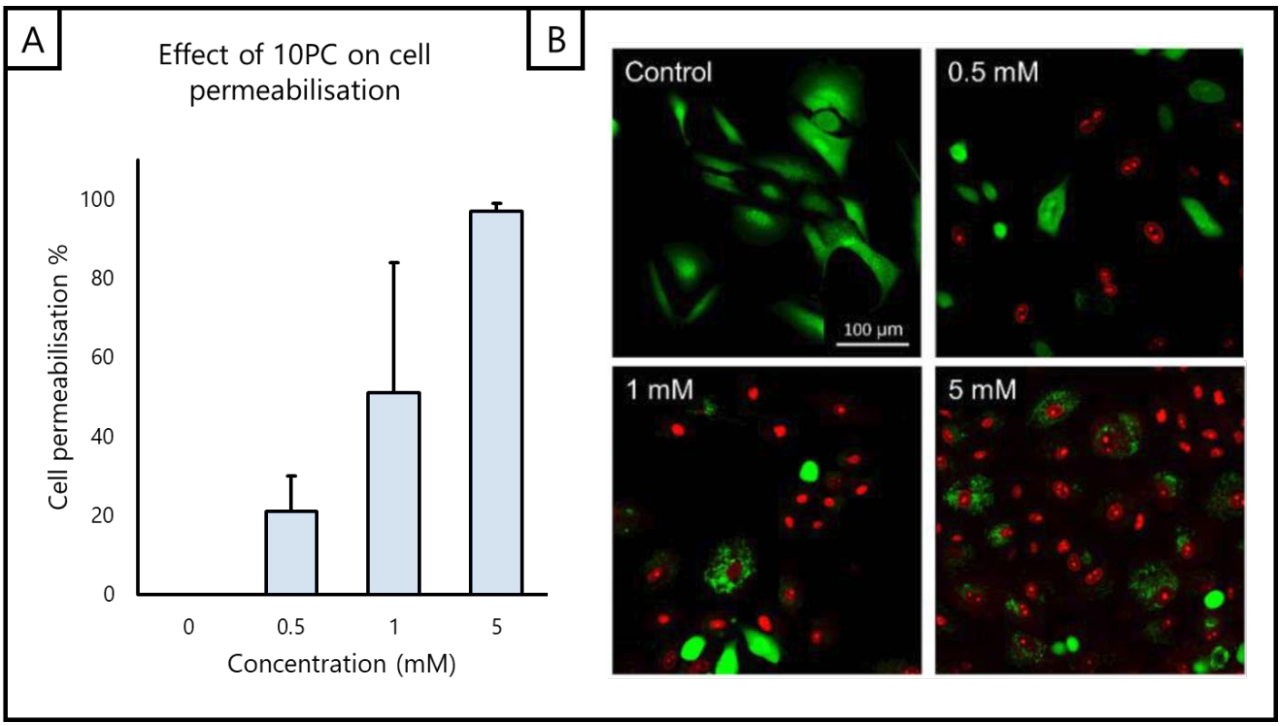

Figure 7.1.2: The effect of 10PC on A-549 cell permeability. (A) The percentage of cells permeabilized by as the concentration of 10PC is increased, measured by Propidium Iodide uptake. (B) Representative fluorescence microscopy images of cells stained with Calcein-AM (green) and Propidium Iodide (red) exposed to 10PC at 0, 0.5, 1, and 5 mM.

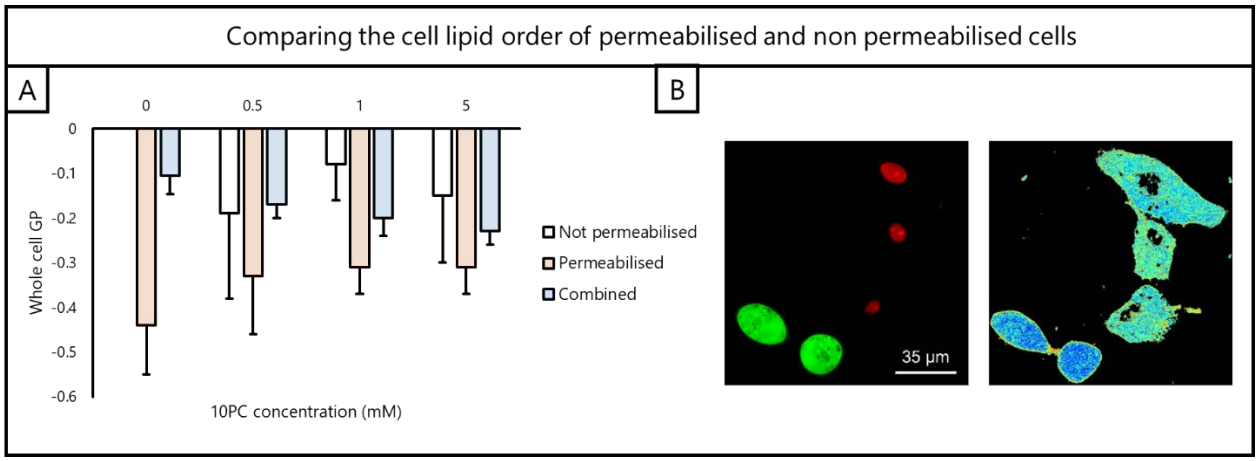

Figure 7.1.3: This plot combines the findings of Figure 7.1.1 and Figure 7.1.2. A-549 cells permeabilised by 10PC also exhibit modulated lipid order. Cells were exposed to 10PC at 37°C for ~90 s prior to spectral imaging with C-Laurdan and fluorescence microscopy with Calcein-AM and Propidium Iodide (PI). (A) Whole cell GP at different 10PC concentrations for permeabilised (PI staining) and non-permeabilised (Calcein-AM staining only) respectively. (B) Some representative cells imaged by fluorescence microscopy with Calcein-AM (green) and PI (red), and spectral imaging with C-Laurdan.

Therefore, 10PC was not taken forward as a candidate lipid for modulating the fluidity of cell membranes. As one of the key aims of this research is enhancing drug delivery in the ultrasound focus, whilst reducing off-target side effects, 10PC is far from ideal, especially when compared to some of the other lipids tested elsewhere in this Chapter, particularly 16-lyso-PC (Section 4.8.3).

7.2. Further effects of 14PC on cell membrane fluidity

It was found that a 10 minute exposure of 14PC to A-549 cells significantly ($p < 0.05$) reduced membrane lipid order at both 5mM and 12.5mM (Figure 7.2.1). However, this decrease was smaller than that observed with 12PC (Figure 4.5.3), and the 14PC exposure did not significantly affect the whole cell GP over the same time period. Therefore, 12PC was chosen, along with 16-lyso-PC (Section 4.5.3), as a candidate lipid for modulating cell membrane fluidity in the sonoporation experiments in Section 4.6.

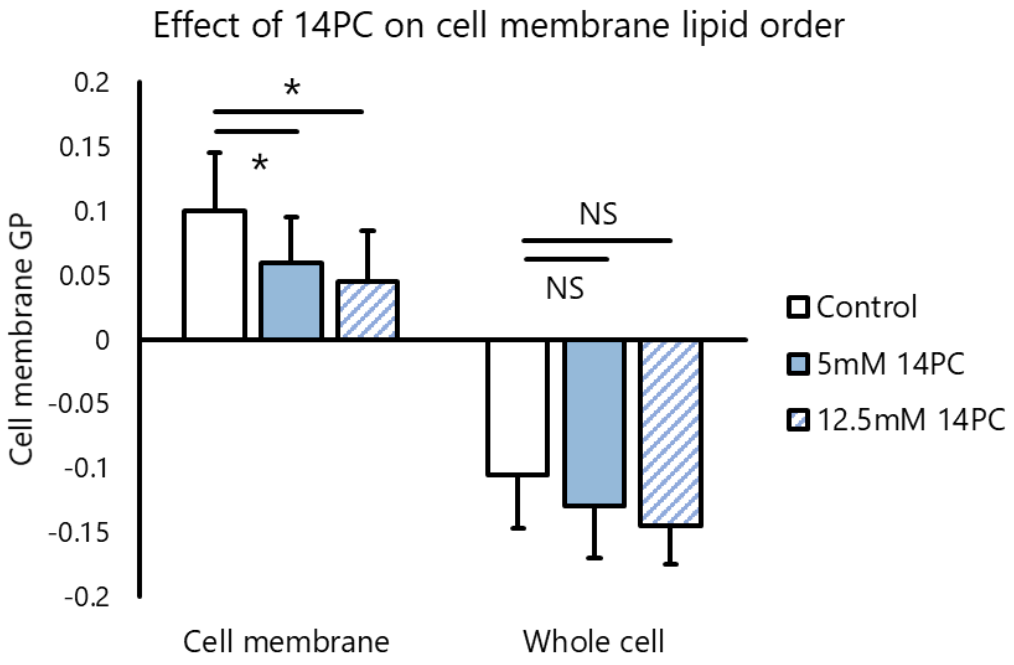

Figure 7.2.1: Effect of 14PC on A-549 lipid order. A-549 cells were exposed to 14PC at either 5 mM or 12.5 mM at 37°C for 10 minutes and measured using C-Laurdan and spectral imaging. Cell membrane results are significant ($p < 0.05$) but whole cell results are not.

7.3. Stability of Lyso-MBs

Figure 7.3.1 shows how the concentration and diameter of both Control-MBs and Lyso-MBs change over time relative to their initial values. Figure 7.3.1A shows that the concentration of both Control-MBs and Lyso-MBs decreases over time and Figure 7.3.1B shows that their diameter begins to increase. These two plots combined indicate that the Control-MBs coalesced over time, whereas Lyso-MBs do not over the timescales tested. As such, all experiments were conducted between 0 and 4 hours after MB manufacture.

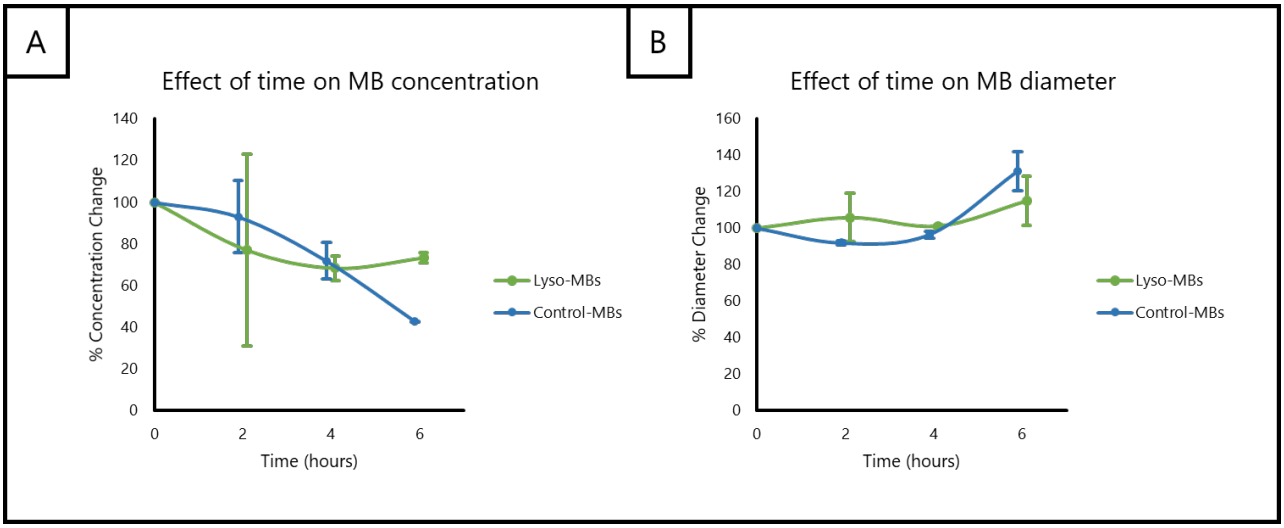

Figure 7.3.1: Stability of Control-MBs and Lyso-MBs as indicated by their diameter and concentration changes over time. Data points have been shifted slightly relative to the axes to allow easier visualisation of error bars.

7.4. Lysolipid transfer between microbubbles and cells

7.4.1. Introduction

A fluorescently tagged lysolipid was also used to allow direct visualisation of any lipid transfer between MBs and cells. However, it is not included in the main body of the thesis due to the differences between the fluorescent lysolipid used (18:1 NBD-lyso-PE) and (16-lyso-PC). These differences are due to commercial availability. The predicted effects of these differences on MB-cell transfer and cell membrane fluidity are:

- **Chain length:** Lipids with a longer hydrocarbon chain length transfer less readily to cell membranes.[484] The 18 carbon version of 16-lyso-PC (18-lyso-PC) would be expected to have less effect on the cell membrane fluidity than 16-lyso-PC due to the greater similarity in lipid chain length to endogenous lipids and based on the cell lipid order for different chain length lipids in Section 4.9.
- **Headgroup:** 18:1 NBD-lyso-PE has a phosphotatidylethanolamine (PE) head rather than the phosphotidylcholine (PC) headgroup that all of the other lipids analysed in this Chapter have. A lysolipid with a PE head would be expected to have a lower effect on cell membrane fluidity than a lysolipid with a PC head (and equivalent chain length) due to a PE head being smaller than a PC head (causing a reduction in the conical nature of the lysolipid).
- **Fluorescent tag:** The NBD molecule tagged to 18:1 NBD-lyso-PE may have affected both lipid transfer and cell membrane fluidity. However, fluorescently tagging the lipid is the only way to directly observe lipid transfer and so any influence of the fluorophore is unavoidable. Previous work that has reported lipid transfer[280] actually observed transfer of DiI, not the lipid itself. Transfer of DiI does not guarantee lipid transfer.
- **Saturation:** 18:1 NBD-lyso-PE is an unsaturated lipid (with a carbon-carbon double bond in its hydrocarbon chain) whereas all other lipids in this Chapter are saturated (do not have the carbon-carbon double bond). This double bond creates a kink in the hydrocarbon chain and

removes the 'conical' shape. Unsaturated lipids have higher transfer rates and cause a greater increase in cell membrane fluidity than saturated lipids[558,559] due to their irregular shapes. Therefore, 18:1 NBD-lyso-PE would definitely have a higher lipid transfer rate than 18:0 NBD-lyso-PE (the saturated equivalent) but due to the other differences outlined here, it is uncertain whether the transfer rates would be greater or lower than those of 16-lyso-PC.

Despite the clear differences between 18:1 NBD-lyso-PE and the lysolipid (16-lyso-PC) used in Chapters 4 and 5 of this thesis, 18:1 NBD-lyso-PE is the only commercially available fluorescently tagged lysolipid. The lipid transfer results in this Section are the first time to the author's knowledge that a fluorescently tagged lipid has been observed to transfer between MBs and cells in response to ultrasound.

7.4.2. Methods

A-549 human lung cancer cells were cultured in 6.5mm Transwell plates (Corning, Germany) as detailed in Section 4.6.4. After washing once with PBS, 100µl of NBD-lyso-MBs (at 1 x 10^8 MBs per ml, outlined in Section 4.5.1 and manufactured as in Section 4.6.2) was added to the cells. This configuration was then exposed to ultrasound (180kPa PRP, 500kHz, CW, 60 seconds exposure) from a H107 transducer (Sonic Concepts, US) in the setup shown in Figure 7.4.1.

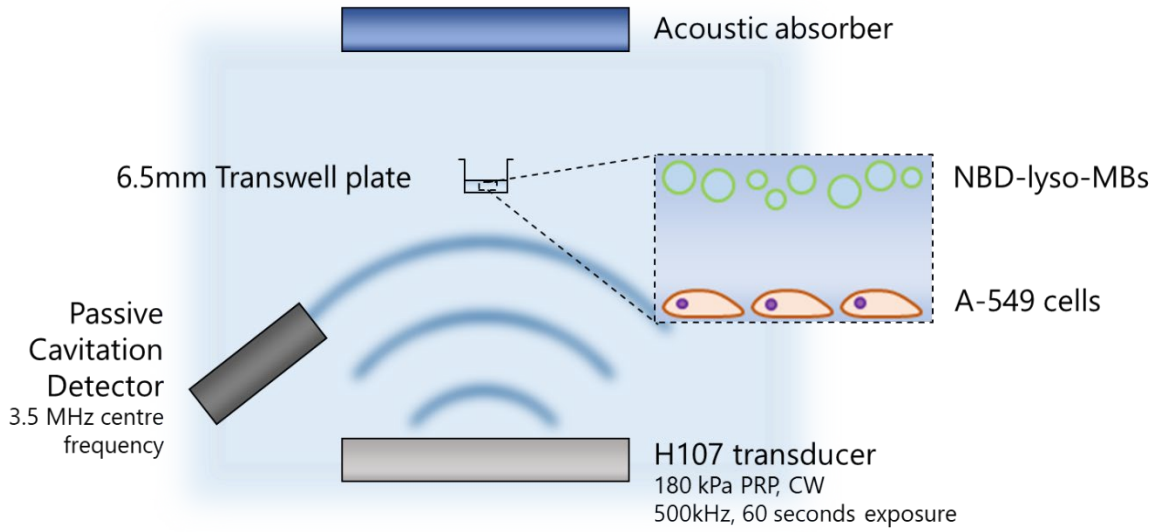

Figure 7.4.1: Diagram of the ultrasound setup used in the lipid transfer experiments. Cells were exposed to NBD-lyso-MBs in a 6.5mm Transwell plate, washed twice with PBS and then stained with CellMask Deep Red plasma membrane stain. To quantify transfer of NBD tagged lysolipid from the MBs to the cell membrane, cells were subsequently imaged using dual wavelength fluorescence microscopy.

Cells were then washed twice more with PBS before being incubated for ten minutes with CellMask Deep Red Plasma Membrane Stain (Thermofisher Scientific, US). Dual wave fluorescence microscopy on a Zeiss LSM 780 confocal microscope (Carl Zeiss AG, Germany) allowed imaging of both the CellMask in the cell membranes and any NBD-lyso-PE present in the cell membranes. The differences between the fluorescent lysolipid used and the lysolipid used elsewhere in this Chapter are outlined in Section 4.2.1. Images were collected of cells before exposure to NBD-lyso-MBs, after exposure to just NBD-lyso-MBs and exposure to NBD-lyso-MBs plus ultrasound. All images were captured with the same gain and exposure times, and were captured in the plane of maximum green fluorescence. Quantification of the proportion of cells with visible uptake of NBD-lyso-PE was carried out by eye. Quantification of the area and the average NBD fluorescence intensity of each cell was calculated by manually segmenting each cell in ImageJ.

7.4.3. MB washing

MBs were washed using the same protocol as detailed in 2.2.4. NBD-lyso-MBs were washed prior to lipid transfer experiments to remove free fluorescent lysolipid from solution. No other MBs in this Chapter were washed.

7.4.4. Verification of lysolipid incorporation into MB shells

NBD-lyso-MBs were prepared via the incorporation of 18:1 NBD lyso-PE into the MB shell as described in Section 4.3.1. Figure 7.4.2 shows washed NBD-lyso-MBs imaged using both brightfield and fluorescence microscopy on a Nikon Eclipse Ti microscope (Nikon, USA) at 4x and 20x. These images show that every MB has a uniform distribution in the shell and the NBD tagged lipid is only in the MB shells. The fact that the fluorescence was visible after washing provides strong evidence for the incorporation of the lipid into the bubble shell; washing MBs where the

fluorophore was not bound to the MB (in Chapter 2) removes all fluorescence from the MBs such that they are indistinguishable from background.

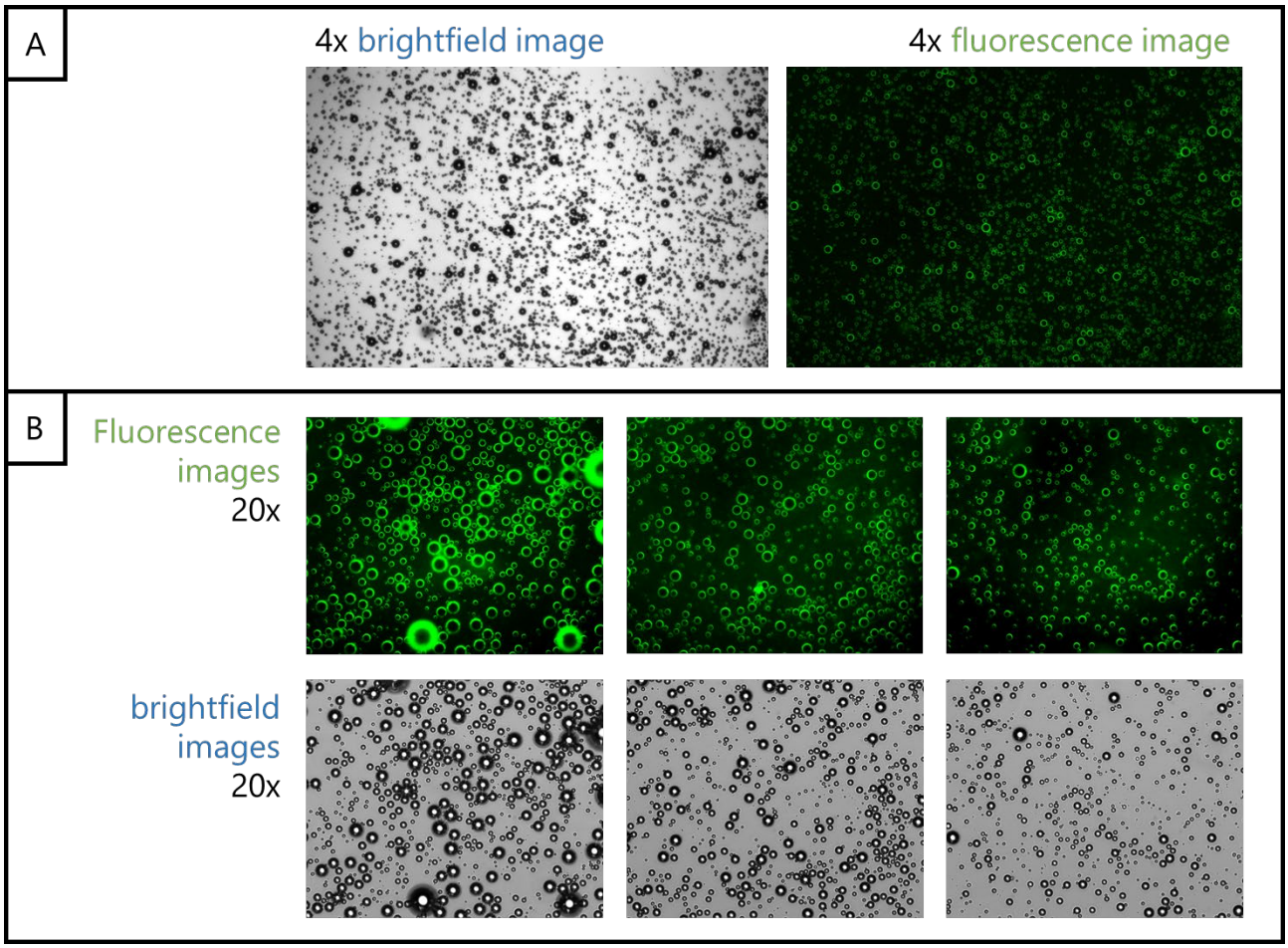

Figure 7.4.2: Brightfield and fluorescence microscopy images of NBD-lyso-MBs after washing. The NBD can clearly be seen incorporated into the bubble shell.

7.4.5. NBD-lyso-MB properties

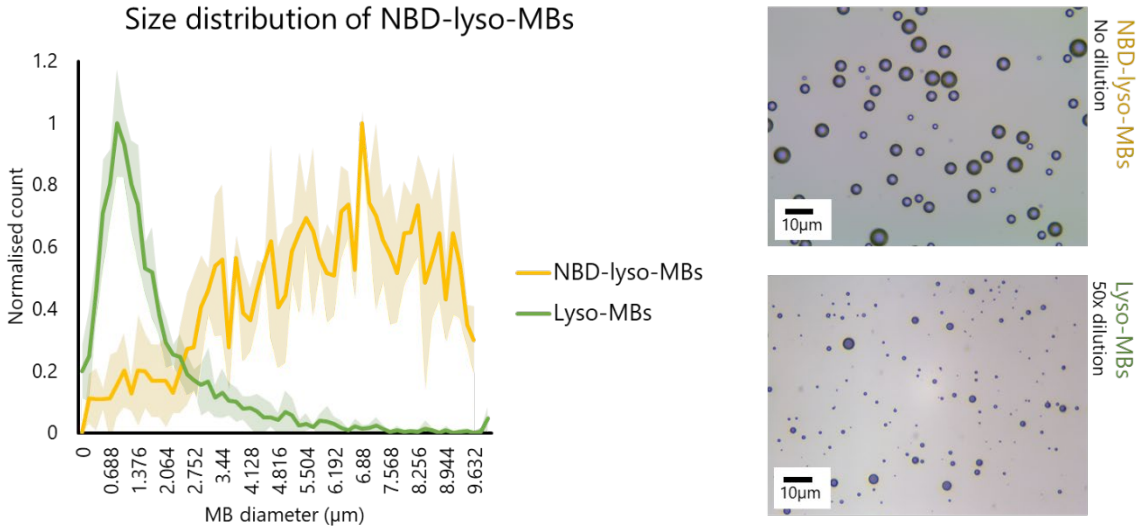

Figure 7.4.3: Size distribution and representative microscope images of NBD-lyso-MBs and lyso-MBs. The images, captured at 40x, show undiluted NBD-lyso-MBs and lyso-MBs that have been diluted by a factor of 50 prior to imaging.

As unsaturated lipids have a kink in one of their hydrocarbon chains (arising from the carbon-carbon double bond), monolayers or bilayers formed by unsaturated lipid molecules are much less tightly packed, and therefore less stable. As 18:1 NBD-lyso-PE, the fluorescent lysolipid used in this Section, is unsaturated, the NBD-lyso-MBs were larger and less concentrated than lyso-MBs (Figure 7.4.3). It is worth noting that this size difference almost certainly arises from the unsaturated nature of these lipids and is not due to either the NBD (fluorescent tag) or the PE headgroup; the MBs used for *in vitro* experiments in Chapter 2 were formed with 1% NBD-DSPE (18:0 NBD-PE), a saturated lipid, exhibited an indistinguishable size distribution from that of lyso-MBs.

7.4.6. Lipid transfer to cell membranes

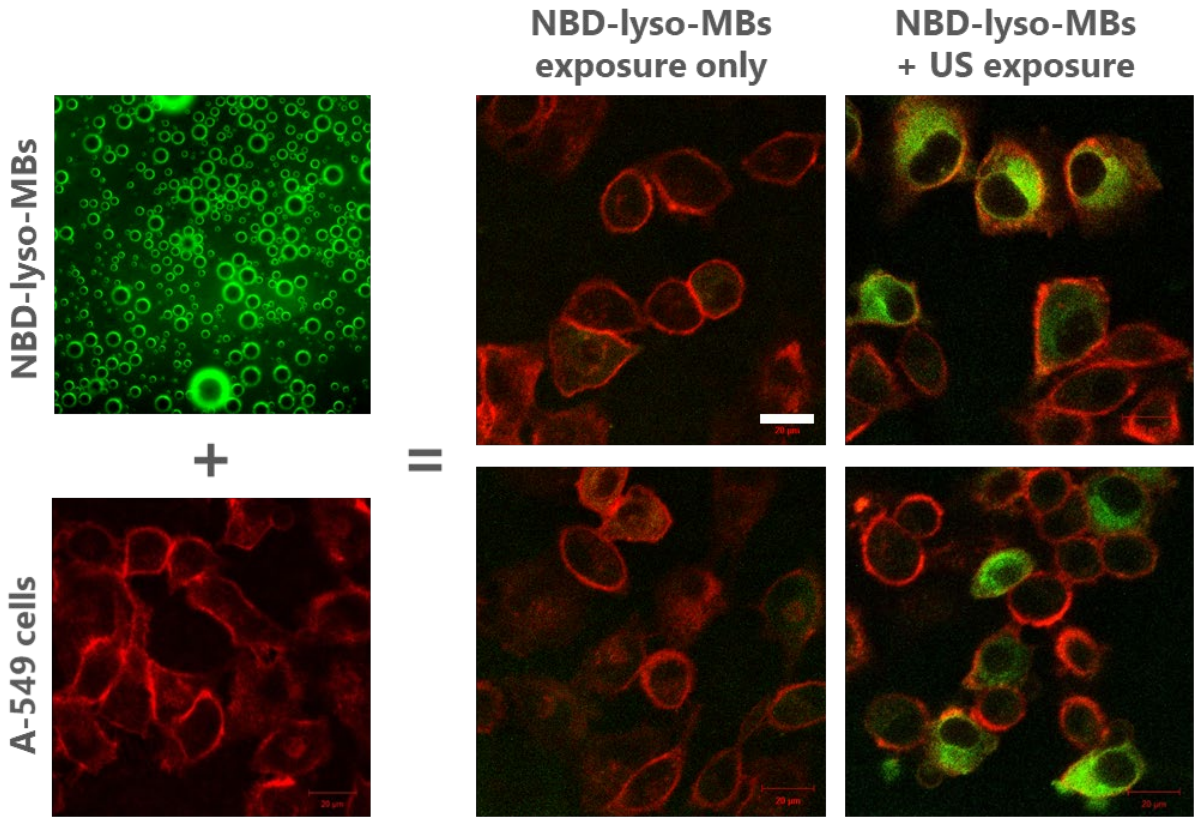

Figure 7.4.4: Representative images showing cells after exposure to either NBD-lyso-MBs or NBD-lyso-MBs plus US. Cell membranes are stained in Cellmask Deep Red (red) and the MBs have NBD-lyso-PE in the shell (green). N = 3 for both MBs and MBs + US conditions. Scale bar = 20µm.

In this experiment, cells and NBD-lyso-MBs were exposed to ultrasound (US) to investigate whether the fluorescent lysolipid in the MBs would transfer visibly to the cell (as detailed in Section 7.4.2). After US exposure, the cells were washed with PBS to remove any extracellular fluorescent lipids and then incubated with CellMask Deep Red plasma membrane stain.

Figure 7.4.4 shows cells imaged in dual wavelength microscopy before exposure to NBD-lyso-MBs, after exposure to just NBD-lyso-MBs and exposure to NBD-lyso-MBs plus US (180kPa PNP, 500kHz, CW, 60 seconds exposure). All of the images were captured with the same gain and exposure times, and were captured in the plane of maximum green fluorescence. From these images, it is clear that after exposure to US, NBD-lyso-PE had been incorporated sufficiently into the cell membranes to resist washing. It appears that only certain cells took up NBD-lyso-PE, and that those that did, appeared to have widespread incorporation across the whole membrane.

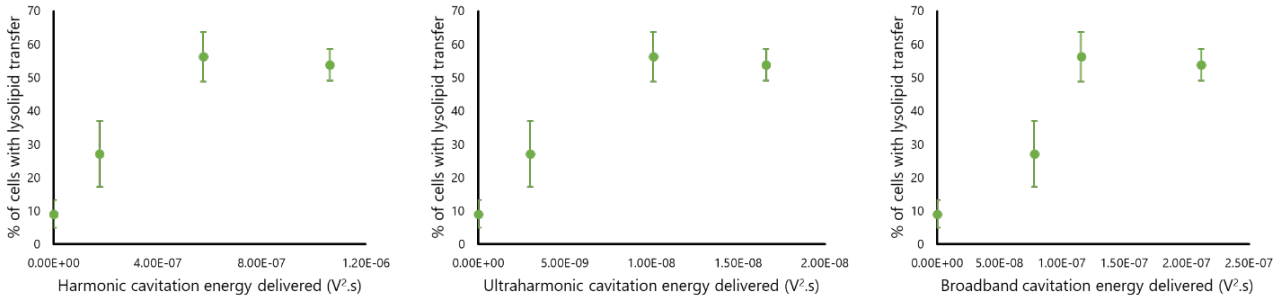

Figure 7.4.5: The percentage of A-549 cells with visible NBD-lyso-PE transfer to the cell membrane plotted as a function of the harmonic, ultraharmonic and broadband energies in the acoustic emissions for each sample.

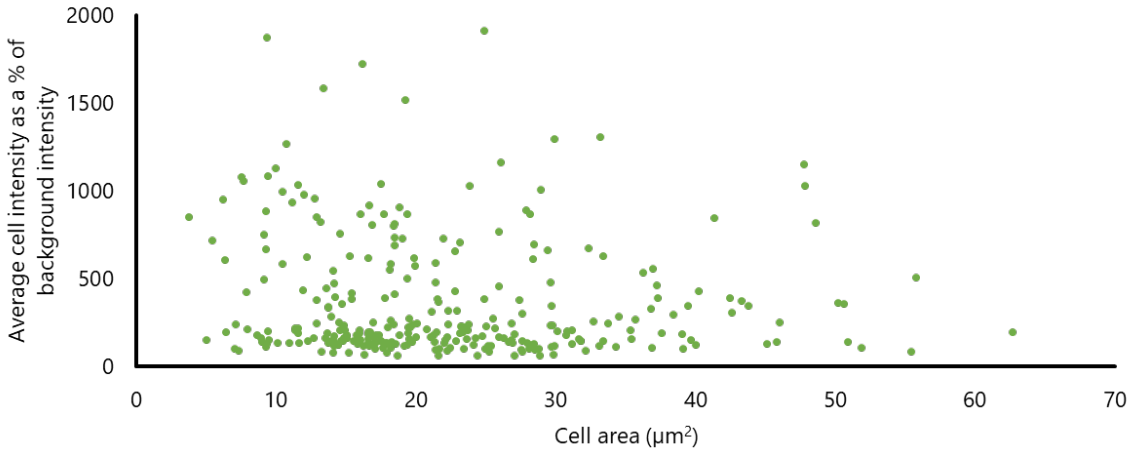

Figure 7.4.6: The relationship between cell area and the fluorescence intensity of NBD in the cell. Each data point is a single cell (n = 300).

Even though each sample in the MBs + US group (n = 3) experienced identical US exposure, they each underwent different amounts of cavitation (as shown by the harmonic, ultraharmonic and broadband energies in the acoustic emissions). Figure 7.4.5 shows the relationship between ultraharmonic cavitation energy delivered and the percentage of cells with visible NBD-lyso-PE uptake. This graph shows that as the cavitation energy delivered increases, the percentage of cells that incorporated NBD-lyso-PE also increased.

The results from Figure 7.4.4 and Figure 7.4.5 combine to indicate that lipid transfer from MB shells to cell membranes both occurs and is enhanced by US. These results also indicate that such transfer is not uniform between proximal cells, something that likely arises from non-spatially uniform cavitation events such as microstreaming.[4]

Figure 7.4.6 shows the relationship between the cell area and the level of NBD fluorescence in the cell. NBD fluorescence is quantified by the calculating the average intensity in the green fluorescence channel over the area of each cell. It is plotted as a percentage of the background intensity to account for slight variations in background fluorescence between images. This plot shows that there is a negligible relationship between cell size and uptake of NBD-lyso-PE, and that the cells can reasonably be seen to separate into two categories in accordance with the visual observations of the images in Figure 7.4.4. The first group, with no observable NBD-lyso-PE uptake when compared to background, can be seen to cluster in a band at the bottom of Figure 7.4.6. The second, with varying levels of fluorescence, can be seen distributed in Figure 7.4.6, with an average NBD fluorescence intensity ranging from ~500% to ~2000% the fluorescent intensity of the image background. It is these cells that, by expressing visibly different fluorescence levels after washing with PBS, are thought to have taken up NBD-lyso-PE.

7.4.7. Lysolipid transfer summary

A fluorescent, unsaturated lysolipid (18:1 NBD-lyso-PE) was used to investigate lipid transfer between MB shells and cell membranes. The findings of Section 7.4 can be summarised as:

- Despite the fluorescent lysolipid used being unsaturated, it was able to incorporate into the shells of MB. As the lysolipid used elsewhere in this Chapter is saturated, it is highly likely that it is also able to incorporate into MB shells.
- This fluorescent lysolipid transferred to the cell membrane. As the MBs were washed (to remove lipids not in the MB shell), the cells were washed before imaging and imaging was carried out 30 minutes after US exposure, these lysolipids are considered to have stably incorporated into the cell membranes over timescales relevant for clinical translation.
- These MBs are capable of cavitating at low ultrasound pressures (180kPa PNP, 500kHz, CW). The more cavitation a cell sample experienced (as measured by broadband, harmonic and ultraharmonic emissions), the higher the lipid transfer.
- The lipid transfer is highly spatially variable. It is hypothesised that this is linked to spatially variable cavitation effects, for example acoustic streaming of microbubbles (microstreaming).

Despite the differences between the fluorescent lysolipid used here and the lysolipid used in Chapters 4 and 5, these results indicate that lipids are capable of transferring from microbubble shells to cell membranes. Previous work has shown transfer of a lipophilic dye between microbubble shells and cell membranes, but this is the first time (to the author's knowledge) that transfer of a fluorescently tagged lipid has been observed in this way.

8. References

1. Vince, O. *et al.* Microbubbles Containing Lysolipid Enhance Ultrasound-Mediated Blood–Brain Barrier Breakdown In Vivo. *Adv. Healthc. Mater.* **10**, 2001343 (2021).
2. Gowers, G.-O. F. *et al.* Entirely Off-Grid and Solar-Powered DNA Sequencing of Microbial Communities during an Ice Cap Traverse Expedition. *Genes (Basel).* **10**, 902 (2019).
3. Aron, M., Vince, O., Gray, M., Mannaris, C. & Stride, E. Investigating the role of lipid transfer in microbubble mediated drug delivery. *Langmuir* acs.langmuir.9b02404 (2019) doi:10.1021/acs.langmuir.9b02404.
4. Pereno, V. *et al.* Layered acoustofluidic resonators for the simultaneous optical and acoustic characterisation of cavitation dynamics, microstreaming, and biological effects. *Biomicrofluidics* **12**, (2018).
5. WHO World Cancer Report 2014. *World Heal. Organ.* (2014).
6. Steeg, P. S. Tumor metastasis: Mechanistic insights and clinical challenges. *Nat. Med.* **12**, 895–904 (2006).
7. Institute, N. C. Metastatic Cancer. https://www.cancer.gov/types/metastatic-cancer.
8. Nathoo, N., Chahlavi, A. & Barnett, G. H. Pathobiology of brain metastases. *J Clin Pathol* **58**, 237–242 (2005).
9. Talmadge, J. E. & Fidler, I. J. AACR Centennial Series: The Biology of Cancer Metastasis: Historical Perspective. *AACR Centen. Ser.* **70**, 5649–5669 (2010).
10. Xie, K. *et al.* Mouse models of metastatic pancreatic adenocarcinoma. *Int. J. Pancreatol.* **29**, 25–35 (2001).
11. Shi, Q. & Xie, K. Experimental animal models of pancreatic cancer (review). *Int. J. Oncol.* **17**, 217–25 (2000).
12. Vaupel, P., Kallinowski, F. & Okunieff, P. Blood flow, oxygen and nutrient supply, and metabolic microenvironment of human tumors: a review. *Cancer Res.* **49**, 6449–65 (1989).
13. Boucher, Y., Baxter, L. T. & Jain, R. K. Interstitial pressure gradients in tissue-isolated and subcutaneous tumors: implications for therapy. *Cancer Res.* **50**, 4478–84 (1990).
14. Christiano, Yoshida, Dubauskas, Sokoloff & Rinker-Schaeffer. Development of markers of prostate cancer metastasis. Review and perspective. *Urol. Oncol.* **5**, 217–223 (2000).
15. Poste, G. & Fidler, I. J. The pathogenesis of cancer metastasis. *Nature* vol. 283 139–146 (1980).
16. MacDonald, N. J. & Steeg, P. S. Molecular basis of tumour metastasis. *Cancer Surv.* **16**, 175–99 (1993).
17. Nicolson, G. L. *et al.* Brain metastasis: role of trophic, autocrine, and paracrine factors in tumor invasion and colonization of the central nervous system. *Curr. Top. Microbiol. Immunol.* **213 (Pt 2)**, 89–115 (1996).
18. Yano, S. *et al.* Expression of Vascular Endothelial Growth Factor Is Necessary but not Sufficient for Production and Growth of Brain Metastasis. *Cancer Res.* **59**, 99–106 (2000).
19. Kienast, Y. *et al.* Real-time imaging reveals the single steps of brain metastasis formation. *Nat. Med.* **16**, 116–122 (2010).
20. Weiss, L. *et al.* Haematogenous metastatic patterns in colonic carcinoma: an analysis of 1541

necropsies. *J. Pathol.* **150**, 195–203 (1986).

21. Eichler, A. F. *et al.* The biology of brain metastases-translation to new therapies. (2011) doi:10.1038/nrclinonc.2011.58.
22. Lorger, M. & Felding-Habermann, B. Capturing changes in the brain microenvironment during initial steps of breast cancer brain metastasis. *Am. J. Pathol.* **176**, 2958–71 (2010).
23. Carbonell, W. S., Ansorge, O., Sibson, N., Muschel, R. & Santoro, S. The Vascular Basement Membrane as "Soil" in Brain Metastasis. *PLoS One* **4**, e5857 (2009).
24. Yamamoto, M., Ueno, Y., Hayashi, S. & Fukushima, T. The role of proteolysis in tumor invasiveness in glioblastoma and metastatic brain tumors. *Anticancer Res.* **22**, 4265–8.
25. Vassalli, J. D., Sappino, A. P. & Belin, D. The plasminogen activator/plasmin system. *J. Clin. Invest.* **88**, 1067–1072 (1991).
26. Bos, P. D. *et al.* Genes that mediate breast cancer metastasis to the brain. *Nature* **459**, 1005–9 (2009).
27. Lorger, M., Krueger, J. S., O'Neal, M., Staflin, K. & Felding-Habermann, B. Activation of tumor cell integrin alphavbeta3 controls angiogenesis and metastatic growth in the brain. *Proc. Natl. Acad. Sci. U. S. A.* **106**, 10666–71 (2009).
28. Felding-Habermann, B. *et al.* Integrin activation controls metastasis in human breast cancer. *Proc. Natl. Acad. Sci. U. S. A.* **98**, 1853–8 (2001).
29. Hess, K. R. *et al.* Metastatic patterns in adenocarcinoma. *Cancer* **106**, 1624–1633 (2006).
30. Patel, J. K., Didolkar, M. S., Pickren, J. W. & Moore, R. H. Metastatic pattern of malignant melanoma. A study of 216 autopsy cases. *Am. J. Surg.* **135**, 807–10 (1978).
31. Paget, S. The disribution of secondary growths in cancer of the breast. *Lancet* **133**, 571–573 (1889).
32. Duda, D. G. *et al.* Malignant cells facilitate lung metastasis by bringing their own soil. *Proc. Natl. Acad. Sci. U. S. A.* **107**, 21677–82 (2010).
33. Pasqualini, R. & Ruoslahti, E. Organ targeting in vivo using phage display peptide libraries. *Nature* **380**, 364–366 (1996).
34. Uehara, H. *et al.* Effects of blocking platelet-derived growth factor-receptor signaling in a mouse model of experimental prostate cancer bone metastases. *J. Natl. Cancer Inst.* **95**, 458–70 (2003).
35. Carmeliet, P. & Jain, R. K. Molecular mechanisms and clinical applications of angiogenesis. *Nature* **473**, 298–307 (2011).
36. Carmeliet, P. & Jain, R. K. Angiogenesis in cancer and other diseases. *Nature* vol. 407 249–257 (2000).
37. Folkman, J. Angiogenesis: An organizing principle for drug discovery? *Nat. Rev. Drug Discov.* **6**, 273–286 (2007).
38. Leenders, W. P. J. *et al.* Antiangiogenic therapy of cerebral melanoma metastases results in sustained tumor progression via vessel co-option. *Clin. Cancer Res.* **10**, 6222–30 (2004).
39. Chang, C. & Werb, Z. The many faces of metalloproteases: cell growth, invasion, angiogenesis and metastasis. *Trends Cell Biol.* **11**, S37 (2001).
40. Küsters, B. *et al.* Vascular Endothelial Growth Factor-A165 Induces Progression of Melanoma Brain Metastases without Induction of Sprouting Angiogenesis. *Cancer Res.* **62**, (2002).

41. Chambers, A. F., MacDonald, I. C., Schmidt, E. E., Morris, V. L. & Groom, A. C. Clinical targets for anti-metastasis therapy. *Adv. Cancer Res.* **79**, 91–121 (2000).

42. Fidler, I. J. Critical determinants of metastasis. *Semin. Cancer Biol.* **12**, 89–96 (2002).

43. Fidler, I. J. The role of the organ microenvironment in brain metastasis. *Semin. Cancer Biol.* **21**, 107–12 (2011).

44. Lin, Q. *et al.* Reactive astrocytes protect melanoma cells from chemotherapy by sequestering intracellular calcium through gap junction communication channels. *Neoplasia* **12**, 748–54 (2010).

45. Kim, S.-J. *et al.* Astrocytes upregulate survival genes in tumor cells and induce protection from chemotherapy. *Neoplasia* **13**, 286–98 (2011).

46. Fidler, I. J., Yano, S., Zhang, R.-D., Fujimaki, T. & Bucana, C. D. The seed and soil hypothesis: vascularisation and brain metastases. *Lancet. Oncol.* **3**, 53–7 (2002).

47. Bullitt, E. *et al.* Vessel tortuosity and brain tumor malignancy: A blinded study. in *Academic Radiology* vol. 12 1232–1240 (2005).

48. FEIGIN, I., ALLEN, L. B., LIPKIN, L. & GROSS, S. W. The endothelial hyperplasia of the cerebral blood vessels with brain tumors, and its sarcomatous transformation. *Cancer* **11**, 264–77.

49. Yuan, F. *et al.* Vascular permeability and microcirculation of gliomas and mammary carcinomas transplanted in rat and mouse cranial windows. *Cancer Res.* **54**, 4564–8 (1994).

50. Jain, R. K. Normalization of tumor vasculature: An emerging concept in antiangiogenic therapy. *Science* vol. 307 58–62 (2005).

51. Fukumura, D., Duda, D. G., Munn, L. L. & Jain, R. K. Tumor microvasculature and microenvironment: Novel insights through intravital imaging in pre-clinical models. *Microcirculation* vol. 17 206–225 (2010).

52. Delattre, J. Y., Krol, G., Thaler, H. T. & Posner, J. B. Distribution of brain metastases. *Arch. Neurol.* **45**, 741–4 (1988).

53. Osborn, A. G. *Diagnostic imaging: Brain, Diagnostic Imaging Series*. (2004).

54. Potts, D. G., Abbott, G. F. & von Sneidern, J. V. National Cancer Institute study: evaluation of computed tomography in the diagnosis of intracranial neoplasms. III. Metastatic tumors. *Radiology* **136**, 657–64 (1980).

55. Lim, M. *et al.* Innovative therapeutic strategies for effective treatment of brain metastases. *International Journal of Molecular Sciences* vol. 20 (2019).

56. Markesbery, W. R., Brooks, W. H., Gupta, G. & Young, A. B. Treatment for Patients with Cerebral Metastases. *Arch. Neurol.* **35**, 754–756 (1978).

57. Langley, R. R. & Fidler, I. J. The Biology of Brain Metastasis. (2012) doi:10.1373/clinchem.2012.193342.

58. Nussbaum, E. S., Djalilian, H. R., Cho, K. H. & Hall, W. A. Brain metastases. Histology, multiplicity, surgery, and survival. *Cancer* **78**, 1781–8 (1996).

59. Patchell, R. Brain Metastases. *Handb. Neurol.* **25**, 135–149 (1997).

60. Posner, J. B. Management of brain metastases. *Rev. Neurol. (Paris).* **148**, 477–87 (1992).

61. Johnson, J. D. & Young, B. Demographics of brain metastasis. *Neurosurg. Clin. N. Am.* **7**, 337–44 (1996).

62. Davis, F. G., Dolecek, T. A., McCarthy, B. J. & Villano, J. L. Toward determining the lifetime occurrence of metastatic brain tumors estimated from 2007 United States cancer incidence data. *Neuro. Oncol.* **14**, 1171–1177 (2012).

63. Yamanaka, R. Medical management of brain metastases from lung cancer (Review). *Oncol. Rep.* **22**, 1269–1276 (2009).

64. Barnholtz-Sloan, J. S. *et al.* Incidence Proportions of Brain Metastases in Patients Diagnosed (1973 to 2001) in the Metropolitan Detroit Cancer Surveillance System. *J. Clin. Oncol.* **22**, 2865–2872 (2004).

65. Schouten, L. J., Rutten, J., Huveneers, H. A. M. & Twijnstra, A. Incidence of brain metastases in a cohort of patients with carcinoma of the breast, colon, kidney, and lung and melanoma. *Cancer* **94**, 2698–705 (2002).

66. Gavrilovic, I. T. & Posner, J. B. Brain metastases: epidemiology and pathophysiology. *J. Neurooncol.* **75**, 5–14 (2005).

67. Eichler, A. F. *et al.* The biology of brain metastases—translation to new therapies. *Nat. Rev. Clin. Oncol.* **8**, 344–56 (2011).

68. Loeffler, J. S., Patchell, R. & Sawaya, R. E. Treatment of metastatic cancer. in *Cancer: Principles and Practice of Oncology* (eds. DeVita, V. T. J., Hellman, S. & Rosenberg, S. A.) (Philadelphia: Lippincott-Raven Publishers; 1997, 1997).

69. Posner, J. B. No Title. in *Neurologic Complications of Cancer* 77–110 (FA Davis, 1995).

70. Paterson, A. H. G., Agarwal, M., Lees, A., Hanson, J. & Szafran, O. Brain metastases in breast cancer patients receiving adjuvant chemotherapy. *Cancer* **49**, 651–654 (1982).

71. Frisk, G. *et al.* Incidence and time trends of brain metastases admissions among breast cancer patients in Sweden. *Br. J. Cancer* **106**, 1850–1853 (2012).

72. Smedby, K. E., Brandt, L., Bäcklund, M. L. & Blomqvist, P. Brain metastases admissions in Sweden between 1987 and 2006. *Br. J. Cancer* **101**, 1919–1924 (2009).

73. Pelletier, E. M., Shim, B., Goodman, S. & Amonkar, M. M. Epidemiology and economic burden of brain metastases among patients with primary breast cancer: Results from a US claims data analysis. *Breast Cancer Res. Treat.* **108**, 297–305 (2008).

74. Svokos, K. A., Salhia, B. & Toms, S. A. Molecular biology of brain metastasis. *Int. J. Mol. Sci.* **15**, 9519–9530 (2014).

75. Chang, E. L. *et al.* A Pilot Study Of Neurocognitive Function In Patients With One To Three New Brain Metastases Initially Treated With Stereotactic Radiosurgery Alone. *Neurosurgery* **60**, 277–284 (2007).

76. Mehta, M. P. *et al.* Survival and neurologic outcomes in a randomized trial of motexafin gadolinium and whole-brain radiation therapy in brain metastases. *J. Clin. Oncol.* **21**, 2529–36 (2003).

77. Siu, T. L., Jeffree, R. L. & Fuller, J. W. Current strategies in the surgical management of cerebral metastases: an evidence-based review. *J. Clin. Neurosci.* **18**, 1429–34 (2011).

78. Taggar, A. *et al.* Survival was Significantly Better with Surgical/Medical/Radiation Co-interventions in a Single-Institution Practice Audit of Frameless Stereotactic Radiosurgery. *Cureus* **8**, e612 (2016).

79. Lamba, N. *et al.* Stereotactic radiosurgery versus whole-brain radiotherapy after intracranial metastasis resection: a systematic review and meta-analysis. *Radiat. Oncol.* **12**, 106 (2017).

80. Bartsch, R., Berghoff, A. S. & Preusser, M. Optimal management of brain metastases from

breast cancer: Issues and considerations. *CNS Drugs* vol. 27 121–134 (2013).

81. Pessina, F. *et al.* Role of Surgical Resection in Patients with Single Large Brain Metastases: Feasibility, Morbidity, and Local Control Evaluation. *World Neurosurg.* **94**, 6–12 (2016).

82. Salvati, M. *et al.* Multiple brain metastases: a surgical series and neurosurgical perspective. *Neurol. Sci.* **39**, 671–677 (2018).

83. Jung, J. *et al.* Discordances in ER, PR, and HER2 between primary breast cancer and brain metastasis. *J. Neurooncol.* **137**, 295–302 (2018).

84. Kaidar-Person, O. *et al.* Discrepancies between biomarkers of primary breast cancer and subsequent brain metastases: an international multicenter study. *Breast Cancer Res. Treat.* **167**, 479–483 (2018).

85. Cummings, M. *et al.* Single-Fraction Radiosurgery Using Conservative Doses for Brain Metastases: Durable Responses in Select Primaries With Limited Toxicity. *Neurosurgery* **83**, 437–444 (2018).

86. Suzuki, S., Inoue, T. & Ishido, K. Factors influencing local tumor control after Gamma Knife radiosurgery for intracranial metastases from breast cancer. *J. Clin. Neurosci.* **33**, 154–158 (2016).

87. Wolf, A. *et al.* Toward the complete control of brain metastases using surveillance screening and stereotactic radiosurgery. *J. Neurosurg.* **128**, 23–31 (2018).

88. Andrews, D. W. *et al.* Whole brain radiation therapy with or without stereotactic radiosurgery boost for patients with one to three brain metastases: phase III results of the RTOG 9508 randomised trial. *Lancet* **363**, 1665–1672 (2004).

89. Kocher, M. *et al.* Adjuvant whole-brain radiotherapy versus observation after radiosurgery or surgical resection of one to three cerebral metastases: results of the EORTC 22952-26001 study. *J. Clin. Oncol.* **29**, 134–41 (2011).

90. Robinet, G. *et al.* Results of a phase III study of early versus delayed whole brain radiotherapy with concurrent cisplatin and vinorelbine combination in inoperable brain metastasis of non-small-cell lung cancer: Groupe Francais de Pneumo- Cancerologie (GFPC) Protocol 95-1*. *Ann. Oncol.* **12**, 59–67 (2001).

91. Verger, E. *et al.* Temozolomide and concomitant whole brain radiotherapy in patients with brain metastases: a phase II randomized trial. *Int. J. Radiat. Oncol. Biol. Phys.* **61**, 185–91 (2005).

92. Lauko, A., Thapa, B., Venur, V. A. & Ahluwalia, M. S. Management of Brain Metastases in the New Era of Checkpoint Inhibition. *Current Neurology and Neuroscience Reports* vol. 18 (2018).

93. Tawbi, H. A. *et al.* Combined nivolumab and ipilimumab in melanoma metastatic to the brain. *N. Engl. J. Med.* **379**, 722–730 (2018).

94. Tran, T. T. *et al.* Complications associated with immunotherapy for brain metastases. *Curr. Opin. Neurol.* 1 (2019) doi:10.1097/WCO.0000000000000756.

95. Kodack, D. P., Askoxylakis, V., Ferraro, G. B., Fukumura, D. & Jain, R. K. Emerging Strategies for Treating Brain Metastases from Breast Cancer. *Cancer Cell* vol. 27 163–175 (2015).

96. Purandare, N. C. Inclusion of brain in FDG PET/CT scanning techniques in cancer patients: Does it obviate the need for dedicated brain imaging? *Indian J. Nucl. Med.* **26**, 64–6 (2011).

97. Schellinger, P. D., Meinck, H. M. & Thron, A. Diagnostic accuracy of MRI compared to

CCT in patients with brain metastases. *J. Neurooncol.* **44**, 275–81 (1999).

98. Suzuki, K. *et al.* Magnetic resonance imaging and computed tomography in the diagnoses of brain metastases of lung cancer. *Lung Cancer* **46**, 357–60 (2004).

99. Antoch, G. Whole-Body Dual-Modality PET/CT and Whole-Body MRI for Tumor Staging in Oncology. *JAMA* **290**, 3199 (2003).

100. Zhang, X. & Lam, E. Y. Superresolution reconstruction using nonlinear gradient-based regularization. *Multidimens. Syst. Signal Process.* **20**, 375–384 (2009).

101. Kennedy, J. A., Israel, O., Frenkel, A., Bar-Shalom, R. & Haim Azhari, H. Super-resolution in PET imaging. *IEEE Trans. Med. Imaging* **25**, 137–147 (2006).

102. Griffeth, L. K. *et al.* Brain metastases from non-central nervous system tumors: evaluation with PET. *Radiology* **186**, 37–44 (1993).

103. Rohren, E. M., Provenzale, J. M., Barboriak, D. P. & Coleman, R. E. Screening for Cerebral Metastases with FDG PET in Patients Undergoing Whole-Body Staging of Non–Central Nervous System Malignancy. *Radiology* **226**, 181–187 (2003).

104. Sarkiss, C. A. & Germano, I. M. Machine Learning in Neuro-Oncology: Can Data Analysis from 5,346 Patients Change Decision Making Paradigms? *World Neurosurg.* (2019) doi:10.1016/j.wneu.2019.01.046.

105. Lotan, E., Jain, R., Razavian, N., Fatterpekar, G. M. & Lui, Y. W. State of the Art: Machine Learning Applications in Glioma Imaging. *AJR. Am. J. Roentgenol.* **212**, 26–37 (2019).

106. Ainsworth, N. L. *et al.* Quantitative and textural analysis of magnetization transfer and diffusion images in the early detection of brain metastases. *Magn. Reson. Med.* **77**, 1987–1995 (2017).

107. Yin, G. *et al.* Predicting brain metastases for non-small cell lung cancer based on magnetic resonance imaging. *Clin. Exp. Metastasis* **34**, 115–124 (2017).

108. Serres, S. *et al.* Molecular MRI enables early and sensitive detection of brain metastases. *Proc. Natl. Acad. Sci. U. S. A.* **109**, 6674–9 (2012).

109. Zarghami, N. *et al.* Optimization of molecularly targeted MRI in the brain: empirical comparison of sequences and particles. *Int. J. Nanomedicine* **Volume 13**, 4345–4359 (2018).

110. Pankhurst, Q. A., Thanh, N. T. K., Jones, S. K. & Dobson, J. Progress in applications of magnetic nanoparticles in biomedicine. *J. Phys. D. Appl. Phys.* **42**, 224001 (2009).

111. Lübbe, A. S., Alexiou, C. & Bergemann, C. Clinical Applications of Magnetic Drug Targeting. *J. Surg. Res.* **95**, 200–206 (2001).

112. Rapoport, N. Y., Kennedy, A. M., Shea, J. E., Scaife, C. L. & Nam, K.-H. Controlled and targeted tumor chemotherapy by ultrasound-activated nanoemulsions/microbubbles. *J. Control. Release* **138**, 268–276 (2009).

113. Hill, C. & Carlisle, R. Achieving systemic delivery of oncolytic viruses. *Expert Opinion on Drug Delivery* vol. 16 607–620 (2019).

114. Ferguson, M. S., Lemoine, N. R. & Wang, Y. Systemic delivery of oncolytic viruses: hopes and hurdles. *Adv. Virol.* **2012**, 805629 (2012).

115. Miller, A. *et al.* Reporter gene imaging identifies intratumoral infection voids as a critical barrier to systemic oncolytic virus efficacy. *Mol. Ther. - Oncolytics* **1**, 14005 (2014).

116. Katakami, N. *et al.* Magnetic resonance evaluation of brain metastases from systemic malignances with two doses of gadobutrol 1.0 m compared with gadoteridol: a multicenter,

phase ii/iii study in patients with known or suspected brain metastases. *Invest. Radiol.* **46**, 411–8 (2011).

117. Nomoto, Y., Miyamoto, T. & Yamaguchi, Y. Brain metastasis of small cell lung carcinoma: comparison of Gd-DTPA enhanced magnetic resonance imaging and enhanced computerized tomography. *Jpn. J. Clin. Oncol.* **24**, 258–62 (1994).

118. Kazantsev, A. G. & Outeiro, T. F. Drug discovery for CNS disorders: from bench to bedside. *CNS Neurol. Disord. Drug Targets* **9**, 668 (2010).

119. Gabathuler, R. Approaches to transport therapeutic drugs across the blood-brain barrier to treat brain diseases. *Neurobiol. Dis.* **37**, 48–57 (2010).

120. Dhankhar, R. *et al.* Advances in novel drug delivery strategies for breast cancer therapy. *Artif. Cells. Blood Substit. Immobil. Biotechnol.* **38**, 230–49 (2010).

121. Maeda, H. & Matsumura, Y. A new concept for macromolecular therapeutics in cancer chemotherapy: mechanism of tumoritropic accumulation of proteins and the antitumor agent smancs. *Cancer Res.* **46**, 6387–6392 (1986).

122. Kamal, N. H., El-Amrawy, F., Ali, H. A., Edafiogho, I. & Nounou, M. I. Is active targeting of brain metastases of breast cancer superior to passive targeting? *J. Cancer Metastasis Treat.* **2019**, (2019).

123. Golombek, S. K. *et al.* Tumor targeting via EPR: Strategies to enhance patient responses. *Advanced Drug Delivery Reviews* vol. 130 17–38 (2018).

124. Folkman, J. Tumor angiogenesis: therapeutic implications. *N. Engl. J. Med.* **285**, 1182–6 (1971).

125. Dvorak, H. F. Discovery of vascular permeability factor (VPF). *Experimental Cell Research* vol. 312 522–526 (2006).

126. Verheul, H. M. & Pinedo, H. M. The role of vascular endothelial growth factor (VEGF) in tumor angiogenesis and early clinical development of VEGF-receptor kinase inhibitors. *Clin. Breast Cancer* **1 Suppl 1**, S80-4 (2000).

127. Nagy, J. A., Chang, S.-H., Dvorak, A. M. & Dvorak, H. F. Why are tumour blood vessels abnormal and why is it important to know? *Br. J. Cancer* **100**, 865–9 (2009).

128. Hashizume, H. *et al.* Openings between defective endothelial cells explain tumor vessel leakiness. *Am. J. Pathol.* **156**, 1363–80 (2000).

129. Singh, R. & Lillard, J. W. Nanoparticle-based targeted drug delivery. *Experimental and Molecular Pathology* vol. 86 215–223 (2009).

130. Blanco, E., Shen, H. & Ferrari, M. Principles of nanoparticle design for overcoming biological barriers to drug delivery. *Nat. Biotechnol.* **33**, 941–51 (2015).

131. Din, F. U. *et al.* Effective use of nanocarriers as drug delivery systems for the treatment of selected tumors. *International Journal of Nanomedicine* vol. 12 7291–7309 (2017).

132. Weissenböck, A., Wirth, M. & Gabor, F. WGA-grafted PLGA-nanospheres: preparation and association with Caco-2 single cells. *J. Control. Release* **99**, 383–92 (2004).

133. Hamidi, M., Azadi, A. & Rafiei, P. Pharmacokinetic consequences of pegylation. *Drug Delivery* vol. 13 399–409 (2006).

134. Salmaso, S. & Caliceti, P. Stealth Properties to Improve Therapeutic Efficacy of Drug Nanocarriers. *J. Drug Deliv.* **2013**, 1–19 (2013).

135. Vail, D. M. *et al.* Pegylated liposomal doxorubicin: proof of principle using preclinical

animal models and pharmacokinetic studies. *Semin. Oncol.* **31**, 16–35 (2004).

136. Anders, C. K. *et al.* Pharmacokinetics and efficacy of PEGylated liposomal doxorubicin in an intracranial model of breast cancer. *PLoS One* **8**, e61359 (2013).

137. Liechty, W. B. & Peppas, N. A. Expert opinion: Responsive polymer nanoparticles in cancer therapy. in *European Journal of Pharmaceutics and Biopharmaceutics* vol. 80 241–246 (2012).

138. Davis, M. E., Chen, Z. G. & Shin, D. M. Nanoparticle therapeutics: an emerging treatment modality for cancer. *Nat. Rev. Drug Discov.* **7**, 771–782 (2008).

139. Wesselinova, D. Current major cancer targets for nanoparticle systems. *Curr. Cancer Drug Targets* **11**, 164–83 (2011).

140. Sindhwani, S. *et al.* The entry of nanoparticles into solid tumours. *Nat. Mater.* 1–10 (2020) doi:10.1038/s41563-019-0566-2.

141. Harrington, K. J. *et al.* Effective targeting of solid tumors in patients with locally advanced cancers by radiolabeled pegylated liposomes. *Clin. Cancer Res.* **7**, 243–54 (2001).

142. Tanaka, N. *et al.* Whole-tissue biopsy phenotyping of three-dimensional tumours reveals patterns of cancer heterogeneity. *Nat. Biomed. Eng.* **1**, 796–806 (2017).

143. Hori, K. *et al.* Fluctuations in tumor blood flow under normotension and the effect of angiotensin II-induced hypertension. *Jpn. J. Cancer Res.* **82**, 1309–16 (1991).

144. Hori, K. *et al.* Tumor-selective blood flow decrease induced by an angiotensin converting enzyme inhibitor, temocapril hydrochloride. *Jpn. J. Cancer Res.* **91**, 261–9 (2000).

145. Boucher, Y., Baxter, L. T. & Jain, R. K. Interstitial pressure gradients in tissue-isolated and subcutaneous tumors: implications for therapy. *Cancer Res.* **50**, 4478–84 (1990).

146. Padera, T. P. *et al.* Pathology: cancer cells compress intratumour vessels. *Nature* **427**, 695 (2004).

147. Roose, T., Netti, P. A., Munn, L. L., Boucher, Y. & Jain, R. K. Solid stress generated by spheroid growth estimated using a linear poroelasticity model. *Microvasc. Res.* **66**, 204–12 (2003).

148. Dudley, A. C. Tumor endothelial cells. *Cold Spring Harb. Perspect. Med.* **2**, a006536 (2012).

149. Wilhelm, S. *et al.* Analysis of nanoparticle delivery to tumours. *Nature Reviews Materials* vol. 1 (2016).

150. Laginha, K. M., Verwoert, S., Charrois, G. J. R. & Allen, T. M. Determination of doxorubicin levels in whole tumor and tumor nuclei in murine breast cancer tumors. *Clin. Cancer Res.* **11**, 6944–9 (2005).

151. van Vlerken, L. E., Duan, Z., Little, S. R., Seiden, M. V & Amiji, M. M. Biodistribution and pharmacokinetic analysis of Paclitaxel and ceramide administered in multifunctional polymer-blend nanoparticles in drug resistant breast cancer model. *Mol. Pharm.* **5**, 516–26.

152. Cui, Y. *et al.* Dual-Targeting Magnetic PLGA Nanoparticles for Codelivery of Paclitaxel and Curcumin for Brain Tumor Therapy. *ACS Appl. Mater. Interfaces* **8**, 32159–32169 (2016).

153. van Vlerken, L. E., Duan, Z., Little, S. R., Seiden, M. V. & Amiji, M. M. Biodistribution and pharmacokinetic analysis of paclitaxel and ceramide administered in multifunctional polymer-blend nanoparticles in drug resistant breast cancer model. in *Molecular Pharmaceutics* vol. 5 516–526 (2008).

154. Bogart, L. K. *et al.* Nanoparticles for imaging, sensing, and therapeutic intervention. *ACS*

Nano **8**, 3107–3122 (2014).

155. Alexis, F., Pridgen, E., Molnar, L. K. & Farokhzad, O. C. Factors affecting the clearance and biodistribution of polymeric nanoparticles. in *Molecular Pharmaceutics* vol. 5 505–515 (2008).

156. Rodriguez-Devora, J. I. *et al.* Physically facilitating drug-delivery systems. *Ther. Deliv.* **3**, 125–39 (2012).

157. Lammers, T., Hennink, W. E. & Storm, G. Tumour-targeted nanomedicines: Principles and practice. *British Journal of Cancer* vol. 99 392–397 (2008).

158. Prinzen, L. *et al.* Optical and magnetic resonance imaging of cell death and platelet activation using annexin a5-functionalized quantum dots. *Nano Lett.* **7**, 93–100 (2007).

159. Shi, J., Xiao, Z., Kamaly, N. & Farokhzad, O. C. Self-assembled targeted nanoparticles: Evolution of technologies and bench to bedside translation. *Accounts of Chemical Research* vol. 44 1123–1134 (2011).

160. Bertrand, N., Wu, J., Xu, X., Kamaly, N. & Farokhzad, O. C. Cancer nanotechnology: the impact of passive and active targeting in the era of modern cancer biology. *Adv. Drug Deliv. Rev.* **66**, 2–25 (2014).

161. Farokhzad, O. C. & Langer, R. Impact of nanotechnology on drug delivery. *ACS Nano* **3**, 16–20 (2009).

162. Ruoslahti, E. Tumor penetrating peptides for improved drug delivery. *Adv. Drug Deliv. Rev.* **110**–**111**, 3–12 (2017).

163. Hamilton, A. M. *et al.* Nanoparticles coated with the tumor-penetrating peptide iRGD reduce experimental breast cancer metastasis in the brain. *J. Mol. Med. (Berl).* **93**, 991–1001 (2015).

164. Lin, N. U. Targeted therapies in brain metastases. *Curr. Treat. Options Neurol.* **16**, 276 (2014).

165. Jones, A. R. & Shusta, E. V. Blood-brain barrier transport of therapeutics via receptor-mediation. *Pharm. Res.* **24**, 1759–71 (2007).

166. Regina, A. *et al.* ANG4043, a novel brain-penetrant peptide-mAb conjugate, is efficacious against HER2-positive intracranial tumors in mice. *Mol. Cancer Ther.* **14**, 129–40 (2015).

167. Thomas, F. C. *et al.* Uptake of ANG1005, a novel paclitaxel derivative, through the blood-brain barrier into brain and experimental brain metastases of breast cancer. *Pharm. Res.* **26**, 2486–94 (2009).

168. Demeule, M. *et al.* High transcytosis of melanotransferrin (P97) across the blood-brain barrier. *J. Neurochem.* **83**, 924–33 (2002).

169. Dörries, R. The role of T-cell-mediated mechanisms in virus infections of the nervous system. *Curr. Top. Microbiol. Immunol.* **253**, 219–45 (2001).

170. Chiou, B. *et al.* Pharmaceutical iron formulations do not cross a model of the human blood-brain barrier. *PLoS One* **13**, (2018).

171. Lameijer, M. A., Tang, J., Nahrendorf, M., Beelen, R. H. J. & Mulder, W. J. M. Monocytes and macrophages as nanomedicinal targets for improved diagnosis and treatment of disease. *Expert Rev. Mol. Diagn.* **13**, 567–80 (2013).

172. Choi, M. R. *et al.* Delivery of nanoparticles to brain metastases of breast cancer using a cellular Trojan horse. *Cancer Nanotechnol.* **3**, 47–54 (2012).

173. Schackert, G., Simmons, R. D., Buzbee, T. M., Hume, D. A. & Fidler, I. J. Macrophage

infiltration into experimental brain metastases: occurrence through an intact blood-brain barrier. *J. Natl. Cancer Inst.* **80**, 1027–34 (1988).

174. Rosenblum, D., Joshi, N., Tao, W., Karp, J. M. & Peer, D. Progress and challenges towards targeted delivery of cancer therapeutics. *Nature Communications* vol. 9 (2018).

175. Meacham, C. E. & Morrison, S. J. Tumour heterogeneity and cancer cell plasticity. *Nature* vol. 501 328–337 (2013).

176. Stuchbery, R. *et al.* Target Acquired: Progress and Promise of Targeted Therapeutics in the Treatment of Prostate Cancer. *Curr. Cancer Drug Targets* **15**, 394–405 (2015).

177. Arruebo, M. Drug delivery from structured porous inorganic materials. *Wiley Interdiscip. Rev. Nanomedicine Nanobiotechnology* **4**, 16–30 (2012).

178. Lübbe, A. S. *et al.* Clinical experiences with magnetic drug targeting: a phase I study with 4'-epidoxorubicin in 14 patients with advanced solid tumors. *Cancer Res.* **56**, 4686–93 (1996).

179. Owen, J., Pankhurst, Q. & Stride, E. Magnetic targeting and ultrasound mediated drug delivery: Benefits, limitations and combination. *Int. J. Hyperth.* **28**, 362–373 (2012).

180. Barar, J., Rafi, M. A., Pourseif, M. M. & Omidi, Y. Blood-brain barrier transport machineries and targeted therapy of brain diseases. *Bioimpacts* **6**, 225–248 (2016).

181. Chen, Y. & Liu, L. Modern methods for delivery of drugs across the blood–brain barrier. *Adv. Drug Deliv. Rev.* **64**, 640–665 (2012).

182. Abbott, N. J., Rönnbäck, L. & Hansson, E. Astrocyte-endothelial interactions at the blood-brain barrier. *Nat. Rev. Neurosci.* **7**, 41–53 (2006).

183. Ballabh, P., Braun, A. & Nedergaard, M. The blood-brain barrier: an overview: structure, regulation, and clinical implications. *Neurobiol. Dis.* **16**, 1–13 (2004).

184. Abbott, N. J., Patabendige, A. a K., Dolman, D. E. M., Yusof, S. R. & Begley, D. J. Structure and function of the blood-brain barrier. *Neurobiol. Dis.* **37**, 13–25 (2010).

185. Dong, X. Current strategies for brain drug delivery. *Theranostics* vol. 8 1481–1493 (2018).

186. Butt, A. M., Jones, H. C. & Abbott, N. J. Electrical resistance across the blood-brain barrier in anaesthetized rats: a developmental study. *J. Physiol.* **429**, 47–62 (1990).

187. van Tellingen, O. *et al.* Overcoming the blood-brain tumor barrier for effective glioblastoma treatment. *Drug Resist. Updat.* **19**, 1–12 (2015).

188. Rip, J., Schenk, G. J. & de Boer, A. G. Differential receptor-mediated drug targeting to the diseased brain. *Expert Opin. Drug Deliv.* **6**, 227–37 (2009).

189. Abbott, N. J. & Friedman, A. Overview and introduction: the blood-brain barrier in health and disease. *Epilepsia* **53 Suppl 6**, 1–6 (2012).

190. Banks, W. A. Characteristics of compounds that cross the blood-brain barrier. in *BMC Neurology* vol. 9 S3 (BioMed Central, 2009).

191. Levin, V. A. Relationship of Octanol/Water Partition Coefficient and Molecular Weight to Rat Brain Capillary Permeability. *J. Med. Chem.* **23**, 682–684 (1980).

192. Pan, W. & Kastin, A. J. Changing the chemokine gradient: CINC1 crosses the blood-brain barrier. *J. Neuroimmunol.* **115**, 64–70 (2001).

193. Pardridge, W. M. & M., W. Blood-brain barrier drug targeting: the future of brain drug development. *Mol. Interv.* **3**, 90–105, 51 (2003).

194. Banks, W. A. From blood-brain barrier to blood-brain interface: new opportunities for CNS

drug delivery. *Nat. Rev. Drug Discov.* **15**, 275–92 (2016).

195. Ginguené, C. *et al.* P-glycoprotein (ABCB1) and breast cancer resistance protein (ABCG2) localize in the microvessels forming the blood-tumor barrier in ependymomas. *Brain Pathol.* **20**, 926–935 (2010).

196. Löscher, W. Animal models of epilepsy for the development of antiepileptogenic and disease-modifying drugs. A comparison of the pharmacology of kindling and post-status epilepticus models of temporal lobe epilepsy. *Epilepsy Res.* **50**, 105–23 (2002).

197. Lu, J. F., Pokharel, D. & Bebawy, M. MRP1 and its role in anticancer drug resistance. *Drug Metabolism Reviews* vol. 47 406–419 (2015).

198. Declèves, X., Amiel, A., Delattre, J.-Y. & Scherrmann, J.-M. Role of ABC transporters in the chemoresistance of human gliomas. *Curr. Cancer Drug Targets* **6**, 433–45 (2006).

199. Veringa, S. J. E. *et al.* In Vitro Drug Response and Efflux Transporters Associated with Drug Resistance in Pediatric High Grade Glioma and Diffuse Intrinsic Pontine Glioma. *PLoS One* **8**, (2013).

200. Agarwal, S. *et al.* Active efflux of dasatinib from the brain limits efficacy against murine glioblastoma: Broad implications for the clinical use of molecularly targeted agents. *Mol. Cancer Ther.* **11**, 2183–2192 (2012).

201. Mittapalli, R. K. *et al.* ABCG2 and ABCB1 limit the efficacy of dasatinib in a PDGF-B-driven brainstem glioma model. *Mol. Cancer Ther.* **15**, 819–829 (2016).

202. Deeken, J. F. & Löscher, W. The blood-brain barrier and cancer: transporters, treatment, and Trojan horses. *Clin. Cancer Res.* **13**, 1663–74 (2007).

203. Fukumura, D. *et al.* Hypoxia and acidosis independently up-regulate vascular endothelial growth factor transcription in brain tumors in vivo. *Cancer Res.* **61**, 6020–4 (2001).

204. Hobbs, S. K. *et al.* Regulation of transport pathways in tumor vessels: Role of tumor type and microenvironment. *Proc. Natl. Acad. Sci. U. S. A.* **95**, 4607–4612 (1998).

205. Jain, R. K. *et al.* Augmentation of transvascular transport of macromolecules and nanoparticles in tumors using vascular endothelial growth factor. *Cancer Res.* **59**, 4129–35 (1999).

206. Boado, R. J. & Pardridge, W. M. The Trojan Horse Liposome Technology for Nonviral Gene Transfer across the Blood-Brain Barrier. *J. Drug Deliv.* **2011**, 1–12 (2011).

207. Pardridge, W. M. Molecular Trojan horses for blood-brain barrier drug delivery. *Curr. Opin. Pharmacol.* **6**, 494–500 (2006).

208. Morshed, R. A. *et al.* Cell-Penetrating Peptide-Modified Gold Nanoparticles for the Delivery of Doxorubicin to Brain Metastatic Breast Cancer. *Mol. Pharm.* **13**, 1843–54 (2016).

209. Fu, B. *et al.* Enhanced antitumor effects of the BRBP1 compound peptide BRBP1-TAT-KLA on human brain metastatic breast cancer. *Sci. Rep.* **5**, 8029 (2015).

210. Li, Y., Zheng, X., Gong, M. & Zhang, J. Delivery of a peptide-drug conjugate targeting the blood brain barrier improved the efficacy of paclitaxel against glioma. *Oncotarget* **7**, 79401–79407 (2016).

211. Meyers, J. D., Doane, T., Burda, C. & Basilion, J. P. Nanoparticles for imaging and treating brain cancer. *Nanomedicine* vol. 8 123–143 (2013).

212. Pardridge, W. M. Vector-mediated drug delivery to the brain. *Adv. Drug Deliv. Rev.* **36**, 299–321 (1999).

213. Motzer, R. J. *et al.* Phase III randomized trial of conventional-dose chemotherapy with or without high-dose chemotherapy and autologous hematopoietic stem-cell rescue as first-line treatment for patients with poor-prognosis metastatic germ cell tumors. *J. Clin. Oncol.* **25**, 247–56 (2007).

214. Motzer, R. J. *et al.* High-dose carboplatin, etoposide, and cyclophosphamide with autologous bone marrow transplantation in first-line therapy for patients with poor-risk germ cell tumors. *J. Clin. Oncol.* **15**, 2546–52 (1997).

215. Kumagai, T. *et al.* Intra-arterial Chemotherapy for Malignant Tumors of Head and Neck Region Using Three Types of Modified Injection Method. *Interv. Neuroradiol.* **9**, 113–123 (2003).

216. Yokoyama, J. *et al.* Impact of intra-arterial chemotherapy including internal carotid artery for advanced paranasal sinus cancers involving the skull base. *Br. J. Cancer* **111**, 2229–2234 (2014).

217. Zeng, X. T. *et al.* Intra-arterial chemotherapy for high-grade gliomas. *Cochrane Database Syst. Rev.* (2017) doi:10.1002/14651858.CD010549.pub2.

218. Mangraviti, A., Tyler, B. & Brem, H. Interstitial chemotherapy for malignant glioma: Future prospects in the era of multimodal therapy. *Surg. Neurol. Int.* **6**, S78–S84 (2015).

219. Bota, D. A., Desjardins, A., Quinn, J. A., Affronti, M. L. & Friedman, H. S. Interstitial chemotherapy with biodegradable BCNU (Gliadel) wafers in the treatment of malignant gliomas. *Ther. Clin. Risk Manag.* **3**, 707–15 (2007).

220. Wood, R. & Loomis, A. The physical and biological effects of high-frequency sound-waves of great intensity. *London, Edinburgh, Dublin Philos. Mag. J. Sci.* **4**, 417–436 (1927).

221. Harrogate, S. R., Yick, L. M. S., Williams, J. C., Cleveland, R. O. & Turney, B. W. Quantification of the Range of Motion of Kidney and Ureteral Stones During Shockwave Lithotripsy in Conscious Patients. *J. Endourol.* **30**, 406–410 (2016).

222. Nwokeoha, S., Carlisle, R. & Cleveland, R. O. The Application of Clinical Lithotripter Shock Waves to RNA Nucleotide Delivery to Cells. *Ultrasound Med. Biol.* **42**, 2478–2492 (2016).

223. Cui, H. W. *et al.* CT Texture Analysis of *Ex Vivo* Renal Stones Predicts Ease of Fragmentation with Shockwave Lithotripsy. *J. Endourol.* **31**, 694–700 (2017).

224. Shoar, K., Lyka, E., Coussios, C. & Cleveland, R. Passive acoustic mapping of cavitation during shock wave lithotripsy. *J. Acoust. Soc. Am.* **141**, 3673–3673 (2017).

225. Cornwall, H. L., Schmitz, K., Spencer, M., Turney, B. W. & Cleveland, R. O. The Hare and the Tortoise: Does Shock Wave Rate Matter in Lithotripsy? A UK Pilot Study. *Int. J. Surg.* **55**, S1 (2018).

226. Cleveland, R. O. & McAteer, J. A. Physics of Shock-Wave Lithotripsy. in *Smith's Textbook of Endourology* vol. 1 527–558 (Wiley-Blackwell, 2012).

227. Khokhlova, T. D. *et al.* Ultrasound-guided tissue fractionation by high intensity focused ultrasound in an in vivo porcine liver model. *Proc. Natl. Acad. Sci. U. S. A.* **111**, 8161–8166 (2014).

228. Darayash B. Tata, Biglow, J., Junru, W., Tritton, T. R. & Dunn, F. Ultrasound-enhanced hydroxyl radical production from two clinically employed anti-cancer drugs, adriamycin and mitomycin C. *Ultrason. - Sonochemistry* **1**, 39–45 (1996).

229. Umemura, S. I., Yumita, N., Nishigaki, R. & Umemura, K. Sonochemical activation of

hematoporphyrin - a potential modality for cancer treatment. in *IEEE 1989 Ultrasonics Symposium* 955–960 (IEEE, 1989).

230. Diederich, C. J. & Hynynen, K. Ultrasound technology for hyperthermia. *Ultrasound Med. Biol.* **25**, 871–87 (1999).

231. Tung, Y.-S. *et al.* Contrast-agent-enhanced ultrasound thermal ablation. *Ultrasound Med. Biol.* **32**, 1103–10 (2006).

232. Maxwell, A. D. *et al.* Noninvasive treatment of deep venous thrombosis using pulsed ultrasound cavitation therapy (histotripsy) in a porcine model. *J. Vasc. Interv. Radiol.* **22**, 369–377 (2011).

233. Unger, E. C., Hersh, E., Vannan, M., Matsunaga, T. O. & McCreery, T. Local drug and gene delivery through microbubbles. *Prog. Cardiovasc. Dis.* **44**, 45–54 (2001).

234. Pitt, W. G., Husseini, G. & Staples, B. J. Ultrasonic drug delivery - A general review. *Expert Opinion on Drug Delivery* vol. 1 37–56 (2004).

235. Carlisle, R. *et al.* Enhanced tumor uptake and penetration of virotherapy using polymer stealthing and focused ultrasound. *J. Natl. Cancer Inst.* **105**, 1701–1710 (2013).

236. Bao, S., Thrall, B. D. & Miller, D. L. Transfection of a reporter plasmid into cultured cells by sonoporation in vitro. *Ultrasound Med. Biol.* **23**, 953–9 (1997).

237. Miller, D. L. *et al.* Ultrasonic enhancement of gene transfection in murine melanoma tumors. *Ultrasound Med. Biol.* **25**, 1425–30 (1999).

238. Miller, D. L., Dou, C. & Song, J. DNA transfer and cell killing in epidermoid cells by diagnostic ultrasound activation of contrast agent gas bodies in vitro. *Ultrasound Med. Biol.* **29**, 601–7 (2003).

239. Konofagou, E. E. *et al.* Ultrasound-induced blood-brain barrier opening. *Curr. Pharm. Biotechnol.* **13**, 1332–45 (2012).

240. Stride, E. & Coussios, C. C. Nucleation, mapping and control of cavitation for drug delivery. *Nat. Rev. Phys.* (2019) doi:https://doi.org/10.1038/s42254-019-0074-y.

241. Fechheimer, M. *et al.* Transfection of mammalian cells with plasmid DNA by scrape loading and sonication loading. *Proc. Natl. Acad. Sci. U. S. A.* **84**, 8463–8467 (1987).

242. Kennedy, J. E. High-intensity focused ultrasound in the treatment of solid tumours. *Nat. Rev. Cancer* **5**, 321–7 (2005).

243. Crum, L. A. Cavitation microjets as a contributory mechanism for renal calculi disintegration in ESWL. *J. Urol.* **140**, 1587–90 (1988).

244. Yang, F. *et al.* Superparamagnetic nanoparticle-inclusion microbubbles for ultrasound contrast agents. *Phys. Med. Biol* **53**, 6129–6141 (2008).

245. Yang, F. *et al.* Superparamagnetic iron oxide nanoparticle-embedded encapsulated microbubbles as dual contrast agents of magnetic resonance and ultrasound imaging. *Biomaterials* **30**, 3882–3890 (2009).

246. Vlaskou, D. *et al.* Magnetic and Acoustically Active Lipospheres for Magnetically Targeted Nucleic Acid Delivery. *Adv. Funct. Mater.* **20**, 3881–3894 (2010).

247. Sirsi, S. R. & Borden, M. A. Microbubble compositions, properties and biomedical applications. *Bubble Science, Engineering and Technology* vol. 1 3–17 (2009).

248. Carpentier, A. *et al.* Clinical trial of blood-brain barrier disruption by pulsed ultrasound. *Sci. Transl. Med.* **8**, 343re2 (2016).

249. Stride, E. Physical Principles of Microbubbles for Ultrasound Imaging and Therapy. *Cerebrovasc. Dis.* **27**, 1–13 (2009).

250. Schutt, E. G., Klein, D. H., Mattrey, R. M. & Riess, J. G. Injectable microbubbles as contrast agents for diagnostic ultrasound imaging: The key role of perfluorochemicals. *Angew. Chemie - Int. Ed.* **42**, 3218–3235 (2003).

251. Geers, B., Dewitte, H., De Smedt, S. C. & Lentacker, I. Crucial factors and emerging concepts in ultrasound-triggered drug delivery. *J. Control. Release* **164**, 248–55 (2012).

252. Lentacker, I. *et al.* Drug loaded microbubble design for ultrasound triggered delivery. *Soft Matter* **5**, 2161 (2009).

253. Mulvana, H. *et al.* Characterization of Contrast Agent Microbubbles for Ultrasound Imaging and Therapy Research. *IEEE Trans. Ultrason. Ferroelectr. Freq. Control* **64**, 232–251 (2017).

254. Tinkov, S. *et al.* New doxorubicin-loaded phospholipid microbubbles for targeted tumor therapy: in-vivo characterization. *J. Control. Release* **148**, 368–72 (2010).

255. Geers, B. *et al.* Self-assembled liposome-loaded microbubbles: The missing link for safe and efficient ultrasound triggered drug-delivery. *J. Control. Release* **152**, 249–56 (2011).

256. Fix, S. M., Borden, M. A. & Dayton, P. A. Therapeutic gas delivery via microbubbles and liposomes. *J. Control. Release* **209**, 139–49 (2015).

257. Owen, J., Pankhurst, Q. & Stride, E. Magnetic targeting and ultrasound mediated drug delivery : Benefits , limitations and combination. **28**, 362–373 (2012).

258. Flowmetry, U. D. *et al.* Magnetic Targeting of Microbubbles against Physiologically Relevant Flow Conditions. *J. Acoust. Soc. Am.* **28**, 8303–8327 (2015).

259. Owen, J., Grove, P., Rademeyer, P. & Stride, E. The influence of blood on targeted microbubbles. (2014).

260. Owen, J. *et al.* Understanding the structure and mechanism of formation of a new magnetic microbubble formulation. *Theranostics* **2**, 1127–1139 (2012).

261. Mullin, L. *et al.* Effect of anesthesia carrier gas on in vivo circulation times of ultrasound microbubble contrast agents in rats. *Contrast Media Mol. Imaging* **6**, 126–131 (2011).

262. Chomas, J. E., Dayton, P., May, D. & Ferrara, K. Threshold of fragmentation for ultrasonic contrast agents. *J. Biomed. Opt.* **6**, 141 (2001).

263. Zhou, Y. Application of acoustic droplet vaporization in ultrasound therapy. doi:10.1186/s40349-015-0041-8.

264. Hua, X. *et al.* Construction of thrombus-targeted microbubbles carrying tissue plasminogen activator and their in vitro thrombolysis efficacy: a primary research. *J. Thromb. Thrombolysis* **30**, 29–35 (2010).

265. Lee, J. Y. *et al.* Nanoparticle-Loaded Protein-Polymer Nanodroplets for Improved Stability and Conversion Efficiency in Ultrasound Imaging and Drug Delivery. *Adv. Mater.* **27**, 5484–5492 (2015).

266. Rapoport, N. *et al.* Ultrasound-mediated tumor imaging and nanotherapy using drug loaded, block copolymer stabilized perfluorocarbon nanoemulsions. *J. Control. Release* **153**, 4–15 (2011).

267. Sheeran, P. S. & Dayton, P. A. Phase-change contrast agents for imaging and therapy. *Curr. Pharm. Des.* **18**, 2152–65 (2012).

268. Yin, T. *et al.* IJN-28830-nanobubbles-for-enhanced-ultrasound-imaging-of-tumors. *Int. J. Nanomedicine* **7**, 895–904 (2012).

269. Zhou, Y. *et al.* Microbubbles from Gas-Generating Perfluorohexane Nanoemulsions for Targeted Temperature-Sensitive Ultrasonography and Synergistic HIFU Ablation of Tumors. *Adv. Mater.* **25**, 4123–4130 (2013).

270. Kwan, J. J. *et al.* Ultrasound-Propelled Nanocups for Drug Delivery. *Small* **11**, 5305–5314 (2015).

271. Mannaris, C. *et al.* Gas-Stabilizing Gold Nanocones for Acoustically Mediated Drug Delivery. *Adv. Healthc. Mater.* **7**, e1800184 (2018).

272. Chen, H. & Konofagou, E. E. The size of blood-brain barrier opening induced by focused ultrasound is dictated by the acoustic pressure. *J. Cereb. Blood Flow Metab.* **34**, 1197–1204 (2014).

273. Rahim, A. *et al.* Physical parameters affecting ultrasound/microbubble-mediated gene delivery efficiency in vitro. *Ultrasound Med. Biol.* **32**, 1269–1279 (2006).

274. Yoon, Y. Il, Yoon, T. J. & Lee, H. J. Optimization of ultrasound parameters for microbubble-nanoliposome complex-mediated delivery. *Ultrasonography* **34**, 297–303 (2015).

275. Konofagou, E. E. Optimization of the ultrasound-induced blood-brain barrier opening. *Theranostics* vol. 2 1223–1237 (2012).

276. Tung, Y. S. *et al.* In vivo transcranial cavitation threshold detection during ultrasound-induced blood-brain barrier opening in mice. *Phys. Med. Biol.* **55**, 6141–6155 (2010).

277. Choi, J. J. *et al.* Microbubble-size dependence of focused ultrasound-induced blood brain barrier opening in mice in vivo. *IEEE Trans. Biomed. Eng.* **57**, 145–154 (2010).

278. Tung, Y.-S., Vlachos, F., Feshitan, J. A., Borden, M. A. & Konofagou, E. E. The mechanism of interaction between focused ultrasound and microbubbles in blood-brain barrier opening in mice. *J. Acoust. Soc. Am.* **130**, 3059–3067 (2011).

279. Wang, S., Samiotaki, G., Olumolade, O., Feshitan, J. A. & Konofagou, E. E. Microbubble type and distribution dependence of focused ultrasound-induced blood-brain barrier opening. *Ultrasound Med. Biol.* **40**, 130–137 (2014).

280. Carugo, D. *et al.* Modulation of the molecular arrangement in artificial and biological membranes by phospholipid-shelled microbubbles. *Biomaterials* **113**, 105–117 (2017).

281. Sheikov, N., McDannold, N., Vykhodtseva, N., Jolesz, F. & Hynynen, K. Cellular mechanisms of the blood-brain barrier opening induced by ultrasound in presence of microbubbles. *Ultrasound Med. Biol.* **30**, 979–89 (2004).

282. Rodriguez, A., Tatter, S. B. & Debinski, W. Neurosurgical techniques for disruption of the blood–brain barrier for glioblastoma treatment. *Pharmaceutics* vol. 7 175–187 (2015).

283. Hynynen, K., McDannold, N., Vykhodtseva, N. & Jolesz, F. a. Noninvasive MR imaging-guided focal opening of the blood-brain barrier in rabbits. *Radiology* **220**, 640–646 (2001).

284. Vykhodtseva, N., McDannold, N. & Hynynen, K. Progress and problems in the application of focused ultrasound for blood-brain barrier disruption. *Ultrasonics* **48**, 279–296 (2008).

285. Stride, E., Mulvana, H., Eckersley, R. J., Tang, M.-X. & Pankhurst, Q. Magnetic microbubbles. 499–522 (2011).

286. Sheikov, N., McDannold, N., Vykhodtseva, N., Jolesz, F. & Hynynen, K. Cellular mechanisms of the blood-brain barrier opening induced by ultrasound in presence of microbubbles. *Ultrasound Med. Biol.* **30**, 979–989 (2004).

287. De Cock, I. *et al.* Ultrasound and microbubble mediated drug delivery: Acoustic pressure as determinant for uptake via membrane pores or endocytosis. *J. Control. Release* **197**, 20–28 (2015).

288. Aryal, M., Arvanitis, C. D., Alexander, P. M. & McDannold, N. Ultrasound-mediated blood-brain barrier disruption for targeted drug delivery in the central nervous system. *Adv. Drug Deliv. Rev.* **72**, 94–109 (2014).

289. Nhan, T. *et al.* Drug delivery to the brain by focused ultrasound induced blood-brain barrier disruption: Quantitative evaluation of enhanced permeability of cerebral vasculature using two-photon microscopy. *J. Control. Release* **172**, 274–280 (2013).

290. Beekers, I. *et al.* Combined Confocal Microscope and Brandaris 128 Ultra-High-Speed Camera. *Ultrasound Med. Biol.* (2019) doi:10.1016/j.ultrasmedbio.2019.06.004.

291. Zhou, Y., Kumon, R. E., Cui, J. & Deng, C. X. The size of sonoporation pores on the cell membrane. *Ultrasound Med. Biol.* **35**, 1756–60 (2009).

292. Deng, C. X., Sieling, F., Pan, H. & Cui, J. Ultrasound-induced cell membrane porosity. *Ultrasound Med. Biol.* **30**, 519–526 (2004).

293. Jin, L. F. *et al.* Ultrasound targeted microbubble destruction stimulates cellular endocytosis in facilitation of adeno-associated virus delivery. *Int. J. Mol. Sci.* **14**, 9737–9750 (2013).

294. Delalande, A., Leduc, C., Midoux, P., Postema, M. & Pichon, C. Efficient Gene Delivery by Sonoporation Is Associated with Microbubble Entry into Cells and the Clathrin-Dependent Endocytosis Pathway. *Ultrasound Med. Biol.* **41**, 1913–26 (2015).

295. Meijering, B. D. M. *et al.* Ultrasound and Microbubble-Targeted Delivery of Macromolecules Is Regulated by Induction of Endocytosis and Pore Formation. *Circ. Res.* **104**, 679–687 (2009).

296. Lentacker, I., De Cock, I., Deckers, R., De Smedt, S. C. & Moonen, C. T. W. Understanding ultrasound induced sonoporation: Definitions and underlying mechanisms. *Adv. Drug Deliv. Rev.* **72**, 49–64 (2014).

297. Nyborg, W. L. Acoustic Streaming near a Boundary * sound Defining sketch. *J. Acoust. Soc. Am.* **30**, 329–339 (1958).

298. Elder, S. & Nyborg, W. L. Acoustic Streaming Resulting from a Resonant Bubble. *J. Acoust. Soc. Am.* **28**, 155–155 (1956).

299. Marmottant, P. & Hilgenfeldt, S. Controlled vesicle deformation and lysis by single oscillating bubbles. *Nature* **423**, 153–156 (2003).

300. Wiedemair, W., Tuković, Ž., Jasak, H., Poulikakos, D. & Kurtcuoglu, V. On ultrasound-induced microbubble oscillation in a capillary blood vessel and its implications for the blood–brain barrier. *Phys. Med. Biol.* **57**, 1019–1045 (2012).

301. Qin, S. & Ferrara, K. W. Acoustic response of compliable microvessels containing ultrasound contrast agents. *Phys. Med. Biol.* **51**, 5065–5088 (2006).

302. Hosseinkhah, N., Goertz, D. E. & Hynynen, K. Microbubbles and blood-brain barrier opening: a numerical study on acoustic emissions and wall stress predictions. *IEEE Trans. Biomed. Eng.* **62**, 1293–304 (2015).

303. Wu, J. Theoretical study on shear stress generated by microstreaming surrounding contrast agents attached to living cells. *Ultrasound Med. Biol.* **28**, 125–129 (2002).

304. Ooi, A., Tho, P. & Manasseh, R. *Cavitation microstreaming patterns in single and multiple bubble systems*. *The Journal of the Acoustical Society of America* vol. 122 (2007).

305. Jia, C. *et al.* Generation of Reactive Oxygen Species in Heterogeneously Sonoporated Cells by Microbubbles with Single-Pulse Ultrasound. *Ultrasound Med. Biol.* **44**, 1074–1085 (2018).

306. Enayati, M., al Mohazey, D., Edirisinghe, M. & Stride, E. Ultrasound-stimulated drug release from polymer micro and nanoparticles. *Bioinspired, Biomim. Nanobiomaterials* **2**, 3–10 (2013).

307. Li, Y.-S. J., Haga, J. H. & Chien, S. Molecular basis of the effects of shear stress on vascular endothelial cells. *J. Biomech.* **38**, 1949–1971 (2005).

308. Haidekker, M. a, L'Heureux, N. & Frangos, J. a. Fluid shear stress increases membrane fluidity in endothelial cells: a study with DCVJ fluorescence. *Am. J. Physiol. - Hear. Circ. Physiol.* **278**, H1401–H1406 (2000).

309. Jalali, S., Huang, Y., Dumont, D. J. & Hynynen, K. Focused ultrasound-mediated bbb disruption is associated with an increase in activation of AKT: experimental study in rats. *BMC Neurol.* **10**, 114 (2010).

310. Butler, P. J., Tsou, T.-C., Li, J. Y.-S., Usami, S. & Chien, S. Rate sensitivity of shear-induced changes in the lateral diffusion of endothelial cell membrane lipids: a role for membrane perturbation in shear-induced MAPK activation. *FASEB J.* **16**, 216–8 (2002).

311. Kooiman, K., Van Der Steen, A. F. W. & Jong, N. Role of intracellular calcium and reactive oxygen species in microbubble-mediated alterations of endothelial layer permeability. *IEEE Trans. Ultrason. Ferroelectr. Freq. Control* **60**, 1811–1815 (2013).

312. Juffermans, L. J. M. *et al.* Ultrasound and Microbubble-Induced Intra- and Intercellular Bioeffects in Primary Endothelial Cells. *Ultrasound Med. Biol.* **35**, 1917–1927 (2009).

313. Juffermans, L. J. M., Dijkmans, P. a, Musters, R. J. P., Visser, C. a & Kamp, O. Transient permeabilization of cell membranes by ultrasound-exposed microbubbles is related to formation of hydrogen peroxide. *Am. J. Physiol. Heart Circ. Physiol.* **291**, H1595–H1601 (2006).

314. Cho, H. S. *et al.* Localized Down-regulation of P-glycoprotein by Focused Ultrasound and Microbubbles induced Blood-Brain Barrier Disruption in Rat Brain. *Sci. Rep.* **6**, (2016).

315. Aryal, M. *et al.* Effects on P-glycoprotein expression after blood-brain barrier disruption using focused ultrasound and microbubbles. *PLoS One* **12**, (2017).

316. Hynynen, K., McDannold, N., Sheikov, N. a., Jolesz, F. a. & Vykhodtseva, N. Local and reversible blood-brain barrier disruption by noninvasive focused ultrasound at frequencies suitable for trans-skull sonications. *Neuroimage* **24**, 12–20 (2005).

317. Wang, F. *et al.* Focused ultrasound microbubble destruction-mediated changes in blood-brain barrier permeability assessed by contrast-enhanced magnetic resonance imaging. *J. Ultrasound Med.* **28**, 1501–9 (2009).

318. Marty, B. *et al.* Dynamic study of blood-brain barrier closure after its disruption using ultrasound: a quantitative analysis. *J. Cereb. Blood Flow Metab.* **32**, 1948–58 (2012).

319. Park, J., Zhang, Y., Vykhodtseva, N., Jolesz, F. A. & McDannold, N. J. The kinetics of blood brain barrier permeability and targeted doxorubicin delivery into brain induced by focused ultrasound. *J. Control. Release* **162**, 134–42 (2012).

320. Olumolade, O. O., Wang, S., Samiotaki, G. & Konofagou, E. E. Longitudinal Motor and Behavioral Assessment of Blood-Brain Barrier Opening with Transcranial Focused Ultrasound. *Ultrasound Med. Biol.* **42**, 2270–82 (2016).

321. Samiotaki, G., Vlachos, F., Tung, Y.-S. & Konofagou, E. E. A quantitative pressure and microbubble-size dependence study of focused ultrasound-induced blood-brain barrier opening reversibility in vivo using MRI. *Magn. Reson. Med.* **67**, 769–777 (2012).

322. Marquet, F., Tung, Y. S., Teichert, T., Ferrera, V. P. & Konofagou, E. E. Noninvasive, transient and selective Blood-Brain barrier opening in Non-Human primates in vivo. *PLoS One* **6**, (2011).

323. McDannold, N., Vykhodtseva, N., Raymond, S., Jolesz, F. A. & Hynynen, K. MRI-guided targeted blood-brain barrier disruption with focused ultrasound: Histological findings in rabbits. *Ultrasound Med. Biol.* **31**, 1527–1537 (2005).

324. Beccaria, K. *et al.* Opening of the blood-brain barrier with an unfocused ultrasound device in rabbits. *J. Neurosurg.* **119**, 887–98 (2013).

325. McDannold, N., Arvanitis, C. D., Vykhodtseva, N. & Livingstone, M. S. Temporary disruption of the blood-brain barrier by use of ultrasound and microbubbles: Safety and efficacy evaluation in rhesus macaques. *Cancer Res.* **72**, 3652–3663 (2012).

326. Carpentier, A. *et al.* Clinical trial of blood-brain barrier disruption by pulsed ultrasound. *Sci. Transl. Med.* **8**, (2016).

327. Kovacsa, Z. I. *et al.* Disrupting the blood-brain barrier by focused ultrasound induces sterile inflammation. *Proc. Natl. Acad. Sci. U. S. A.* **114**, E75–E84 (2017).

328. McMahon, D. & Hynynen, K. Acute inflammatory response following increased blood-brain barrier permeability induced by focused ultrasound is dependent on microbubble dose. *Theranostics* **7**, 3989–4000 (2017).

329. Sinharay, S. *et al.* In vivo imaging of sterile microglial activation in rat brain after disrupting the blood-brain barrier with pulsed focused ultrasound: [18F]DPA-714 PET study. *J. Neuroinflammation* **16**, 155 (2019).

330. Treat, L. H. *et al.* Targeted delivery of doxorubicin to the rat brain at therapeutic levels using MRI-guided focused ultrasound. *Int. J. Cancer* **121**, 901–907 (2007).

331. Treat, L. H., McDannold, N., Zhang, Y., Vykhodtseva, N. & Hynynen, K. Improved Anti-Tumor Effect of Liposomal Doxorubicin After Targeted Blood-Brain Barrier Disruption by MRI-Guided Focused Ultrasound in Rat Glioma. *Ultrasound Med. Biol.* **38**, 1716–1725 (2012).

332. Yang, F. Y. *et al.* Treating glioblastoma multiforme with selective high-dose liposomal doxorubicin chemotherapy induced by repeated focused ultrasound. *Int. J. Nanomedicine* **7**, 965–974 (2012).

333. Aryal, M., Vykhodtseva, N., Zhang, Y.-Z., Park, J. & McDannold, N. Multiple treatments with liposomal doxorubicin and ultrasound-induced disruption of blood-tumor and blood-brain barriers improve outcomes in a rat glioma model. *J. Control. Release* **169**, 103–11 (2013).

334. Kovacs, Z. *et al.* Prolonged survival upon ultrasound-enhanced doxorubicin delivery in two syngenic glioblastoma mouse models. *J. Control. Release* **187**, 74–82 (2014).

335. Shen, Y. *et al.* Enhanced delivery of paclitaxel liposomes using focused ultrasound with microbubbles for treating nude mice bearing intracranial glioblastoma xenografts. *Int. J. Nanomedicine* **12**, 5613–5629 (2017).

336. Wei, K. C. *et al.* Focused Ultrasound-Induced Blood-Brain Barrier Opening to Enhance Temozolomide Delivery for Glioblastoma Treatment: A Preclinical Study. *PLoS One* **8**, 1–10 (2013).

337. Beccaria, K. *et al.* Ultrasound-induced opening of the blood-brain barrier to enhance temozolomide and irinotecan delivery: an experimental study in rabbits. *J. Neurosurg.* **124**, 1602–10 (2016).

338. Goldwirt, L. *et al.* Enhanced brain distribution of carboplatin in a primate model after blood-brain barrier disruption using an implantable ultrasound device. *Cancer Chemother. Pharmacol.* **77**, 211–6 (2016).

339. Dréan, A. *et al.* Temporary blood-brain barrier disruption by low intensity pulsed ultrasound increases carboplatin delivery and efficacy in preclinical models of glioblastoma. *J. Neurooncol.* **144**, 33–41 (2019).

340. Liu, H.-L. *et al.* Blood-brain barrier disruption with focused ultrasound enhances delivery of chemotherapeutic drugs for glioblastoma treatment. *Radiology* **255**, 415–425 (2010).

341. Chen, L. *et al.* MR-guided focused ultrasound: enhancement of intratumoral uptake of [^{3}H]-docetaxel in vivo. *Phys. Med. Biol.* **55**, 7399–410 (2010).

342. Askoxylakis, V., Arvanitis, C. D., Wong, C. S. F., Ferraro, G. B. & Jain, R. K. Emerging strategies for delivering antiangiogenic therapies to primary and metastatic brain tumors1. Askoxylakis, V., Arvanitis, C. D., Wong, C. S. F., Ferraro, G. B. & Jain, R. K. Emerging strategies for delivering antiangiogenic therapies to primary and. *Advanced Drug Delivery Reviews* vol. 119 159–174 (2017).

343. Idbaih, A. *et al.* Safety and Feasibility of Repeated and Transient Blood-Brain Barrier Disruption by Pulsed Ultrasound in Patients with Recurrent Glioblastoma. *Clin. Cancer Res.* **25**, 3793–3801 (2019).

344. antibodies delivery through bbb with mrgfuskinoshita 2006.pdf.

345. Timbie, K. F., Mead, B. P. & Price, R. J. Drug and gene delivery across the blood-brain barrier with focused ultrasound. *J. Control. Release* **219**, 61–75 (2015).

346. Stavarache, M. A. *et al.* Safe and stable noninvasive focal gene delivery to the mammalian brain following focused ultrasound. *J. Neurosurg.* **130**, 989–998 (2018).

347. Delaney, L. J. *et al.* Breast Cancer Brain Metastasis Response to Radiation After Microbubble Oxygen Delivery in a Murine Model. *J. Ultrasound Med.* (2019) doi:10.1002/jum.15031.

348. Park, E.-J., Zhang, Y.-Z., Vykhodtseva, N. & McDannold, N. Ultrasound-mediated blood-brain/blood-tumor barrier disruption improves outcomes with trastuzumab in a breast cancer brain metastasis model. *J. Control. Release* **163**, 277–284 (2012).

349. Arvanitis, C. D. *et al.* Mechanisms of enhanced drug delivery in brain metastases with focused ultrasound-induced blood–tumor barrier disruption. *PNAS* **115**, 8717–8726 (2018).

350. Alkins, R., Burgess, A., Kerbel, R., Wels, W. S. & Hynynen, K. Early treatment of HER2-amplified brain tumors with targeted NK-92 cells and focused ultrasound improves survival. *Neuro. Oncol.* **18**, 974–981 (2016).

351. Alkins, R. *et al.* Focused ultrasound delivers targeted immune cells to metastatic brain tumors. *Cancer Res.* **73**, 1892–1899 (2013).

352. Chen, K. T., Wei, K. C. & Liu, H. L. Theranostic strategy of focused ultrasound induced blood-brain barrier opening for CNS disease treatment. *Frontiers in Pharmacology* vol. 10 (2019).

353. Lipsman, N. *et al.* Blood–brain barrier opening in Alzheimer's disease using MR-guided focused ultrasound. *Nat. Commun.* **9**, (2018).

354. Insightec website. https://www.insightec.com/.

355. Meng, Y. *et al.* Safety and efficacy of focused ultrasound induced blood-brain barrier opening, an integrative review of animal and human studies. *J. Control. Release* **309**, 25–36 (2019).

356. Liu, H.-L. & Huang, W.-C. Noninvasively low-frequency ultrasonic apparatus for brain therapy - US Patent Application Publication. (2010).

357. Carpentier, A. *et al.* Clinical trial of blood-brain barrier disruption by pulsed ultrasound. *Sci. Transl. Med.* **8**, (2016).

358. Lipsman, N. Clinical trial: Blood Brain Barrier Disruption (BBBD) Using MRgFUS in the Treatment of Her2-positive Breast Cancer Brain Metastases (BBBD). https://clinicaltrials.gov/ct2/show/NCT03714243.

359. Lebbe, C. & Resch-Rigon, M. Clinical Trial: Safety and Efficacy of Sonocloud Device Combined With Nivolumab in Brain Metastases From Patients With Melanoma (SONIMEL01). https://clinicaltrials.gov/ct2/show/NCT04021420.

360. Kü sters, B. *et al.* Vascular Endothelial Growth Factor-A 165 Induces Progression of Melanoma Brain Metastases without Induction of Sprouting Angiogenesis. *CANCER Res.* **62**, 341–345 (2002).

361. Läubli, H. & Borsig, L. Selectins as Mediators of Lung Metastasis. *Cancer Microenviron.* **3**, 97–105 (2010).

362. Ludwig, R. J. *et al.* Endothelial P-Selectin as a Target of Heparin Action in Experimental Melanoma Lung Metastasis. *CANCER Res.* **64**, 2743–2750 (2004).

363. Khatib, A.-M. *et al.* Rapid Induction of Cytokine and E-Selectin Expression in the Liver in Response to Metastatic Tumor Cells. *CANCER Res.* **59**, 1356–1361 (1999).

364. Vidal-Vanaclocha, F. *et al.* IL-18 regulates IL-1beta-dependent hepatic melanoma metastasis via vascular cell adhesion molecule-1. *Proc. Natl. Acad. Sci. U. S. A.* **97**, 734–9 (2000).

365. Langley, R. *et al.* Endothelial Expression of Vascular Cell Adhesion Molecule-1 Correlates with Metastatic Pattern in Spontaneous Melanoma. *Microcirculation* **8**, 335–345 (2001).

366. Ley, K., Laudanna, C., Cybulsky, M. I. & Nourshargh, S. Getting to the site of inflammation: the leukocyte adhesion cascade updated. *Nat. Rev. Immunol.* **7**, 678–89 (2007).

367. Cannella, B. & Raine, C. S. The adhesion molecule and cytokine profile of multiple sclerosis lesions. *Ann. Neurol.* **37**, 424–435 (1995).

368. Piraino, P. . *et al.* Prolonged reversal of chronic experimental allergic encephalomyelitis using a small molecule inhibitor of α4 integrin. *J. Neuroimmunol.* **131**, 147–159 (2002).

369. Polman, C. H. *et al.* A Randomized, Placebo-Controlled Trial of Natalizumab for Relapsing Multiple Sclerosis. *N. Engl. J. Med.* **354**, 899–910 (2006).

370. Yednock, T. A. *et al.* Prevention of experimental autoimmune encephalomyelitis by antibodies against α4βl integrin. *Nature* **356**, 63–66 (1992).

371. Rice, G. E. & Bevilacqua, M. P. An inducible endothelial cell surface glycoprotein mediates melanoma adhesion. *Science* **246**, 1303–6 (1989).

372. Giavazzi, R., Foppolo, M., Dossi, R. & Remuzzi, A. Rolling and adhesion of human tumor cells on vascular endothelium under physiological flow conditions. *J. Clin. Invest.* **92**, 3038–44 (1993).

373. Bennicelli, J. L. & Guerry, D. P. Production of multiple cytokines by cultured human

melanomas. *Exp. Dermatol.* **2**, 186–190 (1993).

374. Burrows, F. J. *et al.* Influence of tumor-derived interleukin 1 on melanoma-endothelial cell interactions in vitro. *Cancer Res.* **51**, 4768–75 (1991).

375. Lee, J.-H. *et al.* A novel human anti-VCAM-1 monoclonal antibody ameliorates airway inflammation and remodelling. *J. Cell. Mol. Med.* **17**, 1271–81 (2013).

376. Garofalo, A. *et al.* Involvement of the very late antigen 4 integrin on melanoma in interleukin 1-augmented experimental metastases. *Cancer Res.* **55**, 414–9 (1995).

377. Higashiyama, A., Watanabe, H., Okumura, K. & Yagita, H. Involvement of tumor necrosis factor alpha and very late activation antigen 4/vascular cell adhesion molecule 1 interaction in surgical-stress-enhanced experimental metastasis. *Cancer Immunol. Immunother.* **42**, 231–6 (1996).

378. Okahara, H., Yagita, H., Miyake, K. & Okumura, K. Involvement of very late activation antigen 4 (VLA-4) and vascular cell adhesion molecule 1 (VCAM-1) in tumor necrosis factor alpha enhancement of experimental metastasis. *Cancer Res.* **54**, 3233–6 (1994).

379. Bevilacqua, M. P. Endothelial-leukocyte adhesion molecules. *Annu Rev Immunol* **11**, 767–804 (1993).

380. Mcateer, M. A. *et al.* In vivo magnetic resonance imaging of acute brain inflammation using microparticles of iron oxide. *Nat Med* **13**, 1253–1258 (2007).

381. Elices, M. J. *et al.* VCAM-1 on activated endothelium interacts with the leukocyte integrin VLA-4 at a site distinct from the VLA-4/fibronectin binding site. *Cell* **60**, 577–84 (1990).

382. Carlos, T. M. *et al.* Vascular cell adhesion molecule-1 mediates lymphocyte adherence to cytokine-activated cultured human endothelial cells [published erratum appears in Blood 1990 Dec 1;76(11):2420]. *Blood* **76**, 965–970 (1990).

383. Ferrante, E. A., Pickard, J. E., Rychak, J., Klibanov, A. & Ley, K. Dual targeting improves microbubble contrast agent adhesion to VCAM-1 and P-selectin under flow. *J. Control. Release* **140**, 100–107 (2009).

384. Southworth, R. *et al.* Renal vascular inflammation induced by Western diet in ApoE-null mice quantified by (19)F NMR of VCAM-1 targeted nanobeacons. *Nanomedicine* **5**, 359–67 (2009).

385. Phillips, L. C., Klibanov, A. L., Wamhoff, B. R. & Hossack, J. A. Intravascular ultrasound detection and delivery of molecularly targeted microbubbles for gene delivery. *IEEE Trans. Ultrason. Ferroelectr. Freq. Control* **59**, 1596–1601 (2012).

386. Cybulsky, M. I. *et al.* A major role for VCAM-1, but not ICAM-1, in early atherosclerosis. *J. Clin. Invest.* **107**, 1255–1262 (2001).

387. Nakashima, Y., Raines, E. W., Plump, A. S., Breslow, J. L. & Ross, R. Upregulation of VCAM-1 and ICAM-1 at atherosclerosis-prone sites on the endothelium in the apoE-deficient mouse. *Arterioscler. Thromb. Vasc. Biol.* **18**, 842–851 (1998).

388. Orosz, C. G. *et al.* Role of the endothelial adhesion molecule VCAM in murine cardiac allograft rejection. *Immunol. Lett.* **32**, 7–12 (1992).

389. Maurer, C. A. *et al.* Over-expression of ICAM-1, VCAM-1 and ELAM-1 might influence tumor progression in colorectal cancer. *Int. J. cancer* **79**, 76–81 (1998).

390. Ding, Y. Bin *et al.* Association of VCAM-1 overexpression with oncogenesis, tumor angiogenesis and metastasis of gastric carcinoma. *World J. Gastroenterol.* **9**, 1409–1414 (2003).

391. Dedrick, R. L., Bodary, S. & Garovoy, M. R. Adhesion molecules as therapeutic targets for autoimmune diseases and transplant rejection. *Expert Opin. Biol. Ther.* **3**, 85–95 (2003).

392. Gosk, S., Gottstein, C. & Bendas, G. Targeting of immunoliposomes to endothelial cells expressing VCAM: a future strategy in cancer therapy. *Int. J. Clin. Pharmacol. Ther.* **43**, 581–2 (2005).

393. Soto, M. S., Serres, S., Anthony, D. C. & Sibson, N. R. Functional role of endothelial adhesion molecules in the early stages of brain metastasis. *Neuro. Oncol.* **16**, 540–551 (2014).

394. Sibson, N. R. *et al.* MRI detection of early endothelial activation in brain inflammation. *Magn. Reson. Med.* **51**, 248–252 (2004).

395. Palmieri, D. *et al.* Her-2 overexpression increases the metastatic outgrowth of breast cancer cells in the brain. *Cancer Res.* **67**, 4190–8 (2007).

396. Venur, V. A. & Ahluwalia, M. S. Targeted Therapy in Brain Metastases: Ready for Primetime? *Am. Soc. Clin. Oncol. Educ. B.* e123–e130 (2016) doi:10.1200/EDBK_100006.

397. Kü, B. *et al.* Differential Effects of Vascular Endothelial Growth Factor A Isoforms in a Mouse Brain Metastasis Model of Human Melanoma. *CANCER Res.* **63**, 5408–5413 (2003).

398. Kim, L. S., Huang, S., Lu, W., Lev, D. C. & Price, J. E. Vascular endothelial growth factor expression promotes the growth of breast cancer brain metastases in nude mice. *Clin. Exp. Metastasis* **21**, 107–18 (2004).

399. Villanueva, F. S. *et al.* Microbubbles targeted to intercellular adhesion molecule-1 bind to activated coronary artery endothelial cells. *Circulation* **98**, 1–5 (1998).

400. Kaufmann, B. A. & Lindner, J. R. Molecular imaging with targeted contrast ultrasound. *Curr. Opin. Biotechnol.* **18**, 11–6 (2007).

401. Khanicheh, E. *et al.* Noninvasive Ultrasound Molecular Imaging of the Effect of Statins on Endothelial Inflammatory Phenotype in Early Atherosclerosis. *PLoS One* **8**, 1–9 (2013).

402. Wu, J. *et al.* Efficacy of contrast-enhanced US and magnetic microbubbles targeted to vascular cell adhesion molecule-1 for molecular imaging of atherosclerosis. *Radiology* **260**, 463–71 (2011).

403. Weinkauf, C. C. *et al.* Vascular Cell Adhesion Molecule 1 Is a Promising Target to Identify High-Risk Carotid Plaques Using Contrast-Enhanced Duplex Ultrasound. *J. Vasc. Surg.* **64**, 549 (2016).

404. Tlaxca, J. L. *et al.* Ultrasound-based molecular imaging and specific gene delivery to mesenteric vasculature by endothelial adhesion molecule targeted microbubbles in a mouse model of Crohn's disease. *J. Control. Release* **165**, 216–25 (2013).

405. Hernot, S. *et al.* Nanobody-coupled microbubbles as novel molecular tracer. *J. Control. Release* **158**, 346–53 (2012).

406. X. Wang, A.K. Searle, Y.C. Chen, K. P. Downregulation of vascular cell adhesion molecule-1 using targeted microbubbles for the delivery of microRNA-126: treatment and prevention of abdominal aortic aneurysm. *Eur. Heart J.* **38**, 4087285 (2017).

407. Phillips, L. C., Klibanov, A. L., Wamhoff, B. R. & Hossack, J. A. Targeted gene transfection from microbubbles into vascular smooth muscle cells using focused, ultrasound-mediated delivery. *Ultrasound Med. Biol.* **36**, 1470–80 (2010).

408. Willmann, J. K. *et al.* Dual-targeted contrast agent for US assessment of tumor angiogenesis in vivo. *Radiology* **248**, 936–44 (2008).

409. Willmann, J. K. *et al.* Targeted microbubbles for imaging tumor angiogenesis: assessment of whole-body biodistribution with dynamic micro-PET in mice. *Radiology* **249**, 212–9 (2008).

410. Wang, J., Qin, B., Chen, X., Wagner, W. R. & Villanueva, F. S. Ultrasound Molecular Imaging of Angiogenesis Using Vascular Endothelial Growth Factor-Conjugated Microbubbles. *Mol. Pharm.* **14**, 781–790 (2017).

411. Deshpande, N., Ren, Y., Foygel, K., Rosenberg, J. & Willmann, J. K. Tumor angiogenic marker expression levels during tumor growth: longitudinal assessment with molecularly targeted microbubbles and US imaging. *Radiology* **258**, 804–11 (2011).

412. Mancini, M. *et al.* Imaging of thyroid tumor angiogenesis with microbubbles targeted to vascular endothelial growth factor receptor type 2 in mice. *BMC Med. Imaging* **13**, (2013).

413. Decano, J. L., Moran, A. M., Ruiz-Opazo, N. & Herrera, V. L. M. Molecular imaging of vasa vasorum neovascularization via DEspR-targeted contrast-enhanced ultrasound micro-imaging in transgenic atherosclerosis rat model. *Mol. imaging Biol.* **13**, 1096–106 (2011).

414. Tardy, I. *et al.* Ultrasound molecular imaging of VEGFR2 in a rat prostate tumor model using BR55. *Invest. Radiol.* **45**, 573–578 (2010).

415. Klibanov, A. L. *et al.* Targeted ultrasound contrast agent for molecular imaging of inflammation in high-shear flow. *Contrast Media Mol. Imaging* **1**, 259–266 (2006).

416. Guenther, F. *et al.* An ultrasound contrast agent targeted to P-selectin detects activated platelets at supra-arterial shear flow conditions. *Invest. Radiol.* **45**, 586–91 (2010).

417. Günther, F. *et al.* Dual targeting improves capture of ultrasound microbubbles towards activated platelets but yields no additional benefit for imaging of arterial thrombosis. *Sci. Rep.* **7**, (2017).

418. Deshpande, N. *et al.* Quantification and monitoring of inflammation in murine inflammatory bowel disease with targeted contrast-enhanced US. *Radiology* **262**, 172–80 (2012).

419. Chadderdon, S. M. *et al.* Proinflammatory endothelial activation detected by molecular imaging in obese nonhuman primates coincides with onset of insulin resistance and progressively increases with duration of insulin resistance. *Circulation* **129**, 471–478 (2014).

420. Bachmann, C. *et al.* Targeting Mucosal Addressin Cellular Adhesion Molecule (MAdCAM)-1 to Noninvasively Image Experimental Crohn's Disease. *Gastroenterology* **130**, (2006).

421. Weller, G. E. R., Villanueva, F. S., Tom, E. M. & Wagner, W. R. Targeted ultrasound contrast agents: In vitro assessment of endothelial dysfunction and multi-targeting to ICAM-1 and sialyl Lewisx. *Biotechnol. Bioeng.* **92**, 780–788 (2005).

422. Korpanty, G., Grayburn, P. A., Shohet, R. V & Brekken, R. A. Targeting vascular endothelium with avidin microbubbles. *Ultrasound Med. Biol.* **31**, 1279–83 (2005).

423. Wang, X. *et al.* Novel single-chain antibody-targeted microbubbles for molecular ultrasound imaging of thrombosis: Validation of a unique noninvasive method for rapid and sensitive detection of thrombi and monitoring of success or failure of thrombolysis in mice. *Circulation* **125**, 3117–3126 (2012).

424. Yeh, J. S.-M. *et al.* A Targeting Microbubble for Ultrasound Molecular Imaging. *PLoS One* **10**, e0129681 (2015).

425. Borden, M. A., Streeter, J. E., Sirsi, S. R. & Dayton, P. A. In vivo demonstration of cancer molecular imaging with ultrasound radiation force and buried-ligand microbubbles. *Mol. Imaging* **12**, (2013).

426. Anderson, C. R. *et al.* ScVEGF microbubble ultrasound contrast agents: A novel probe for

ultrasound molecular imaging of tumor angiogenesis. *Invest. Radiol.* **45**, 579–585 (2010).

427. Thurber, G. M., Schmidt, M. M. & Wittrup, K. D. Antibody tumor penetration: Transport opposed by systemic and antigen-mediated clearance. *Advanced Drug Delivery Reviews* vol. 60 1421–1434 (2008).

428. Takalkar, A. M., Klibanov, A. L., Rychak, J. J., Lindner, J. R. & Ley, K. Binding and detachment dynamics of microbubbles targeted to P-selectin under controlled shear flow. *J. Control. Release* **96**, 473–482 (2004).

429. Wu, J. *et al.* Efficacy of Contrast-enhanced US and Magnetic Microbubbles Targeted to Vascular Cell Adhesion Molecule–1 for Molecular Imaging of Atherosclerosis. *Radiology* **260**, 463–471 (2011).

430. Yang, F. Y. *et al.* Focused ultrasound and interleukin-4 receptor-targeted liposomal doxorubicin for enhanced targeted drug delivery and antitumor effect in glioblastoma multiforme. *J. Control. Release* **160**, 652–658 (2012).

431. Fan, C. H. *et al.* Antiangiogenic-targeting drug-loaded microbubbles combined with focused ultrasound for glioma treatment. *Biomaterials* **34**, 2142–2155 (2013).

432. Fan, C. H. *et al.* Folate-conjugated gene-carrying microbubbles with focused ultrasound for concurrent blood-brain barrier opening and local gene delivery. *Biomaterials* **106**, 46–57 (2016).

433. Chang, E. L. *et al.* Angiogenesis-targeting microbubbles combined with ultrasound-mediated gene therapy in brain tumors. *J. Control. Release* **255**, 164–175 (2017).

434. Sennoga, C. A. *et al.* On Sizing and Counting of Microbubbles Using Optical Microscopy. *Ultrasound Med. Biol.* **36**, 2093–2096 (2010).

435. Gosk, S., Moos, T., Gottstein, C. & Bendas, G. VCAM-1 directed immunoliposomes selectively target tumor vasculature in vivo. *Biochim. Biophys. Acta - Biomembr.* **1778**, 854–863 (2008).

436. Poste, G., Doll, J., Hart, I. R. & Fidler, I. J. In vitro selection of murine B16 melanoma variants with enhanced tissue-invasive properties. *Cancer Res.* **40**, 1636–44 (1980).

437. Zhang, C., Zhang, F., Tsan, R. & Fidler, I. J. Transforming growth factor-β2 is a molecular determinant for site-specific melanoma metastasis in the brain. *Cancer Res.* **69**, 828–835 (2009).

438. Perepelkina, O. V., Golibrodo, V. A., Lilp, I. G. & Poletaeva, I. I. Mice selected for large and small brain weight: The preservation of trait differences after the selection was discontinued. *Adv. Biosci. Biotechnol.* **04**, 1–8 (2013).

439. Hahne, M., Lenter, M., Jäger, U. & Vestweber, D. A novel soluble form of mouse VCAM-1 is generated from a glycolipid-anchored splicing variant. *Eur. J. Immunol.* **24**, 421–8 (1994).

440. Hammelrath, L. *et al.* Morphological maturation of the mouse brain: An in vivo MRI and histology investigation. *Neuroimage* **125**, 144–152 (2016).

441. Shapiro, E. M. *et al.* MRI detection of single particles for cellular imaging. *Proc. Natl. Acad. Sci. U. S. A.* **101**, 10901–10906 (2004).

442. Song, K. H., Harvey, B. K. & Borden, M. A. State-of-the-art of microbubble-assisted blood-brain barrier disruption. *Theranostics* vol. 8 4393–4408 (2018).

443. Tsai, H. C. *et al.* Safety evaluation of frequent application of microbubble-enhanced focused ultrasound blood-brain-barrier opening. *Sci. Rep.* **8**, (2018).

444. Monnier, J. *et al.* Expression, Regulation and Function of Atypical Chemerin Receptor

CCRL2 on Endothelial Cells. *J. Immunol.* **189**, (2012).

445. Schindelin, J. *et al.* Fiji: an open-source platform for biological-image analysis. *Nat. Methods* **9**, 676–682 (2012).

446. Ballermann, B. J., Dardik, A., Eng, E. & Liu, A. Shear stress and the endothelium. in *Kidney International, Supplement* vol. 54 S100–S108 (Elsevier, 1998).

447. Remuzzi, A. *et al.* Three-dimensional reconstructed glomerular capillary network: Blood flow distribution and local filtration. *Am. J. Physiol. - Ren. Fluid Electrolyte Physiol.* **263**, (1992).

448. Sakariassen, K. S., Orning, L. & Turitto, V. T. The impact of blood shear rate on arterial thrombus formation. *Futur. Sci. OA* **1**, FSO30 (2015).

449. Blamire, A. M. *et al.* Interleukin-1beta -induced changes in blood-brain barrier permeability, apparent diffusion coefficient, and cerebral blood volume in the rat brain: a magnetic resonance study. *J. Neurosci.* **20**, 8153–9 (2000).

450. Cheng, V. W. T. *et al.* VCAM-1–targeted MRI Enables Detection of Brain Micrometastases from Different Primary Tumors. *Clin. Cancer Res.* **25**, 533–543 (2019).

451. Kitic, M. *et al.* Intrastriatal injection of interleukin-1 beta triggers the formation of neuromyelitis optica-like lesions in NMO-IgG seropositive rats. *Acta Neuropathol. Commun.* **1**, 5 (2013).

452. Manning, C. F., Bundros, A. M. & Trimmer, J. S. Benefits and pitfalls of secondary antibodies: Why choosing the right secondary is of primary importance. *PLoS One* **7**, (2012).

453. Golding, H., Cuchens, M. A., Leslie, G. A. & Rittenberg, M. B. Cross-reactivity of rat, mouse, and human IgD. *J. Immunol.* **123**, 2751–5 (1979).

454. Takeda, S., Sato, N. & Morishita, R. Systemic inflammation, blood-brain barrier vulnerability and cognitive/non-cognitive symptoms in Alzheimer disease: relevance to pathogenesis and therapy. *Front. Aging Neurosci.* **6**, 171 (2014).

455. Lopez-Ramirez, M. A. *et al.* MicroRNA-155 negatively affects blood–brain barrier function during neuroinflammation. *FASEB J.* **28**, 2551–2565 (2014).

456. Sonar, S. A. & Lal, G. Blood-brain barrier and its function during inflammation and autoimmunity. *J. Leukoc. Biol.* **103**, 839–853 (2018).

457. Varatharaj, A. & Galea, I. The blood-brain barrier in systemic inflammation. *Brain. Behav. Immun.* **60**, 1–12 (2017).

458. Smith, N. M. *et al.* Inflammation and blood-brain barrier breach remote from the primary injury following neurotrauma. *J. Neuroinflammation* **15**, 201 (2018).

459. Fiala, M. *et al. TNF-a Opens a Paracellular Route for HIV-1 Invasion across the Blood-Brain Barrier*. https://www.ncbi.nlm.nih.gov/pmc/articles/PMC2230176/pdf/molmed00032-0069.pdf (1997).

460. Duchini, A., Govindarajan, S., Santucci, M., Zampi, G. & Hofman, F. M. Effects of tumor necrosis factor-alpha and interleukin-6 on fluid-phase permeability and ammonia diffusion in CNS-derived endothelial cells. *J. Investig. Med.* **44**, 474–82 (1996).

461. De Vries, H. E. *et al. The influence of cytokines on the integrity of the blood-brain barrier in vitro*. *Journal of Neuroimmunology* vol. 64 https://www.jni-journal.com/article/0165-5728(95)00148-4/pdf (1996).

462. Gloor, S. M., Weber, A., Adachi, N. & Frei, K. Interleukin-1 Modulates Protein Tyrosine Phosphatase Activity and Permeability of Brain Endothelial Cells. *Biochem. Biophys. Res.*

Commun. **239**, 804–809 (1997).

463. Albulescu, R. *et al.* Cytokine patterns in brain tumour progression. *Mediators Inflamm.* **2013**, 979748 (2013).

464. Sowers, J. L., Johnson, K. M., Conrad, C., Patterson, J. T. & Sowers, L. C. The Role of Inflammation in Brain Cancer. in 75–105 (Springer, Basel, 2014). doi:10.1007/978-3-0348-0837-8_4.

465. Kruse, C. *et al.* Chronic inflammation drives glioma growth: cellular and molecular factors responsible for an immunosuppressive microenvironment. *Neuroimmunol. Neuroinflammation* **1**, 66 (2014).

466. Doron, H., Pukrop, T. & Erez, N. A Blazing Landscape: Neuroinflammation Shapes Brain Metastasis. *Cancer Res.* **79**, 423–436 (2019).

467. Berghoff, A. S., Venur, V. A., Preusser, M. & Ahluwalia, M. S. Immune Checkpoint Inhibitors in Brain Metastases: From Biology to Treatment. *Am. Soc. Clin. Oncol. Educ. B.* e116–e122 (2016) doi:10.1200/EDBK_100005.

468. Berghoff, A. S. & Preusser, M. The inflammatory microenvironment in brain metastases: potential treatment target? *Chinese Clin. Oncol.* **4**, (2015).

469. Sankowski, R., Mader, S. & Valdés-Ferrer, S. I. Systemic Inflammation and the Brain: Novel Roles of Genetic, Molecular, and Environmental Cues as Drivers of Neurodegeneration. *Front. Cell. Neurosci.* **9**, 28 (2015).

470. Amor, S., Puentes, F., Baker, D. & van der Valk, P. Inflammation in neurodegenerative diseases. *Immunology* **129**, 154–69 (2010).

471. Scolding, N. RECOGNISING AND DIAGNOSING INFLAMMATORY BRAIN DISEASE. *J. Neurol. Neurosurg. Psychiatry* **85**, e3–e3 (2014).

472. Pardridge, W. M. The Blood-Brain Barrier: Bottleneck in Brain Drug Development. *J. Am. Soc. Exp. Neurother.* **2**, 3–14 (2005).

473. *IUPAC. Compendium of Chemical Terminology, 2nd ed. (the 'Gold Book'). Compiled by A. D. McNaught and A. Wilkinson. Blackwell Scientific Publications, Oxford (1997). Online version (2019-) created by S. J. Chalk.IUPAC. Compendium of Chemical Terminology, 2. Choice Reviews Online* vol. 39 (2013).

474. Wymann, M. P. & Schneiter, R. Lipid signalling in disease. *Nat. Rev. Mol. Cell Biol.* **9**, 162–176 (2008).

475. Subramaniam, S. *et al.* Bioinformatics and Systems Biology of the Lipidome. *Chem. Rev.* **111**, 6452–6490 (2011).

476. Farine, L., Niemann, M., Schneider, A. & Bütikofer, P. Phosphatidylethanolamine and phosphatidylcholine biosynthesis by the Kennedy pathway occurs at different sites in Trypanosoma brucei OPEN. *Nat. Sci. Reports* **5**, 1–11 (2015).

477. Abou-Saleh, R. H., Swain, M., Evans, S. D. & Thomson, N. H. Poly(ethylene glycol) Lipid-Shelled Microbubbles: Abundance, Stability, and Mechanical Properties. *Langmuir* **30**, 5557–5563 (2014).

478. Spector, A. & Yorek, M. Membrane lipid composition and cellular function. *J. Lipid Res.* **26**, 1015–1035 (1985).

479. Mishkind, M. Phosphatidylethanolamine - In a pinch. *Trends in Cell Biology* vol. 10 368 (2000).

480. Vénien, C. & Le Grimellec, C. The involvement of cytoskeletal proteins in the maintenance

of phospholipid topology in renal brush-border membranes. *BBA - Biomembr.* **946**, 307–314 (1988).

481. Higgins, J. A. & Evans, W. H. Transverse organization of phospholipids across the bilayer of plasma-membrane subfractions of rat hepatocytes. *Biochem. J.* **174**, 563–567 (1978).

482. Schick, P. K., Kurica, K. B. & Chacko, G. K. Location of phosphatidylethanolamine and phosphatidylserine in the human platelet plasma membrane. *J. Clin. Invest.* **57**, 1221–1226 (1976).

483. WHITE & A., D. The phospholipid composition of mammalian tissues. *Form Funct. Phospholipids* 441–482 (1973).

484. Ferrell, J. E., Lee, K. J. & Huestis, W. H. Lipid transfer between phosphatidylcholine vesicles and human erythrocytes: exponential decrease in rate with increasing acyl chain length. *Biochemistry* **24**, 2857–2864 (1985).

485. Seelig, J. Deuterium magnetic resonance: Theory and application to lipid membranes. *Q. Rev. Biophys.* **10**, 353–418 (1977).

486. Seelig, A. & Seelig, J. Dynamic structure of fatty acyl chains in a phospholipid bilayer measured by deuterium magnetic resonance. *Biochemistry* **13**, 4839–4845 (1974).

487. Seelig, J. & Niederberger, W. Deuterium-Labeled Lipids as Structural Probes in Liquid Crystalline Bilayers. A Deuterium Magnetic Resonance Study. *J. Am. Chem. Soc.* **96**, 2069–2072 (1974).

488. Chapman, D. Phase transitions and fluidity characteristics of lipids and cell membranes. *Q. Rev. Biophys.* **8**, 185 (1975).

489. Bittman, R. & Blau, L. Phospholipid-cholesterol interaction. Kinetics of water permeability in liposomes. *Biochemistry* **11**, 4831–4839 (1972).

490. Carruthers, A. & Melchior, D. L. Studies of the Relationship between Bilayer Water Permeability and Bilayer Physical State. *Biochemistry* **22**, 5797–5807 (1983).

491. Huang, L. & Pagano, R. E. Interaction of phospholipid vesicles with cultured mammalial cells. I. Characteristics of uptake. *J. Cell Biol.* **67**, 38–48 (1975).

492. Pagano, R. E. & Huang, L. Interaction of phospholipid vesicles with cultured mammalian cells. II. Studies of mechanism. *J. Cell Biol.* **67**, 49–60 (1975).

493. Sandra, A. & Pagano, R. E. Liposome-cell interactions: studies of lipid transfer using isotopically asymmetric vesicles. *J. Biol. Chem.* **254**, 2244–2249 (1979).

494. Sleight, R. G. & Pagano, R. E. Transport of a fluorescent phosphatidylcholine analog from the plasma membrane to the Golgi apparatus. *J. Cell Biol.* **99**, 742–51 (1984).

495. Schroeder, F., Holland, J. F. & Vagelos, P. R. Physical properties of membranes isolated from tissue culture cells with altered phospholipid composition. *J. Biol. Chem.* **251**, 6747–56 (1976).

496. Sleight, R. G. & Pagano, R. E. Transbilayer movement of a fluorescent phosphatidylethanolamine analogue across the plasma membranes of cultured mammalian cells. *J. Biol. Chem.* **260**, 1146–54 (1985).

497. Pagano, R. E. & Longmuir, K. J. Phosphorylation, transbilayer movement, and facilitated intracellular transport of diacylglycerol are involved in the uptake of a fluorescent analog of phosphatidic acid by cultured fibroblasts. *J. Biol. Chem.* **260**, 1909–16 (1985).

498. Vanderkooi, J., Fischkoff, S. & Chance, B. Fluorescent probe analysis of the lipid architecture of natural and experimental cholesterol-rich membranes. *Biochemistry* **13**, 1589–

1595 (1974).

499. Rintoul, D. A., Sklar, L. A. & Simoni, R. D. Membrane lipid modification of chinese hamster ovary cells. Thermal properties of membrane phospholipids. *J. Biol. Chem.* **253**, 7447–52 (1978).

500. Simon, I., Burns, C. P. & Spector, A. A. Electron spin resonance studies on intact cells and isolated lipid droplets from fatty acid-modified L1210 murine leukemia. *Cancer Res.* **42**, 2715–21 (1982).

501. King, M. E. & Spector, A. A. Effect of specific fatty acyl enrichments on membrane physical properties detected with a spin label probe. *J. Biol. Chem.* **253**, 6493–501 (1978).

502. Maulucci, G. *et al.* Fatty acid-related modulations of membrane fluidity in cells: detection and implications. *Free Radic. Res.* **50**, S40–S50 (2016).

503. Luan, Y. *et al.* Lipid shedding from single oscillating microbubbles. *Ultrasound Med. Biol.* **40**, 1834–46 (2014).

504. Loughian, C. Der *et al.* Jumping acoustic bubbles on lipid bilayers. *Soft Matter* **11**, 3460–3469 (2015).

505. Tartis, M. S. *et al.* Dynamic microPET imaging of ultrasound contrast agents and lipid delivery. *J. Control. Release* **131**, 160–6 (2008).

506. Hu, Y., Wan, J. M. F. & Yu, A. C. H. Membrane Perforation and Recovery Dynamics in Microbubble-Mediated Sonoporation. *Ultrasound Med. Biol.* **39**, 2393–2405 (2013).

507. van Wamel, A. *et al.* Vibrating microbubbles poking individual cells: Drug transfer into cells via sonoporation. *J. Control. Release* **112**, 149–155 (2006).

508. van Wamel, A., Bouakaz, A., Versluis, M. & de Jong, N. Micromanipulation of endothelial cells: Ultrasound-microbubble-cell interaction. *Ultrasound Med. Biol.* **30**, 1255–1258 (2004).

509. Yamamoto, K. & Ando, J. Endothelial cell and model membranes respond to shear stress by rapidly decreasing the order of their lipid phases. *J. Cell Sci.* **126**, 1227–1234 (2013).

510. Haidekker, M. A., L'Heureux, N. & Frangos, J. A. Fluid shear stress increases membrane fluidity in endothelial cells: a study with DCVJ fluorescence. *Am. J. Physiol. Circ. Physiol.* **278**, H1401–H1406 (2000).

511. Butler, P. J., Norwich, G., Weinbaum, S. & Chien, S. Shear stress induces a time- and position-dependent increase in endothelial cell membrane fluidity. *Am. J. Physiol. Physiol.* **280**, C962–C969 (2001).

512. Watanabe, H. *et al.* Alterations of human erythrocyte membrane fluidity by oxygen-derived free radicals and calcium. *Free Radic. Biol. Med.* **8**, 507–14 (1990).

513. Chen, X., Leow, R. S., Hu, Y., Wan, J. M. F. & Yu, A. C. H. Single-site sonoporation disrupts actin cytoskeleton organization. *J. R. Soc. Interface* **11**, 20140071 (2014).

514. Fan, Z., Liu, H., Mayer, M. & Deng, C. X. Spatiotemporally controlled single cell sonoporation. *Proc. Natl. Acad. Sci.* **109**, 16486–16491 (2012).

515. Leow, R. S., Wan, J. M. F. & Yu, A. C. H. Membrane blebbing as a recovery manoeuvre in site-specific sonoporation mediated by targeted microbubbles. *J. R. Soc. Interface* **12**, 20150029 (2015).

516. Tran, T. A., Le Guennec, J. Y., Bougnoux, P., Tranquart, F. & Bouakaz, A. Characterization of cell membrane response to ultrasound activated microbubbles. *IEEE Trans. Ultrason. Ferroelectr. Freq. Control* **55**, 44–49 (2008).

517. Kumon, R. E. *et al.* Spatiotemporal effects of sonoporation measured by real-time calcium imaging. *Ultrasound Med. Biol.* **35**, 494–506 (2009).

518. Israelachvili, J. N., Mitchell, D. J. & Ninham, B. W. Theory of self-assembly of hydrocarbon amphiphiles into micelles and bilayers. *J. Chem. Soc. Faraday Trans. 2* **72**, 1525 (1976).

519. Needham, D., Anyarambhatla, G., Kong, G. & Dewhirst, M. W. A new temperature-sensitive liposome for use with mild hyperthermia: characterization and testing in a human tumor xenograft model. *Cancer Res.* **60**, 1197–201 (2000).

520. Chi, L.-M., Wu, W., Kuo-Li Paul Sung & Chien, S. Biophysical correlates of lysophosphatidylcholine- and ethanol-mediated shape transformation and hemolysis of human erythrocytes. Membrane viscoelasticity and NMR measurement. *Biochim. Biophys. Acta - Biomembr.* **1027**, 163–171 (1990).

521. Golan, D, E., Furlong, S, T., Brown, C, S. & Caulfield, J, P. Monopalmitoylphosphatidylcholine incorporation into human erythrocyte ghost membranes causes protein and lipid immobilization and cholesterol depletion. *Biochemistry* **27**, 2661–2667 (1988).

522. May, S. A molecular model for the line tension of lipid membranes. *Eur. Phys. J. E* **3**, 37–44 (2000).

523. Karjiban, R. A., Shaari, N. S., Gunasakaran, U. V. & Basri, M. A Coarse-Grained Molecular Dynamics Study of DLPC, DMPC, DPPC, and DSPC Mixtures in Aqueous Solution. *J. Chem.* **2013**, (2013).

524. Parasassi, T., De Stasio, G., Ravagnan, G., Rusch, R. M. & Gratton, E. Quantitation of lipid phases in phospholipid vesicles by the generalized polarization of Laurdan fluorescence. *Biophys. J.* **60**, 179–89 (1991).

525. Kim, H. M. *et al.* A Two-Photon Fluorescent Probe for Lipid Raft Imaging: C-Laurdan. *ChemBioChem* **8**, 553–559 (2007).

526. Sezgin, E., Waithe, D., Bernardino De La Serna, J. & Eggeling, C. Spectral imaging to measure heterogeneity in membrane lipid packing. *ChemPhysChem* **16**, (2015).

527. Aron, M. *et al.* Spectral imaging toolbox: segmentation, hyperstack reconstruction, and batch processing of spectral images for the determination of cell and model membrane lipid order. *BMC Bioinformatics* **18**, 254 (2017).

528. Carugo, D., Owen, J., Crake, C., Lee, J. Y. & Stride, E. Biologicallyand acoustically compatible chamber for studying ultrasound-mediated delivery of therapeutic compounds. *Ultrasound Med. Biol.* **41**, 1927–1937 (2015).

529. Riccardi, C. & Nicoletti, I. Analysis of apoptosis by propidium iodide staining and flow cytometry. *Nat. Protoc.* **11**, 1458–1461 (2006).

530. Uggeri, J. *et al.* Calcein-AM is a detector of intracellular oxidative activity. *Histochem. Cell Biol.* **122**, 499–505 (2000).

531. Otsu, N. A Threshold Selection Method from Gray-Level Histograms. *IEEE Trans. Syst. Man. Cybern.* **9**, 62–66 (1979).

532. Lyon, P. C. *et al.* Clinical trial protocol for TARDOX: a phase I study to investigate the feasibility of targeted release of lyso-thermosensitive liposomal doxorubicin (ThermoDox®) using focused ultrasound in patients with liver tumours. *J. Ther. ultrasound* **5**, 28 (2017).

533. Ríos-Marco, P., Marco, C., Gálvez, X., Jiménez-López, J. M. & Carrasco, M. P. Alkylphospholipids: An update on molecular mechanisms and clinical relevance. *Biochim.*

Biophys. Acta - Biomembr. **1859**, 1657–1667 (2017).

534. Jaffrès, P.-A. *et al.* Alkyl ether lipids, ion channels and lipid raft reorganization in cancer therapy. *Pharmacol. Ther.* **165**, 114–131 (2016).

535. Aron, M. Investigating the role of microbubble composition in ultrasound mediated drug delivery. (2018).

536. Choi, J., Pernot, M., Brown, T. R., Small, S. A. & Konofagou, E. E. Spatio-temporal analysis of molecular delivery through the blood–brain barrier using focused ultrasound. *Phys. Med. Biol.* **52**, 5509–5530 (2007).

537. Langer, R. Drug delivery and targeting. *Nature* **392**, 5–10 (1998).

538. Paul, S. M. *et al.* How to improve RD productivity: The pharmaceutical industry's grand challenge. *Nature Reviews Drug Discovery* vol. 9 203–214 (2010).

539. Adams, C. P. & Brantner, V. V. Spending on new drug development. *Health Econ.* **19**, 130–141 (2010).

540. Adams, C. P. & Brantner, V. V. Estimating The Cost Of New Drug Development: Is It Really $802 Million? *Health Aff.* **25**, 420–428 (2006).

541. DiMasi, J. A., Hansen, R. W. & Grabowski, H. G. The price of innovation: new estimates of drug development costs. *J. Health Econ.* **22**, 151–85 (2003).

542. Harrison, C. The patent cliff steepens. *Nat. Rev. Drug Discov.* **10**, 12–13 (2011).

543. Stride, E. & Edirisinghe, M. Novel microbubble preparation technologies. *Soft Matter* **4**, 2350–2359 (2008).

544. Martin, K. H. & Dayton, P. A. Current Status and Prospects for Microbubbles in Ultrasound Theranostics. doi:10.1002/wnan.1219.

545. *Advice Statement: Is magnetic resonance guided focused ultrasound surgery (MRgFUS) for the treatment of uterine fibroids clinically effective, safe and cost effective compared with uterine artery embolisation (UAE), myomectomy and hysterectomy?* (2015).

546. Sampson, J. H. *et al.* Colocalization of gadolinium-diethylene triamine pentaacetic acid with high-molecular-weight molecules after intracerebral convection-enhanced delivery in humans. *Neurosurgery* **69**, 668–676 (2011).

547. Yang, Y. *et al.* Cavitation dose painting for focused ultrasound-induced blood-brain barrier disruption. *Sci. Rep.* **9**, (2019).

548. Marquet, F. *et al.* Real-time, transcranial monitoring of safe blood-brain barrier opening in non-human primates. *PLoS One* **9**, (2014).

549. Gorick, C. M., Sheybani, N. D., Curley, C. T. & Price, R. J. Listening in on the microbubble crowd: Advanced acoustic monitoring for improved control of blood-brain barrier opening with focused ultrasound. *Theranostics* vol. 8 2988–2991 (2018).

550. Burgess, M. T., Apostolakis, I. & Konofagou, E. E. Power cavitation-guided blood-brain barrier opening with focused ultrasound and microbubbles. *Phys. Med. Biol.* **63**, 065009 (2018).

551. Hattori, M. *et al.* Mechanisms of glomerular macrophage infiltration in lipid-induced renal injury. *Kidney Int.* **56**, S47–S50 (1999).

552. Kita, T. *et al.* Oxidized LDL and expression of monocyte adhesion molecules. *Diabetes Res. Clin. Pract.* **45**, 123–126 (1999).

553. Khan, B. V, Parthasarathy, S. S., Alexander, R. W. & Medford, R. M. *Modified Low Density*

*Lipoprotein and Its Constituents Augment Cytokine-activated Vascular Cell Adhesion Molecule-I Gene Expression in Human Vascular Endothelial Cells lipoprotein X fatty acid hydroperoxide-adhesion * oxidation * endothe-lium*. *Clin. Invest* vol. 95 https://pdfs.semanticscholar.org/61db/6e130bb0a4e8e5113bb11d64d6ad2e26eaf3.pdf (1995).

554. Kita, T. *et al.* Induction of endothelial platelet-derived growth factor-B-chain and intercellular adhesion molecule-1 by lysophosphatidylcholine. in *Annals of the New York Academy of Sciences* vol. 811 70–75 (Blackwell Publishing Inc., 1997).

555. Kume, N., Cybulsky, M. I. & Gimbrone, M. A. Lysophosphatidylcholine, a component of atherogenic lipoproteins, induces mononuclear leukocyte adhesion molecules in cultured human and rabbit arterial endothelial cells. *J. Clin. Invest.* **90**, 1138–1144 (1992).

556. Zhu, Y., Lin, J. H.-C., Liao, H.-L., Verna, L. & Stemerman, M. B. Activation of ICAM-1 promoter by lysophosphatidylcholine: Possible involvement of protein tyrosine kinases. *Biochim. Biophys. Acta - Lipids Lipid Metab.* **1345**, 93–98 (1997).

557. Kume, N. & Gimbrone, M. A. Lysophosphatidylcholine transcriptionally induces growth factor gene expression in cultured human endothelial cells. *J. Clin. Invest.* **93**, 907–911 (1994).

558. Cooper, G. *The Cell: A Molecular Approach. 2nd edition. 2000*. (Sinauer Associates: Sunderland (MA)).

559. Alberts, B., Johnson, A. & Lewis, J. *Molecular Biology of the Cell. 4th edition*. (2002). doi:10.1038/nrm2335.